P PhD-FDTC-2018-37
The Faculty of Sciences, Technology and Communication

DISSERTATION

Defence held on 31/05/2018 in Luxembourg

to obtain the degree of

DOCTEUR DE L'UNIVERSITÉ DU LUXEMBOURG

EN PHYSIQUE

by

Alexander Michael SCHOBER
Born on 20 September 1989 in Nabburg (Germany)

ADVANCED RAMAN SPECTROSCOPY OF ULTRATHIN RNiO$_3$ FILMS

Dissertation defence committee

Prof. Dr. Jens Kreisel, dissertation supervisor
Professor, Université du Luxembourg, Luxembourg Institute of Science and Technology

Prof. Dr. Ludger Wirtz, chairman
Professor, Université du Luxembourg

Prof. Dr. Noheda Beatriz, vice-chairman
Professor, University of Gröningen

Prof. Dr. Philippe Ghosez, *member*
Professor, Université de Liège

Dr. Mael Guennou, *member*
Luxembourg Institute of Science and Technology

Abstract

The present work aims at investigating the structural properties of ultrathin rare-earth nickelate films by Raman Spectroscopy. Two remarkable cases are studied: $LaNiO_3$ deposited epitaxially on $LaAlO_3$, which shows a metal-to-insulator (MIT) transition but only in the ultrathin film regime, and $NdNiO_3$ deposited epitaxially on $NdGaO_3$ showing an upward shift of its MIT temperature by 130 K but only when deposited along the $[111]_{pc}$ direction of the substrate. The extremely small size of the films and overlap of the film and substrate signatures represent an experimental challenge, and requires the development of ingenious measurement and analysis strategies. To overcome these limitations, we propose the creation of a multidimensional dataset through depth profile acquisitions, in combination with multivariate analysis tools that were employed to extract the signature of the films. Different analysis strategies were used in both cases to adapt to the specificities of the respective samples.

For the LNO films deposited along the $[001]_{pc}$ orientation of LAO, Raman depth profile measurements in combination with a Principal Component Analysis (PCA) allowed us to dissociate the signals from the film and the substrate. The evolution of the LNO peaks does not suggest any phase transition, thus, suggesting that a mechanisms unrelated to the MIT of other nickelates is triggering the insulating state. This was further validated by *ab initio* calculations and TEM imaging. All acquired data point towards the following: as LNO becomes very thin, the surface layer ($\approx 2_{pc}$ u.c.), which is the most rigid part of the structure, imposes its structural and insulating characteristic. In the ultrathin regime this continues to a point where the surface of the film alters the interfacial unit cells of the substrate.

For the NNO films deposited along the $[111]_{pc}$ orientation of NGO, depth profile measurements in combination with a Non-negative Matrix Factorisation (NMF) allowed us to dissociate the signals from the film and the substrate. The dissociation was performed at room temperature and the acquired knowledge was then utilised to fit an entire temperature series from 5 to 390 K. Comparing the tendency of the Raman signatures with other rare-earth nickelate allowed to support the proposed position of the film in the phase diagram of nickelates by a structural measurement.

More generally, the methodology developed in this work is applicable to other systems and opens new perspectives for application of Raman spectroscopy on ultra-thin films.

Aknowledgement

The last four years that I spent at the Luxembourg Institute for Science and Technology (LIST), formerly known as the Centre de Recherche Public Gabriel Lippmann (CRPG), have been enriching in scientific, technical and social interactions. It is the continuous support and enthusiasm of all involved individuals led to the completion of the present project.

I would like to extend my sincere gratitude to Prof. Dr. Jens Kreisel for the unique opportunity to perform a Ph.D. in a young and vibrant environment such as LIST. His guidance inspired me to turn any problem I encountered into a scientific challenge while staying aware of the objectives at hand. Both his professional support and personal guidance are what allowed me to successfully complete this thesis. I could not have hoped for a better supervisor and mentor and hope that our paths will cross again in the continuation of our scientific careers.

I would also like to particularly acknowledge Dr. Mael Guennou, who has been a great co-supervisor but also a great colleague and friend during this period. His availability for my professional and personal endeavours made my time as a Ph.D. student at LIST as enjoyable as could be. His scientific input was always incredibly thorough, methodic and precise thus allowing me to follow up on challenges in a very comprehensive manner.

A special acknowledgment for the members of my *'Comité d'encadrement de Thèse'* (CET) composed of the Prof. Dr. Ludger Wirtz, Dr. Brahim Dhkil. Their guidance throughout the Ph.D. with input on the scientific direction of the project allows for a regular assessment of its performance.

I would like to thank again Prof. Dr. Ludger Wirtz for also being president of the thesis jury. Similarly I would like to extend my gratitude to both Prof. Dr. Noheda Beatriz (university of Gröningen) and Prof. Dr. Philippe Ghosez (university of Liège) for agreeing to be the vice chairman and a member of the Jury, respectively.

Furthermore, I would like to thank our collaborators from the DPMQ of the University of Geneva. Especially Prof. Dr. Jena-Marc Triscone for his substantial input of time and resources by providing all samples investigated in the present work as well as Jennifer Fowlie and Dr. Sara Catalano for growing the samples. Their support in discussion our results was essential for the output of

the present project.

A particular thank is in order for Dr. Jorge Íñiguez and Dr. Hong Jian Zhao for performing computational investigations as well as helping in the interpretations of the problematic presented in this work. It was a true pleasure to have such dedicated and passionate individuals to collaborate with.

I would also like to thank the Fond National pour la Recherche which has funded the entirety of my Ph.D. project over the last four years.

A particular thank goes to all the former, present and new colleagues at the Luxembourg Institute of Science and Technology, for their scientific, extra-scientific and social input. Especially to:

- Dr. Mads Weber for his most useful input related to the project. Ultimately it was the corridor talks that allowed us to conceptualise the methods presented in this work. His help allowed me to settle in at LIST. It is also through him that I encountered many individuals in Luxembourg.
- Shankari Nadupalli for spending the last four years alongside in the same office and always being in a good and cheerful mood.
- Carlos Escorihuela Sayalero for being a great colleague always interested in the thematics I was invested in. He deserves a particular thank for his continuous support as I started to develop the software package that eventually allowed me to perform all investigations presented in this work.
- Dr. Constance Toulouse, Cosme Milesi-Brault and Àlvar Torelló for creating an enjoyable environment throughout the end of my PhD.
- Emanuel Defay for managing the group and coordination and being available for me in times of need.
- Corinne Lavorel for all her administrative assistance.

Furthermore I would like to thank all other members of the FMT group and of the MRT unit.

A special thank goes to the friends from Luxembourg that filled my days outside of work. This concerns Fabian Mejia Pinto, Aida Horaniet Ibañez, Anastacia Georgantzopoulou and Cecilia Cassella. All of them are incredible individuals filled with compassion and humility and accepted me into their friendship. This can be extended my Turkish friends Duygu, Canaras, Aslı, Doruk as well as Gizem for all the great moments spent together. Furthermore to Abdelaziz, Laure and Jeremy for the countless hours of relaxing discussion about important and rather less important subjects.

I would like to thank my parents Helmut and Anita for encouraging me to become whatever I set out to be. Their dedication towards their children is admirable and shaped my personality as well as my devotion towards bettering it through every opportunity. I would like to extend this acknowledgement to my sisters Rafaëla and Carmen Schober, which have been supportive of me through the entirety of my scientific endeavour and make for great siblings.

Finally, I would like to bow down in humility and admiration for my wife Canan. She is by far the strongest person I have met throughout my life. She supported me every single day and showed the outmost compassion and understanding for the difficult period that the PhD thesis is. We can only be grateful when another individual has our back and makes us flourish. She has been this individual for the last four years and filled my life with joy and happiness. I am also eternally grateful to her for bringing our son to this world.

Contents

Introduction

Today's society has transited into the age of micro- and nano-technology. Every day a more performant, versatile, adaptive and economic set of technologies is required. While various steps a necessary to conceptualise a microelectronic chip, such as the design of the architecture and the development of its instruction sets, the physical building block remain a variety of transistors. The constant need for their improvement raise new challenges in the field of material sciences, more particularly the engineering of new functional materials. One material group that has attracted a lot of interest are the perovskite oxides with the formula ABO_3 [1]. The application of a physical constraints can induce a multitude of different physical properties. By physical constraint we refer to the temperature or pressure as well as electric or magnetic fields, while the induced effects could be metallic/insulator states, magnetic ordering or ferroelectricity. A strong link has been established between their structural arrangement and the properties they exhibit.

A particular subfamily of the perovskite oxides ABO_3 are the ones where B is a transition metal (TM). The TM, with its partially filled d shell, induces remarkable structural, electronic, magnetic and optical properties. Of particularly high interest is the competition between different electronic and magnetic phases [2]. These are often linked to the competition of distinct structural phases linked to the structural parameters. This is why, in transition metal oxide perovskites, the possibility to alter the structural parameters allows to fine tune the electronic or magnetic transition boundaries. A material with such a propriety could have widespread applications in the sensor or microelectronic industry and, in consequence, sparked an important amount of research in the field.

The family of Rare-earth nickel oxides (shortened as nickelates) stand in this very context. Indeed their metal-to-insulator transition is controlled by solely one structural parameter making the associated phase diagram a canonical example of the physics of phase transitions in correlated oxides [3]. The structural parameters and therefore the physical properties can be modulated through different environmental parameters such as pressure, size of the rare-earth, temperature or epitaxial strain in thin films and heterostructures. The latter has caught most of the attention in the recent years with the successful synthesis of high quality epitaxially deposited thin nickelate films. The interplay of these various parameters allows, in principle, to tune the metal-to-insulator behaviour in a nearly continuous manner.

Yet, the structural behaviour is not fully understood when it comes to epitaxially deposited thin and ultrathin films of perovskite oxides. While transmission electron microscopy (TEM), performed along to the interface planes of the heterostructure, showcase the very local structure and interface, it is limited in revealing averaged structural details. As a result no dynamical information is obtained. This is even more critical as the film gets thiner and the interface and surface layers gain in importance. Another observation that was reported through TEM measurements but not treated explicitly, is the distortion of the substrate lattice induced by the film. Yet, it is those properties that are crucial for the further understanding on how important the structural arrangement is in the physical properties of nickelates films.

We propose in this work to use Raman spectroscopy as an investigation tool to probe the behaviour of both thin nickelate films and the substrate they are epitaxially deposited on. Raman spectroscopy is a non-destructive method to measure some of the phonon vibrations of the crystal lattice. These vibration represent a fingerprint of the crystal structure and their alteration indicates structural variations. This makes Raman spectroscopy a reliable tool to investigate crystalline structures. Unfortunately, the method relies on the inelastic scattering of visible light radiation, thus is limited by the diffraction limit. This means that it does not perform exceptionally well on thin and especially ultrathin films with thicknesses down to 1.2 nm. The acquired signal is often consisting only of the bulk substrate, while the sample, because of the small interaction volume, vanishes into the noise. In this work we present a new methodology combining measurements at different sample depths (depth series acquisitions) with multivariate data analysis procedures, allowing to use the increased statistic to separate the signal coming from different layer of the sample (film and substrate).

The manuscript will be divided in four parts. The first part will consist of a bibliographic introduction to the structural particularities of the perovskites followed by the nickelate subgroup. In the second part we will do a bibliographic introduction of the Raman effect and the measurement apparatus and the physical and experimental limitations. The third part will then explain in depth the new methodology that allowed us to overcome the experimental imitations. Finally, in the last part, we will use this methodology to investigate two particular nickelate systems.

Part I

Perovskite oxides

Chapter 1

Perovskites

The mineral Perovskite, also known as calcium titanium oxide ($CaTiO_3$), was initially discovered by Prussian mineralogist Gustav Rose and in the Ural mountains of Russia and named in honour of the Russian Napoleonic-wars veteran and later minister of the interior Lev Perovski [4]. $CaTiO_3$ is only found in magma solidification when the environmental parameters did not allow for a slow cooling. The designation perovskite was later attributed to a whole family of crystals with a structural arrangement similar to $CaTiO_3$. The formulation of this subgroup is ABX_3, where A is a cation larger than the cation B, but similar in size to the anion X [1]. In this work, only oxide-type structures will be considered leading to X being O^{2-}. The most striking structural characteristic of oxide-type perovskites is the formation of BO_6 octahedra with oxygens at their edges and B-site cations at their centres. These rather rigid substructures drive most of the physical and structural properties in perovskite oxides. Improvements in experimental growth of these structures allowed the tuning of their physical properties by modifying either chemical composition or changing the environmental parameters. This led to the advent of oxide-type perovskites towards application-based research.

1.1 The Perovskite structure

The ideal ABO_3 structure in the cubic $Pm\bar{3}m$ crystallographic space group can be seen in Figure 1.1. $CaTiO_3$ is naturally found in the orthorhombic $Pnma$ space group within the $2/m\ 2/m\ 2/m$ point group [5], which can be obtained through minor distortions of the ideal cubic structure. For a perovskite to adopt the ideal cubic phase, a relation between the size of the A, B and O atoms has to be satisfied. Assuming that R_i expresses the atomic radius of the atom i, the relation can be written as:

$$R_O + R_A = \sqrt{2}(R_O + R_B). \tag{1.1.1}$$

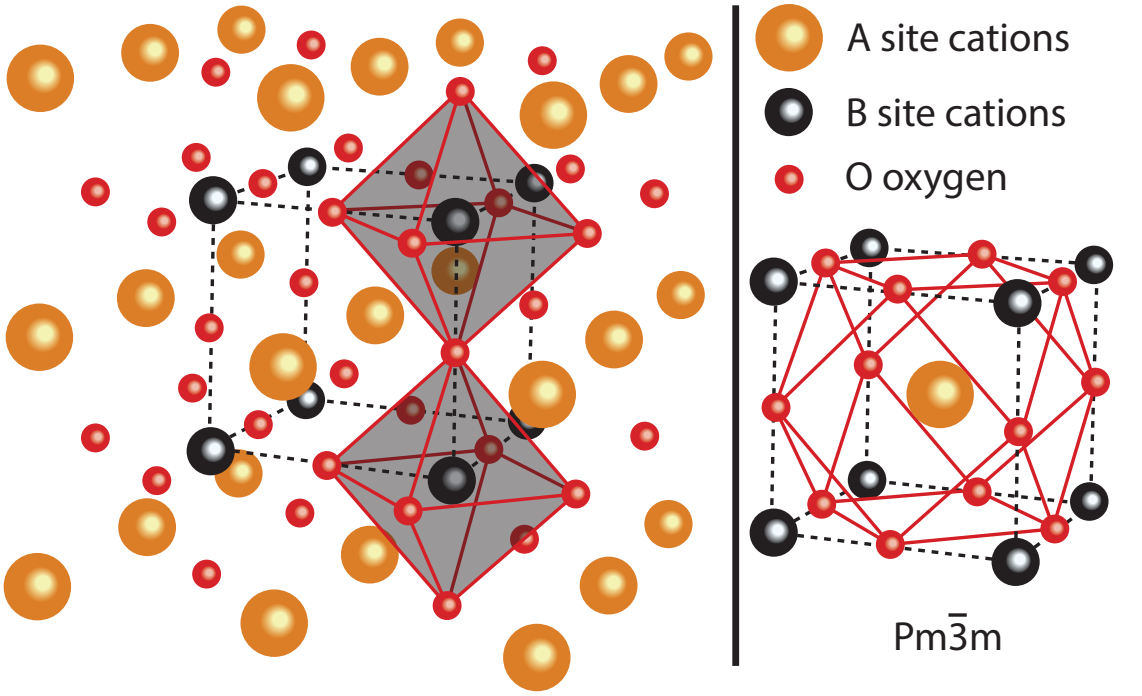

Figure 1.1 – Left: Arrangements of the atoms in a conventional cubic perovskite displaying the octahedral structure. **Right:** Arrangement of the unit cell of the perovskite ABO_3. For both parts, the size of the atoms are not to scale. In fact, the O site oxygens are usually the largest and then come the A site cations followed by the smaller B site cations.

This formulation is no more than a geometrical equation between the sides and diagonals of the perovskite structure in a cubic arrangement as seen in Figure 1.1. As already mentioned, $CaTiO_3$ does not verify this condition, thus suggesting that other perovskites with different A and B site atoms might not follow it either. This motivated Goldschmidt in 1926 [6] to introduce the tolerance factor t as an dimensionless geometrical parameter, defined as follows:

$$t = \frac{R_O + R_A}{\sqrt{2}(R_O + R_B)}. \tag{1.1.2}$$

$t = 1$ corresponds to the ideal cubic case. There are two ways to interpret the tolerance factor. Either as an indicator as to how distorted the structure will be in a perovskite arrangement, or as an indicator on how unfavourable the cubic arrangement is. It is found, that t should have a value between 0.8 and 1.2 to allow a compound of the chemical formula ABO_3 to crystallise in the perovskite structure. Further observation obtained from the tolerance factor value are the following list [1]:

- $t > 1$: in this configuration, either the A-site cation is too big or the B-site cation too small to accommodate the cubic arrangement. Values of t between 1.0 and 1.2 usually result in a

t <0.9			0.9 <t <1		
Compound	t	Space group	Compound	t	Space group
$CaTiO_3$	0.81[7]	$Pnma$[7]	$BaTiO_3$	0.93[7]	$P4mm$[7]
$LaCrO_3$	0.88[7]	$Pm\bar{3}m$[7]	$LaAlO_3$	0.94[7]	$R\bar{3}c$[7]
			$NdAlO_3$	0.90[7]	$R\bar{3}c$[7]
			$NdNiO_3$	0.971[8]	$Pbnm$[8]
			$SrTiO_3$	1.0[1]	$Pm\bar{3}m$[1]

Table 1.1 – Table of a few perovskite compounds and their calculated tolerance factor and observed space group at 300 K. It is already clear from this sample that a one to one relation between the tolerance factor and the space group does not exist.

ferroelectric instability. Above 1.2, the perovskite structure is unstable and the compound is likely to form the hexagonal polymorph.

- $0.9 < t < 1$: This represents the ideal range for t to form a perovskite structure with a cubic arrangement. This being said, some compounds adopt a rhombohedral symmetry [3].
- $0.71 < t < 0.9$: The A-site cation is small and therefore favours a rotation of the octahedra to accommodate the space. This can either result in orthorhombic or rhombohedral arrangements.

However, because of its geometric nature, thus not taking into account covalent bonds nor any other interaction mechanisms between the atoms, the tolerance factor can only be used as an approximative indicator. Some particular examples are given in Table 1.1.

The mere substitution of either one of the cations can result in different space groups as shown in Table 1.1. This is before considering the vast amount of structural modifications potentially induced by pressure, temperature or epitaxial strain. With each different space group comes a different set of basis vectors. This can, in some cases, render the comparison between structures tedious. The distortions away from the cubic unit cell is small, thus allows for the introduction of a pseudo cubic cell, defined by the approximate cubic shape of eight B-site cations. This simplified approach allows to compare structural characteristics in a comparable basis. When we express a crystal parameter within the pseudo-cubic unit cell the subscript 'pc' will be appended to it.

The most prominent feature of the perovskite structure are its oxygen octahedra. They span as a chain across the crystal with B-site cations within and A-site cations in-between them. They are the result of a strong bond of oxygens atoms with the B-site cations. It is found that they form the most rigid elementary structure of the perovskite family. As a result, they tend to be less affected by the internal or external stress that is forcing the structure to reorganise itself. This is why the most common distortion in perovskites is the tilting of these octahedra with respect to each other. In 1975 that A.M. Glazer [9] proposed a classification of perovskites relying solely on their octahedral tilt pattern along the pseudo-cubic axes. This notion will be introduced in the

following sections. This will be followed by a section relaxing the assumption on rigidity, thus introducing octahedral distortion mechanisms. Cationic displacements will also be treated.

1.2 Octahedral tilting

Within this section, it is assumed that the oxygen octahedra forming the perovskite oxide structure are rigid. As a result the oxygen octahedra can be perceived as the elementary building block. These are interconnected to each other at their edges. The only available degree of freedom is the rotation along the pseudo-cubic axes (Figure 1.2). As a direct consequence of their interconnection, a rotation of one octahedra along a basis axis induces a rotations of all other octahedra within the plane described perpendicular to this axis. On the other hand, there is no constraint of the rotation of successive octahedra along the same rotation axis. Thus leaving the possibility for in-phase or in anti-phase rotation of successive octahedral planes. The notion of phase or anti-phase refers to the same or opposite rotation sign of successive octahedra respectively. In total, 23 distinct tilt patterns are possible within the octahedra framework [11]. As a pioneer of this approach, Glazer introduced a nomenclature to classify these patterns. Commonly, three letters a, b and c, are used to specify the magnitude of the rotation along the three pseudo-cubic axes. Tilts along different axes, but of the same magnitude, will be given the same letter. Therefore, if the tilt around the first and second axes are of same magnitude they will both be denoted as a while the third one will carry the letter b. If the neighbour octahedra along the rotation axis tilt in the same direction (in phase) as the first one, the superscript $+$ will be added to the letter. On the other, hand if the tilt direction is opposite (in anti-phase), $-$ will be used. When no tilt is observed along this axis the superscript 0 is added. This nomenclature can be pictured in Figure 1.2.

Some of the mentioned tilt systems are found to be equivalent by crystal symmetry. It was discovered that the 23 tilt possibilities initially discovered by Glazer could be reduced to a mere 15 [10] . Furthermore, while keeping the condition imposed on the oxygen octahedra rigidity, the tilting motion induces a variation of distance between their respective centres. This is typically where the B-site cation is located (in a displacement free case). Because of this change in the inter octahedron distance, a reduction of the pseudo-cubic cell size is expected. If α, β and γ are considered to be the angles by which the octahedron is tilted along the pseudo-cubic axes $[100]_{pc}$, $[010]_{pc}$ and $[001]_{pc}$ respectively, the modified cell parameters can be approximated as [9]:

$$a_p = a_0 \cos(\beta)\cos(\gamma), \tag{1.2.1}$$

$$b_p = a_0 \cos(\alpha)\cos(\gamma), \tag{1.2.2}$$

$$c_p = a_0 \cos(\alpha)\cos(\beta) \tag{1.2.3}$$

where a_0 is the initial cell parameter in the cubic cell and a_p, b_p, c_p represent the new pseudo-cubic unit cell parameters. Due to geometrical continuity between successive octahedra, tilts will

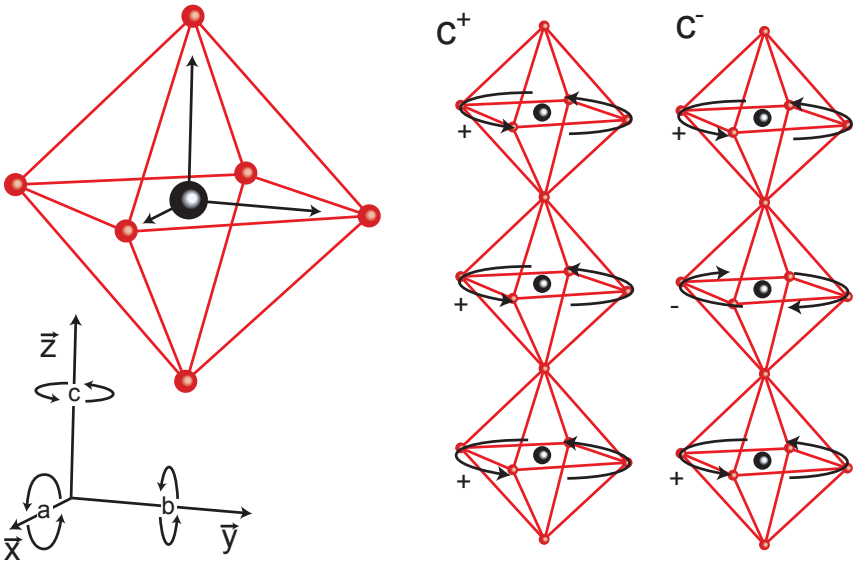

Figure 1.2 – Schematic description of the Glazer notation. Visualisation of the Glazer tilt parameters a, b and c with respect to their associated pseudo cubic directions, $\vec{x}$, $\vec{y}$ and $\vec{z}$. The two rows on the right schematically describe what is understood with the '+' and '-' superscript. In fact all octahedra rotate in phase in the same direction under '+' and in anti-phase in different directions under '-'.

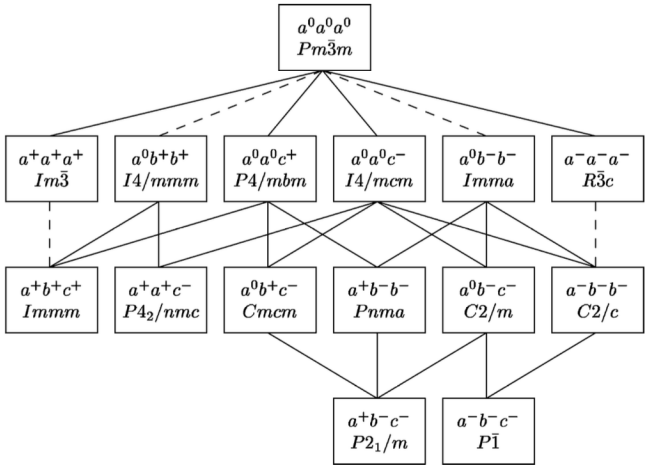

Figure 1.3 – Representation of the groups and sub-groups induced by systematic rotations of the octahedra following the Glazer notation. Symmetry analysis performed by Howard and Stokes reduces the initial 23 tilt systems to 15 [10].

effectively double these newly expressed pseudo-cubic parameters. This doubling affects the two directions perpendicular to the tilting axis. The crystallographic space groups associated to the different tilt patterns can be seen in Figure 1.3.

1.3 Octahedral distortion

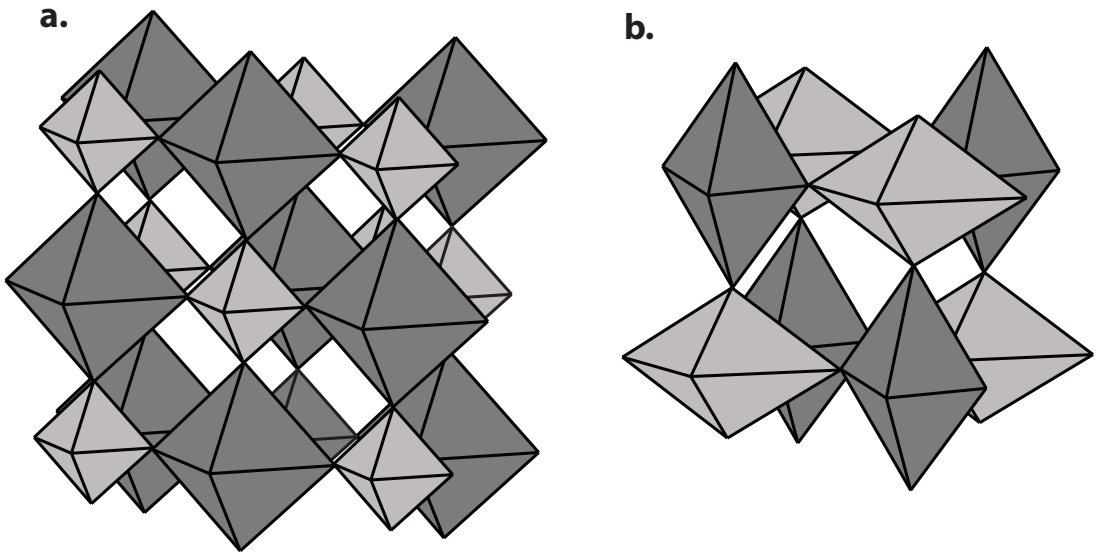

Figure 1.4 – a: Sketch of a perovskite with two different octahedra sizes. **b:** A more complex structural arrangement where the octahedra are not distorted isotropically.

The previous section discussed the tilting motions of oxide octahedra under the assumption of total rigidity. This assumption can be relaxed depending on the bonding structure of the B-site cation. An example of an octahedral distortion would be the change in size of alternating octahedra. So each one of them is connected to six other of another size as seen in Figure 1.4.**a.**. The absence of this leads to a $Fm\bar{3}m$ space group, also known under rock-salt structure.

In the last scenario the oxygen octahedra were supposed to conserve their octahedral symmetry. This is not necessarily true. It is possible that the bond interaction between the B-site cation and the oxygens forming the octahedron are not equivalent in all six directions. The strongest example of such an effect is the Jahn-Teller distortion [12] named after its discoverers H.A. Jahn and E. Teller. In this scenario the bond length of the octahedra are tightly related to the electronic configuration of the B-site transition metal such as Mn^{3+}, Cr^{2+} or Ni^{3+}. Further insight on the behaviours of the orbital structure of transition metals is given in section 1.5.1. An exaggerated sketch of such a distortion can be seen in Figure 1.4.**b.**.

1.4 Cation displacements

Another distortion away from the cubic cell is the displacement of A and B-site cations. In fact, it is possible for both cations to induce an increased covalence with the oxygens forming the oxygen octahedra. This might lead to directional bonds along corners of the octahedron for the B-site cation or plane of the cub-octahedron for the A-site cation. The displacement of all cations into the same direction effectively breaks the inversion symmetry of the system and induces a spontaneous polarisation. An exaggerated sketch of such a displacement is shown in Figure 1.5. It is this mechanism which drives the piezo-electric response in compounds such as $BaTiO_3$ [13].

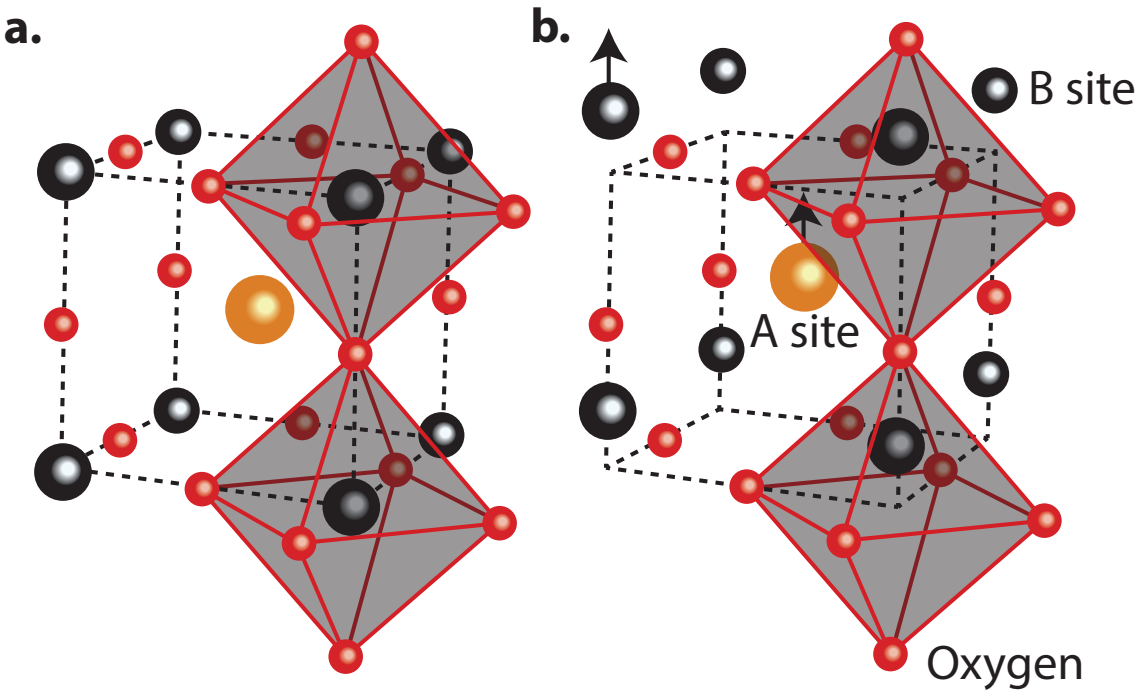

Figure 1.5 – Sketch of a cation displacement in the perovskite scturcutre.

1.5 Electric conduction in transition metal perovskite oxides

The last section focused on the geometrical understanding of how the perovskite oxide type structure can distort away from the cubic phase. The notion of octahedral tilting and distortion in combination with cation displacement were depicted as most common. Such rearrangements of the interatomic distance can also induce changes in the orbital configuration. One of the

physical properties affected by this is the electric conductivity. In fact, it has been found that metallic or insulating properties of some perovskite families such as nickelates (characterised by $R\text{NiO}_3$, where R is a rare-earth) are tightly linked to the octahedral tilting [3]. This section aims at providing some insight about the different mechanisms driving these phenomena.

Within the formalism developed by F. Bloch in 1929 [14], the definition of metallic and insulating crystal structures was introduced as a dependency on the filling state at the Fermi level. An insulator would have all level completely filled at the Fermi level, thus inhibits any mobility of the electrons within the lattice. On the other hand, a partially filled band, thus with free energy levels would result in a charge carrier mobility and, therefore, a conducting state.

While the formulation proposed by Bloch produced acceptable predictions for most cases it was found too simplistic for others. More specifically, it was unable to predict the insulating behaviour of transition metal oxides [15]. Further work on electron-electron interactions revealed their role in inducing insulating states described by the *Mott-Hubbard* insulator (Subsection 1.5.2). Another model known as *Charge Transfer* insulator (CT) considered the exchange of electrons between the transition metals and the ligands surrounding them (Subsection 1.5.3). Finally a system combining both characters is introduced in Subsection 1.5.4. All these models rely on the orbital arrangement of transition metal oxides, introduced in the following subsection.

1.5.1 Transition Metal oxides

Transition metals (TM) are characterised by their partially filled d shell [16]. Cobalt, nickel or copper are some of the elements belonging to this family. The d shell is characterised by an orbital momentum equal to 2. This leads to a five-fold degeneracy per spin: $L_Z = -2, -1, 0, 1, 2$, and therefore a ten-fold degeneracy in electron occupation states. TMs typically occupy the B-site of the perovskite structure, leading to the use of an octahedral referential to describe their orbital arrangement. The $d_{x^2-y^2}$ and d_{z^2} orbitals are oriented towards the oxygen sites of the octahedral cage. The d_{xy}, d_{yz} and d_{xy} orbitals occupy the space in between. This particular arrangement can be observed in Figure 1.6.

The degeneracy of the TM's d orbital is partially lifted through the surrounding crystal field [17]. The crystal field theory (CFT) considers the ionic characteristic of the TM as well as the ligands surrounding it. Both the metal and the ligands are described as point charges. A partial lifting of the d orbital degeneracy is observed when the CFT is applied with an octahedral crystal field onto a transition metal (TM). Because of the ionic repulsion, the $d_{x^2-y^2}$ and d_{z^2} orbitals see their energy increased above the d_{xy}, d_{yz} and d_{xy} orbitals. The two new subgroups of orbitals are called e_g and t_{2g} respectively. In light TMs such as Ti, V, and Cr only the lower t_{2g} band is partially filled. The others such as Cu and Ni are characterised by a fully occupied t_{2g} band.

The electric conduction of transition metal perovskite oxides (TMO) is associated to the mobility of the charge carriers between the partially filled d shell of the TMO and the p shell of the oxygens

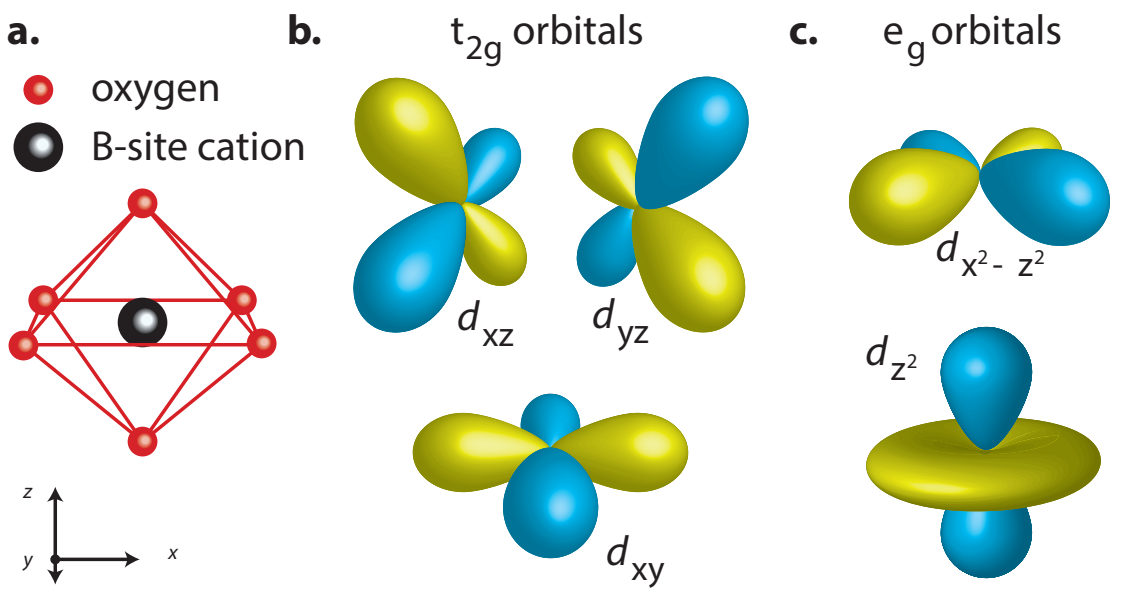

Figure 1.6 – a: Representation of the classical octahedral arrangement with the respective axes. **b:** The d_{xy}, d_{yz} and d_{xy} orbitals in their respective orientation within the octahedra perovskite structure. **c:** The $d_{x^2-y^2}$ and d_{z^2} orbitals in their respective orientation within the octahedra perovskite structure.

surrounding it. TMOs represent a rather large large group of materials with a substantial amount of structural configurations for each one of them. On top of that, there are multiple distinct mechanisms driving the conduction, therefore rendering its identification rather challenging. The following subsections will provide an introduction to the Mott-Hubbard insulator (MH), the charge transfer insulator (CT) and negative charge transfer insulator (NCT).

1.5.2 Mott-Hubbard Insulator

In the beginning of this section it was assumed that electrons are weakly or non-interacting. This pillar of the Bloch model ignores the repulsive Coulomb interaction between the electrons themselves. In 1949, N. F. Mott [18] reworked the model from an itinerant to a localised electronic regime described by the *Hubbard model*.

As an electron relocates from one position to another, a vacancy or *hole* is created at the former, while an over occupied state is created at the latter. The inter-electron Coulomb repulsion on the over occupied site corresponds to an increase of potential energy by U relative to an interaction free ground state. This leads to the opening of a gap in the band structure between a lower Hubbard (UH) and a higher Hubbard (UH) band. As a consequence, the charge carriers need a kinetic energy comparable to U to overcome this gap, without whom an insulating state is

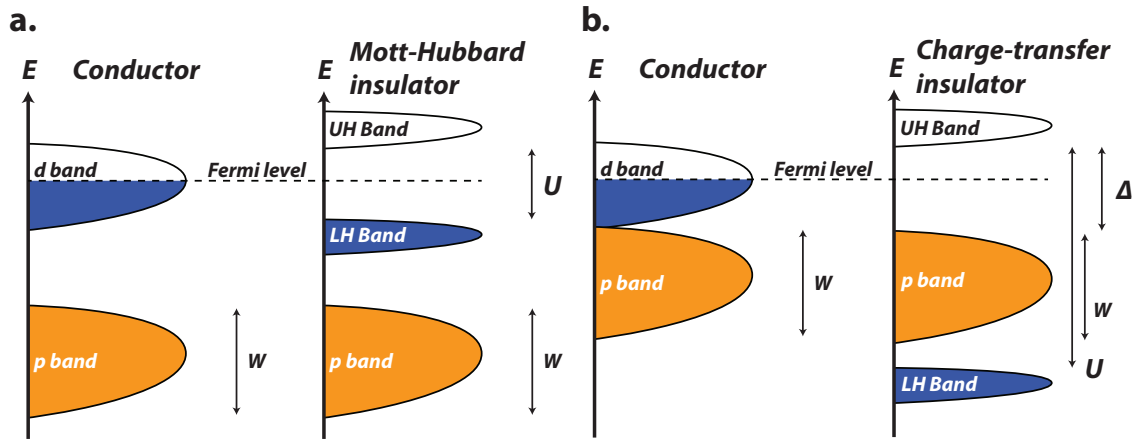

Figure 1.7 – a.Left: Conductor arrangement of the classical *d* band and the *p* band. **Right:** Mott Hubbard insulator band diagram. **b. Left:** The arrangement of the local band structure for Mott-Hubbard insulators. **Right:** Same as left but for the charge-transfer arrangement.

obtained. Taking this into account, the modified Hubbard Hamiltonian is expressed through:

$$H = -t \sum_{(i,j),\sigma} c^{\dagger}_{i,\sigma} c_{j,\sigma} + U \sum_{i} n_{i,\uparrow} n_{i,\downarrow}, \tag{1.5.1}$$

where the first term still expresses the inter site hoping of the electron as explained by the tight binding model. The second term describes the added Coulomb repulsion. The associated band diagram is presented in Figure 1.7.

1.5.3 Charge-Transfer Insulator

The previous section treated the Hubbard model as an improvement over the initial Bloch model. And yet this model only captures the variations within the same Bloch band, thus focusing on the $d-d$ inter and intra-orbital excitations. Meaning that any interaction with the neighbouring oxygens and the associated p orbital is disregarded. This is even more relevant as the d states have a relatively small bandwidth in comparison with the oxygen p states [17]. To address this, the possibility of charges migrating (often referred to as inter-site hoping) between the oxygen p band to the TM d band is considered. Such motion of an electron induces the creation of a ligand hole L at the oxygen orbital and increasing occupation state of the TM's d orbital:

$$d^n \rightarrow d^{n+1}L. \tag{1.5.2}$$

The energy required to overcome the associated barrier is called the charge transfer gap Δ.

The charge transfer gap Δ and the Mott-Hubbard gap U are considered as competing entities. As the bandwidth of the system W decreases, one of these is chosen to be the driving force

for the insulating behaviour. When $\Delta > U$ a Mott-Hubbard insulator is obtained. In the opposite case a charge-transfer insulator is obtained. This model named the ZSA scheme named after Zaanen, Sawatzky and Allen [19]. A metallic behaviour is expected when both gaps are below the kinetic energy of the electrons.

1.5.4 Negative Charge-Transfer Insulator

Transition metal oxides with high valence such as Cu^{3+}, Ni^{3+} and Fe^{4+} are not correctly described by the ZSA model introduced in the previous Subsection. All of these compounds should be characterised by a very small if not negative CT gap Δ and should be described as metallic. But it has been reported that all rare-earth nickelates except $LaNiO_3$ behave as insulators. $NaCuO_3$, which displays the same properties was extensively studied through x-ray photo-emission and absorption by Mizokawa *et al.* [20], resulting in the first accurate description of these compounds. The insulating gap is found to follow a $p-p$ interaction where the contribution comes from a $d^{n+1}L$ state strongly hybridised with the d^n configuration. Thus resulting in the following process:

$$(d^{n+1}L)_i + (d^{n+1}L)_j \rightarrow (d^{n+1}L^2)_i + (d^{n+1})_j. \tag{1.5.3}$$

This third insulator type was then added to the ZSA scheme as negative charge transfer insulators.

1.5.5 Summary on metallic and insulating behaviour

The last three subsections have shown that the electric conduction in perovskite transition metal oxides is rather complex and depends greatly on the nature of the metal oxide. The extended ZSA scheme combines the notions of *Mott-Hubbard*, *Charge Transfer* (CT) and *negative Charge Transfer* mechanisms in an attempt to accurately describe it. All of these are based on the particular TM d and oxygen p orbital interactions. One could therefore conceptualise that by changing the crystallographic symmetry and interatomic distances, it should be possible to influence the magnitude of the insulator gap or even the insulator type.

Octahedral tilting was presented as one of the mechanisms allowing the perovskite structure to relax away from the cubic phase. This tilt is a parameter having a direct effect on the inter-TM distance as well as the orbital overlap between TM t_{2g} and oxygen p orbitals, thus affecting the insulator mechanisms. One way to significantly alter the tilt parameter of a perovskite is the use of epitaxy, thus using a substrate material that imposes an in-plane constraint on the lattice constant. There are, for examples, multiple reports of tuning the metal to insulator transition in rare-earth nickelates ($RNiO_3$) [3, 21]. This can go as far as inducing phase transitions through epitaxy [22].

1.6 Control through epitaxy

1.6.1 Epitaxy

It was shown, in sections 1.2 through 1.4, what mechanisms perovskite structures have at their disposal to relieve internal stress. The main contribution being octahedral rotations and distortions with the addition of A and B-site cation displacement. In fact, it is possible to influence the structural arrangement of perovskite through external parameters such as temperature, pressure, electric or magnetic fields. Another interesting way, within the scope of nanometric structures, is the use of epitaxial strain. Coming from the greek *epi* meaning 'above' or 'upon' and *taxis* meaning 'in an ordered manner', it translates into 'arranging upon'. It is defined as the growth of a film on a crystalline substrate that imposes the growth direction and orientation to the film. This is achieved by depositing the film above the substrate while sharing the atoms of the interface so that the structural constraint imposed by the substrate is transmitted to the film. One refers to homoepitaxy when the deposited structure is similar to the substrate and of heteroepitaxy when they are not.

This section will focus on epitaxy between compounds from the perovskite oxide family, thus a homoepitaxial growth. Let there be two perovskite oxide compounds denoted $A_fB_fO_3$ and $A_sB_sO_3$. The compound with 'f' in the subscript is the film and the substrate has 's' in its subscript. The manner in which the deposition will take place is conditioned by the termination plane of the substrate. This specific plane is characterised by the atomic composition observed at the surface of the substrate. In the case of perovskite oxides, it can be either formed B_sO_2 or by the A_sO atomic planes. This two type of terminations are shown in Figure 1.8. The orientation of film deposited on the substrate depends equally on the orientation of the termination plane in respect to the pseudo cubic cell. In this work, two deposition directions will be investigated: the $[001]_{pc}$ (Figure 1.8.**c.**) and the $[111]_{pc}$ (Figure 1.8.**d.**) directions. While the first arrangement provides merely one oxygen at the interface per octahedron the second provides three.

The concept of growing thin films on top of lattice mismatched substrates was already introduced in 1945 by Frank *et al.* [23]. In the case of perovskite oxides, the lattice mismatch between the substrate and the film is expressed through the ratio of the shared pseudo cubic unit cell parameters. It was Hwang [24] who formulated the mismatch ratio as follows:

$$\varepsilon_{xx} = \frac{(a_{\text{film}} - a_{\text{sub}})}{a_{\text{sub}}}, \tag{1.6.1}$$

where a_{film} is the lattice parameter of the deposited film while a_{sub} is the same parameter from the substrate. The parameters are taken when the film is fully relaxed in its bulk form. The xx subscript on ε describes the in-plane characteristic of the mismatch.

Section 1.2 introduced that perovskite oxides can release internal stress through rotations and distortions of the oxygen octahedra. The external stress acts on the same degrees of freedom

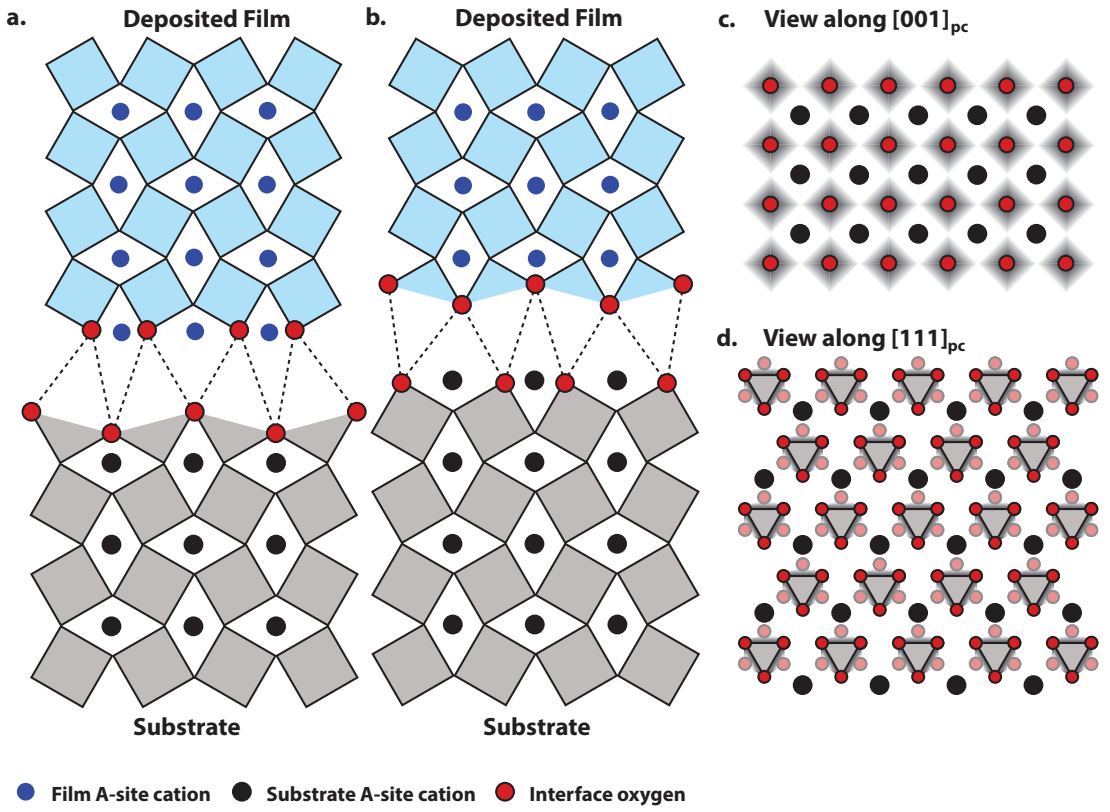

Figure 1.8 – a. Visualisation of a oxygen terminated surface epitaxy. **b.** Visualisation of a A-site terminated surface epitaxy. **c.** View of the interface plane when the deposition is performed along the $[001]_{pc}$ orientation of the pseudo cubic unit cell. **d.** View of the interface plane when the deposition is performed along the $[111]_{pc}$ orientation of the pseudo cubic unit cell.

of the structure, thus uses the same mechanisms to relief the epitaxial strain. This is why they represent a topmost candidate for tuning their structural arrangement through epitaxy. This is even more interesting as the physical characteristics of perovskites such as the conductivity, magnetism, optical response and many more are dependent on the structure, and thus can be fine tuned by epitaxially straining the films.

When the deposited film becomes thicker, the ratio between the film-substrate interface and the core of the film will diminish. In a similar approach to surface effects, their contribution is expected to become negligible after a characteristic dimension of this ratio is reached, thus allowing the crystal to fully restore its bulk arrangement. This critical dimension is called the relaxation length [24]. For example, recent work evaluated the critical thickness of $SrTiO_3$ epitaxially grown on $(La_{0.3}Sr_{0.7})(Al_{0.65}Ta_{0.35})$ at 180 nm [25] using the misfit dislocation model introduced by Merwe [23].

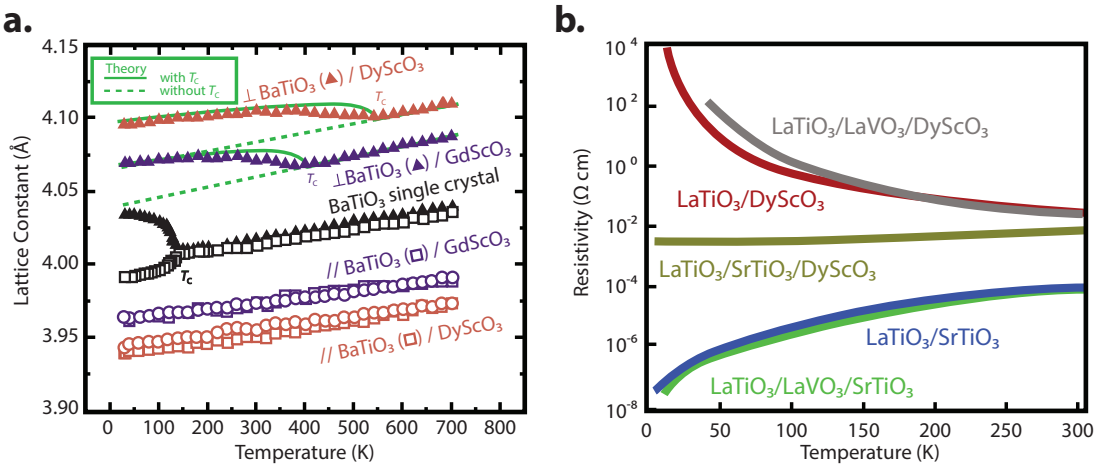

Figure 1.9 – a. In-plane and out-of-plane lattice parameters of $BaTiO_3$ as single crystal and deposited epitaxially on $DyScO_3$ and $GdScO_3$ [28]. **b.** Investigation of the resistive behaviour of $LaTiO_3$ deposited epitaxially on various substrates [30].

1.6.2 Control of properties through epitaxy

Epitaxy, in recent years, has emerged as a very effective tool to tune functional properties of perovskite films [26]. A particular example is the study on how epitaxial strain affects ferroelectricity in compounds such as $BaTiO_3$, $PbTiO_3$ and $LiNbO_3$ [27, 28, 29]. From these studies it is evident that the strain has a impact onto the ferroelectric Curie temperature and the polarisation. K. J. Choi *et al.* [28] proposed a theoretical and experimental investigation of the ferroelectric Curie temperature of $BaTiO_3$ under various strain condition. The substrates chosen were $GdScO_3$ and $DyScO_3$ which result in a miss fit ratio of -1.0 and -1.7% respectively. The structural parameters in-plane and out-of-plane were measured using X-Ray diffraction. The relative shift of the Curie temperature can be seen in Figure 1.9.**a.**. The T_C of $BaTiO_3$ deposited on $GdScO_3$ and $DyScO_3$ is $\approx 400°$C and $\approx 540°$C respectively, thus, demonstrating that epitaxial strain can be used as a tuning mechanism.

Another property being intensively studied under epitaxy is the metal-to-insulator transition (MIT) in transition metal (TM) perovskites. Titanates form a subgroup of TMO perovskites with compounds such as $LaTiO_3$. A study performed by He *et al.* [30] investigated the conductive properties of $LaTiO_3$ epitaxially deposited on various compounds and demonstrated a transition from a metal to an insulator depending on the chosen substrate. The trend followed by the resistivity with the temperature can be seen in Figure 1.9.**b.**.

These two examples showcase how epitaxial strain can be used to modify physical properties of the deposited film. This field is further motivated by combining functional substrates with functional films and allow epitaxy to control their distinct physical properties. A ferroelectric com-

pound could therefore be epitaxially linked to a ferromagnetic material, thus allowing an electric field to induced structural transitions on the former that propagate to the latter and ultimately induce a magnetic behaviour [31]. Such an arrangement would overcome the physical complexity of obtaining both behaviour within the same compound.

Chapter 2

Rare-earth nickelates RNiO$_3$

2.1 Introduction

Nickelates form a subgroup of the perovskites with formula RNiO$_3$, where R is any of the rare earths from Lutetium (Lu) to Lanthanum (La). Because of their rich landscape of structural and physical properties, nickelates are subject to a tremendous amount of investigations. The most notable property being the metal to insulator transition (MIT) of almost all bulk nickelate compounds except LaNiO$_3$. The transition temperature shows a direct dependance with the size of the rare-earth. The change of the rare-earth induces a change in the octahedral tilt angle. The associated diagram relating the MIT transition temperature to the tolerance factor and the tilt angle is shown in Figure 2.1. Investigations of this phase diagram have been reviewed by M. J. Medarde in 1997 [8] and G. Catalan in 2008 [32] and on nickelate heterostructure by S.Middey *et al.* in 2016 [21] and Catalano *et al.* in 2017 [3].

As nickelates transit from metals to insulators they undergo a phase transition from an orthorhombic $Pbnm$ to monoclinic $P2_1/n$ [33]. The latter is characterised by two inequivalent Ni sites, thus resulting in non equivalent Ni-O bond lengths and oxygen octahedra with different sizes (this type of distortion was shown in Chapter 1.3). Nickelates also undergo a magnetic transition, either below or simultaneously with the metal to insulator transition. No structural transition have been reported during the magnetic ordering. It is possible to separate the diagram into three distinct regions:

- The region around LaNiO$_3$ has no transition whatsoever and stays paramagnetic metal for all temperatures. It is also the only compound of the nickelate family crystallising into the $R\bar{3}c$ space group.
- The region around NdNiO$_3$ and PrNiO$_3$ combines both the MIT and Néel transitions at the

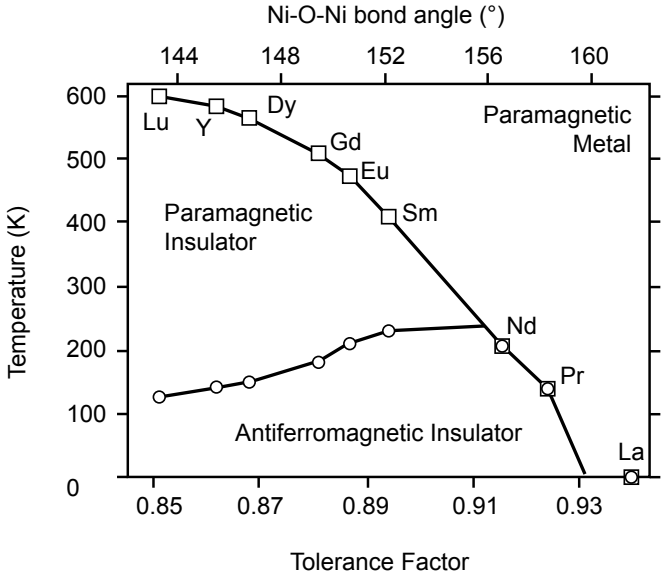

Figure 2.1 – Phase diagram for the Nickelate perovskite group RNiO$_3$ with R ranging from Lutetium (Lu) to Lanthanum (La). The squares indicate the metal to insulator transition temperature T_{MI}, while the Néel transition temperature $T_{Néel}$ is depicted by circles. This diagram is adapted from M. J. Medarde [8, 34].

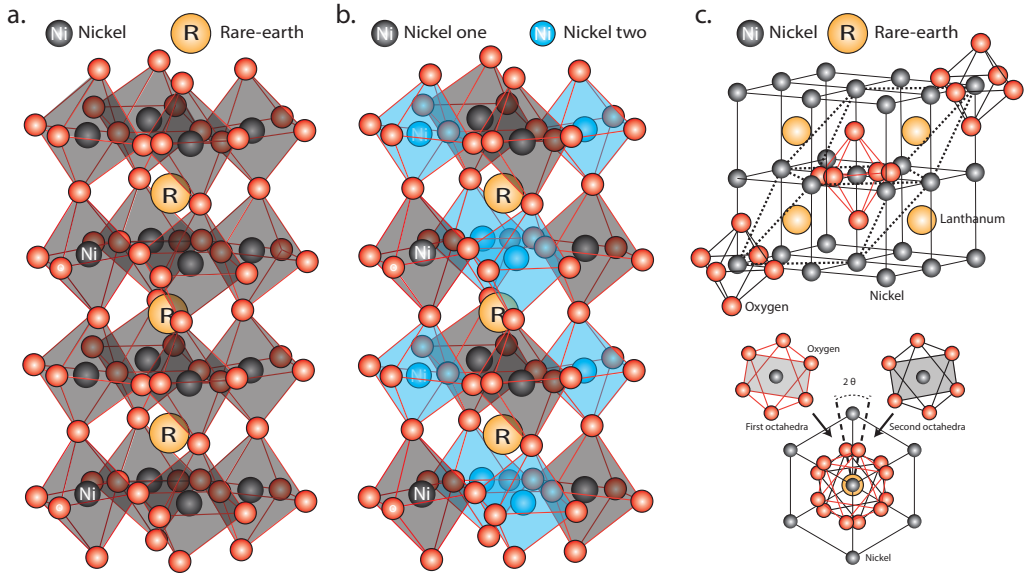

Figure 2.2 – Visualisation of the RNiO$_3$ perovskite in the three main crystallographic structures. In red the oxygens, black the Nickels and in yellow the Rare-earth. **a.** The $Pbnm$ representations **b.** The $P2_1/n$ representation **c.** The $R\bar{3}c$ representation

same temperature.

- The region below SmNiO$_3$ shows both a MIT and Néel transition temperature but at different temperatures.

At higher temperatures ($>$800 K) PrNiO$_3$ is found to go through a transition towards $R\bar{3}c$ while remaining in the same conductor behaviour [35], i.e. it adopts the structure of LaNiO$_3$ at room temperature. A sketch of the $Pbnm$, $P2_1/n$, $R\bar{3}c$ perovskite models can be seen in Figure 2.2.

2.2 Metal to Insulator transition in nickelates

The metal to insulator transition (MIT) in RNiO$_3$ compounds is a fascinating example of bandwidth-controlled transitions [17]. The increase of the orthorhombic distortion, characterised by a change in the O-Ni-O bond angle, changes the overlap of the transition metal d and oxygen p orbitals, thus modifying the transition temperature from 0 K in-between LaNiO$_3$ and PrNiO$_3$ up to 600 K for LuNiO$_3$. The distortion is directly linked to the size of the rare-earth.

The investigation of the MIT in nickelates therefore demands a clearer understanding of the orbital configuration. Nickel has an electronic configuration [Ar] $3d^8$ $4s^2$. As a consequence the oxidation state Ni^{3+}, used within the perovskite structure, is defined by [Ar] $3d^7$ with 7 electrons on the d shell. The d^7 low spin orbital configuration of Ni^{3+} is expected to be t_{2g}^6 and e_g^1 [36]. In the presence of a homogeneous octahedral crystal field an equal occupation of the x^2-y^2 and $3z^2-r^2$ orbitals is expected.

The metal to insulator transition in nickelates is linked to a lowering of the symmetry from $Pbnm$ to a monoclinic structure accompanied by a breathing distortion of the oxygen octahedra. This distortion is characterised by two non-equivalent Ni sites, with long and short Ni-O bonds. It was initially believed that this change in bond lengths would be associated to a charge disproportionation at the Ni sites, thus resulting in the following alteration:

$$d^7 + d^7 \rightarrow d^{7+\delta} + d^{7-\delta}, \tag{2.2.1}$$

where δ is the effective charge exchange. A value of 0.45 ± 0.4 e.v was measured for δ through resonant X-Ray scattering for thin NdNiO$_3$ films [37]. The plausibility of this interpretation was reinforced by a wide range of experimental methods [3].

It is ultimately *ab-initio* calculations, which do not predict a charge rearrangement of this magnitude, that challenged the bond disproportionation model [38]. This led to the consideration of an orbital interaction between the transition metal and oxygens from the octahedral cage surrounding it. The *Charge Transfer* model would assume a mechanism $d^7 \rightarrow d^8 + L$. The system would therefore be in a mixed state $\alpha d^7 + \beta d^8 L$ with a dominance of the ground state d^7. A Jahn-Teller distortion would then remove the e_g orbital degeneracy [39]. Yet, low temperature

investigations reveal that a d^8L is the predominant ground state of the Ni sites. This indicates that the nickelates do not favour orbital ordering which would have induced a Jahn-Teller type distortion [36]. The predominance of this ground state in junction with the vanishing charge transfer gap Δ between Ni^{3+} and O [40, 41, 42, 43] suggests a *Negative Charge Transfer* insulator scenario (section 1.5.4), with a charge transport mechanism described as follows [44]:

$$(d^8L)_i + (d^8L)_j \rightarrow (d^8L^2)_i + (d^8)_j. \tag{2.2.2}$$

i and j refer to two distinct nickel sites and L represents a ligand hole in the oxygen p orbital. Interestingly, the Ni site with the d^8 configuration can be seen as a Ni^{2+} oxidation state having a large oxygen octahedral cage surrounding it. On the other hand the Ni site with a d^8L^2 configuration is comparable to a Ni^{4+} oxidation state, thus reducing the size of the surrounding cage. This explains the breathing distortion within the insulating phase of nickelates. In summary, the metal to insulator transition is characterised by a splitting of the dispersive d^8L band of the metallic phase into two localised bands with an associated insulating gap [41, 45, 46].

2.3 Tuning the MIT through epitaxial strain

The previous section summarised the current knowledge of the metal to insulator transition mechanism in nickelates. Yet the simplistic view that nickelates from a perovskite family with a bandwidth-controlled transition remain a usefull thinking approach. The bandwidth depends on a structural deformation away from the ideal cubic arrangement into an orthorhombic configuration through an $a^-a^-c^+$ tilting pattern of the oxygen octahedra. The nickelate phase diagram shown in section 2.1 reveals a direct dependency between the size of the rare-earth, the octahedral tilt angle and the metal to insulator transition, suggesting that it is possible to alter the transition point by influencing the structural properties.

The wide variety of available substrates with their respective crystallographic space group lead to a considerable amount of novel configurations to be investigated. A few relations between commonly used substrates and $LaNiO_3$, $NdNiO_3$, $SmNiO_3$ are displayed in Table 2.1. The lattice mismatch ε_{xx} is expressed according the definition introduced in Chapter 1.6 using the pseudo cubic lattice parameters 3.84 Å, 3.808 Å, 3.790 Å for $LaNiO_3$, $NdNiO_3$, $SmNiO_3$ respectively.

An example is the control of the metal to insulator transition of $SmNiO_3$ when deposited epitaxially onto various substrates along the $[001]_{pc}$ orientation [47]. The extracted resistivity data can be seen in Figure 2.3. The most striking change is the loss of the metal-to-insulator transition when $YAlO_3$ is chosen as a substrate. Another notable observation is that independently of the chosen substrate the transition temperature seems to always be lowered.

Substrate	Structure	Space group	Lattice constant	ε_{xx} ($LaNiO_3$)	ε_{xx} ($NdNiO_3$)	ε_{xx} ($SmNiO_3$)
$YAlO_3$	Orthorhombic	$Pbnm$	3.69	-4.0%	-3.1%	-2.3%
$NdAlO_3$	Rhombohedral	$R\bar{3}c$	3.76	-2.1%	-1.3%	-0.9%
$LaAlO_3$	Rhombohedral	$R\bar{3}c$	3.79	-1.3%	-0.5%	-0.1%
$NdGaO_3$	Orthorhombic	$Pbnm$	3.86	+0.5%	+1.5%	+1.9%
LSAT	Cubic	$Pm\bar{3}m$	3.87	+0.8%	+1.6%	+2.1%
$DyScO_3$	Orthorhombic	$Pbnm$	3.94	+2.5%	+3.6%	+4.0%

Table 2.1 – Strain configurations between $LaNiO_3$, $NdNiO_3$, $SmNiO_3$ and a variety of common substrates: $YAlO_3$, $NdAlO_3$, $LaAlO_3$, $NdGaO_3$, LSAT and $DyScO_3$ at 300 K. The positive and negative signs of the mismatch parameter ε_{xx} corresponds to tensile and compressive strain, respectively.

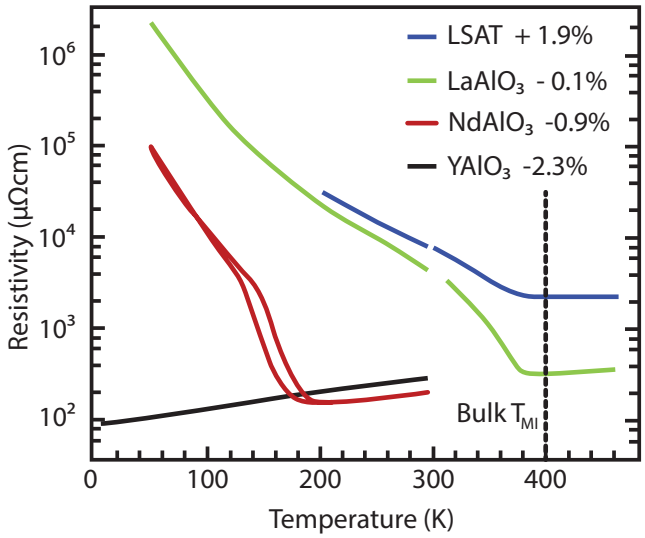

Figure 2.3 – Resistivity data of $SmNiO_3$ epitaxially deposited on LSAT, $LaAlO_3$, $NdAlO_3$ and $YAlO_3$ along the $[001]_{pc}$ orientation extracted from Catalano *et al.* [47]

2.4 Magnetic transition in Nickelates

Below the Néel transition temperature, represented by circles in the phase diagram (Figure 2.1), nickelates become antiferromagneticaly ordered with a Bragg vector of $q_{\text{Bragg}} = [1/4, 1/4, 1/4]_{pc}$ or $[1/2, 0, 1/2]$ in the orthorhombic axes. This would therefore imply a periodicity of 4_{pc} monolayers along $[111]_{pc}$ [39]. For compounds where the MIT and the Néel transitions are separated, the latter is characterised by a second order type transition. When $T_{MIT} = T_{Néel}$ on the other hand, a first order transition is observed [3]. An example of the magnetic investigation of $SmNiO_3$ can be seen in Figure 2.4.

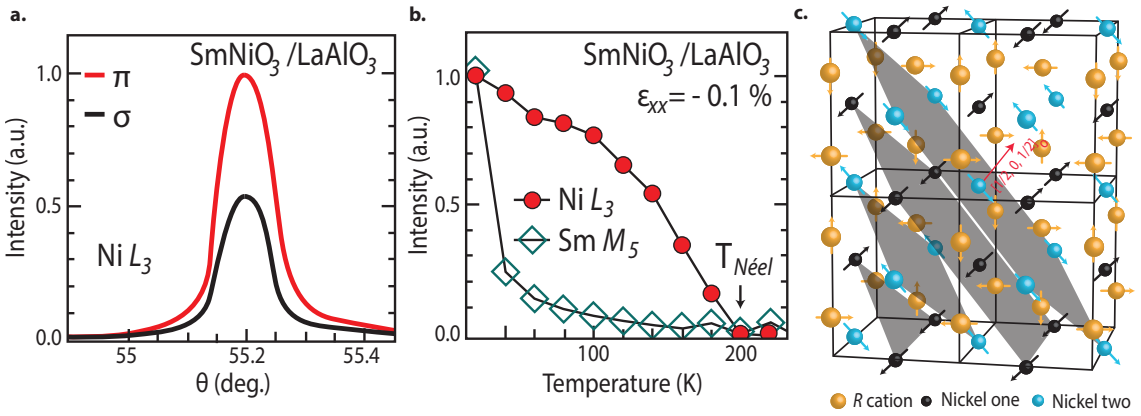

Figure 2.4 – a. Bragg vector determined through resonant soft X-Ray scattering at the Ni L_3 edge with π and σ polarised light, indicating the $[111]_{pc}$ direction. **b.** Evolution of intensities at the Ni L_3 and Sm M_5 edges for SmNiO$_3$ deposited on LaAlO$_3$. **c.** Sketch of a non-collinear magnetic structure proposed for nickelates [3]

The intensity evolution of the Ni L_3 and Sm M_5 edges with temperature (Figure 2.4.**b.**) suggests that two magnetic ordering regimes are present. One relative to the Ni and one related to the Sm atoms. It is reported that it is the magnetisation of the nickel structure that induces a magnetisation in the rare-earth cations. Initial investigations performed by Garcia-Muñoz *et al.* [39] suggested an up and down configuration along the $[111]_{pc}$ direction accompanied by an orbital superlattice. But both collinear and non-collinear models of the magnetic spin arrangement satisfied the observations, thus asking for further investigations. It was Scagnoli *et al.* that demonstrated that the magnetic structure in NdNiO$_3$ is described by a non-collinear model [48]. It was also suggested, in experimental works by Merdarde [8], that the stabilisation of the magnetic phase is only possible below the MIT. This states, that the Néel transition is quenched by the MIT for NdNiO$_3$ and SmNiO$_3$.

2.5 Lanthanum nickel oxide LaNiO$_3$

Lanthanum is the element of Lanthanides (also known as rare-earth elements) with the largest ionic radius and, therefore, constitutes an end member of the Rare-earth nickelate phase diagram. LNO crystallises in the $R\bar{3}c$ space group [49] where La occupies the $2a\left(\frac{1}{4},\frac{1}{4},\frac{1}{4}\right)$, Ni the $2b\,(0,0,0)$ and oxygen the $6e\left(x,\bar{x}+\frac{1}{2},\frac{1}{4}\right)$ Wickoff positions [50]. The rhombohedral unit cell is depicted by dashed lines in Figure 2.2, where oxygen octahedra follow an $a^-a^-a^-$ tilt configuration, which can also be interpreted as an anti-phase rotation about the pseudo cubic diagonal threefold axis.

As already mentioned in section 2, bulk LNO is metallic from 1.5 to 600 K. Furthermore, no

structural transition is observed within the same range. Accurate investigations through neutron diffraction experiments reported an decrease of the rhombohedral distortion as the temperature increases. This reflects a decrease of the octahedral tilt angle towards the cubic structure [51].

2.5.1 Epitaxial investigations

It is the strain induced by the lattice mismatch of thin LNO films epitaxially grown on other substrates that disclosed other structural arrangements. In a study published by S. J. May (2010) [52], thin films were grown on $SrTiO_3$ (STO) and $LaAlO_3$ (LAO), resulting in a 1.7% tensile and 1.1% compressive lattice mismatch respectively. Both substrates were oriented in the $[001]_{pc}$ direction. STO is cubic at room temperature and without octahedral rotations. LAO, on the other hand, is rhombohedral like LNO. Such a study of LNO epitaxially deposited on LAO could reveal if the epitaxy transmits the tilt pattern of the substrate to the film. Both samples were investigated with high flux synchrotron X-Ray diffraction (XRD). The associated results are shown in Table 2.2. The XRD results indicate that a differentiation of in-plane and out-of-plane components takes place both from the lattice constants and the octahedral tilt arrangement.

	LNO/STO (XRD)	LNO/LAO (XRD)	LNO/STO (DFT)	LNO/LAO (DFT)
$d_{\text{in-plane}}$ (Å)	1.968 ± 0.002	1.916 ± 0.005	1.970	1.921
$d_{\text{out-of-plane}}$ (Å)	1.933 ± 0.002	1.946 ± 0.002	1.935	1.950
$\omega_{\text{in-plane}}$ (deg)	165.8 ± 0.5	164.0 ± 2.0	164.7	161.5
$\omega_{\text{out-of-plane}}$ (deg)	159.9 ± 0.6	175.2 ± 0.6	159.3	173.7

Table 2.2 – XRD and DFT results for the LNO on STO and LNO on LAO sample setups extracted from May *et al.* [52]

The same investigation was then completed through Density Functional Theory (DFT) calculations, which exposed a similar trend (the associated results are shown in the same table). Both the XRD measurements and the DFT calculations suggest that the epitaxial strain induced a change from the $R\bar{3}c$ towards a lower symmetry monoclinic $C2/c$ space group. This is characterised by a change from a $a^-a^-a^-$ to a $a^-a^-c^-$ tilt pattern. The same investigation also pointed out that negative, up to 0.5% values of epitaxial mismatch favoured a lengthening of the apical Ni-O bond while values above favoured the lengthening of the equatorial bond, thus similarly affecting the tilt angle of the octahedra. However, in all cases, they argue that the film keeps a monoclinic $C2/c$ structure.

This interesting behaviour of LNO under epitaxial strain nourished more in depth investigations on further substrates as shown by M. C. Weber *et al.* in 2016 [22]. This investigation utilised X-Ray diffraction aided by DFT calculations similar to the previously introduced of May *et al.* with the addition of Raman spectroscopy measurements. The Raman signature is a fingerprint of the crystal structure and is directly affected by structural parameters, meaning that even slight variations of these can result in abrupt variations of the Raman signature. It was found that

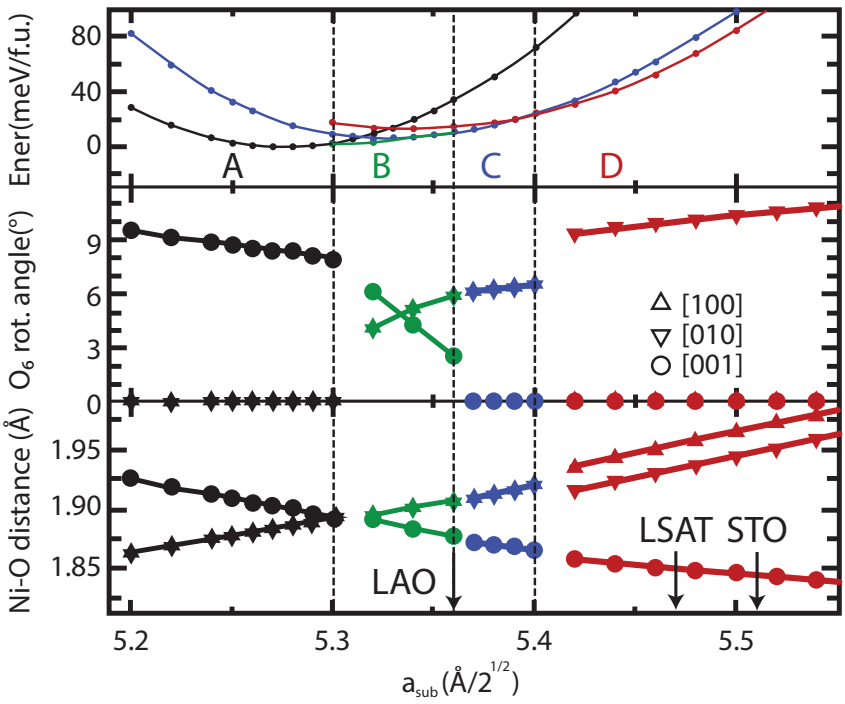

Figure 2.5 – Extracted Figure from Weber *et al.* [22]. Computed energy (top panel), rotation angles of O_6 octahedra (central), and Ni-O distances (bottom) as a function of the substrate lattice constant a_{sub}. Four stable phases indicated in the top panel: Phase A has space group $I4/mcm$; phase B: $C2/c$; phase C: $Imma$; and phase D: $Fmmm$. In all the found phases there is a single crystallographic position for Ni (i.e., all NiO_6 groups are equivalent by symmetry). The rotations in the central panel correspond to antiphase patterns, with all the O_6 octahedra in the cell tilting by the indicated angles. Rotation amplitudes about the three pseudocubic axes are shown. In the bottom panel, the Ni-O distances for bonds aligned with the three pseudocubic directions are indicated. The values of a_{sub} corresponding to the experimental LAO, LSAT, and STO substrates are indicated with arrows.

the transmitted strain depends on the thickness of the deposited film. Thinner films will present higher strain than thicker films as the relaxation process is found to be dependant on its thickness. This allowed to probe the region between 0 and 0.5% epitaxial mismatch. The obtained Raman measurements show varying spectral signatures for different arrangements suggesting that the epitaxial strain expresses a multitude of different phases for LNO in this region. DFT calculations using the Local Density Approximation (LDA) support this interpretation by suggesting different phases to be energetically favourable at different strain values and can be seen in Figure 2.5.

2.5.2 Ultrathin film regime

An investigation on the conductive behaviour of LNO in the ultrathin regime epitaxially deposited on LAO along the $[001]_{pc}$ direction was published by Fowlie *et al.* in 2016. It was reported that, in this particular configuration, strong variations of the conductivity of the LNO film can be observed. The minima is observed at around 10_{pc} unit cells. This is then followed by a strong increase of the resistivity and thus decrease of the conductivity as the film enters thicknesses below 10_{pc} u.c. This effectively renders LNO, which is considered conductive at any temperatue in the bulk, resistive in the ultrathin film regime.

This exceptional transition of LNO to an insulator regime raises the fundamental question, if the metal to insulator phase transition is accompanied by a structural phase transition, similarly to other nickelates. Transmission electron microscopy (TEM) measurements revealed variations of the structural parameters such as the bond lengths and the octahedral tilt patterns but could not reveal if there is indeed a structural transition, thus leaving the question unanswered.

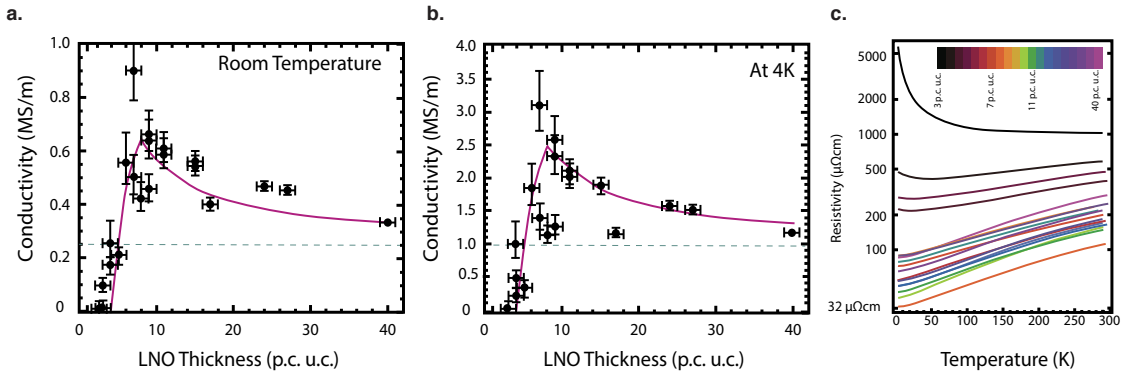

Figure 2.6 – a. Values of the conductivity at room temperature for different thicknesses of LNO on LAO. **b.** Values of the Conductivity at 4 K for different thicknesses of LNO on LAO. **c.** Resistivity curves of ultrathin LNO films at different thicknesses.

On the other hand, the same TEM measurements (shown in Figure 2.7) revealed distinct regions within the LNO ultrathin film and LAO substrate. A region being defined by a different unit cell parameter in relation with the ideal bulk LAO unit cell parameter. Using this approach it is possible to determine three LNO and two LAO regions [53]:

- A distinct but thickness invariant arrangement at the surface of LNO with a characteristic thickness of about 2_{pc} unit cells. This region is independent of the thickness of the film and was observed down to 3_{pc} unit cells.
- The second LNO region scales linearly with the thickness of the ultrathin film. It shows

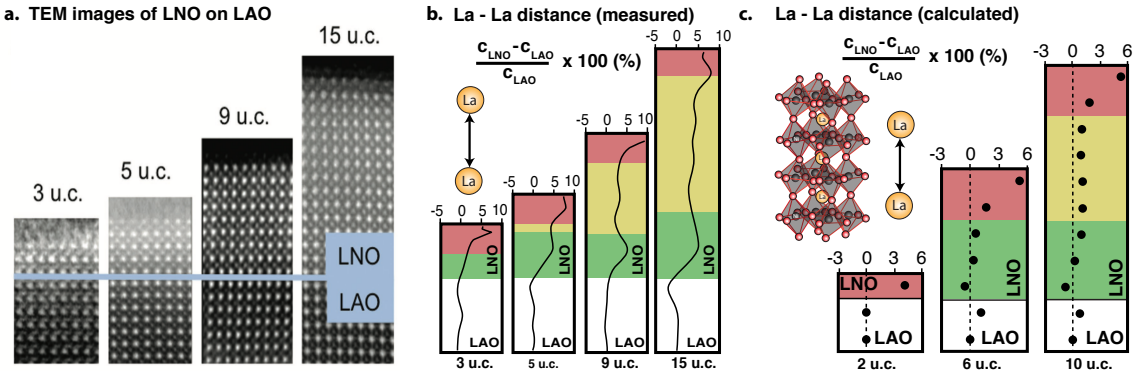

Figure 2.7 – a. TEM images extracted from J. Fowlie *et al.* [53] **b.** Inter Lanthanum distances normalised over the Bulk LAO distances for the TEM images shown in **a.** **b.** Same quantity as a. for the calculated structure.

the anticipated arrangement of epitaxially strained LNO on $[001]_{pc}$ oriented LAO. As a consequence, this region is inexistent when the film is to thin to accommodate it.

- The last LNO region consists of an epitaxially distorted structure with a characteristic thickness of about 2-4$_{pc}$ u.c.. Similar to the surface layer, the size of this distortion seems to be thickness independent. This being said, when the film is thin enough to have the second region vanish, it is the present layer who falls to the mercy of the surface layer.

- Another, less expected, region is the distorted LAO layer at the epitaxial interface. While the distortion seems to be always present, it reacts differently depending in the thickness of the LNO film. This can be understood as a dependance of which LNO region it has to accommodate. When the film is thin enough to only consist of the LNO surface region (described above), the substrate is greatly affected. This gives also an idea on the rigidity of this LNO region as it does not accommodate the LAO epitaxial strain.

- The last region is the relaxed LAO substrate.

These TEM measurements were then interpreted by *ab-initio* calculations. Both coming to the same type of arrangement and concluding that in the ultrathin regime, the contribution of the border regions cannot be neglected anymore. The inter lattice distance for both investigations is showcased in Figure 2.7. Using this insight it is possible to built a resistivity model. Each region is allowed a different resistivity value. The model is then fitted to the measured values. This leads to the following values: 1 kSm^{-1} for the LNO surface layer, 0.25 MSm^{-1} for the LNO semi relaxed section and 1.3 MSm^{-1} for the LNO interface region. This values are valid at a temperature of 4 K. This validates the structural calculations and the understanding of the conductive behaviour of LNO deposited on LAO along the $[001]_{pc}$ direction in the ultrathin film regime.

2.6 Neodymium nickel oxide NdNiO$_3$

NNO is the last nickelate of the family, situated after LaNiO$_3$ and PrNiO$_3$, still having both transitions simultaneously. The adjacent compound, SmNiO$_3$ (SNO), has both transitions at distinct temperatures. It is therefore the particular location of NNO in this region of the phase diagram, that led to the interest in the compound. The physical properties of NdNiO$_3$ can be modified through the octahedral tilt parameter. This can be achieved in various ways such as solid solution engineering or epitaxial strain, both discussed in the following sections.

2.6.1 A strategic position within the phase diagram

Solid solutions made out of Sm$_x$Nd$_{1-x}$NiO$_3$ (SNNO) is one possible approach to modify NdNiO$_3$ both in terms of structural and physical properties, as illustrated in Table 2.3. Figure 2.8 presents the positions of these transition temperature in the nickelate phase diagram between SmNiO$_3$ and NdNiO$_3$. The observed trend is an argument that the geometric tilt angle of the octahedra is the main parameter influencing the transition temperature.

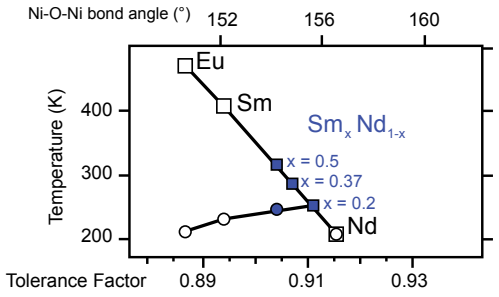

Figure 2.8 – Phase diagram for the solid solution of Sm$_x$Nd$_{1-x}$NiO$_3$ reported in Table 2.3.

Composition	Tolerance Factor	MIT (K)	Ref.
NdNiO$_3$	0.915	210	[32]
Sm$_{0.20}$NdNi$_{0.80}$O$_3$	0.911	250	[54]
Sm$_{0.37}$NdNi$_{0.63}$O$_3$	0.907	307	[54]
Sm$_{0.50}$NdNi$_{0.50}$O$_3$	0.904	343	[54]
SmNiO$_3$	0.894	400	[54]

Table 2.3 – Representation of the Sm$_x$Nd$_{1-x}$NiO$_3$ metal to insulator transition (MIT) temperatures.

2.6.2 Epitaxial films and strain

The effects of the epitaxial strain on the resistivity can be seen in Figure 2.9 extracted from Catalano *et al.* [55]. It is found that in general the MIT of NdNiO$_3$ is decreased through epitaxial strain in comparison with its *bulk* value of 200 K. In particular deposition on the $[001]_{pc}$ direction of NGO, induces a decrease of the transition temperature down from 200 to 160 K [55, 56].

Only one configuration has been found to deviate from this trend. It was reported that the metal-to-insulator and magnetic transition temperatures of NdNiO$_3$ epitaxially deposited on $[111]_{pc}$ oriented NdGaO$_3$ (further referenced to as NGO) increased in temperature and shifted from 200 K to 330 K, and 230 K respectively [55]. This study made use of resistivity and resonant

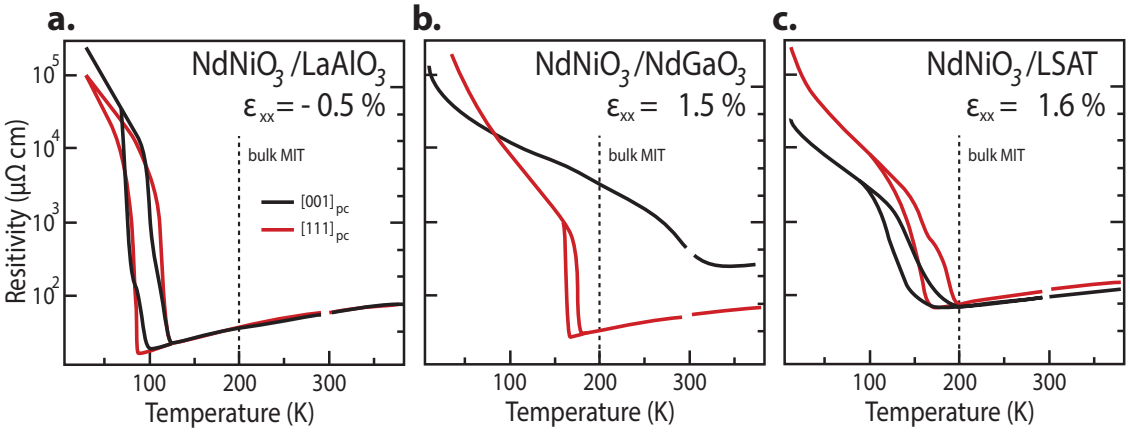

Figure 2.9 – a. - c. Resistivity measurements of $NdNiO_3$ films deposited on $LaAlO_3$, $NdGaO_3$ and LSAT along both the $[001]_{pc}$ and $[111]_{pc}$ orientations.

X-Ray reflectivity measurements to identify the MIT and magnetic transition temperatures (Figure 2.10.**a.**). A prediction on the approximate inter-octahedral bond angle was made using the nickelate phase diagram. The value identified for NNO epitaxially deposited along the $[111]_{pc}$ direction is $\approx$153.8° [55], which is in close vicinity of the tilt parameter of $SmNiO_3$ at $\approx$152.2°. The modified phase diagram can be seen in Figure 2.10.**b.**. The obtained value appears reasonable as the octahedral tilt angle of the substrate is of 153.2°, meaning that NGO would effectively impose its own tilt angle onto the NNO octahedra.

This result is astonishing not only by the difference in magnitude but by the opposite variation direction. This would confirm that the way epitaxial strain is expressed strongly depends on the orientation of the epitaxial plane. Following the hypothesis that the metal to insulator transition depends solely on the tilt angle between successive oxygen octahedra, would then suggest that this parameter is affected differently depending on the deposition orientation. Indeed the interpretation, provided by Catalano *et al.* [55], states that the $[001]_{pc}$ orientation provides only one oxygen anchor point per octahedra at the interface between NNO and NGO. The $[111]_{pc}$ orientation on the other hand provides three oxygen anchor points, thus transmitting the tilt parameter with a greater *stiffness* from the substrate to the film. This description still remains to be better understood as a similar behaviour is not obtained on other substrates as shown for NNO on LAO in Figure 2.9.**a.** or NNO on LSAT as seen in Figure 2.9.**c.**.

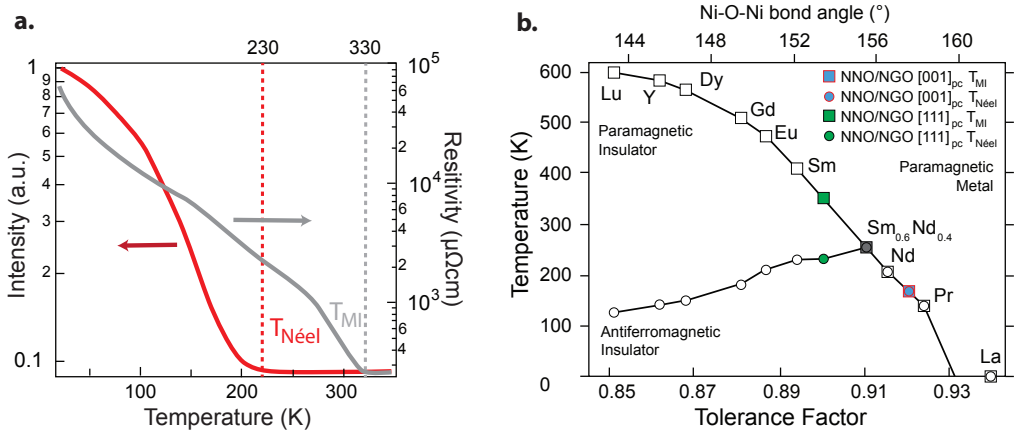

Figure 2.10 – a. Results from resistivity and resonant X-Ray reflectivity measurements illustrating the two metal-to-insulator and magnetic transitions temperatures. **b.** Modified phase diagram accounting for the $Sm_{0.6}Nd_{0.4}NiO_3$ solid solution and $NdNiO_3$ deposited on $NdGaO_3$ along $[001]_{pc}$ and $[111]_{pc}$, respectively.

2.7 Objectives of this work

This work stands in the overall context of functional oxides which present a significant interest for both for the fundamental understanding they can provide in materials physics and for their recognised application potential.

Among functional oxides, the family of ABO_3 perovskites have attracted a particular attention due to their remarkable electronic, magnetic and optical properties. Such a range of behaviour expands the potential for the development of novel electronic devices. The physical properties of perovskites are strongly correlated to the underlying structure, which is often discussed in terms of cation displacements and rotations (tilts) of the octahedra. A distinctive feature of perovskites is that these structural aspects can be largely varied (tuned) by parameters such as temperature, pressure, chemical composition etc... , leading to complex and intriguing phase diagrams for physical and structural properties.

In conjunction with the increasing interest in the understanding of perovskites under 'common' external parameters, recent years have seen great advances in the growth of high quality epitaxial films and heterostructures, allowing to explore in more detail the effect strain engineering, interface-induced phenomena and reduced dimensionality in functional oxides. Such investigations have allowed for the discovery of new, and elucidation of existing, physical phenomena. One of the challenges in the field of thin and ultrathin films and heterostructures is to access the fine structural details of such nano-objects sitting on a large substrate.

As we have seen in the introduction, a particularly interesting case is the family of perovskite nickelates, which is described by the chemical formula RNiO3, where R is a trivalent rare-earth R = La, Pr, Nd, Sm, . . . , Lu. These nickelates are characterised by a rich landscape of structural and physical properties. The phase diagram of the RNiO3 family stands as a canonical example of the physics of phase transitions in correlated oxides to which the electron-lattice coupling contributes significantly. One of the main characteristics of nickelates, with the exception of R = La, is a sharp metal-to-insulator transition (MIT), which is mainly determined by the Ni-O-Ni bond angle. Thin film deposition techniques now yield highly crystalline RNiO3 thin films and enable advanced atomic-scale control of their lattice and electronic properties. Such thin films have recently attracted a significant interest, but a detailed understanding of their local structure is missing.

This is the very context of this work. The objective of this work to gain an increased understanding of the structure of perovskite-type RNiO3 in the ultrathin limit.

Towards this objective, we have selected two specific materials: (i) $LaNiO_3$, which presents an interesting, and relatively simple, model system as its lattice distortion can be described by just one type of octahedral rotation and because it presents no phase transition in its bulk form. This compound will allow to answer the question of how stable octahedra tilts in the ultrathin limit are. (ii) $NdNiO_3$, which is the model nickelate for presenting at the same temperature a

MI, magnetic and structural phase transition. Here, it will be interesting to see how strain can potentially disentangle these three phase transitions.

In this work, we have chosen to investigate the structural properties of the above two ultrathin compounds by using Raman Spectroscopy which is known to be a well-adapted probe for investigating even subtle structural details and changes in perovskites. Also, Raman spectroscopy provides via the investigation of phonons a view into collective dynamic properties of films and hereby complements literature investigations by TEM, which provides a static look. We will see throughout the work that standard Raman approaches are not sufficient for such an investigation, but that advanced experimental and statistical approaches need to be developed towards our objective. These developments will form an important part of this work.

Part II

Raman Spectroscopy

Chapter 3

Raman spectroscopy

3.1 Light scattering

Raman scattering is the inelastic scattering of light by a material. When a photon impinges on a molecular structure, multiple forms of scattering processes can occur. Lord Rayleigh [57] discovered that light interacting with small particles like atoms or molecules induce small oscillating dipoles. The resulting radiation of these dipoles was later referred to as Rayleigh scattering. In 1923 Adolf Smekal predicted that there must be inelastic phenomena outside of Rayleigh scattering related to the vibrational modes of the molecules [58]. This was confirmed experimentally by C.V. Raman in 1928 [59], which led to the Nobel prize in 1930.

In this chapter, ω will refer to angular frequency linked to the conventional time frequency ν by $\omega = 2\pi\nu$. In Raman spectroscopy it is also common to use the wavenumber $\tilde{\nu}$ which relates to ω through: $\omega = 2\pi c\tilde{\nu}$ (where c is the speed of light in vacuum). All further considerations are done under the hypothesis of a perfectly monochromatic non divergent coherent light beam incident on a homogeneous material structure. No further assumptions are made on the physical properties of the sample. The photons of this beam are characterised by a frequency ω_{incid}, a polarisation state P^i relative to its propagation direction $\boldsymbol{k}_i$. The scattered photons, on the other hand, are not required to maintain the same characteristics during the scattering process. This includes relative changes in energy, momentum and direction.

When an electromagnetic wave circulates through a media it can interact with it. One of these possibility is an interaction with the charged particles of the structure to induce a dipolar arrangements. This quantity is referred to as induced dipole moment $\boldsymbol{P}$. A decomposition of this quantity along the electromagnetic field allows to write:

$$\boldsymbol{P} = \boldsymbol{P}^{(0)} + \boldsymbol{P}^{(1)} + \boldsymbol{P}^{(2)} + \boldsymbol{P}^{(3)} + ..., \tag{3.1.1}$$

where the superscripts indicate to which order this component depends on the radiation. $\boldsymbol{P}^{(0)}$

depicts the spontaneous polarisation. The first three components that follow it are:

$$\boldsymbol{P}^{(1)} = \alpha \cdot \boldsymbol{E} \tag{3.1.2}$$

$$\boldsymbol{P}^{(2)} = \frac{1}{2}\beta \cdot \boldsymbol{E}\boldsymbol{E} \tag{3.1.3}$$

$$\boldsymbol{P}^{(3)} = \frac{1}{6}\gamma \cdot \boldsymbol{E}\boldsymbol{E}\boldsymbol{E}. \tag{3.1.4}$$

In general the linear interaction is much stronger than all other higher order components [60], resulting in $\boldsymbol{P}^{(1)} \gg \boldsymbol{P}^{(2)} \gg \boldsymbol{P}^{(3)}$. The linear response probability is expressed through the electric polarisability tensor $\boldsymbol{\alpha}$ while the second and third orders are respectively expressed through the first β and second order γ hyperpolarisbility tensors.

It is the linear component that allows for all single particle processes such as Rayleigh and conventional Raman scattering. The other components capture triple or double particle combination effects, thus allowing for hyper Raman processes to take place (Not discussed in the scope of this work). We can also write $\boldsymbol{E} = \boldsymbol{E}_0 \cdot \cos(\omega_{incid} t)$ and a polarisability tensor $\boldsymbol{\alpha}$ oscillating with a periodic modulation $\boldsymbol{Q}(t)$. The frequency of the latter is introduced as ω with:

$$\boldsymbol{Q}(t) = \boldsymbol{Q_0} \cdot \cos(\omega t - \delta), \tag{3.1.5}$$

where δ is a phase factor taking into account the difference between the incident radiation and the oscillation. Performing a Taylor expansion of $\boldsymbol{\alpha}$ in $\boldsymbol{Q}(t)$ yields:

$$\boldsymbol{P}^{(1)}(t) = \boldsymbol{\alpha}(\boldsymbol{Q}(t)) \cdot \boldsymbol{E}_0 \cdot \cos(\omega_{incid} t) \tag{3.1.6}$$

$$= \left(\boldsymbol{\alpha}_0 + \left.\frac{d\boldsymbol{\alpha}}{d\boldsymbol{Q}}\right|_0 \boldsymbol{Q}(t) + ...\right) \cdot \boldsymbol{E}_0 \cdot \cos(\omega_{incid} t) \tag{3.1.7}$$

$$= \boldsymbol{\alpha}_0 \cdot \boldsymbol{E}_0 \cdot \cos(\omega_{incid} t) + \left.\frac{d\boldsymbol{\alpha}}{d\boldsymbol{Q}}\right|_0 \boldsymbol{Q}_0 \cdot \cos(\omega t - \delta) \cdot \boldsymbol{E}_0 \cdot \cos(\omega_{incid} t)$$

Using basic trigonometric identities, the cosine multiplication can be expressed as follows:

$$\begin{aligned} \boldsymbol{P}^{(1)}(t) &= \boldsymbol{\alpha}_0 \cdot \boldsymbol{E}_0 \cdot \cos(\omega_{incid} t) \\ &+ \frac{\boldsymbol{E}_0}{2} \cdot \left.\frac{d\boldsymbol{\alpha}}{d\boldsymbol{Q}}\right|_0 \boldsymbol{Q}_0 \cdot [\cos((\omega_{incid} + \omega)t + \delta) + \cos((\omega_{incid} - \omega)t - \delta)] \end{aligned} \tag{3.1.8}$$

The elastic Rayleigh component corresponds to the first term. The second and third terms correspond to Stokes ($\omega_{incid} - \omega$) and anti Stokes ($\omega_{incid} + \omega$) Raman scattering. The Raman tensor is defined as:

$$\boldsymbol{R} = \left.\frac{d\boldsymbol{\alpha}}{d\boldsymbol{Q}}\right|_0, \tag{3.1.9}$$

which corresponds to the derivate of the polarisability tensor over the displacement modulation $\boldsymbol{Q}$.

3.2 The polarisability tensor

The polarisability, introduced in the previous section, quantifies the ability of a set of particles to interact with the incident electromagnetic radiation. Imagining a system with a certain particle arrangement in a three dimensional space defined by $\boldsymbol{x}$, $\boldsymbol{y}$, $\boldsymbol{z}$. The incident radiation is applied with the electric field described by $\boldsymbol{E} = (E_x, E_y, E_z)$. The polarisation $\boldsymbol{P}$ is described by the three directions (P_x, P_y, P_z) and is linearly proportional to the applied electric field (in the limit of small fields). Therefore, it is possible to express the transformation for any component as follows:

$$P_j = \alpha_{ji} E_i, \tag{3.2.1}$$

where i and j can be any of the three spatial vectors. Generalising this leads to the following expression:

$$\begin{pmatrix} P_x \\ P_y \\ P_z \end{pmatrix} = \begin{pmatrix} \alpha_{xx} & \alpha_{xy} & \alpha_{xz} \\ \alpha_{yx} & \alpha_{yy} & \alpha_{yz} \\ \alpha_{zx} & \alpha_{zy} & \alpha_{zz} \end{pmatrix} \begin{pmatrix} E_x \\ E_y \\ E_z \end{pmatrix}. \tag{3.2.2}$$

The nine components, linking the polarisation to the incident electric field, form a second rank tensor of polarisability α.

3.2.1 Symmetry of the tensor

The work required to displace a particle with a charge q by a distance dx along a direction $\boldsymbol{x}$ through an electric field E_x is equal to $qE_x dx$ [61]. This can be generalised per unit volume of the system composed of N particles as $qE_x N dx$. The change of polarisation dP_x is defined by $qNdx$. Therefore, the work required to change the polarisation is expressed by $E_x dP_x$ along $\boldsymbol{x}$ and $\boldsymbol{E}d\boldsymbol{P}$ when taken on all directions of space. To obtain a polarisation $\boldsymbol{P}$ the work has to be integrated from 0 to P, leading to the energy u_P to reach a polarisation state $\boldsymbol{P}$:

$$u_P = \frac{1}{2}\boldsymbol{E}\boldsymbol{P} = \frac{1}{2}\sum_i E_i P_i. \tag{3.2.3}$$

Substituting the relation linking $\boldsymbol{P}$ and $\boldsymbol{E}$ through the tensor of polarisability leads to:

$$u_P = \frac{1}{2}\sum_i \sum_j \alpha_{ij} E_i E_j \tag{3.2.4}$$

An example can be conceptualised where an initial system with no electric field becomes polarised by an incident $(E_x, 0, 0)$ field. Then the field is modified to $(E_x, E_y, 0)$ before having the E_x and E_y components brought successively back to 0. This involves the expression of four work

functions expressing the transitions:

$$u_{(0,0,0)\to(E_x,0,0)} = \int_0^{E_x} \alpha_{xx} E_x dE_x = \frac{1}{2}\alpha_{xx}(E_x)^2 \tag{3.2.5}$$

$$u_{(E_x,0,0)\to(E_x,E_y,0)} = \int_0^{E_y} [\alpha_{yy}E_y + \alpha_{xy}E_x]\, dE_y = \frac{1}{2}\alpha_{yy}(E_y)^2 + \alpha_{xy}E_xE_y \tag{3.2.6}$$

$$u_{(E_x,E_y,0)\to(0,E_y,0)} = \int_{E_x}^{0} [\alpha_{yx}E_y + \alpha_{xx}E_x]\, dE_x = -\frac{1}{2}\alpha_{xx}(E_x)^2 - \alpha_{yx}E_yE_x \tag{3.2.7}$$

$$u_{(0,E_y,0)\to(0,0,0)} = \int_{E_y}^{0} \alpha_y E_y dE_y = -\frac{1}{2}\alpha_{yy}(E_y)^2 \tag{3.2.8}$$

The total energy change should be equal to 0 as the initial and final states of the system are equivalent. This imposes that:

$$\alpha_{xy} = \alpha_{yx}. \tag{3.2.9}$$

This procedure can be done on any direction and demonstrates the symmetric nature of the tensor of polarisability, leading to $\alpha_{yx} = \alpha_{xy}$, $\alpha_{zx} = \alpha_{xz}$ and $\alpha_{zy} = \alpha_{yz}$.

3.2.2 Polarisability ellipsoid

The tensor of polarisability can be expressed in any referential. It is, therefore, possible to transform $\boldsymbol{P'} = (P'_x, P'_y, P'_z)$ through linear combinations of (P_x, P_y, P_z). The associated factors can then be directly applied on $\boldsymbol{\alpha}$ now expressed as $\boldsymbol{\alpha'}$. $\boldsymbol{\alpha}$ can be rewritten as a non-zero diagonal matrix in the proper base $R' = (\boldsymbol{x'}, \boldsymbol{y'}, \boldsymbol{z'})$ with the associated $\boldsymbol{E'}$ field and polarisation $\boldsymbol{P'}$. This leads to the following expression of the polarisability tensor $\boldsymbol{\alpha}^{R'}$:

$$\boldsymbol{\alpha}^{R'} = \begin{pmatrix} \alpha_{x'x'} & 0 & 0 \\ 0 & \alpha_{y'y'} & 0 \\ 0 & 0 & \alpha_{z'z'} \end{pmatrix} \tag{3.2.10}$$

A more visual interpretation of the tensor can be done through parametrisation. In the space described by he components of $\boldsymbol{E'}$ an isosurface can be described for which $|\boldsymbol{P}| = P_0$. The parametrisation is as follows:

$$\frac{E'^2_x}{\left(\frac{1}{\sqrt{\alpha_{x'x'}}}\right)^2} + \frac{E'^2_y}{\left(\frac{1}{\sqrt{\alpha_{y'y'}}}\right)^2} + \frac{E'^2_z}{\left(\frac{1}{\sqrt{\alpha_{z'z'}}}\right)^2} = P_0^2 \tag{3.2.11}$$

$\alpha^{R'}$ in the new base R' is dependent on α form the real base R of the molecule through the transformation matrix Q and its inverse Q^{-1}: $\alpha^{R'} = Q\alpha Q^{-1}$. The coordinates and orientation of the ellipsoid can vary when the parameters of α change accordingly.

Since α is dependent on the relative molecular structure, we have a dependance of the polarisability tensor on the atomic distances and therefore a periodic temporal variation with frequency ω when phonons are present. This is important as the Raman scattering process relies on the first order derivative of the polarisability as seen in section 3.1.

3.2.3 Simple example: CO_2

To visualise this behaviour we will consider the simple molecular system CO_2. Linear molecule systems possess a total of 3N-5 modes, leading to a total of 4 modes for CO_2. Two vibration modes are along O=C=O, while the two others are perpendicular to this axis. The latter are degenerate versions of the same mode, leading to three distinct modes all presented in Figure 3.1. The change of the polarisability tensor is shown in the ellipsoid representation introduced in section 3.2.2.

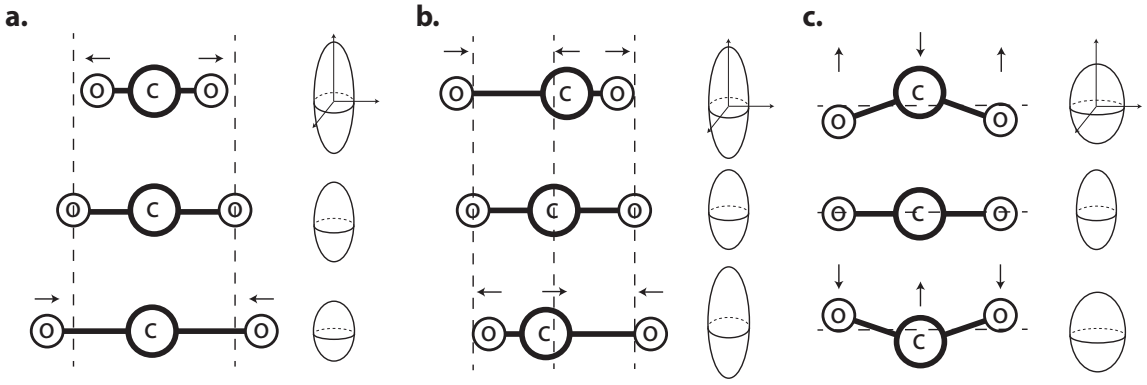

Figure 3.1 – Three vibration modes of a CO_2 molecule with the associated ellipsoid representation of the polarisation tensor.

When the motion of the oxygen atoms relative to the centre carbon element is symmetric, no molecular dipole arises and thus no oscillating dipole is created. This is due to overlapping positive and negative charge centres. On the other hand, if the oscillatory behaviour is asymmetric, a local periodically oscillating dipole is created. The polarisability ellipsoid changes in shape for every mode. But it is the derivative of the transformation that plays a role in the Raman scattering (introduced in Equation 3.1.9). Figure 3.1 shows the different vibration modes of a CO_2 molecule [62].

- Figure 3.1 **a)** shows a symmetric vibration mode with no dipole variation as the charge centres coincide. The polarisability tensor shows a non zero derivative value as the vibration goes through equilibrium. This makes this vibration Raman active according to the formalism introduced in section 3.1.

- Figure 3.1 **b)** shows an asymmetric vibration leading to a longitudinal dipole oscillation. This allows for infrared activity. Both oscillation extreme positions are equivalent in terms of polarisability. The deduction is that the polarisability tensor shows a derivative equal to zero in the equilibrium position, thus the mode is Raman inactive.
- Figure 3.1 **c)** shows an asymmetric vibration leading to a transverse dipole oscillation and therefore infrared activity similar to **b)**. The polarisability has the same characteristic as **b)** around the equilibrium, thus the mode is Raman inactive.

3.3 Raman scattering in the crystal lattice

The scope of this work is to investigate collective vibrations also knows as phonons in the crystalline lattice of perovskite oxides. In the previously introduced Raman tensor it is possible to replace $\boldsymbol{Q}(t)$ by the displacement vector $\boldsymbol{Q}_{n,\boldsymbol{k}}(t)$ at the reciprocal space position $\boldsymbol{k}$ within the first Brillouin zone. This quantity now describes all motion within the lattice for a particular phonon branch n. As a result the Raman tensor can now be rewritten from equation 3.1.9 as:

$$\boldsymbol{R} = \left.\frac{d\boldsymbol{\alpha}}{d\boldsymbol{Q}_{n,\boldsymbol{k}}}\right|_0 \boldsymbol{Q}_{n,\boldsymbol{k}}(t=0), \tag{3.3.1}$$

which corresponds to the derivative of the polarisability tensor over the displacement vector $\boldsymbol{Q}_{n,\boldsymbol{k}}$. As $\boldsymbol{\alpha}$ encapsulates the symmetries of the lattice, $\boldsymbol{R}$ will express the symmetry of the lattice distortion. Through this relation the symmetric aspect of the polarisability tensor is carried over to the Raman tensor.

The Raman activity of the phonon modes is determined by symmetry and can be predicted as soon as the crystal structure (space group and atomic positions) is known. They are usually labelled with the Mulliken symbols for the irreducible representations of the point group of the crystal explained in Table 3.1.

3.3.1 Accessible part of the Brillouin zone

The maximum momentum accessible by this method is obtained with a backscattering geometry and corresponds to twice the energy of the incident radiation. In analogy this upper bound provides an estimation of which parts of the Brillouin zone can be probed though this technique [63]. For example, an incident radiation of 633 nm would corresponds to an upper bound at $\approx$2 x 10^5 cm^{-1}. The structures investigated in the present work have lattice parameter a situated between 4 and 10 Å, thus resulting in a boundary of the Brillouin zone located at $\pi/a \approx 10^8$ cm^{-1}. In conclusion, the Raman spectrometer, in its most favourable configuration, is only able to measure 0.1% of the first Brillouin zone. As a result, it is considered that Raman probes phonons at the zone centre only.

A	Singly degenerated mode Symmetric along the principal axis of the lattice
B	Singly degenerated mode Anti-symmetric along the principal axis of the lattice
E	Doubly degenerated mode
T or F	Triply degenerated mode
subscript 1	Symmetric with respect to a mirror plane perpendicular to the principal axis
subscript 2	Anti-symmetric with respect to a mirror, plane perpendicular to the principal axis
subscript g	Symmetric with respect to the inversion (gerade = even)
subscript u	Anti-symmetric with respect to the inversion (ungerade = odd)
(')	Symmetric with respect to a mirror plane horizontal to the principal rotational axis
(")	Anti-symmetric with respect to a mirror plane horizontal to the principal rotational axis

Table 3.1 – Mulliken symbols for irreducible representations of point groups.

3.3.2 Example: Raman investigation of Diamond

A method used to determine the normal modes of a perovskite unit cell relies on the the nuclear site analysis (NSA). From all methods it requires the least amount of a-priori information. The site symmetry and the Wyckoff positions usually suffice [64]. The total number of normal modes of the crystal lattice can be obtained through the sum of all site groups and occupied Wyckoff positions. In the next part we will use the Diamond structure to determine its normal modes as an illustration.

Let us consider the example of the diamond structure in the $F\bar{4}3m$ space group. The diamond structure has two sites occupied in the primitive cell, which are the Wyckoff point 4a (0,0,0) and 4c (1/4, 1/4, 1/4). These give rise to six normal vibration modes. The procedure at this point requires the investigation of the character table of $F\bar{4}3m$, which is given in the international tables of crystallography [65].

After a thorough identification, the Raman active modes of the diamond structure can be written as $\Gamma_{\text{vib.}}$ [66]:

$$\Gamma_{\text{vib.}} = T_2 \tag{3.3.2}$$

Following the previous explanation that only the Γ point is measurable through Raman spectroscopy, only one triply degenerated phonon mode should be observable. The associated Raman tensors are [67]:

$$T_2(x) = \begin{pmatrix} 0 & 0 & 0 \\ 0 & 0 & d \\ 0 & d & 0 \end{pmatrix}, T_2(y) = \begin{pmatrix} 0 & 0 & d \\ 0 & 0 & 0 \\ d & 0 & 0 \end{pmatrix}, T_2(z) = \begin{pmatrix} 0 & d & 0 \\ d & 0 & 0 \\ 0 & 0 & 0 \end{pmatrix} \tag{3.3.3}$$

Indeed, diamond in the $F\bar{4}3m$ space group has only one triply degenerated Raman mode as shown by the works of S.A. Solin *et al.* [67].

$F\bar{4}3m$	#	1	3	2	-4	m	function
Mult.	-	1	8	3	6	6	-
A_1	Γ_1	1	1	1	1	1	$x^2+y^2+z^2$
A_2	Γ_2	1	1	1	-1	-1	-
E	Γ_3	2	-1	2	0	0	$(2z^2-x^2-y^2, x^2-y^2)$
T_1	Γ_4	3	0	-1	1	-1	(J_x, J_y, J_z)
T_2	Γ_5	3	0	-1	-1	1	$(x,y,z), (xy, xz, yx)$

Table 3.2 – Character table retrieved from the Bilbao crystallography server for $F\bar{4}3m$.

3.4 The Raman apparatus

The Raman setup used within this work was a Renishaw InVia Reflex Raman microscope spectrometer. The incident monochromatic radiation is extracted from different laser sources. This includes a solid state diode (785 nm), a helium-neon (633 nm), a frequency doubled Nd:YAG (532 nm) and a a helium-cadmium (325 / 442 nm) laser. The Rayleigh peak is filtered out with spectral cut-offs at 60 cm^{-1}, 70 cm^{-1}, 80 cm^{-1}, 95 cm^{-1} and 350 cm^{-1} respectively. The incident radiation can be polarised and the measured radiation can be analysed to treat crossed and parallel polarisation configurations. While a larger selection of optical lenses was available, only two were used in the present work: x100 with a N.A. of 0.85 for the depth measurements and x50 with a N.A. 0.5 for the temperature measurements. The sample stage can be moved in three directions with a precision of 0.1 μm. A sketch and a schematic representation of the setup is presented in Figure 3.2.

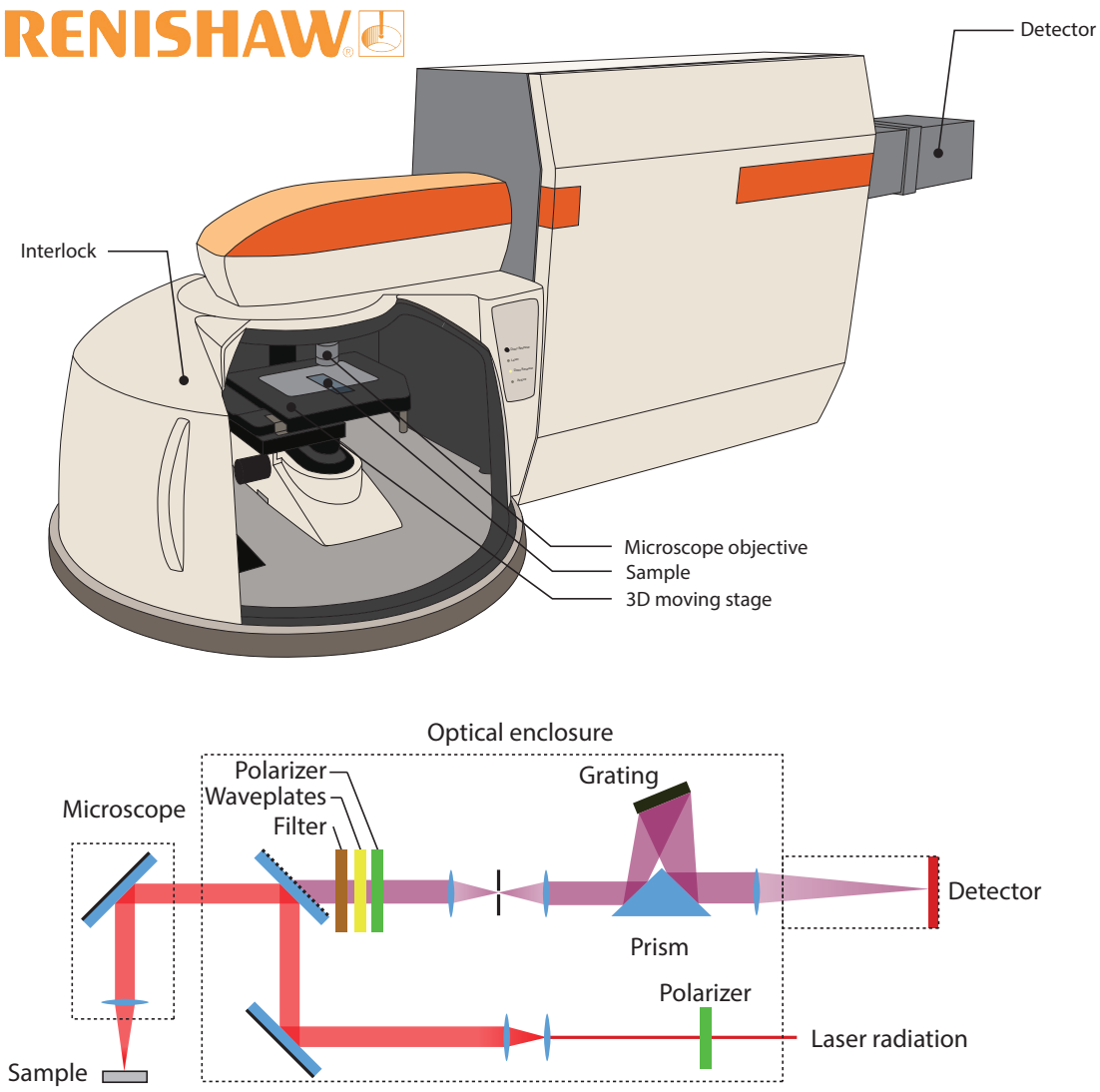

Figure 3.2 – Schema of the experimental setup used in this work. The schematic path of the laser beam is shown in the lower part.

Chapter 4

Raman spectroscopy on thin films

Chapter 3 introduced Raman spectroscopy as a spectroscopic method allowing to probe the centre of the Brillouin zone. The adaptation of Raman scattering to nano structures poses some difficulties. The very axiom defining a lattice is invalidated by their size limitations. This relaxes the phonon definition in the reciprocal space and, therefore, impacts the response to Raman scattering. This so-called phonon confinement effect is understood but may raise difficulties in the interpretation of peak positions and shapes.

Another reason for the scarcity of systematic investigations of thin and ultrathin films of perovskite oxides with Raman spectroscopy is the intrinsically small interaction volume, and therefore, small small signal to noise ratio. Furthermore, when the film is epitaxially deposited onto a similarly Raman active substrate, the comparably large volume occupied by the substrate often masks the film signal.

The present chapter aims at introducing the phonon confinement model and discuss the physical difficulties of small scatter volumes.

4.1 Phonon confinement

An interruption of the lattice breaks the initial assumption of an infinite crystal structure. A finite periodicity implies boundary conditions such that the wave functions describing the phonon has to decay at the boundaries [68]. It is then the limitation of this spatial extent in combination with Heisenberg's uncertainty principle that implies an non negligible uncertainty on the wavevector. In approximation Δq is found to be $\approx \pi/d$ where d is the confined dimension. This uncertainty on q then relaxes the $q \approx 0$ characteristic of the light scattering process established in section 3.3.2, thus allowing a larger range of phonons to contribute to the Raman signal. A more detailed visual interpretation of this phenomena is presented in the work published by Akhilesh K. Arora *et al.* entitled *Phonon Confinement in Nanostructured Materials* [68]. Depending on the dimension of the confinement and on the shape of the associated phonon branch, different scenarios can be observed.

In practice, it is found acceptable to approximate a crystal as infinite for characteristic dimensions above ≈ 100 nm [63]. This corresponds to approximately 250 unit cells for a 4 Å lattice constant. Above this threshold, boundary conditions are deemed negligible and not taken into consideration. In the present work, structures with characteristic dimensions d down to ≈ 1.2 nm (1.5 unit cells in one direction) will be investigated and phonon confinement effects may come into play.

4.1.1 The phonon confinement model

The formalism describing phonon confinement was first introduced by Richter *et al.* in 1981 [69] and further developed by Campbell *et al.* in 1986 [70]. It was proposed to express the modified phonon wave equation through a gaussian confinement function acting as an envelope. Thus leading to:

$$\Psi(\boldsymbol{q_0},\boldsymbol{r}) = W(\boldsymbol{r})u(\boldsymbol{q_0},\boldsymbol{r})e^{-i\boldsymbol{q_0}\cdot\boldsymbol{r}}, \tag{4.1.1}$$

$$\Psi(\boldsymbol{q_0},\boldsymbol{r}) = \Psi'(\boldsymbol{q_0},\boldsymbol{r})u(\boldsymbol{q_0},\boldsymbol{r}), \tag{4.1.2}$$

where $W(r)$ is the envelope, $u(\boldsymbol{q_0},\boldsymbol{r})$ the periodicity of the crystal and $\Psi(\boldsymbol{q_0},\boldsymbol{r})$ the wavefunction of the phonon. Expanding $\Psi'(\boldsymbol{q_0},\boldsymbol{r})$ in a Fourier series leads to:

$$\Psi'(\boldsymbol{q_0},\boldsymbol{r}) = \int C(\boldsymbol{q_0},\boldsymbol{q})e^{i\boldsymbol{q}\cdot\boldsymbol{r}}d\boldsymbol{q}, \tag{4.1.3}$$

with the Fourier coefficients $C(\boldsymbol{q_0},\boldsymbol{q})$ equal to:

$$C(\boldsymbol{q_0},\boldsymbol{q}) = \left(\frac{1}{2\pi}\right)^3 \cdot \int \Psi'(\boldsymbol{q_0},\boldsymbol{r})e^{-i\boldsymbol{q}\cdot\boldsymbol{r}}d\boldsymbol{r}. \tag{4.1.4}$$

The gaussian confinement function can be written:

$$W(\boldsymbol{r}) = e^{-\alpha|\boldsymbol{r}|^2/d^2}, \tag{4.1.5}$$

where α is the factor indicating the decay rate at the boundary and d is the characteristic dimension of the nano-structure. Replacing this function into the definition of $\Psi'(\boldsymbol{q_0}, \boldsymbol{r})$ leads to the following expression of the Fourier factors $C(\boldsymbol{q_0}, \boldsymbol{q})$:

$$|C(\boldsymbol{q_0}, \boldsymbol{q})|^2 \quad = \quad e^{-|\boldsymbol{q}|^2 d^2/2\alpha}. \tag{4.1.6}$$

Different models suggest different values for α. Richter *et al.* used a value of 2 while Campbell *et al.* used $8\pi^2$. The latter seems to better coincide with experimentally verified measurements. When applied to Raman spectroscopy, it is possible to set $\boldsymbol{q_0} = 0$. Using all previous elements results in a calculated Raman intensity equal to:

$$I(\omega) \approx \int \frac{\mathrm{d}\boldsymbol{q}|C(0,\boldsymbol{q})|^2}{(\omega - \omega(\boldsymbol{q}))^2 + (\Gamma_0/2)^2}, \tag{4.1.7}$$

where $I(\omega)$ is the intensity at the wavenumber ω, $\boldsymbol{q}$ is the wave vector, $\omega(\boldsymbol{q})$ is the phonon dispersion, Γ_0 is the FWHM of the mode in the bulk. Depending on the type of the confinement different definitions of the Fourier factor $C(0,\boldsymbol{q})$ are to be used. In the following subsections we will introduce the cases where the confinement is radial for a nano-particle, circular for a nano-rod and along only one spatial direction for thin films.

Three-dimensional confinement

Three-dimensional confinement, which has been investigated most in the literature, relates to the case where all three spatial dimensions become very small. Most commonly nano-particles are treated as spheric, thus leaving only one parameter $|\boldsymbol{r}|$. In this case the Fourier factor $C(0,\boldsymbol{q})$ takes the following form [70]:

$$|C(0,\boldsymbol{q})|^2 \approx \exp\left(-\frac{|\boldsymbol{q}|^2 L^2}{16\pi^2}\right), \tag{4.1.8}$$

where L corresponds to the radius of the nanoparticle.

Two-dimensional confinement

Two-dimensional confinement relates to a case where two of the three spatial dimensions become very small. This would correspond to a rod. In this case the Fourier factor $C(0,\boldsymbol{q})$ takes the following form [70]:

$$|C(0,\boldsymbol{q})|^2 \approx \exp\left(-\frac{q_1^2 L_1^2}{16\pi^2}\right) \exp\left(-\frac{q_2^2 L_2^2}{16\pi^2}\right) \left|1 - erf\left(\frac{iq_1 L_2}{\sqrt{32\pi}}\right)\right|^2, \tag{4.1.9}$$

where q_1 is the component of $\boldsymbol{q}$ perpendicular to the rod axis, thus corresponds to the radial coordinate $|\boldsymbol{r}|$ in a cylindrical coordinate system. L_1 is the associated size along this direction. q_2 is the remaining component from $\boldsymbol{q}$, thus corresponds to second cylindrical coordinate along the length of the rod with a size L_2. erf() is the complex error function.

Uni-dimensional confinement

Uni-dimensional confinement relates to the case where only one of the three spatial dimensions becomes very small. This would correspond to ultra-thin films; it is the relevant case for the present work. The Fourier factor $C(0,\boldsymbol{q})$ in the case of uni-dimensional confinement takes the following form [70]:

$$|C(0,\boldsymbol{q})|^2 \approx \exp\left(-\frac{q_1^2 L_1^2}{16\pi^2}\right)\left|1 - erf\left(\frac{iq_1 L_1}{\sqrt{32\pi}}\right)\right|^2, \tag{4.1.10}$$

where q_1 is the confined component of $\boldsymbol{q}$ in reciprocal space, L_1 is size of the crystal along the confined direction, i.e. the film thickness.

In the next section we will show some Raman investigations on nano-structures, that explicitly treat the introduced phonon confinement models.

4.1.2 Experimental verification of the confinement model

One compound that was extensively studied for phonon confinement is titanium dioxide (TiO_2), which is most commonly synthesised in a polycrystalline form with a variable grain size. A typical Raman spectrum of TiO_2 anatase is presented in Figure 4.1.**a.**. A study performed by Bersani *et al.* reported the shift and broadening of the Raman E_g band located at ≈ 144 cm^{-1} [71]. The broadening of the mode with film thickness is illustrated in Figure 4.1.**b.**. Within this investigation the phonon confinement model for the three-dimensional confinement (Equation 4.1.8) was used to compute the expected shift and broadening of the mode with the grain size shown in Figure 4.1.**c.**. A rather good agreement with the experimentally acquired data was found, as shown in Figure 4.1.**d.**. The study by Bersani *et al.* was then completed by Nasar *et al.* for a much smaller grain size down to 1.5 nm [72]. In this investigation the shift of two Raman E_g modes ($E_g^{(1)}$: ≈ 144 cm^{-1} and $E_g^{(2)}$: ≈ 197 cm^{-1}) was reported. These can be seen in Figure 4.1.**e.** and .**f.**, respectively, for different grain sizes. This more precise study managed to differentiate the contributions to the shift due to the compressive strain induced by the surface pressure from the phonon confinement effects [72].

An investigation of the effects of phonon confinements on the Raman response of the LO mode in nano-wires of GaAs was performed by Arora *at. al.* in 2004 [68]. This corresponds to a two-dimensional confinement, thus requires the use of Equation 4.1.9. The calculated evolution of the Raman LO mode depending on the thickness of the wire is shown in Figure 4.2.**a.**, with the associated shift in position and width in **b.**. The same mode was measured in an investigation by Begum *et al.* [73] as illustrated in Figure 4.2.**c.**. It is found that the phonon confinement model and the experimental data are in good agreement with each other.

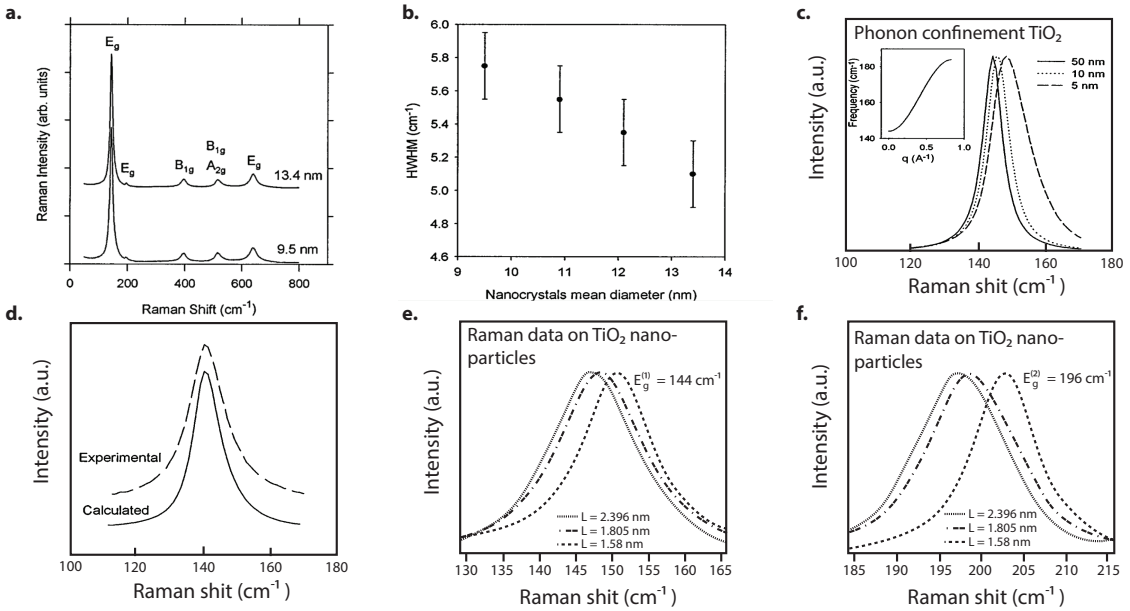

Figure 4.1 – a. Raman spectrum of TiO_2 measured by Bersani *et al.* [71]. **b.** Evolution of the HWHM of the TiO_2 E_g mode located at ≈ 144 cm^{-1} with the nanoparticle size [71]. **c.** Calculated evolution of the TiO_2 E_g mode using the three-dimensional phonon confinement model [71]. **d.** Comparison of the calculated and measured data. Both are in good agreement [71]. **e. & f.** More recent study of the same behaviour of the TiO_2 E_g modes with thickness.

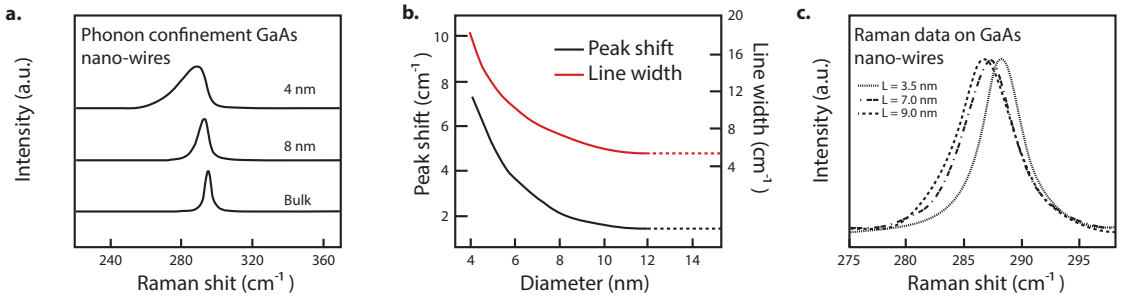

Figure 4.2 – a. Calculated Raman spectra for the confined LO mode of GaAs nano-wires defined by the diameter parameter d [68]. **b.** Raman peak shift and width induced by the phonon confinement [68]. **c.** Experimental result of GaAg nano-wires measured by Begun *et al.* [73].

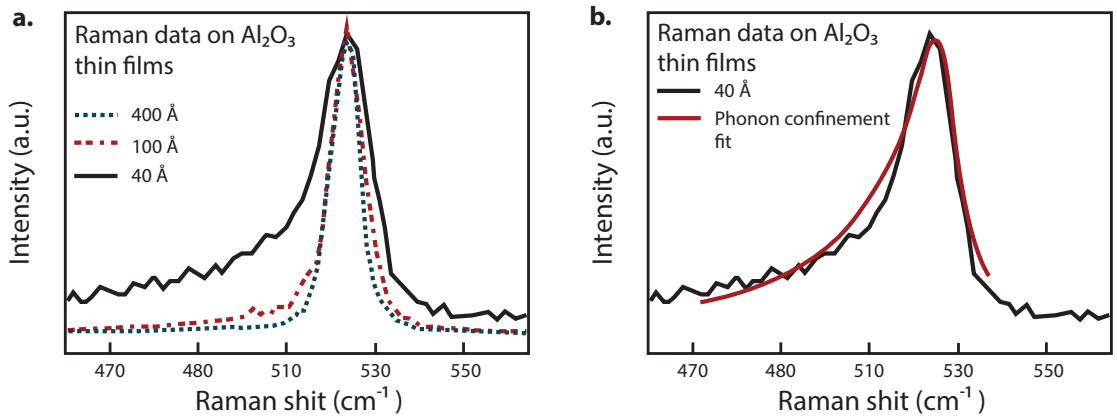

Figure 4.3 – a. Raman measurements of Al_2O_3 with different film thicknesses by Murphy *et al.* [74]. **b.** Comparison between the measurement and the uni-dimensional phonon confinement of Al_2O_3 performed by Campbell *et al.* [70].

The amount of literature available on the effect of phonon confinement on the Raman signatures of thin films, is more scarce. One reported investigation of phonon confinement in crystalline thin films was performed by Campbell *et al.* on the Raman measurements of thin Al_2O_3 films previously performed by Murphy *et al.* [74]. The measured data is illustrated in Figure 4.3.**a.**. No strong shift in the position (at the resolution of the data) is observed. On the other hand, a significant *shouldering* is observed as the film thickness decreases to 40 Å. The uni-dimensional confinement model (Equation 4.1.10) seems to be in good agreement with the data, as shown in Figure 4.3.**b.**.

A substantial set of information can be extracted from these examples. The phonon confinement depends strongly on the shape of the phonon dispersion curve. As a result it is possible to have either a shift in the position or broadening of the lineshape or both of them combined. Furthermore, it was shown that the phonon confinement model allows to investigate the qualitative impact of the phonon confinement model on a Raman mode. Yet, the specific nature of each mode and its behaviour in the reciprocal space, does not allow for a generalised interpretation. Every new investigation will require the calculation (or measurement) of the phonons in the first Brillouin zone followed by the integration with the introduced model.

4.2 Mixing of the film and substrate signal

In the present section a more experimental difficulty will be discussed. The Raman apparatus is an optical acquisition system, meaning that as all equivalent systems it is bound to follow the optical laws and thus is limited by the Abbe diffraction limit. Found in 1873 by Ernst Abbe, this law stipulates that a visible radiation of wavelength λ, refractive index n that converges on a

spot (Raman incident focal point) at an angle θ will make a spot called circle of confusion with a radius d as follows [75]:

$$d = \frac{\lambda}{2n\sin\theta} = \frac{\lambda}{\mathrm{NA}}, \tag{4.2.1}$$

where NA is called the numerical aperture (used in lens systems). The Raman apparatus used in this work utilises a microscope objective with $\mathrm{NA} = 0.9$. Meaning that at a wavelength of 633 nm the circle of confusion has a diameter of $2d \approx 1.2\ \mu$m. This dimension limits the resolution of the Raman apparatus within the plane perpendicular to the optical axis.

In the context of ultrathin epitaxially grown structures, it is the vertical dimension along the optical axis which is of concern. But it is the same diffraction rule that limits the vertical resolution. If rays are traced from the radial edges of the lens through the radial edges of the confusion circle, an estimation of the volume can be observed. These edges correspond to the depth of field, i.e. the maximal vertical resolution. This quantity can be geometrically approximated by $l = \lambda/\mathrm{NA}^2$, resulting in a vertical resolution limit of 0.78 μm with the previously described parameters, which is acceptable for most applications but tends to be too important when the vertical thickness of the investigated object is in the nanometer range. An ultrathin film of 10 nm would fill only 1.3% of the illumination volume.

In our present work, the films are deposited epitaxially onto perovskite substrates, and their signatures will thus be superposed. Typical substrates ($SrTiO_3$, $LaAlO_3$, LSAT, $R$$ScO_3$, $R$$GaO_3$, etc ...) have a very intense Raman spectrum and may therefore dominate the spectrum of the film [76].

4.3 Need for advanced treatment

A way to extract the film signal from the spectrum is to subtract the signal of the substrate. The reference spectrum of the substrate can be obtained on a virgin substrate, or by focusing the laser spot deep into the crystal. Unfortunately this approach, even when perfectly executed, has three fundamental flaws:

- **Noise contribution:** The subtraction of a signal from another one is vulnerable to statistical error. The acquisition noise is therefore simply summed, which can result in a significant loss of information and induce errors in the interpretation. This is particular important in the present work as thin or ultrathin films often have very weak Raman intensities, thus are already dominated by noise. This is why the addition of noise hinders dramatically their interpretation.
- **Relative peak intensities:** The intensities of the peaks constituting the Raman signature are very dependent on the crystalline orientation and therefore the domains within

the crystal. A typical example is the signature of $LaAlO_3$ which is well know for having ferroelastic domains. Indeed the Raman signal depends on the crystal orientation and therefore on the domain orientation [77]. This means that an acquired substrate signature may not be equivalent to the one the user seeks to subtract, hence introducing a strong error component.

- **Epitaxial effects:** The subtraction relies on the hypothesis that the substrate signature is not affected by the deposited film. One possibility is that an epitaxially deposited film induces structural changes to the underlying substrate. This would result in a change of the unit cell parameters at the interface, thus modifying the associated Raman signature. The second factor is related to the optical effects the film can have on the incident and emitted radiations. This can be caused as much by the individual absorption coefficients as the relative indexes of each compound. In both these scenarios, a subtraction of a Raman spectrum acquired on a virgin substrate from the interfacial spectrum would result in errors.

All of theses issues make the subtraction procedure prone to errors. It is because of all these inconveniences that the subtraction method was deemed not suitable for the purpose of the present work. As a result we implemented and used alternative measurement (Chapter 3.4) and advanced numerical methods (Chapter 6).

Part III

Measurement and analysis of Raman depth profiles

Chapter 5

Acquisition and understanding of the Raman depth profiles

5.1 Motivation

The previous chapter introduced the difficulties one can encounter while performing Raman spectroscopy on thin or ultrathin perovskite films deposited on substrates of the same family. One particular challenge is the extraction of an interpretable Raman signature for an ultrathin perovskite film which has been epitaxially deposited onto a similarly Raman active substrate. The following chapter aims at introducing a novel approach consisting of generating multidimensional datasets through the use of Raman depth profile measurements, that will allow the identification and separation of the contributions from the thin film and the underlying substrate.

This chapter will provide a first understanding of the Raman depth profiles through a step by step analysis of how different signal contributions should behave with depth. Last, this will be illustrated with a Raman depth profile simulation followed by an example of ultrathin $NdNiO_3$ film epitaxially deposited on $LaAlO_3$.

5.2 Expected behaviour

The Raman apparatus used in this work was formerly introduced in Chapter 3.4. The setup for depth profile measurements consists of using the same instrument to acquire multiple spectra of the sample at different positions along the vertical incident beam axis. Optimally, the depth range is centred in such a way that its centre coincides approximately with the strongest signal generated by the thin film. At each step a Raman spectrum is acquired. Combining all these spectra results in a Raman depth profile measurement.

The present work aims at acquiring depth profile measurements on ultrathin perovskite films deposited on substrates of the same family. This would then allow to identify the parts of the signature belong to the film and those belonging to the substrate. Yet, it was found that the complexity of the signature in tandem with this novel approach does not yield results that are necessarily intuitive. Within this section we aim at providing a qualitative explanation the expected signal variations during a depth profile measurement.

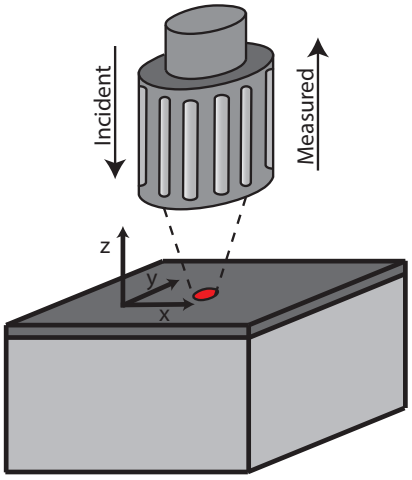

Figure 5.1 – Schematic representation of the Raman depth profile measurement setup depicting the strongly focusing optical lens and the sample composed of a thin film deposited on a substrate.

5.2.1 Incident intensity

We first discuss the profile of the laser beam incident on the sample. The beam shape is gaussian with its origin a the focal position of the lens Δ. The relation linking the intensity of the Gaussian beam $I(z,r)$ at the position (z,r) in cylindrical coordinates is described by:

$$I(z,r) = I_0 \cdot \left(\frac{w_0}{w(\Delta,z)}\right)^2 \cdot \exp\left(\frac{-2r^2}{w(\Delta,z)^2}\right) \tag{5.2.1}$$

$$w(\Delta,z) = w_0 \cdot \sqrt{1+\left(\frac{(z-\Delta)\lambda_{in}}{\pi w_0^2}\right)^2}, \tag{5.2.2}$$

where I_0 represents the initial gaussian intensity, w_0 is the waist at the focal position of the lens $z=\Delta$. Note that here Δ is the depth parameter compared to the surface of the sample.

$w(\Delta,z)$ is the waist at a given distance z and λ_{in} is the wavelength of the beam. The chosen coordinate is cylindrical as there is a rotation symmetry around the optical axis for this type of measurements [78]. Following this description, setting r to 0 results in the Intensity of a Gaussian beam along the optical axis expressed by:

$$I(z,r=0) \quad = \quad I_0 \cdot \left(1+\left(\frac{(z-\Delta)\lambda_{in}}{\pi w_0^2}\right)^2\right)^{-1}, \tag{5.2.3}$$

which corresponds to a Lorentzian modulation of the intensity with the depth centred at z_0. The Half Width at Half Maximum (HWHM$_z$) of this function is given by $\pi w_0^2/\lambda_{in}$. The optics within the Raman apparatus being quite complex, the factor w_0 has to be retrieved experimentally.

We now consider a sample consisting of a thin film on a much thicker substrate. In a first step, no absorption effects are taken into account and both compounds of the sample are assumed to have a refractive index equal to 1. The dimension of the films (all below 30 nm in size and usually around 10 nm) compared to the HWHM$_z$ of the incident Gaussian beam of $\approx$0.78 μm suggests that these can be, as seen by the apparatus, assimilated to Dirac type functions located in z_{film}. As the depth profile is performed, the laser power on the film should correspond to the beam shape along z, therefore to a lorentzian function expressed by I_{film}:

$$I_{\text{film}} \quad \approx \quad I_0 \cdot \left(\frac{w_0}{w\left(\Delta,z_{\text{film}}\right)}\right)^2 \cdot \left[\int_0^\infty \exp\left(\frac{-2r^2}{w\left(\Delta,z_{\text{film}}\right)^2}\right) dr\right]. \tag{5.2.4}$$

On the other hand, the substrate is much thicker than the film and than the HWHM$_z$ of the incident Gaussian beam. As a result, the measured shape along z should be a step function starting defined by its origin z_{film} and with the integration of the deposited intensity according to z_{sub}. The intensity deposited within the substrate is at this point expressed by I_{sub} defined as follows:

$$I_{\text{sub}} \quad \approx \quad \int_{z_{\text{film}}}^\infty I_0 \cdot \left(\frac{w_0}{w\left(\Delta,z_{\text{sub}}\right)}\right)^2 \cdot \left[\int_0^\infty \exp\left(\frac{-2r^2}{w\left(\Delta,z_{\text{sub}}\right)^2}\right) dr\right] dz_{\text{sub}}. \tag{5.2.5}$$

If the deposited intensity is expressed solely along the beam path, equivalent to setting $r = 0$, with sole variable the depth parameter Δ, we should obtain a lorentzian distribution for the film (according to Equation 5.2.4) and a *smoothed* step function for the substrate (according to Equation 5.2.5). By *smoothed* we relate to the fact, that the deposited intensity is not 0 far away from the substrate and, similarly, never saturate as the scan proceeds deeper within the substrate. This being said, the lorentzian shape of the Gaussian beam along z tends to 0 rather fast, making these variation far away from the focal position negligible. An approximative sketch of the deposited intensities can be seen in Figure 5.2.

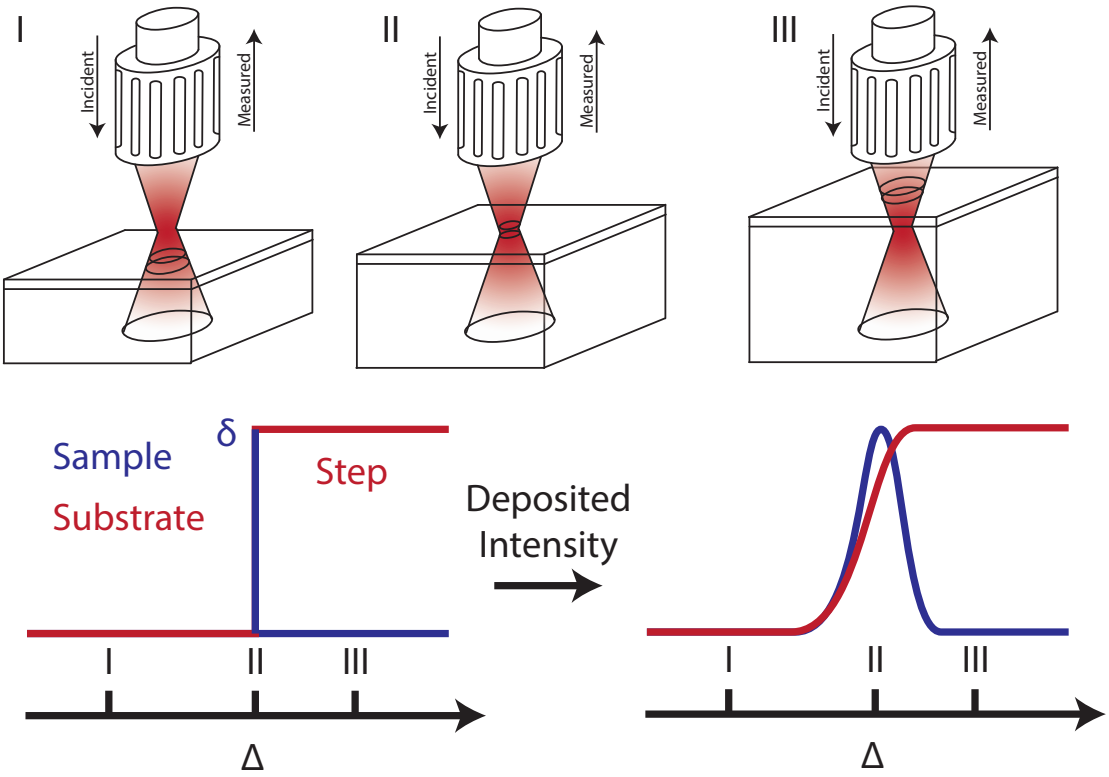

Figure 5.2 – This upper figure shows the measurement setup during a depth scan. On the far left we observe the focal point above the sample. The central image depicts the focal point within the sample. The image on the far right shows the focal point within the substrate. In the lower left we have the hypothetical representation of the film an the substrate as seen by the Raman apparatus. On the right the expected deposited intensity within the film and the substrate.

5.2.2 Acquired Intensity

The acquired intensity depends partly on the Raman tensors and the associated spectral response and on the other part on the optical setup of the Raman apparatus. The Raman process is considered to emit spherical waves at each inelastic scattering event. Exactly like the previous section, no absorption nor diffraction effects are considered in the present treatment. As a result nothing is hindering the propagation of these waves. From a geometrical point of view, only a cone of solid angle Ω reaches the objective lens. This cone depends evidently on the distance from the collection lens as shown in Figure 5.3. An optical setup then focuses the retrieved radiation onto an aperture. This will further limit Ω by systematically filtering out the intensities emerging from positions away from the focal position of the first lens. In summary, the confocality tends to create an envelope centred around this focal position. The acquired signal is then a convolution of this envelope with the deposited intensity multiplied by the Raman spectral response.

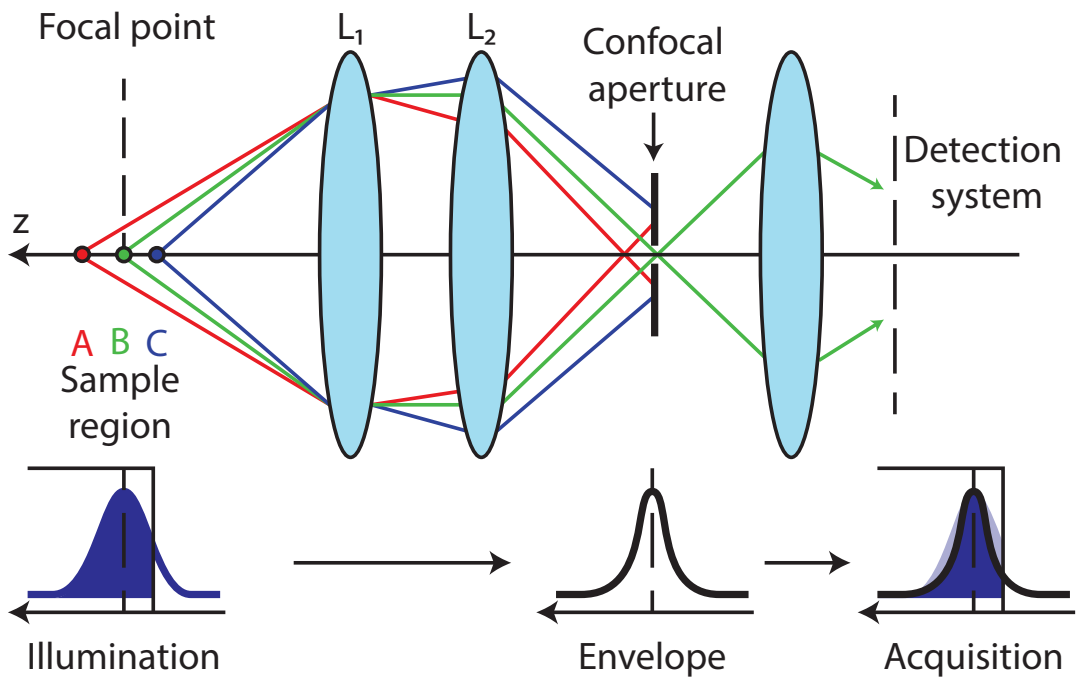

Figure 5.3 – Schematic representation of the confocal aperture in a Raman apparatus. A, B and C represent three positions after, at and before the focal position of the collector lens L_1 [79].

A detailed mathematical explanation of this procedure is shown in the works of Maruyama *et al.* [78].

An interesting remark at this stage relates to the stepping between acquisitions in a depth profile. Decreasing the stepping beyond a certain threshold will not yield a clearer acquisition of the film, nor substrate shapes. Both responses correspond to the direct and the integrated imaging of the gaussian beam shape along z. Smaller steps will only yield a more precise imaging of its shape without providing any additional information related to the investigated compounds.

5.3 Simulated behaviour

The previous section described, in an intuitive manner, the approximate shapes to be expected when performing Raman depth profile measurements on samples consisting of a film deposited onto a substrate. In order to verify these claims and investigate the influence of different instrumental parameters, we developed a simulation engine capable of simulating Raman depth profile measurements. Further details about the simulation engine are given in Appendix A.

5.3.1 Ideal case

In the following simulation, we consider a thin film with a thickness of 4 nm, i.e. much smaller than the depth of field of the microscope. The substrate, on the contrary, was chosen to have a depth of 100 μm, which is much larger than the depth of field. A schematic representation of the sample and the measurement setup can be seen in Figure 5.4.**a.**. Two, very simple but distinct, signatures were attributed to the film and the substrate, as shown in seen in Figure 5.4.**b.**. Each with one lorentzian peak only at 300 and 489 cm^{-1}, respectively. The signature of the film was multiplied by a factor in such a way that the signal from the film and the substrate have the same maximal intensity during the depth measurement. As the film has a thickness of 4 nm and the depth of field of the setup is of ≈ 780 nm the factor was set to $\approx 780/4 \approx 200$. We simulate a depth profile ranging from -5 to 5 μm with a step of 0.1 μm between acquisitions. The incident radiation was set to 633 nm with a gaussian waist w_0 of 350 nm and a confocal pinhole opening radius of 250 μm.

The result of the simulated depth profile is shown in Figure 5.4.**c.** with a contour map of the dataset. A cut along the wavenumber axis at different depths reveals the two signal contributions. On the other hand, a cut along the depth axis at the peak positions reveals the intensity variation with depth.

The first result, that appears to coincide with the intuitive investigation performed in Section 5.2, is the evolution of the intensity with the depth profile in the substrate peak region. It is perfectly comparable with what was guessed in Figure 5.2 by having the shape of a rounded step function. The response within the sample peak region is slightly more complex to understand. It is a summation of the baseline contribution of the substrate with the one from the sample signal. By subtracting the former, the intuitive shape introduced in the previous section is obtained, namely a lorentzian shape, thus suggesting that the signals are superposed in the simulation. Having established this, the simulation results are in good argument with the intuitive approach presented in the last section.

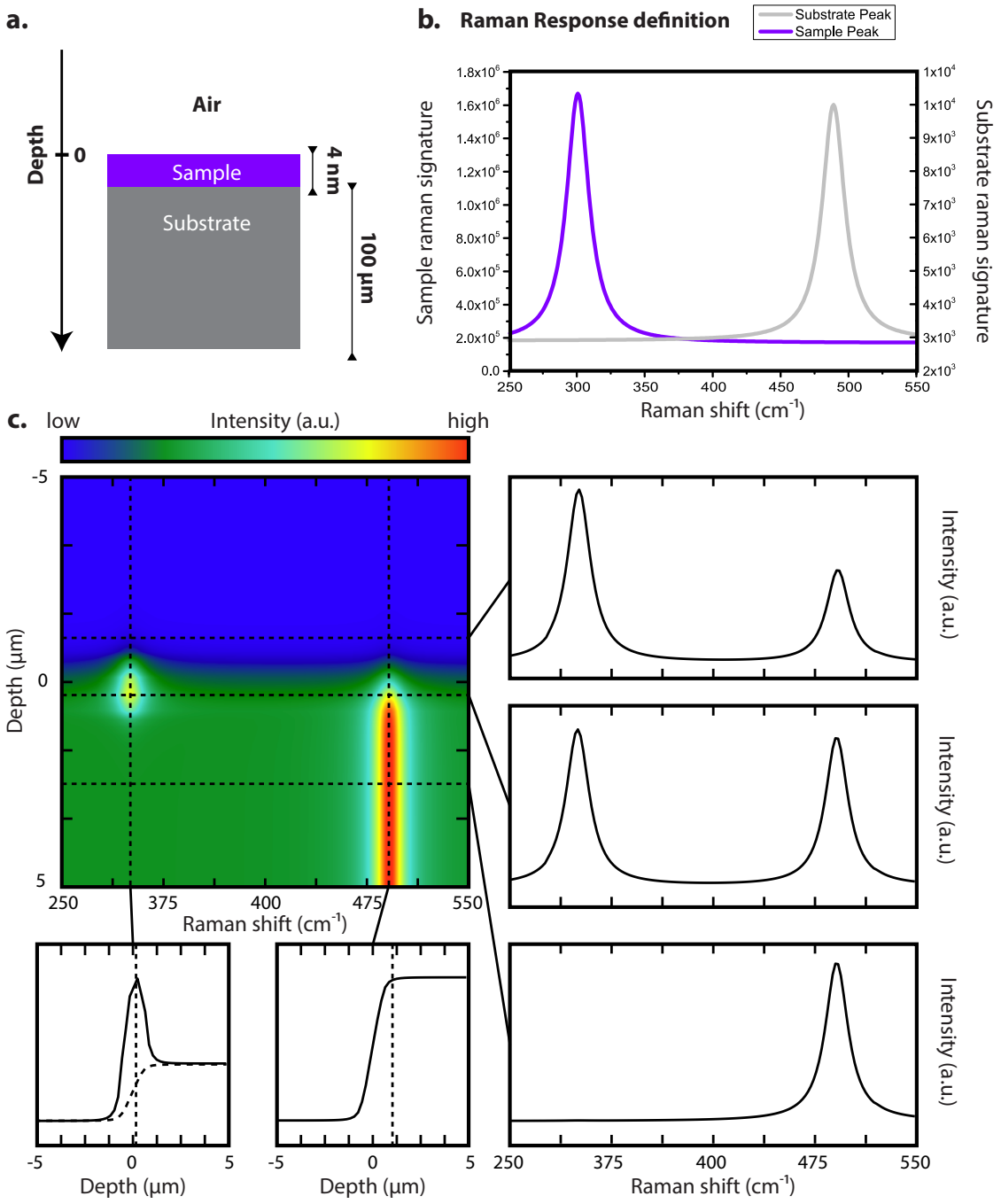

Figure 5.4 – a. Raman depth measurement setup of the sample. **b.** Signatures of the supposed thin film and the substrate. **c.** Result of the simulated depth measurement.

5.3.2 Absorption

The absorption coefficient σ is expressed through the Beer-Lambert absorption law such that:

$$\sigma = -\frac{1}{z}\ln\left(\frac{I_z}{I_0}\right) \tag{5.3.1}$$

This relation has to be taken into account for the incident Raman laser radiation as well as the backscattered radiation from the sample. These radiations have different wavelengths. As a result the absorption coefficient has to be known in an entire spectral range to account for its total impact. In the present investigation we assume that the absorption coefficient is wavelength independent. The simulation result for different depth profile measurements with varying absorption coefficients can be seen in Figure 5.5.**a.**.

The first observation is that the absorption does not seem to affect the shape of the onset as the incident beam enters the sample. A simple decrease of the maximally retrieved intensity os observed. It is the shape after the maximal intensity, as the focused beam gores further into the sample, that is the most affected. It seems to follow an exponential decrease, that could be traced back to the exponential characteristic of the absorption formulation.

5.3.3 Refractive index

In order to study the effects induced by the refractive index, we assume that the sample is 3 μm thick, has a variable refractive index, an absorption coefficient set to 0. The pinhole opening is left unchanged from the previous investigation at 250 μm. The result of these simulations can be seen in Figure 5.5.**b.**.

From the results it seems that the refractive index affects the apparent thickness of the sample. A higher index inducing a proportional thinning of its thickness. Another aspect is the effect of the refractive index on the interference patterns between the Raman responses obtained from different regions within the sample. This phenomenon impacts the distribution of the acquired intensities within the sample and has been shown to contribute to an exponential decay in the depth response similar to the absorption [78]. Unfortunately the presented simulation engine was not designed to handle inferences between rays and could not provide any insight on this behaviour.

5.3.4 Confocality

In order to study the effects induced by different sizes of the pinhole opening, we assume that the sample is 3 μm thick with a refractive index set to 1, an absorption coefficient set to 0 and a variable confocal pinhole opening. The result of these simulations can be seen in Figure 5.5.**c.**.

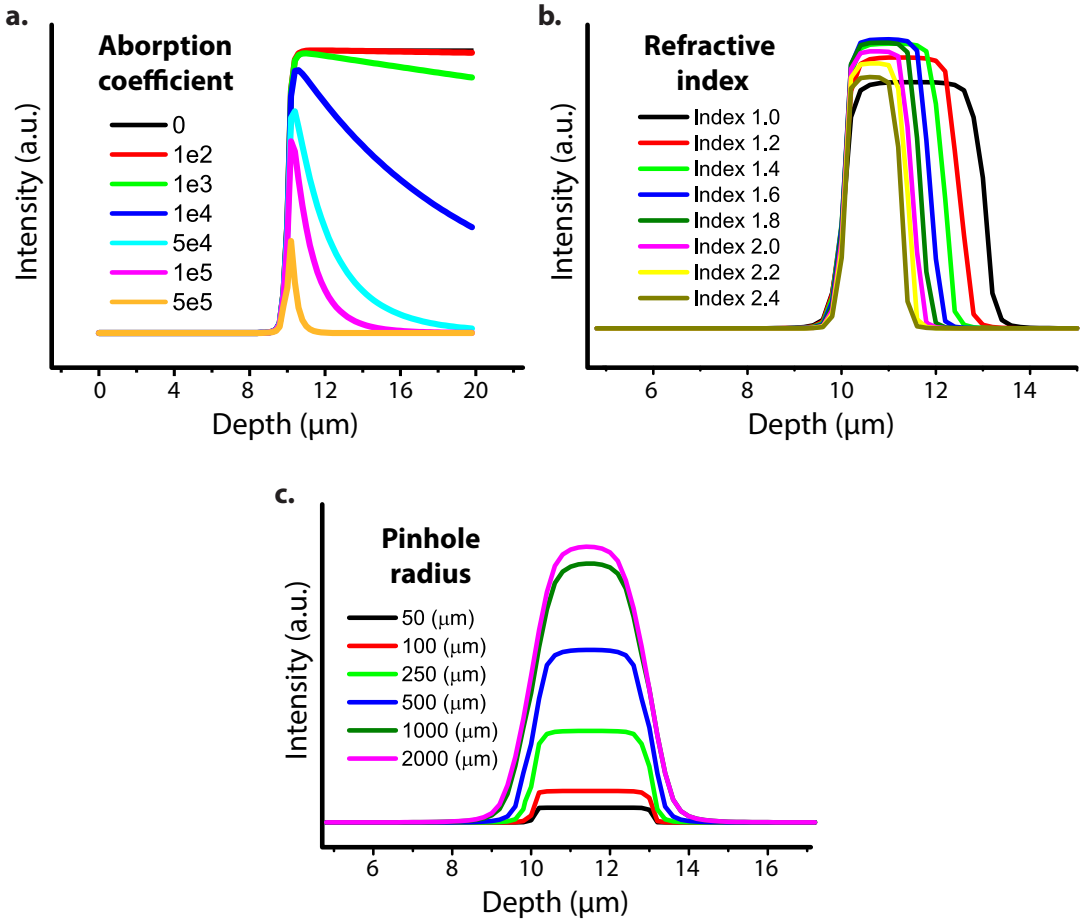

Figure 5.5 – a. Simulation of the effect of absorption in depth profile measurements. **b.** Simulation of the effect of the refractive index in depth profile measurements. **c.** Simulation of the effect of the pinhole radius in depth profile measurements.

One notable consequence is the strong decrease of the overall intensity with decreasing pinhole radius. On the other hand, it can be seen that an increase of the confocality leads to a clearer definition of the sample edges, thus allowing a clearer identification of the regions from different sample regions.

5.4 Example of a real depth profile measurement

In order to verify the present methodology a sample fitting the thematic of the present work was used, consisting of a Raman depth profile measurement of Neodymium Nickel Oxide deposited ($NdNiO_3$) epitaxially grown along the $[001]_{pc}$ orientation of Lanthanum Aluminium Oxide ($LaAlO_3$). The contour map representation of the acquired data is shown in Figure 5.7. The film thickness is of 10_{pc} u.c. which translates into approximately 42 Å. The measurement has been performed with a 633 nm wavelength laser, with a 2400 cm^{-1} grating and a 100x magnifying objective. The measurement itself consists 30 acquisitions of 60 s separated by a depth step of 0.2 μm.

A cut along the depth axis for wavenumbers of 304 and 487 cm^{-1} are exposed in Figure 5.6. The part on the left corresponding to a known signature of NNO does strongly resemble the expected shape for the film contribution displayed in Figure 5.2. On the other hand, the right part shows strong similarities with the substrate shape shown in Figure 5.2. Furthermore both cuts coincide with the simulated results shown previously shown in Figure 5.4. This asserts that the intuition on the Raman depth profile signal evolution and their simulations capture to some accuracy the evolution that is experimentally observed. Furthermore, the spectral signature from the film can be visually separated from the one of the substrate. By following this approach it is possible to identify two peak clustering around 300 and 450 cm^{-1} and single peaks around 180 and 250 cm^{-1} belonging to the film.

This illustrates that in some simple cases a simple look at the colour contour maps of a Raman depth profile suffices to obtain valuable informations regarding the assignment of modes to the film or the substrate. In the next chapter, we will see how multivariate methods allow to systematically analyse such datasets.

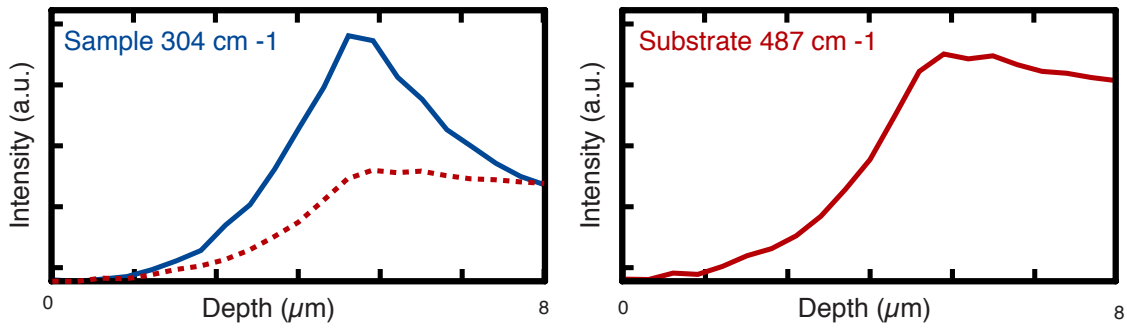

Figure 5.6 – Intensity evolution of the two modes selected from Figure 5.7.

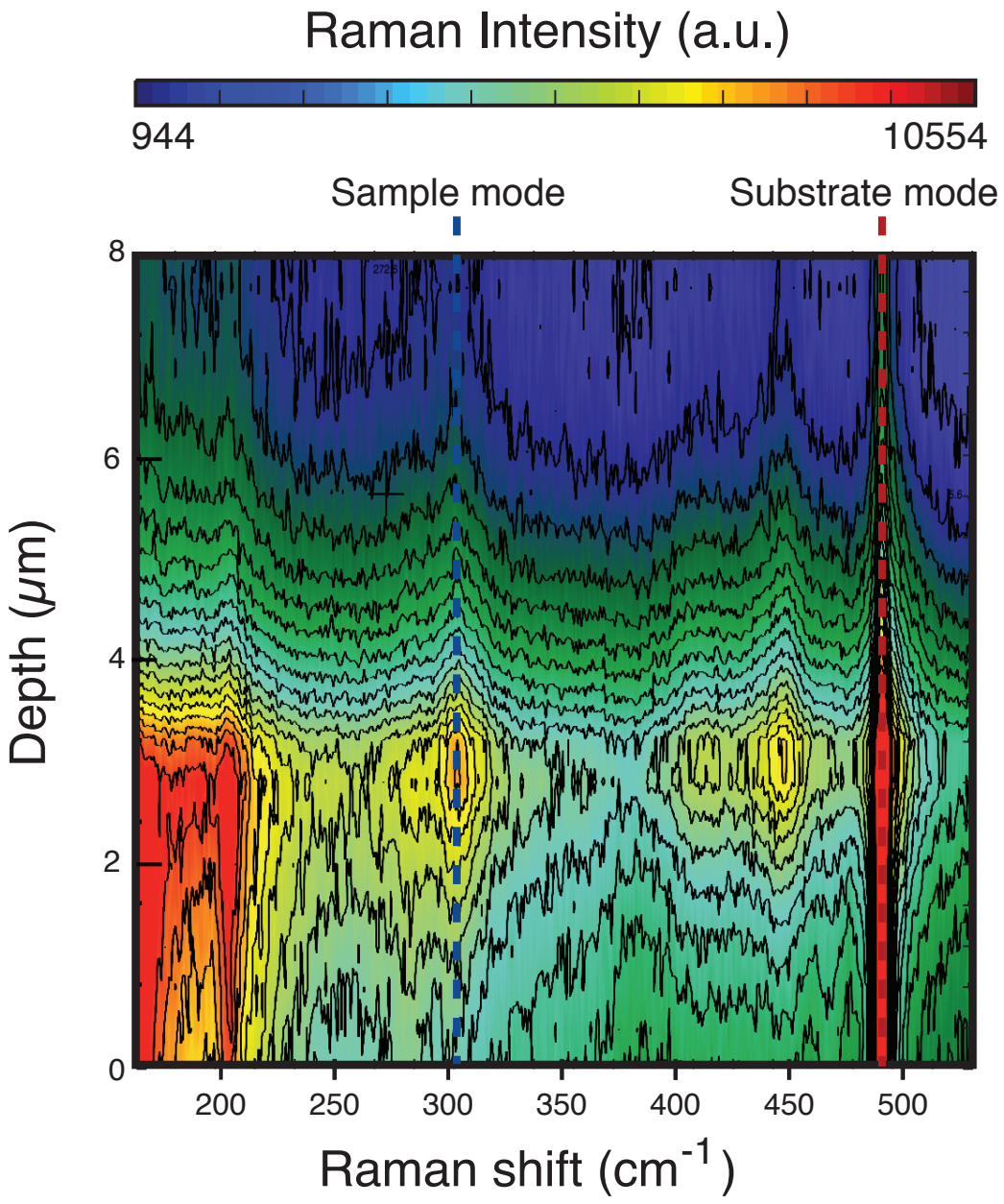

Figure 5.7 – Depth measurement of a 7 u.c. thick $LaNiO_3$ film deposited on $LaAlO_3$ along the $[001]_{pc}$ direction. The scale on the left represents the focal point position of the probing laser and the scale on the bottom represents the classical Raman shift expressed in wavenumber.

Chapter 6

Numerical Analysis of Raman depth profiles

6.1 Motivation

The previous chapter introduced the concept of depth measurement as an ingenious method to investigate epitaxially deposited thin or ultrathin films through Raman spectroscopy. The visual interpretation from contour maps already allowed only for qualitative interpretation of the parts belonging to either the film or the substrate. Yet, ultimately, quantitative information is needed for a full interpretation of the Raman spectra. Classically, this can be done by peak fitting. Chapter 6.2 will present an introduction to the lineshapes used within the present work.

Yet, in some cases, it was discovered that neither fitting nor visually interpreting the depth profile measurements did justice to their multivariate characteristic, thus leaving a substantial amount of spectral information hidden. A large variety of numerical tools have been developed in various scientific fields to push for the extraction of specific data from datasets composed of a multivariate statistic. These are grouped under the field of multivariate analysis. Chapter 6.3 will treat the concept behind them and detail the principal component analysis (PCA) and non-negative matrix factorisation (NMF), two methods extensively used in this work. This will be followed by classical examples of these techniques in other Raman spectroscopy applications followed by a qualitative discussion of the outcome of Raman depth profile spectroscopy.

All of the numerical tools were bundled in a software package developed as part of this work. This includes an advanced fitting interface allowing to track all the characteristics of each peak as well as their evolution with a given parameter such as depth, temperature or time. Furthermore, a principal component analysis (PCA) and a non-negative matrix factorisation (NMF) algorithm with their interfaces were developed allowing to extract most of the available information from

our datasets. Section 6.5 will qualitatively discuss the motivation and idea behind this implementation.

6.2 Implementation of standard peak fitting

The fitting of Raman signatures is an essential tool in the present work. It allows much more thorough investigations than simply following the maximum of a given signature. In this section, without going into details, we will discuss the lineshapes used to fit the data of either the raw depth profiles or of the PCA or NMF results.

The lineshape of an ideal Raman peak is lorentzian parametrised by its position, width, and amplitude. While this symmetric description suffices for most applications it fails to describe asymmetric profiles. This can be due to either physical parameters such as phonon confinement, double peak shouldering below the resolution limit amongst diverse other experimental artefacts. This is why an extended part of the Lorentzian lineshape is proposed that modulates its width parameter to allow for an asymmetric representation. We introduce the following definition of the Half Width at Half Maximum ($\Gamma_{\text{Assym}}(\omega)$) [80]:

$$\Gamma_{\text{Assym}}(\omega) = \frac{\Gamma_0}{1 + e^{\gamma \cdot (\omega - \omega_0)}}, \tag{6.2.1}$$

where Γ_0 is the initial width, ω_0 is the position of the lineshape and γ is the asymmetrical factor. Using this definition of the Half Width at Half Maximum it is possible to build the following asymmetrical Lorentzian lineshape:

$$f_{\text{Assym}}(\omega) = P \cdot \frac{\Gamma^2_{\text{Assym}}(\omega)}{(\omega - \omega_0)^2 + \Gamma^2_{\text{Assym}}(\omega)}, \tag{6.2.2}$$

where P is the amplitude of the Lorentzian function and w_0 is the offset position of both the Lorentzian function and the Half Width at Half Maximum.

A Raman spectrum can be composed of a certain number of Raman active modes and other physical effects such as fluorescence. These other effects induce a background to the acquired signal which also has to be fitted to allow for a precise extraction of the Raman data.

The fitting procedure has some limiting factors. The signal noise is an intrinsic source of error to the fitting procedure, as the cost function is solely minimising the Euclidean square distance between the fitted curve and the data. Another source of error is the density of datapoints. Indeed if one considers that a Lorentzian function has the majority of its weight around its peak position, a high density of data points is required in its vicinity to achieve an accurate fit. It has been observed that an increasing narrower lineshape, as intense as it might be, results in a less and less accurate fit. This consideration comes before addressing the effect from the noise on the few data points finally defining the narrow lineshape. Finally, the effect of the baseline has

to be taken into account as a polynomial fluorescence shape can have a dramatic effect on the position of the fitted peak and therefore its interpretation.

The user contribution to the fitting errors is more subtle. Fitting parameters can be fixed and entire lineshapes can be added to improve an expected result. The PCA and NMF are strong as they deprive the user of these possibilities.

6.3 Multivariate Analysis in Raman spectroscopy

6.3.1 Introduction to multivariate analysis

Two multivariate analysis tools were used in this work to unmix the signatures of thin and ultrathin films from the on the substrates it was deposited on. These were the Principal Component Analysis (PCA) and the Non-Negative Matrix Factorisation (NMF). In the following section will introduce the general concept of multivariate analysis methods allowing us to then introduce both methods with practical examples in Raman spectroscopy.

Multivariate analysis corresponds to the analysis of multivariate statistics. It can be explained by the simultaneous observation and analysis of more than one statistical outcome. For example the monitoring of three type of statistical outputs that characterise an event. Their analysis through multivariate analysis tools can help to identify the correlation patterns to then reduce the dimensionality of the space representing it. The present section will introduce the basic nomenclature associated with the components and the scores as well as the measurement space.

The acquisition space will be defined by a number m of detectors $\boldsymbol{D}_i$. This can be visualised as a m dimensional vectorial space were each one represents a specific unit vector. An output of this detector will correspond to a scalar factor along this unit vector. In this representation an acquired event will be described by a set of m scalars and can be visualised as a position in the acquisition space.

The multivariate approach consists of probing this acquisition space by modifying a parameter that impacts the position of the event in it. Such a parameter could be either time, temperature, pressure or the measurement depth amongst others. In this mindset, a multitude n of measurements are performed while varying the parameter. These can be cast into a data matrix $\mathbf{X}$ having in each row an array of m scalars describing the position of the event in the acquisition space.

At this stage, every single measurement can be considered as a component. The associated score will be an array made of $n-1$ 0s and 1 at the position in the measurement space were it was aquired. Therefore, making up a total of n components and scores. The multivariate analysis aims at reducing the acquisition space through linear combination of the detectors $\boldsymbol{D}_i$ by determining the correlations between the outputs. In this transformed space $\mathbf{X}$ will be represented by

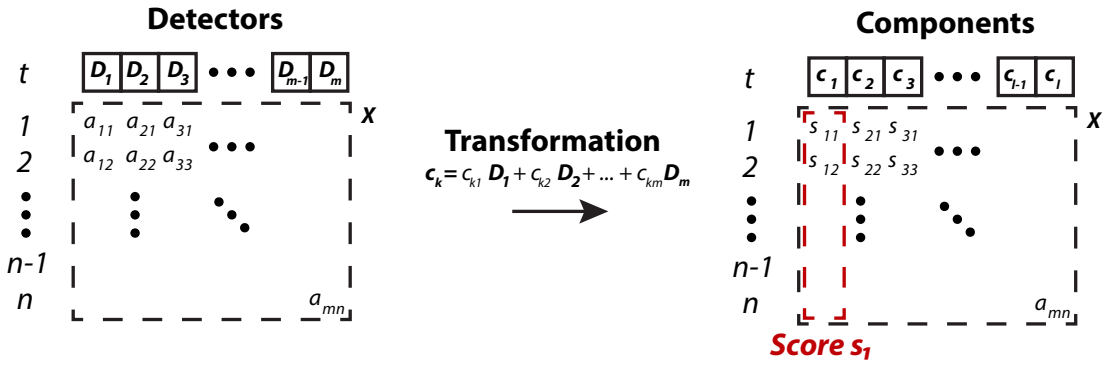

Figure 6.1 – Schema for the multivariate analysis process. All elements are described in section 6.3

new:

- **Components**: The k^{th} component described by $\boldsymbol{c}_k = (c_{k1}, c_{k2}, ..., c_{kn})$, is a vector of length m composed of factors allowing for the linear combination of the initial basis of detectors D_i. All components together are stored in the matrix $\boldsymbol{C}$ of an equal column length and a less or equal row length n_C as $\mathbf{X}$.
- **Scores (loadings)**: The k^{th} score described by $\boldsymbol{s}_k = (s_{k1}, s_{k2}, ..., s_{kn})$ is an array of length n. The i^{th} value represents the position of the i^{th} point projected onto the k^{th} components. As a result the set of i^{th} values of the n_C scores associated to the n_C components describing the dataset for the position of the i^{th} point in the new basis. All scores are stored in the matrix $\mathbf{S}$ of same column length as the row length of $\mathbf{C}$ an equal or row length as $\boldsymbol{X}$.

A visual description of the concepts introduced in this section is shown in Figure 6.1. The present work relates to multivariate methods used specifically for the analysis and interpretation of Raman spectroscopic dataset and thus allows for a less abstract view of the present explanations.

6.3.2 Multivariate analysis in Raman spectroscopy

The use of multivariate analysis methods in the field of Raman spectroscopy data is not particularly well established in the field of solid-state physics. We note, however, that they have been used as a tool to determine the chemical composition of heterogenous biological, geological or pharmaceutical samples [81, 82, 83]. As a result, the concepts introduced in this work are not novel in their definition but rather in their application towards the identification of ultrathin epitaxial film.

In the case of Raman spectroscopy, the detectors $\boldsymbol{D}_i$ are represented by a row of CCD pixels of

the camera. It is assumed that there is a total of m pixels. For the sake of simplicity, we assume that every CCD pixel row simply represents a position in a vectorial space (formerly introduced as acquisition space). A Raman acquisition would, therefore, be expressed by a set of scalars (Intensity values of a Raman spectra) determining its position within this space.

The acquisition of multivariate datasets implies the variation of a parameter describing the system. In Raman spectroscopy this can be either the spatial arrangement of the setup such as the laser spot position in $3d$ space and its orientation or environmental factors affecting the sample such as the pressure or temperature. This parameter, whichever is chosen is then evaluated at different discrete values $P = [p_0, p_1, ..., p_l]$. As a result the Raman spectra acquired by the setup at a p_k is given by $\boldsymbol{R}_k$ such that:

$$\boldsymbol{R}_k = a_{1k} \cdot \boldsymbol{D}_1 + a_{2k} \cdot \boldsymbol{D}_2 + \ ... \ + a_{m-1k} \cdot \boldsymbol{D}_{m-1} + a_{mk} \cdot \boldsymbol{D}_m. \tag{6.3.1}$$

The aim of any multivariate analysis method at this point is to investigate the correlations between variations observed on all intensity factors a_{jk}. When a correlation has been identified the associated component can be introduced as:

$$\boldsymbol{c}_i = c_{1i} \cdot \boldsymbol{D}_1 + c_{2i} \cdot \boldsymbol{D}_2 + \ ... \ + c_{m-1i} \cdot \boldsymbol{D}_{m-1} + c_{mi} \cdot \boldsymbol{D}_m. \tag{6.3.2}$$

and is equivalent to a *spectral type* acquisition. At each discrete step of the parameter p_k the component $\boldsymbol{c}_i$ is multiplied by its associated score s_{ik}. Thus leading to:

$$\boldsymbol{R}_k = \sum_i s_{ik} \boldsymbol{c}_i \tag{6.3.3}$$

This representation does in no way put constraints on the amount and shape of components that can be used to describe the signal. This is why different multivariate analysis methods can yield different results. The present work utilised two techniques known as PCA and NMF, both with different strength and weaknesses for the problems at hand. Each one of them will be introduced in the following sections followed by practical examples in Raman spectroscopy.

6.3.3 The Principal Component Analysis (PCA)

The principal components analysis (PCA) is a multivariate method first developed by Pearson in 1901 [84] and further formulated and named by Hotteling in 1933 [85] aiming at reducing a set of possibly correlated variables into a subset of uncorrelated variables called principal components. The general use of the PCA concerns the correlation of numerical data from different sources. These correlations are then used to engineer predictive models. A daily example would be the weather forecast. In fact, weather data has been analysed over decades from an array of sensors measuring the temperatures, wind speeds and precipitation amongst many more, all this in geographically distinct regions. There is no doubt that while the data collected is comprehensive it is far from complete to evaluate clear correlations leading to a complete accurate forecast. The principal component analysis gives an approximate solution to the problem by allowing to build the most optimal predictive basis from the data at hand [86].

Mathematical definitions within the PCA

A common thought representation of the PCA procedure is the fitting of a n dimensional ellipsoid to the data. Each of the axes of this ellipsoid being a m dimensional vector. These vectors later form the principal components. The score associated to a vector corresponds to the projection of the data on the latter. While this is the tough behind the PCA, the algebraic approach is slightly less intuitive.

Using the definition of the components $\mathbf{C}$ and the scores $\boldsymbol{S}$ introduced in section 6.3.1, the PCA transforms the acquisition space in such a way that:

$$\boldsymbol{X} = \boldsymbol{C}_{\text{PCA}} \cdot \boldsymbol{S}_{\text{PCA}}. \tag{6.3.4}$$

The first component $\boldsymbol{c_1}$ is obtained by diagonalising the dataset and normalising the obtained eigenvectors. The dataset $\boldsymbol{X}$ is then projected onto the later, thus generating the score for each one of them. The score that has the largest variance is then considered to be determining the eigenvector that will be kept as a principal component. If we consider $\boldsymbol{e_i}$ to be one of the N_e eigenvectors of $\mathbf{X}$, then the mathematical definition of $\boldsymbol{c_1}$ is as follows:

$$\boldsymbol{c_1} = \arg\max_{i}^{N_e} \sum_{j}^{n} \left(\frac{\boldsymbol{e_i}}{||\boldsymbol{e_i}||} \cdot x_j \right)^2, \tag{6.3.5}$$

where x_j is a row vector from $\mathbf{X}$. The following component are then obtained subtracting the previous components from $\mathbf{X}$ and then reiterating the procedure that was just described. This procedure can then be repeated until the entirety of the data set is expressed.

Example: PCA with three detectors

This short section is aimed at explaining the PCA component evaluation introduced in the previous section. It is assumed that three detectors $\boldsymbol{D}_1$, $\boldsymbol{D}_2$ and $\boldsymbol{D}_3$ produce data following a physical variable T (time for example). The aim is to investigate the correlation between these detector outputs. To this effect, the data is placed in the vectorial space in which each detector represents a basis vector. The result is shown in Figure 6.2.**a.**. The dataset is then centred by subtracting the mean position within this basis (red cross). The calculated eigenvector with the maximal covariance is shown in Figure 6.2.**b.**. as a blue arrow with the general notation $c_{11} \cdot \boldsymbol{D}_1 + c_{12} \cdot \boldsymbol{D}_2 + c_{13} \cdot \boldsymbol{D}_3$. This constitutes the first basis vector and is called the first PCA component.

The next procedure consists of subtracting the components along this direction to the dataset. This procedure is equivalent to project the dataset onto the plane perpendicular to the first component as shown in Figure 6.2.**c.**. The distance of the entries from the plane will constitute the

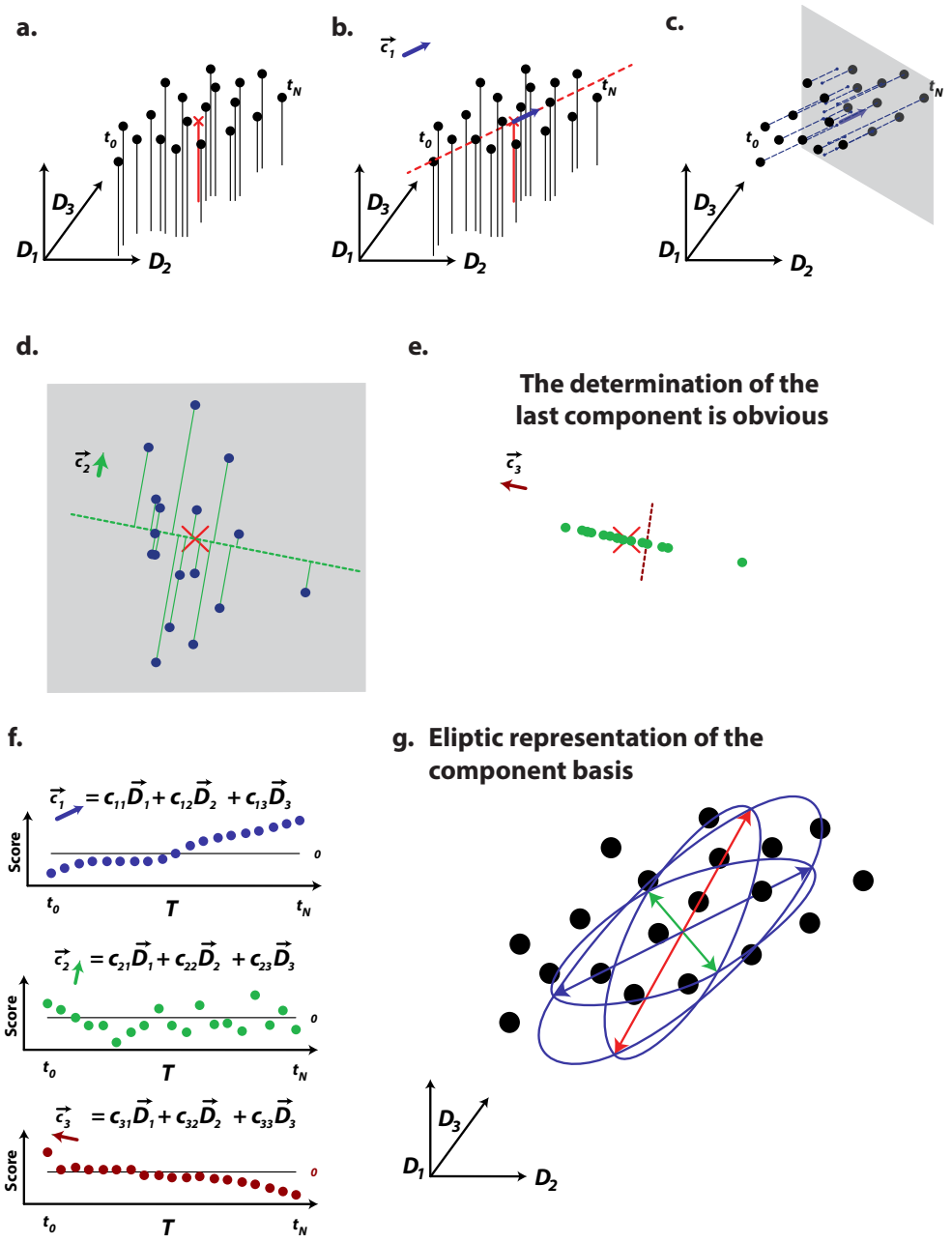

Figure 6.2 – a. - **d.** Different stages of the PCA for the determination of the fist component. The axes D_1, D_2 and D_3 represent three detector outputs. **a.** represents the evaluation of the means. **b.** visualises determination of the eigenvector with the greatest covariance. **c.** shows the subtraction of the determined component. The resulting 2d representation of the data after subtracting the first component is shown in **d.**. **d.** shows the process to obtain the second component and **e.** the third. The components and their evaluated (approximative) scores are shown in **f.** while **g.** shows a representation of the fitted 3d ellipsoid.

first component score if associated to T. The approximate shape of the presented dataset is shown in Figure 6.2.**f.**. This concludes the procedure to evaluate the first component.

The resulting dataset is solely defined within the projection plane. This is why the determination of the second component on this space will give rise to a vector necessarily orthogonal to the first component. It also effectively reduces the dimension of the dataset by one as a component is subtracted. A schematic representation to determine the second and third components is shown in Figure 6.2.**d.** and **e.**, respectively. At the beginning of the last section, it was stated that the PCA is equivalent to fitting a multidimensional ellipsoid to the data. Figure 6.2.**g.** is a visualisation of the obtained fit.

Example of application of PCA in Raman spectroscopy: ferroelastic domains

One observed phenomenon in ferroelastic compounds is the formation of distinct domains with different crystallographic orientations within the same crystal. This is particularly studied because the boundaries, where these domains meet (domain walls), show some remarkable properties [87]. With the orientation of the crystal structure changes the relative incidence vector of the Raman laser and therefore the associated selection rules. This impacts the ratio between the peak intensities of the signature. The domain wall is assimilated to a nano-metric structure that has a different atomic arrangement than the rest of the sample. As a result, one can expect the Raman signature to reflect this difference.

Similar to the depth measurements introduced in Chapter 5, the difficulty is to resolve a structure with a small interaction volume between two other samples with a large interaction volume. This constitutes an ideal example of how Raman spectroscopy combined with a multivariate analysis tool allows to overcome this difficulty. The work published by Nataf *et al.* in 2017 [88] used PCA to extract information of ferroelastic domain walls of $NdGaO_3$ (NGO) of Raman maps. The mapping was done at the surface of the sample across an optically identified domain wall. The PCA result obtained on NGO is displayed in Figure 6.3 [88]. In this example, it is reported that the first two components capture the entirety of the signal variation. The negative contributions within the components emphasises that these do not represent Raman spectra. In the present example, the score clearly attributes the first components as a description of the domains, while the second one is clearly attributed to the domain wall signature.

While this work was performed with a different target and in a different measurement setup it showcases the potential and complexity of the PCA at the same time. It was possible to extract components that could clearly be associated with the domain walls. This lets us believe that the same can be achieved when combining performing depth profile measurements of ultrathin films on top of the various substrate combined with the PCA.

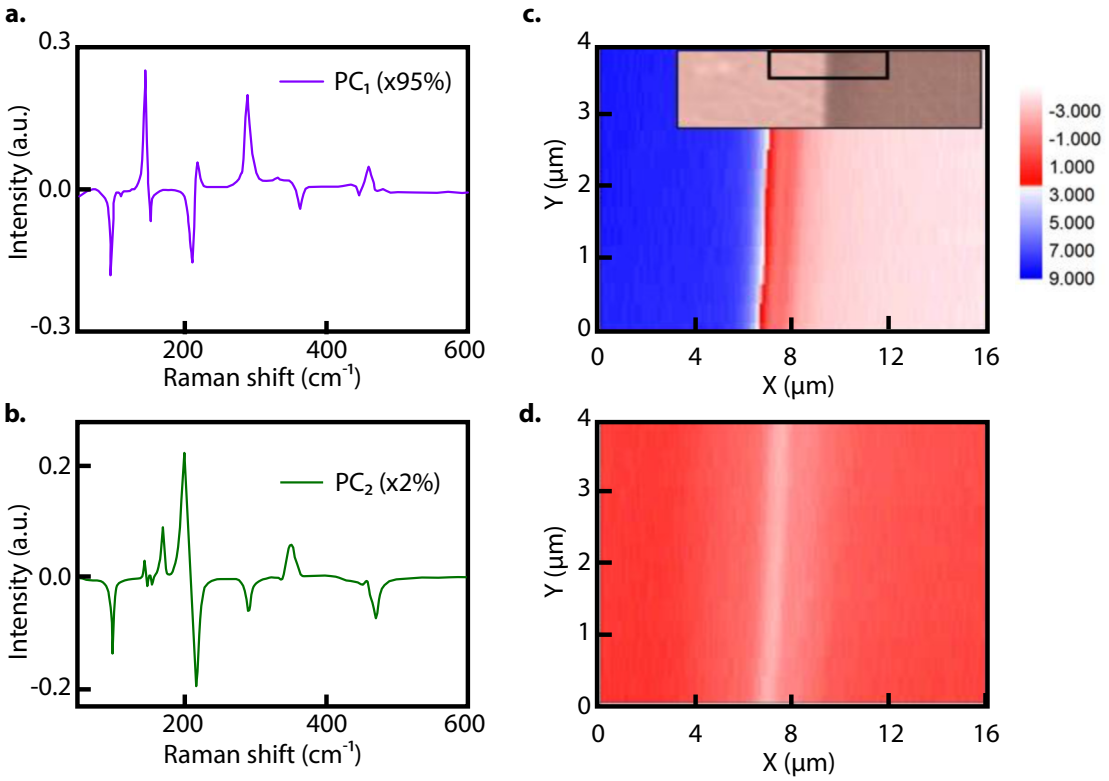

Figure 6.3 – Figure extracted from the the work of Nataf *et al.* in 2017 [88] about the ferroelastic domain walls in $NdGaO_3$. **a.** The first principal component of a mapping shown in the inset of **c.**. **b.** The second principal component. **c.** The score map associated to the first principal component. **d.** The score map associated to the second principal component.

Implementation

The software developed utilises the linear algorithms singular value decomposition (SVD) library from scipy in python to diagonalise the data matrix and evaluate the components. The scores are then reprocessed by projecting the data onto the components. The visual interface is based on a simultaneous visualisation of the components and the score.

6.3.4 The Non-negative matrix factorisation (NMF)

The non-negative matrix factorisation (NMF or NNMF) also known under non-negative matrix approximation [89] is a numerical method from the multivariate analysis toolbox. In comparison to the PCA, the NMF does not rely on diagonalising the dataset but follows a fitting approach. At this point, *a-priori* knowledge is used to determine how many components should be fitted to the dataset $\boldsymbol{X}$. Then set of provided or randomly generated components $\boldsymbol{c}_k$ with their associated scores $\boldsymbol{s}_k$ are iteratively fitted onto the dataset as introduced in section 6.3.1, such that it best satisfies [90]:

$$\boldsymbol{X} \approx \boldsymbol{C}_{\text{NMF}} \cdot \boldsymbol{S}_{\text{NMF}}, \tag{6.3.6}$$

The difference with the PCA is the approximate character. The NMF can be very useful for problems where a systematic loss of information is deemed acceptable or even interesting.

Fitting Procedure

The concept of iterative fitting means that a cost function must be defined, allowing to evaluate how well the fit matches the data. The simplest form would be to use a least square type process by minimising the square of the difference of every element of the matrix, which would correspond to the Euclidean distance. This could be expressed by an element-wise comparison such as:

$$Cost(\boldsymbol{C},\boldsymbol{S}) = \sum_{i,j} \left[\boldsymbol{X}_{i,j}^2 - (\boldsymbol{C}\cdot\boldsymbol{S})_{i,j}^2\right]^2, \tag{6.3.7}$$

where $Cost$ is the cost function depending on $\boldsymbol{C}$ and $\boldsymbol{S}$. This is positive and reaches 0 when $X = \boldsymbol{C}\cdot\boldsymbol{S}$. Using this function it is possible to evaluate the two-dimensional distance of the result from the data. More advanced cost functions have been engineered allowing either for more robustness or better expression of the problem.

A few starting parameters are needed to approximate the data. A pure Lorentzian lineshape, for example, takes three parameters to be fully defined. These are the position, width, and the amplitude and can be formalised as three vectors of a basis. It is then possible to fit the given dataset with this three-dimensional vector space. The optimal results will be evaluated at a certain position within this space. The NMF is similar in its approach as the only information provided is the number of vectors available to express the dataset and the space in which they are defined. In the present case of Raman depth profile measurements, these will consist of an anticipated set Raman-*like* spectra. The numerical procedure then aims at converging this vectors with the adapted scores to minimise the difference with the initially provided dataset.

As a mathematical procedure, the NMF can be expressed as a non-convex optimisation problem [91]. This means that in analogy to a classical fit procedure local minima might be encountered before the global one. This makes the choice of an appropriate update method crucial.

The update method explains how a temporary solution will be modified to probe the local space and thus find preferable alternatives that minimise the previously introduced cost function.

This is why many algorithms have been devised to solve and optimise the solution search. The most popular is the multiplicative updating algorithm shortened by MU-NMF [90, 91]. It simply evaluates a new set of components $\boldsymbol{C}$ and scores $\boldsymbol{S}$ based on a transformation of the previous set. This method has been found to be the most simple update procedure to converge to a solution.

Example of application of the NMF in Raman spectroscopy: graphene on SiC

Graphene has been studied extensively for its behaviour when the reaching the ultrathin limit leading to a strong signature change. A study by Kunc *et al.* [92] used Raman depth profiles combined with NMF to dissociate the Raman signature for graphene grown epitaxially on SiC. The comparison is performed with a classical approach that consisted of simply subtracting the signal of SiC. Within this work the authors opted for Block Principal Pivoting and Active Set updating algorithms [93].

This example visualises the strength of NMF by lifting the condition on orthogonal components of the PCA and adding strictly positive restriction. This provides more physically interpretable components and eases dramatically the interpretation compared to the PCA.

Implementation

A non-negative matrix factorisation algorithm is provided by scipy.optimize.nnls the implementation of the present software was rewritten to adapt to parallel processing. The whole routine is built as a wrapper that can use any of the multiplicative, Block Principal Pivoting or Active Set updating methods. This is left to the discretion of the user. The added multi-processing characteristic allows for more initial components and therefore a better statistical chance to reach the global minimum.

6.4 Multivariate methods to Raman depth profiles

6.4.1 Description

To apply multivariate methods to the Raman depth profile measurements a quick thought experiment has to be performed. Assuming the multivariate analysis introduction of section 6.3.2 we assume that the parameter is now the depth position and therefore position of the Raman spot

within the sample. Each of these spectra is the result of combining the result of each CCD pixel previously described. In the spirit of the previous section, let us combine all the acquired vectors into a matrix $\mathbf{X}$, such that each row is, in fact, a Raman spectra and each column the output of each pixel of the CCD.

These datasets now reflect different characteristics of the investigated sample depending on the layers of different compounds. In the present study, we will focus on thin or ultrathin films epitaxially deposited on substrates. It is assumed that both the film and the substrate are equally Raman active but differ in their spectral signature. It was shown in Chapter 5.2 that such an arrangement acquired through a depth profile measurement leads to spectra where both signatures are mixed with a different ratio depending on the depth parameter.

A primitive description of the visually accessible data of such a measurement shown in Chapter 5.4 already suggests that the ratios of the film and the substrate vary differently with the depth thus making the depth profile measurement susceptible to express multivariate statistics. In such a case multivariate methods can indeed reduce the dataset to the components making up the signal. In this work, two of these methods, namely the PCA and the NMF, were used to compute these components.

6.4.2 Investigation of the components shapes

The lineshape of a typical phonon mode in classical Raman spectroscopy is a Lorentzian. In most cases the peak shape is symmetric, therefore limiting the possibilities of expressing its variation through three parameters: The amplitude, the position, and the width. Unfortunately, these parameter variations cannot necessarily be extracted from components computed by the PCA and the NMF as we shall see.

In the next section, we will display some case scenarios of simulated Raman depth profiles of a film of 1 μm thickness deposited on a substrate of 100 μm. Only one Lorentzian lineshape will be used for each individual signature. It will be assumed that only one parameter varies of this Lorentzian, be it the position, width or the amplitude. Using this hypothetical setup can shed some light on how the PCA and NMF express subtle variations of the signature between two compounds.

Peak intensity variation

There are two distinct ways to express peak amplitude variations. In the first scenario, the peak is captured by only one component. In this case, the score will take over the variation of its intensity thus expressing the true physical variation. The second scenario is slightly more ambiguous as the variation of the peak can be spread through multiple components. Meaning that multiple elements have to be considered in order to extract the exact lineshape. As a result, it is much

harder to retrieve the exact physical variation of the peak.

Raman peak position shift

Similar to the amplitude variation, there are two distinct ways to express a shift in the peak position. The first scenario approximates the peak shift by two components, each of whom represents the start position and the end position respectively. The scores are then related to a decay and an increase. The second possibility is to obtain a spectral and a derivative type component. The latter is characterised by a line with two *bumps*, where one is positively and the other negatively defined.

The PCA seems to favour the second type of component as shown in Figure 6.4.**b.**. The score reflects this behaviour with an intuitive shape. The peak to modify by the second component has to be expressed by the first components, therefore, leading to a non zero score value in this region. It is then upon this signal that the second component acts. The NMF, on the other hand, is restricted to find positive components and thus cannot opt for this representation and therefore opts for the first alternative as shown in Figure 6.4.**d.**.

Raman peak width variation

Similar to the position variation, there are two distinct ways to express a variation in the peak width. The first scenario is the simple expression of each peak in two separate components with their respective scores. Thus providing the real physical representation. The second scenario is represented by one component capturing either one of the peaks and another capturing the changes necessary to reach the second peak shape.

The PCA seems to favor the second type of component as shown in Figure 6.4.**b.**. The score reflects a similar characteristic as shown in the case os peak position shifts. The NMF, on the other hand, has components that are lower bound by 0 and thus cannot opt for this representation and therefore opts for the first alternative as shown in Figure 6.4.**d.**.

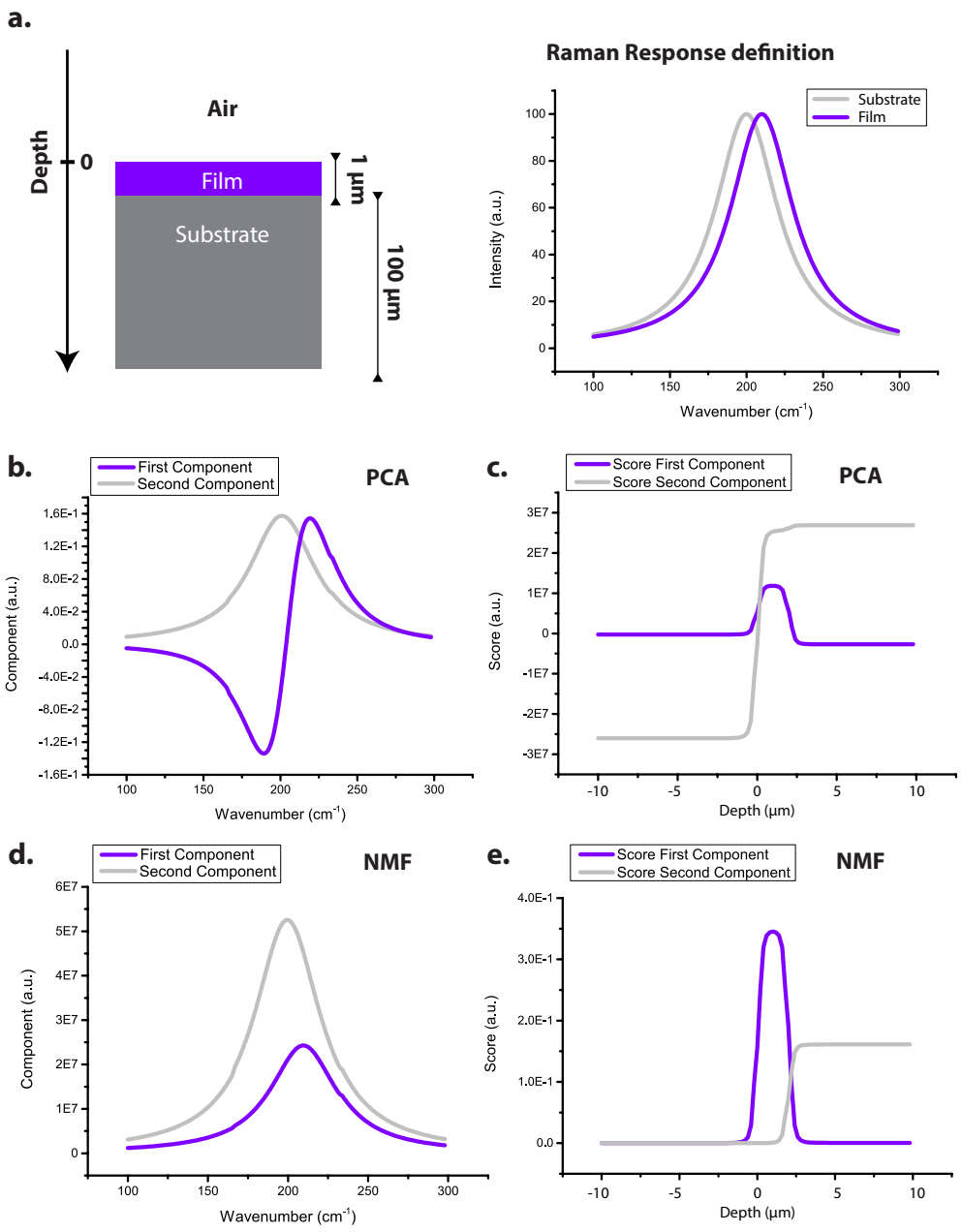

Figure 6.4 – a. Sample environment definition with the associated peaks lineshapes for the film and the substrate. The film peak is positioned at 215 cm^{-1}, while the substrate peak is positioned at 200 cm^{-1}. **b.** First and second PCA components from a simulated depth measurement with a stepping of 0.2 μm. **c.** Scores associated to the PCA treatment. **d.** First and second NMF components. **e.** Scores associated to the NMF treatment.

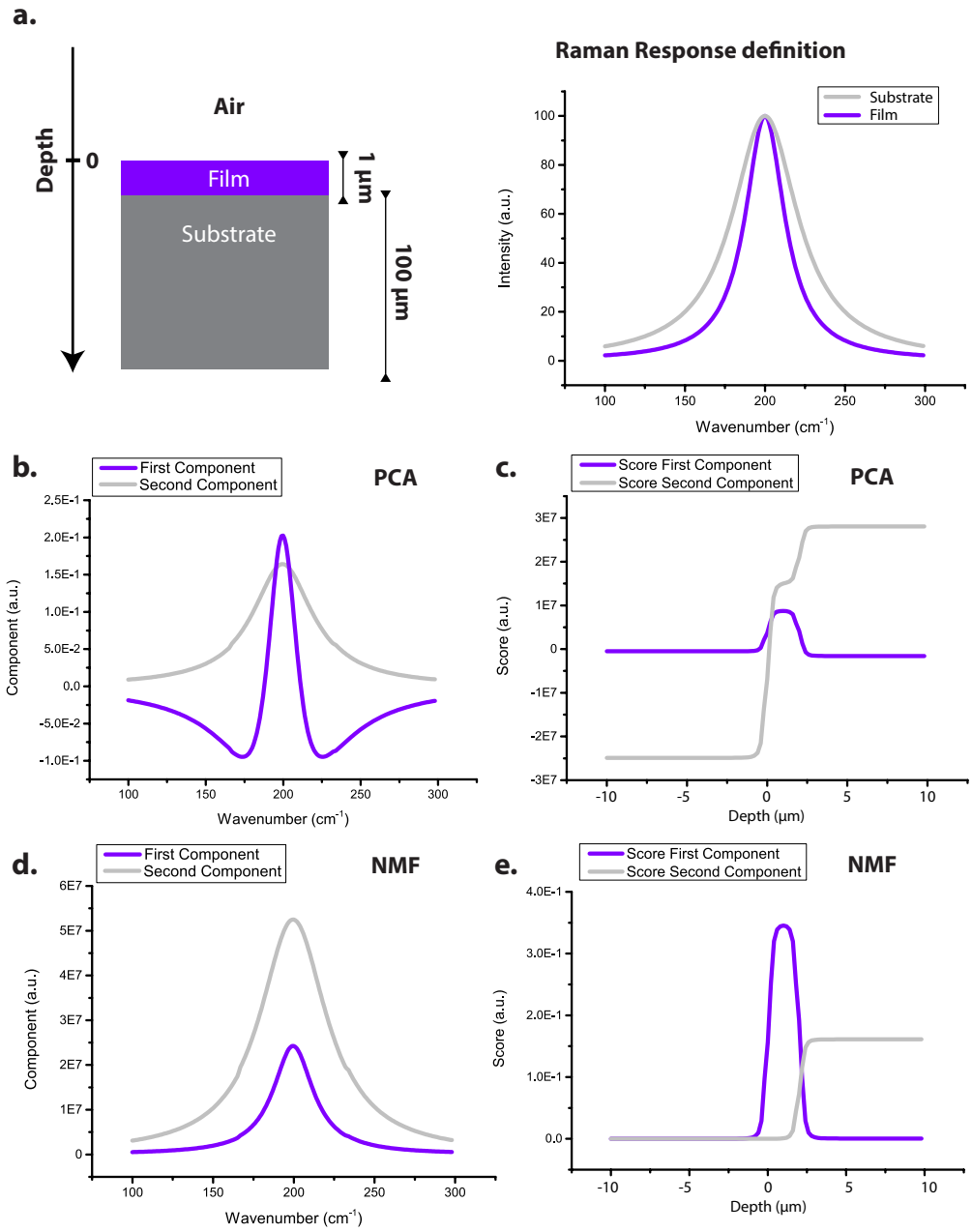

Figure 6.5 – a. Sample environment definition with the associated peaks lineshapes for the film and the substrate. The film and substrate peak are both positioned at 200 cm^{-1}. The substrate peak has a width of 20 cm^{-1}, while the sample peak has a width of 15 cm^{-1}. **b.** First and second PCA components from a simulated depth measurement with a stepping of 0.2 μm. **c.** Scores associated to the PCA treatment. **d.** First and second NMF components. **e.** Scores associated to the NMF treatment.

6.4.3 Comparison between the PCA and the NMF

While some of the advantages and limitations of the PCA and NMF can be derived mathematically, others require a certain amount of experience. In this section we aim at listing all these characteristics to allow a comparison between the two:

- **Input:** Both the PCA and the NMF process a multivariate statistical dataset with arbitrary dimension. The more distinct points in space are resented. While the PCA has no specific condition on the dataset, the NMF requires it to be positively defined. This is, fortunately, no issue when it comes to spectral acquisitions.
- **Process:** The PCA relies on the algebra of singular value decomposition algorithms which performs efficiently. The NMF is as any fitting procedure is a more time-consuming methodology. This also depends on how computationally intense the updating method is.
- **Output:** The PCA will always provide as many components as measurement points, meaning that a depth profile counting 100 Raman acquisitions will lead to 100 components. It is up to the operator to decide what is rather meaningful contributions. The NMF will only provide as many components as the operator asked to be fit.
- **Interpretation:** In this category the PCA shows an incredible complexity. The conditional orthogonality of the components leads to complicated components with negative parts with equally complex scores. In comparison, the NMF excels with its simplicity. The obtained components can directly be interpreted as spectral representations.

Following this listing of strength and weaknesses at each step of the procedure would suggest a preference towards the use of the NMF. Yet one important factor that was omitted is the *niceness* of the dataset. Indeed noise and very low signal render the NMF very unstable in finding the correct components. Noise is a statically random process and has, therefore, a different contribution in each Raman acquisition. It is therefore expressed by the same amount of components as there are measurements. This is why the PCA excels at identifying each noise component away from the stronger contribution, while the NMF simply averages it into the components. The same can happen for signatures that are much weaker than the main contribution.

It is these criteria that motivated the use of the PCA on the ultrathin film of $LaNiO_3$ deposited epitaxially on $NdNiO_3$ (described in Chapter 7) while the NMF was used for thin $NdNiO_3$ film deposited epitaxially on $NdGaO_3$ (described in Chapter 8).

6.5 Software implementation

The new way of using the Raman spectrometer in tandem with the new dataset analysis methods asked for a procedure how to achieve the best possible interpretation of the science at work.

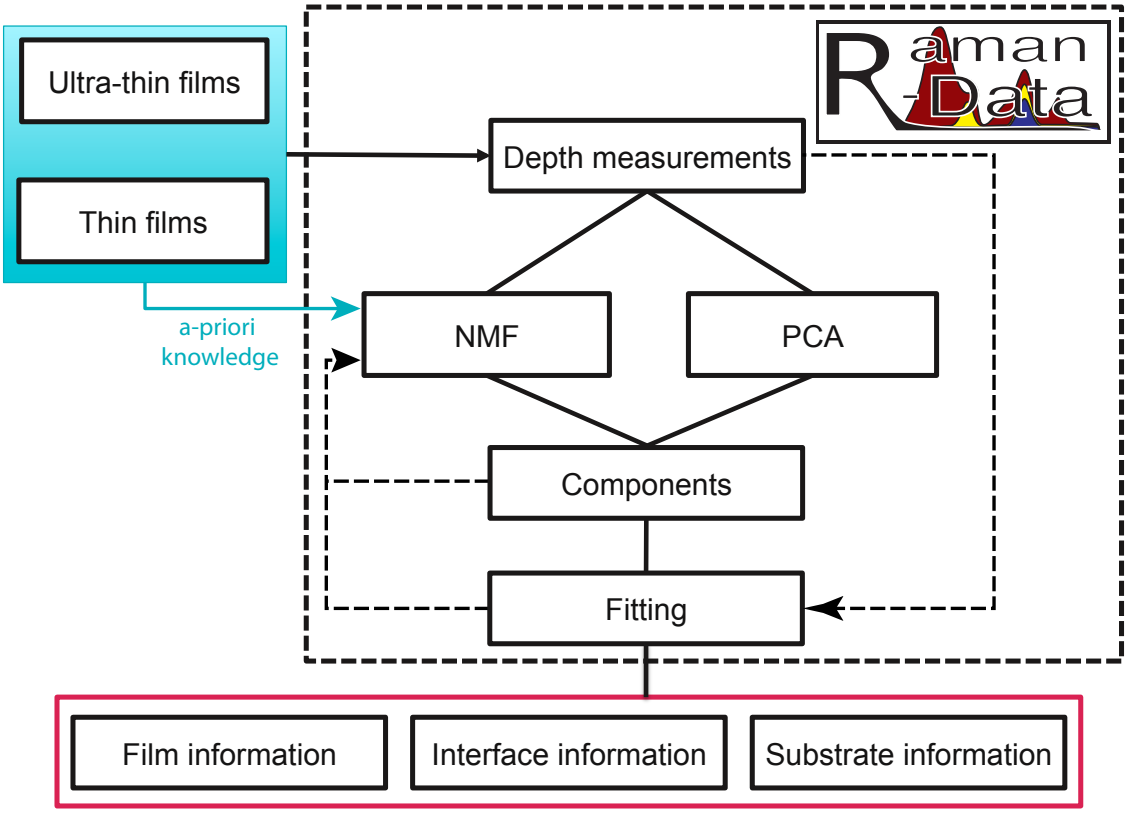

Figure 6.6 – Diagram of the process to analyse Raman depth profile measurements on thin or ultrathin films deposited on any given substrate.

This initial procedure saw the making of a vast set of tools allowing to visualise measurements all of whom were then bundled in a software package following standard file input and output. A strong emphasis has been made towards the fast visualisation and interpretation of these Raman depth profile measurements requiring the least amount of procedural steps (such as converting files, merging them, plotting them with a third party tool etc...). The developed procedure is summarised a schema in Figure 6.6.

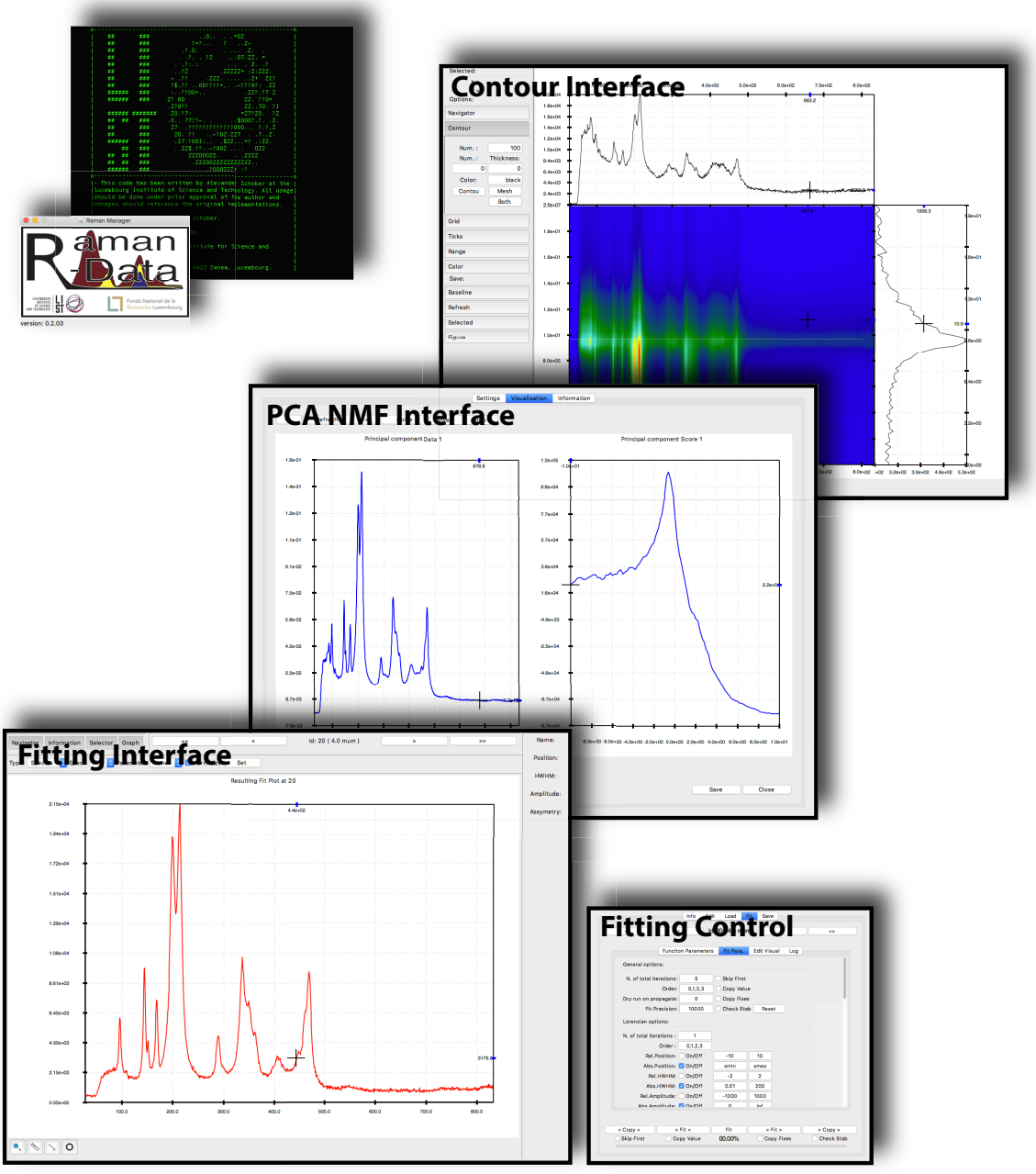

Figure 6.7 – Display of the software apckage.

Part IV

Raman spectroscopy investigations of nickelate thin films

Chapter 7

Ultrathin Lanthanum Nickelate films $LaNiO_3$ (LNO)

7.1 $LaNiO_3$: Raman signature

$LaNiO_3$ (LNO) as a nickelate compound was introduced in Chapter 2.5. From room temperature down to 0 K, LNO crystallises in the rhombohedral $R\bar{3}c$ space group [49]. The rhombohedral unit cell is depicted by dashed lines in Figure 7.1.**a.**, where oxygen octahedra follow an $a^-a^-a^-$ tilt configuration. This can be interpreted as an anti-phase rotation about the pseudo cubic threefold axis. The distortion can be described by a single order parameter corresponding to this unique tilt angle.

A number of publications have been devoted to the vibrational spectrum of LNO. The 10 atoms in the rhombohedral unit cell, with La in the 6a (0,0,1/4), Ni in the 6b (0,0,0) and O in the 18e (x,0,1/4) Wyckoff positions [49], give rise to 30 zone-centre vibrational modes [50, 94]:

$$\Gamma = A_{1g} + 3A_{2g} + 4E_g + 2A_{1u} + 4A_{2u} + 6E_u, \tag{7.1.1}$$

where only $A_{1g} + 4E_g$ are Raman-active. The Raman tensors of the Raman active modes can be written:

$$A_g = \begin{pmatrix} a & 0 & d \\ 0 & a & 0 \\ d & 0 & a \end{pmatrix}, E_{g,1} = \begin{pmatrix} c & 0 & 0 \\ 0 & c & d \\ 0 & d & 0 \end{pmatrix}, E_{g,2} = \begin{pmatrix} 0 & c & d \\ c & 0 & 0 \\ d & 0 & 0 \end{pmatrix} \tag{7.1.2}$$

The nature of the Raman active vibrations, obtained through local spin density approximation calculations (LDSA) [95, 50], can be seen in Figure 7.1.**b.**. Two octahedra rotation modes around the $[1\bar{1}0]_{\text{pc}}$ and $[111]_{\text{pc}}$ directions can be identified. A typical Raman spectrum of LNO deposited

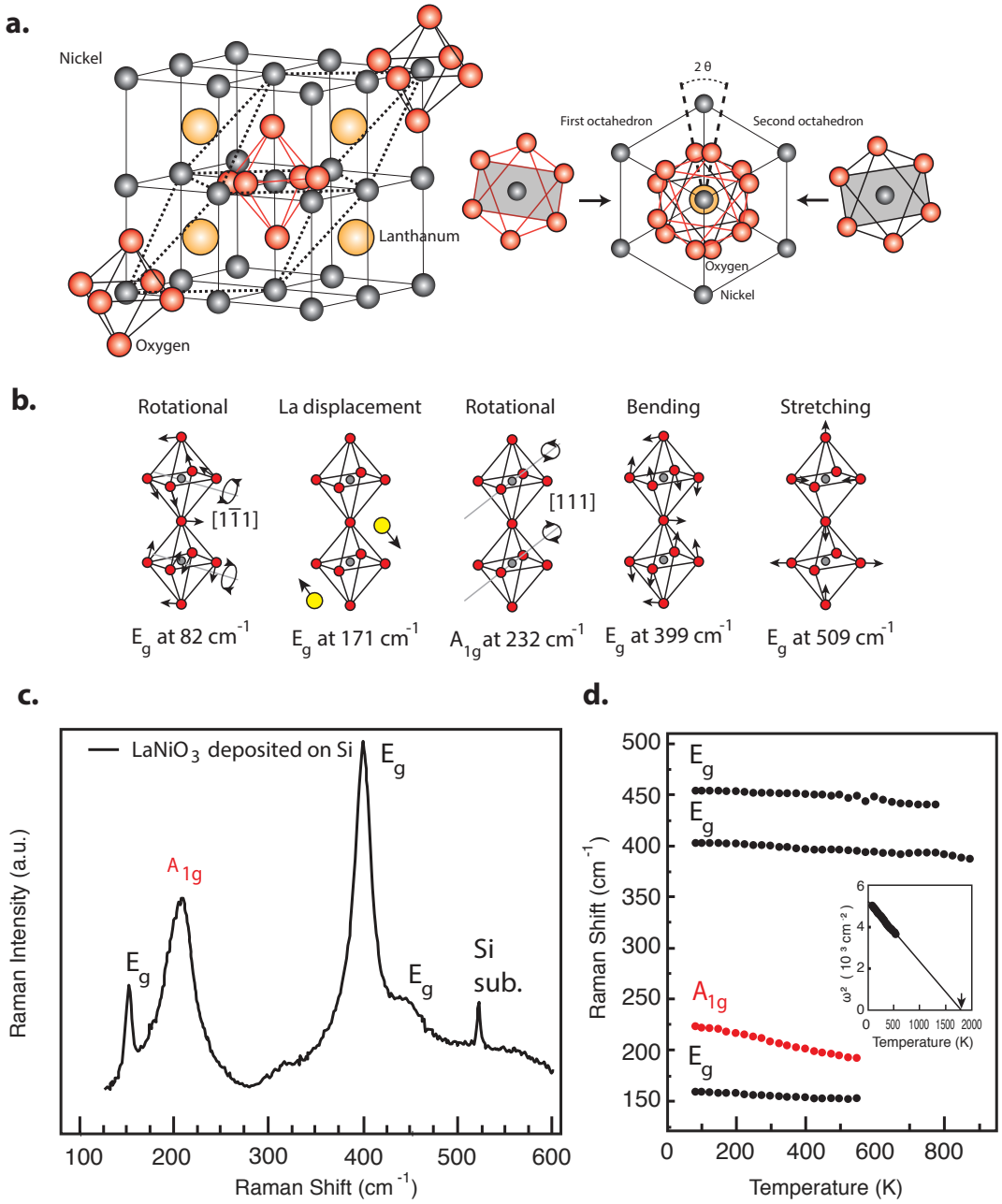

Figure 7.1 – a. Schematic view of $LaNiO_3$ in the rhombohedral $R\bar{3}c$ space group. The representation on the left depicts the relation between the pseudo cubic unit cell in solid black lines and the $R\bar{3}c$ unit cell with dashed lines. The right side showcases a visual along the $[111]_{pc}$ direction. Along this direction successive octahedra are tilted in anti-phase (explained in section 1.2). **b.** Representation of the five Raman active phonon vibrations of LNO in the $R\bar{3}c$ phase. **c.** Raman spectrum of LNO deposited on Silicate extracted from Chaban *et al.* [94]. **d.** Temperature investigation of the modes observed in **c.**. The A_{1g} mode shows a strong dependance with temperature [94].

on Silicon, extracted from Chaban *et al.* [94], is shown in Figure 7.1**c.**. In this study the film was grown on silicon through Metal-Organic Chemical Vapour Deposition (MOCVD). The film was grown sufficiently thick for it to relax, thus allowing the measurement of its bulk Raman signature. In addition, this allowed to almost completely shadow the spectrum of the underlying silicon substrate. Unfortunately, the cut-off of the Raman spectrometer, located at 120 cm^{-1}, did not allow the observation of the E_g oxygen octahedra rotation mode. Nevertheless, it is possible to assign the E_g mode related to pure La displacements, the A_{1g} mode related to rotations of oxygen octahedra along the $[111]_{\text{pc}}$ direction and the E_g modes related to their bending and stretching.

The observed A_{1g} mode is particularly important as it is directly linked to the order parameter, i.e. the tilt angle. It was reported that its frequency scales linearly with the latter [94]. This behaviour was extensively studied for other perovskite structures that also crystallise in the rhombohedral $R\bar{3}c$ space group, such as $LaAlO_3$, $LaCoO_3$ and $LaMnO_3$. Their associated A_{1g} modes are located at 132 cm^{-1}, 232 cm^{-1} and 249 cm^{-1}, respectively [95, 96]. These compounds allowed Illiev *et al.* [97] to establish an empirical relation between the rhombohedral order parameter, namely the tilt angle of the oxygen octahedra, and the A_{1g} mode frequency leading to a scaling of $\approx$ 23.5 cm^{-1}/deg. Using the same factor for $LaNiO_3$ with a reported angle of 9° leads to a calculated position of the A_{1g} mode at $\approx$ 211 cm^{-1}, which is very close to the experimentally measured position at 209 cm^{-1}.

Furthermore, it was reported that perovskites crystallising in the $R\bar{3}c$ structure usually transit to a cubic phase at high temperature [96]. As the structure approaches the cubic phase the octahedral tilt angle goes towards 0°, thus the frequency of the A_{1g} mode approaches 0 cm^{-1}. For this phase transitions the temperature dependency of the frequency $\omega(T)$ is given by: $\omega^2(T) = \omega_0^2(T_c - T)$, where ω_0 is the the frequency at 0 K and T_c the transition temperature. Using the data displayed in Figure 7.1**d.** allows to extrapolate an approximate transition temperature of 1780 K for bulk-like LNO [94].

This example asserts the A_{1g} mode as an ideal spectroscopic indicator for perovskites in the rhombohedral $R\bar{3}c$ space group. We note however, that the linear scaling has been applied and verified on bulk or bulk-like fully relaxed materials only. It is not *a priori* clear how this relation can be transferred to epitaxially strained ultrathin samples.

7.2 $LaNiO_3$: Raman signature under epitaxial strain

An extensive study of thin LNO films epitaxially deposited on different substrates was performed by Weber *et al.* [22]. The Raman measurements were performed on samples with different film thicknesses. In this work it was argued that different film thicknesses allow for different levels of relaxation, thus implying that thinner films will be more strained than thicker ones. This explains the arrangement of the extracted Raman spectra shown in Figure 7.2, namely the

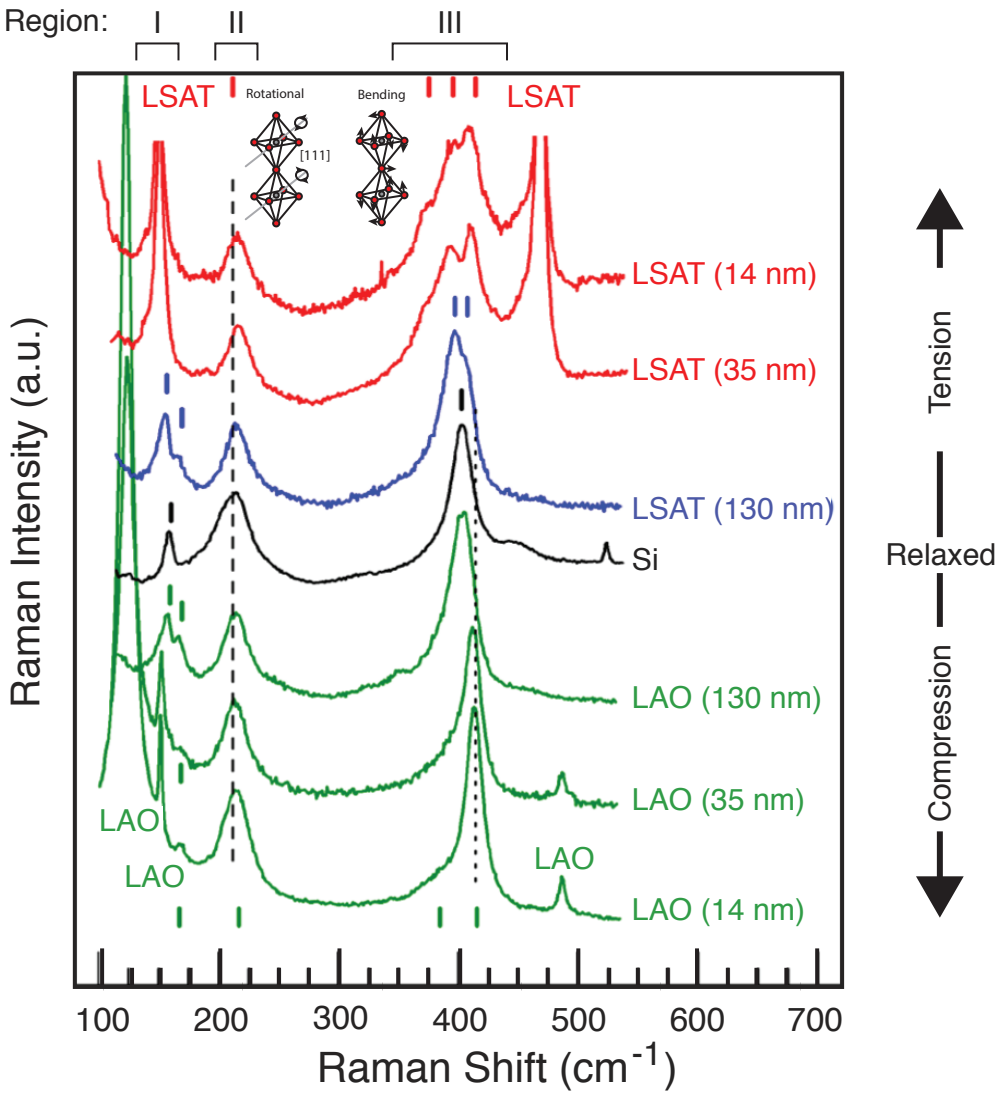

Figure 7.2 – Raman spectra of LNO deposited onto different substrates and different thicknesses. This Figure was reproduced from M.C. Weber *et al.* [22]

thinner films showcasing more strained scenarios than the thicker ones. A solid solution of LSAT was used as substrate to investigate the effects of tensile strain on LNO with a lattice mismatch of 0.5%. The Raman measurements show strong variations in the signatures for different film thicknesses. Most striking are the variations in region I and III suggesting that the LNO film adopts different phases at different strain levels. This is in agreement with the DFT results shown in Chapter 2.5.1, suggesting that different strain levels allow the stabilisation of different phases of LNO.

We emphasised in the previous section that the A_{1g} mode, located in region II, is directly linked to the order parameter. It is therefore conceivable that the epitaxial strain induces variations in the rhombohedral structure, which should then be captured by the soft mode. In a rather unexpected turn of events the soft mode is the only one remaining stable at all strain levels. According to Weber *et al.* [22] only the E_g modes located at 150 and 400 cm^{-1} show a splitting into two distinct modes. This led to the interpretation that the epitaxial strain affects only the distortion of the oxygen octahedra by inducing different Ni-O bond lengths but tends to leave the tilting angle unaffected.

Even if the A_{1g} rotational mode was left unaffected by the epitaxial strain, it provided, with other variation of the measured Raman signature, insight on the type of changes that occur to the structure. This represents a unique proving ground emphasising the utility of this technique. The investigation was limited to thicknesses above 14 nm (roughly equivalent to 35 unit cells). This was partly due to the sample availability but also to the fact that such investigations on ultrathin film have proven to be challenging.

In the next section we aim at resolving these difficulties by using Raman depth profile measurements in combination with Principal Component Analysis tools. The focus will be on the LNO films deposited onto LAO as these did not show any particular structural changes in Raman spectroscopy while a particularly interesting transport properties were observed when the films enter the ultrathin regime [98].

7.3 Ultrathin $LaNiO_3$ films on $LaAlO_3$

In the bulk both LNO and LAO adopt a rhombohedral $R\bar{3}c$ structure. When the former is epitaxially deposited on the latter a theoretical compressive strain of 1.1% is obtained [22]. A typical Raman signature of bulk LNO has been introduced in in Figure 7.1 for a comprehensive strain study and is shown again in Figure 7.3.**a.** in comparison to the Raman signature of $LaAlO_3$ within the same spectral range. Section 4.2 described the purely instrumental limitations associated to the size of the samples. The present series of samples showcases perfectly these effects. Three Raman measurement at an incident laser wavelength of 633 nm on three different LNO deposition thicknesses can be seen in Figure 7.3.**b.**. Two modes of this spectral range can be observed and discussed:

- **LNO A_{1g} at 216 cm^{-1}:**This soft mode is very close to an identified *ghost* mode of LAO at 205 cm^{-1} [95]. It has been reported that it follows the same selection rules as the other A_{1g} mode of LAO. Their proximity is the reason why, even at 11_{pc} u.c., it is difficult to determine what part of the signature is caused by either the film or the substrate. The substrate contribution becomes more distinguishable as the sample signal vanishes which is particularly apparent for 3_{pc} u.c.
- **LNO E_g at 415 cm^{-1}:** This hard mode is isolated from any Raman contribution of the substrate. This allows for a clear view on how the decreasing interaction volume affects the signal to noise ratio. At 3_{pc} u.c., only a bump in the spectrum noise remains observable.

The other features of the signal are identified modes from the substrate with four of them located between 80 and 600 cm^{-1}. Two A_{1g} vibrations at 123 and 203 cm^{-1} accompanied by two E_g modes around 152 and 487 cm^{-1} [95]. The most investigated LAO soft-mode is present in the vicinity of 57 cm^{-1}, but not seen in the chosen range of the current investigation.

In the following section we will apply the methodology introduced in Chapter 5 combined with the Principal Component Analysis introduced in Section 6.3.3.

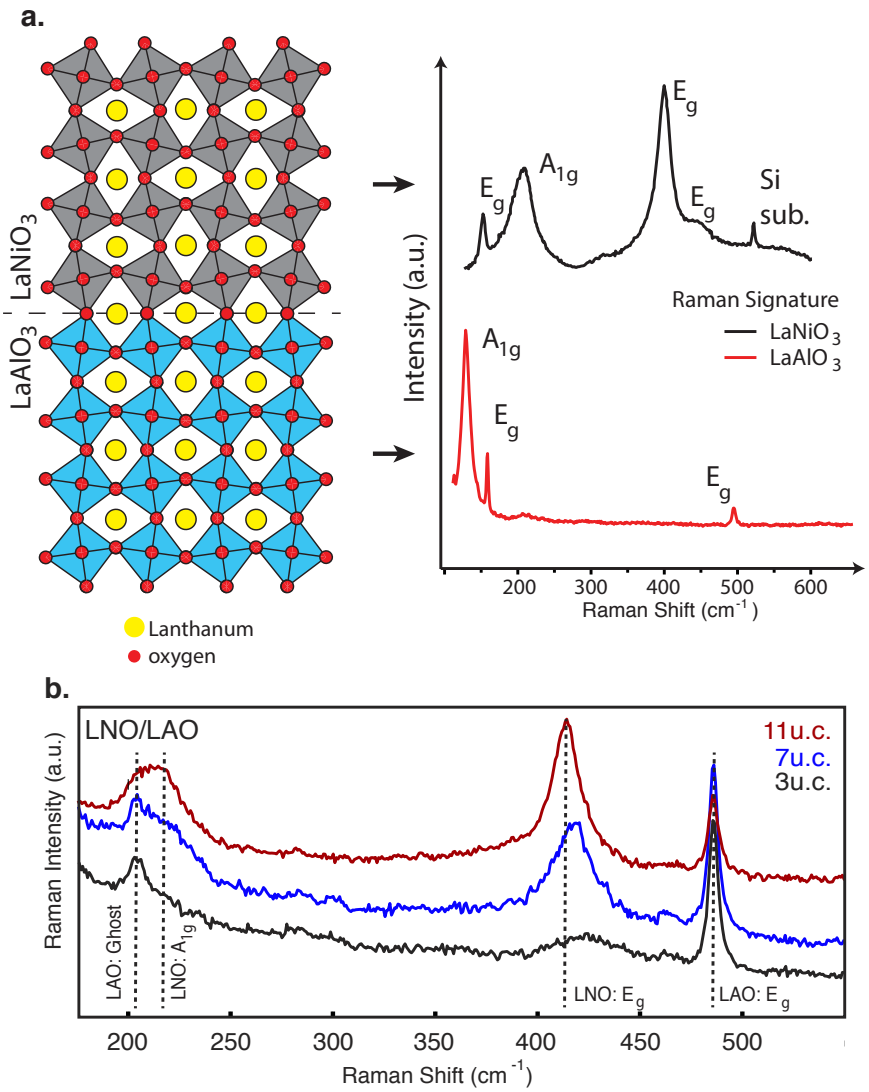

Figure 7.3 – a. Left: Graphical representation of the epitaxial deposition along the $[111]_{pc}$ direction: LNO on LAO. Right: Associated Raman signature with LNO [94] on top and LAO on the bottom. **b.** Raman spectra of three samples with different LNO thicknesses.

7.4 Depth Measurements: First treatment

All measurements shown in this chapter have been done with the same instrumental parameters summarised in Table 7.1. The Raman apparatus used within this work was described in Chapter 3.4.

Raman Parameters		**Measurement Parameters**	
Laser Wavelength:	633 nm	Duration of Acquisition:	60 s
Grating:	2400 cm^{-1}	Acquisitions per Measurement:	30 times
Power:	0.9 mW (10% filter)	Total Time per Measurement:	30 min
Temperature:	Ambient	Measurements	101
Objective:	100x	Depth range	-10 μm to 10 μm
Spectral Range:	100 to 900 cm^{-1}	Step	0.2 μm

Table 7.1 – Table listing the configuration of the Raman apparatus on the left and the acquisition times on the right.

An example of a depth profile measurement performed on a 7_{pc} thick LNO film epitaxially deposited on LAO is presented in Figure 7.4**a.**. Two curves representing the intensity evolution with depth at spectral values of 415 and 485 cm^{-1}, corresponding to the positions of the film and substrate E_g modes are illustrated in Figure 7.4**b.**. The behaviour of these profiles resembles the shapes presented in Chapter 5, namely a sharp peak-like behaviour of the sample signal and a step function like behaviour for the substrate induced signal.

The same type of measurement was performed for all provided LNO samples. This corresponds to LNO film thicknesses of 3_{pc}, 4_{pc}, 5_{pc}, 7_{pc}, 9_{pc}, 11_{pc} and 15_{pc} u.c. The contrast between the film and substrate signal is directly proportional to the film thickness, thus making it difficult to identify the LNO modes for the thinner ones.

Strictly speaking, LNO cannot retain its rhombohedral structure when deposited on LAO [52, 22] but has a monoclinic $C2/c$ symmetry. The assignment of the Raman modes, namely A_{1g} and E_g, inaccurate. Yet, for the lack of clearer nomenclature or understanding on how the vibration modes are affected, the same labelling will be used for the associated modes in the ultrathin film regime.

The present section we treat an investigation assisted though the PCA performed on a restricted spectral range, from 180 to 550 cm^{-1}, of what is available in dataset (Figure 7.4). Including a larger range led to the introduction of spurious contributions, clearly assigned to the substrate, into the component describing the sample, thus rendering its interpretation challenging. Figure 7.5.**a.** compares the identified film and substrate components from the PCA with the Raman spectra of the depth measurement illustrating the highest film contribution. A clear separation of the previously reported film A_{1g} (215 cm^{-1}) mode and substrate ghost mode (205 cm^{-1}) can be observed. Another observation is the clear attribution of the film E_g mode to the film component.

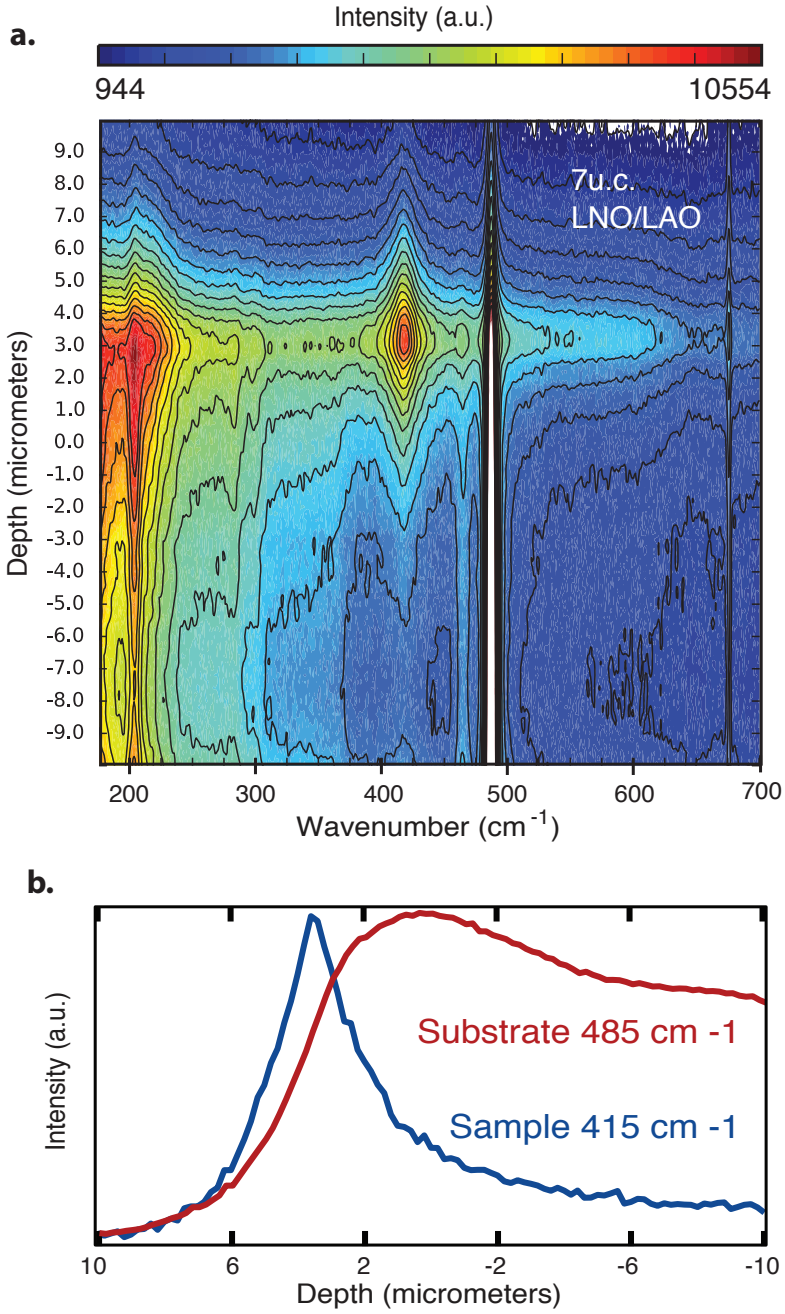

Figure 7.4 – a. Depth measurement performed on a 7_{pc} thick LNO film epitaxially deposited on LAO along the pseudo cubic $[001]_{pc}$ orientation with the introduced spectrometer parameters described in Table 7.1 **b.** Depth dependence of the Raman intensity at 405 and 485 cm^{-1}.

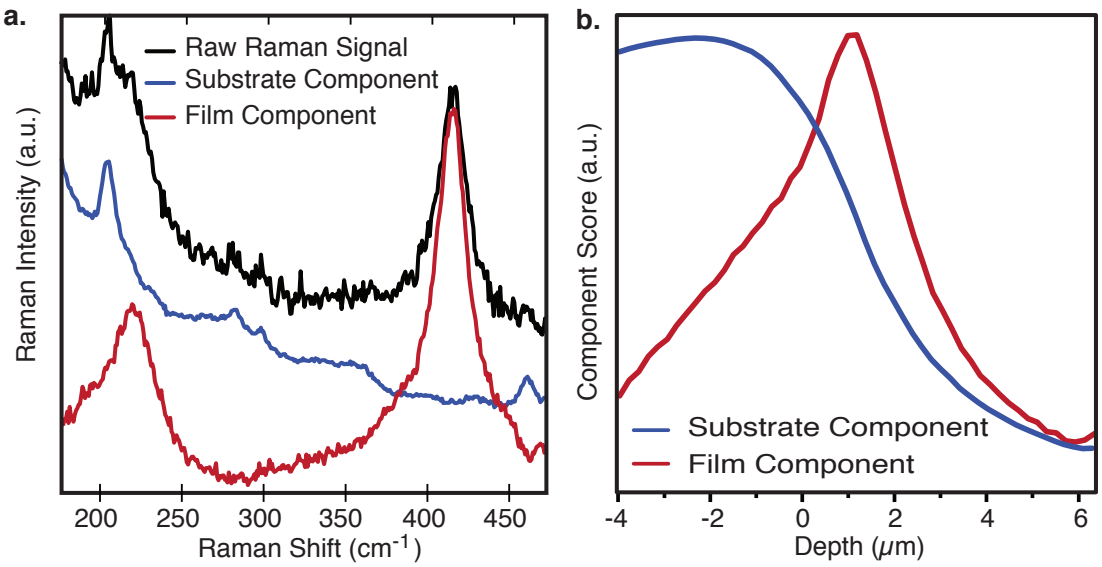

Figure 7.5 – a. The film (red) and substrate (blue) components extracted from a principal component analysis of the dataset shown in Figure 7.4. In this investigation the spectral range for the PCA was set from 180 to 550 cm^{-1}. The components are put in perspective with the raw Raman spectra showing the strongest film signature intensity (black). **b.** The score associated to the components.

On top of this an efficient separation a noise-free substrate component is obtained, showing further undocumented *ghost* modes of LAO, which might not be visible under normal measurement conditions.

Figure 7.6.**a.** represents Raman spectra of the depth measurement for thicknesses of 11_{pc}, 7_{pc} and 3_{pc} unit cells. Figure 7.6.**b.** in comparison shows the associated film components obtained through the PCA. Our methodology, developed in this work, allows to consistently extract a clear signature generated by the LNO film, even for thickness of 3_{pc} unit cells (≈ 1.2 nm). A fitting of these film components was performed with lorentzian line shapes. The fit of A_{1g} and E_g modes are shown in red and green, respectively. The associated position and HWHM are plotted with respect to the film thickness in Figure 7.6.**c.**. The 9_{pc} u.c. thickness presents an anomaly in the HWHM.

Both modes show a steep increase in their position and width with an onset at a thickness of approximately 10_{pc} u.c. The position of the E_g mode, which could still partly be followed without the PCA, shows an increase of approximately 10 cm^{-1} from 15_{pc} to 3_{pc} u.c.. Interestingly, we observe a shift of the A_{1g} mode towards higher rather than lower wavenumbers, therefore countering the idea that similar octahedra vibration modes of the LNO film and the substrate approach each other in the case of a fully strained ultrathin film.

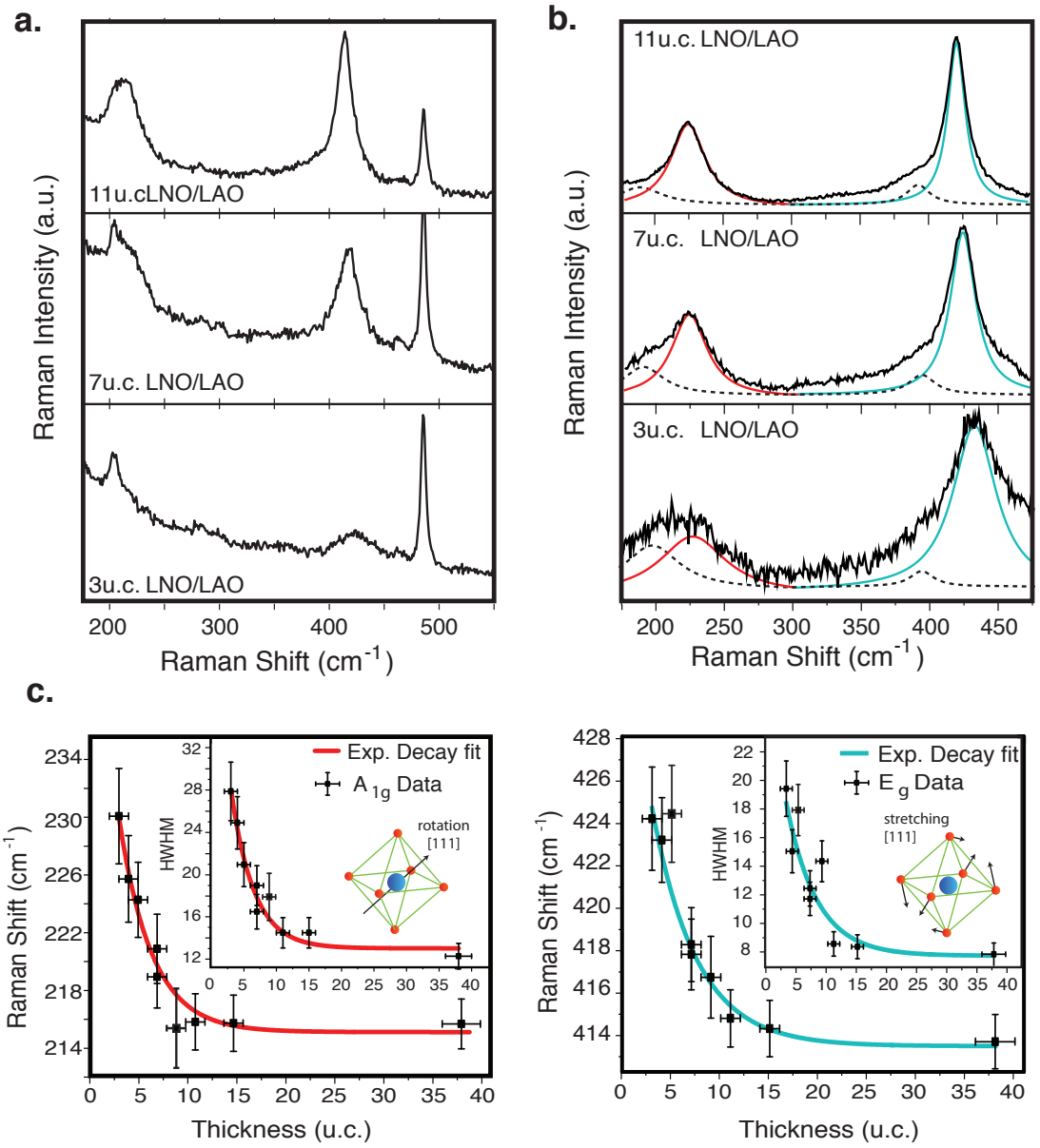

Figure 7.6 – a. Raman spectra of the depth measurement showcasing the highest film induced contribution for thicknesses of 11_{pc}, 7_{pc} and 3_{pc} unit cells. **b.** Identified film components associated to the depth profiles. **c.** Position and HWHM of the A_{1g} and E_g modes of LNO extracted from the fit of the film component.

7.5 Comparison with the Phonon confinement model

In order to understand the change in the spectral shape we compare the evolution of the peak position of both A_{1g} and E_g modes with the phonon confinement effects described in Chapter 4.1. The phonon confinement model integrates the dispersion relation of a given mode over the entirety of the first Brillouin zone. As a result, the knowledge of the full phonon branches is required. These were calculated for LNO in the $R\bar{3}c$ space group by Dr. H. Zhao and Dr. J. Íñiguez at the Luxembourg Institute of Science and Technology.

In $LaNiO_3$, solely one parameter δ suffices to characterise the distortion away from the cubic to the rhombohedral phase. It is assumed that the cubic unit cell is described by $R_{\text{cubic}} = (\boldsymbol{a}, \boldsymbol{b}, \boldsymbol{c})$ as shown in Figure 7.7.**a.**. The rhombohedral basis $R_{\text{rhom}} = (\boldsymbol{a'}, \boldsymbol{b'}, \boldsymbol{c'})$ is written :

$$\boldsymbol{a'} = a \cdot (\delta, 1, 1)_{\text{cubic}}, \tag{7.5.1}$$
$$\boldsymbol{b'} = a \cdot (1, \delta, 1)_{\text{cubic}}, \tag{7.5.2}$$
$$\boldsymbol{b'} = a \cdot (1, 1, \delta)_{\text{cubic}}, \tag{7.5.3}$$

where a the unit cell parameter. This leads to the reciprocal space basis $R^*_{\text{rhom}} = (\boldsymbol{a'^*}, \boldsymbol{b'^*}, \boldsymbol{c'^*})$:

$$\boldsymbol{a'^*} = \frac{2\pi}{a} \frac{(-1-\delta, 1, 1)_{\text{cubic}}}{-\delta^2 - \delta + 2}, \tag{7.5.4}$$
$$\boldsymbol{b'^*} = \frac{2\pi}{a} \frac{(1, -1-\delta, 1)_{\text{cubic}}}{-\delta^2 - \delta + 2}, \tag{7.5.5}$$
$$\boldsymbol{b'^*} = \frac{2\pi}{a} \frac{(1, 1, -1-\delta)_{\text{cubic}}}{-\delta^2 - \delta + 2}. \tag{7.5.6}$$

At this point it is possible to consider the distortion parameter δ to be negligible, thus simplifying the basis, leading to the following basis vectors for the rhombohedral and cubic unit cell in reciprocal space:

$$\boldsymbol{a'^*} = \frac{\pi}{a}(-1, 1, 1)_{\text{cubic}} \text{ and } \boldsymbol{a^*} = \frac{2\pi}{a}(1, 0, 0)_{\text{cubic}}, \tag{7.5.7}$$
$$\boldsymbol{b'^*} = \frac{\pi}{a}(1, -1, 1)_{\text{cubic}} \text{ and } \boldsymbol{b^*} = \frac{2\pi}{a}(0, 1, 0)_{\text{cubic}}, \tag{7.5.8}$$
$$\boldsymbol{b'^*} = \frac{\pi}{a}(1, 1, -1)_{\text{cubic}} \text{ and } \boldsymbol{c^*} = \frac{2\pi}{a}(0, 0, 1)_{\text{cubic}}. \tag{7.5.9}$$

The normal and reciprocal representation can be seen in Figure 7.7.**b.**. In this basis the extraordinary points of the first Brillouin zone are described as:

- **Γ point:**
  - $\boldsymbol{k}_\Gamma = (0, 0, 0)_{\text{rhom}}$

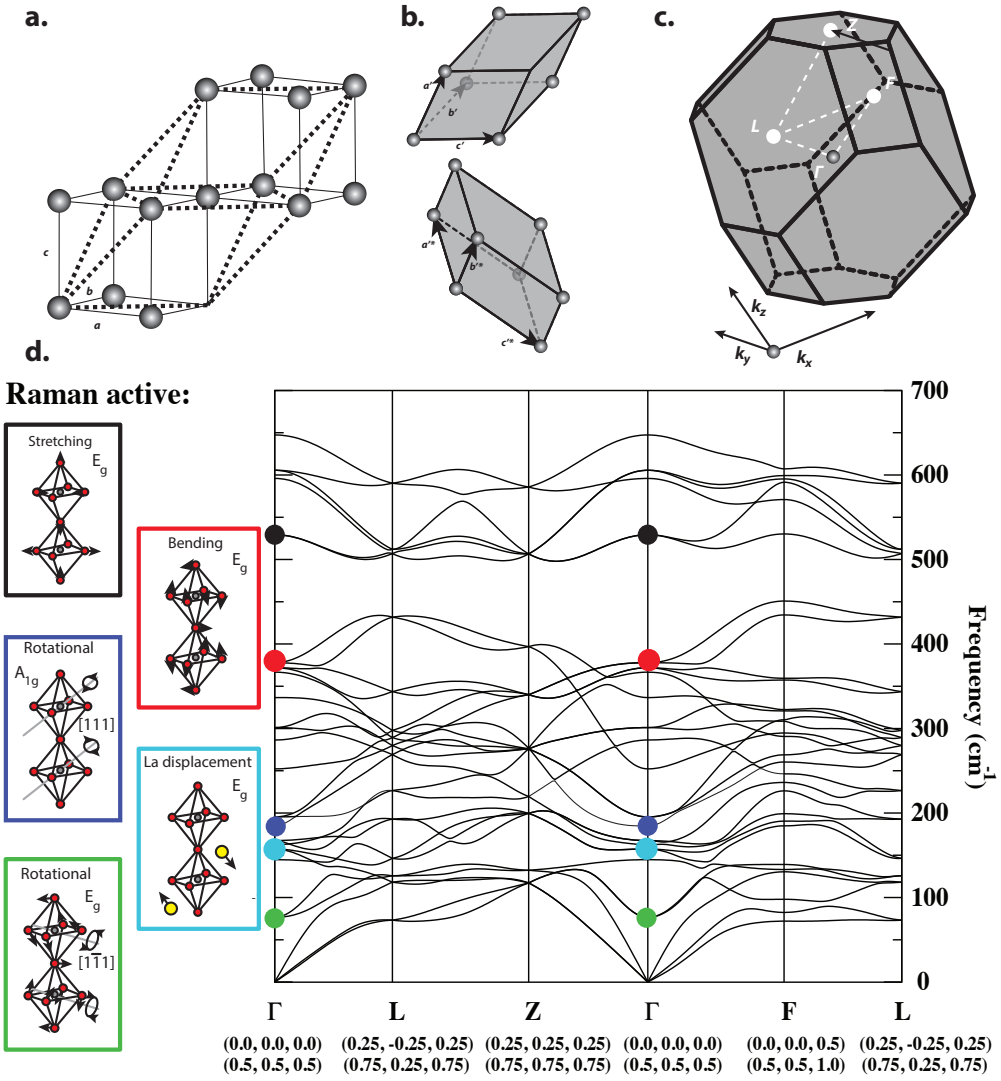

Figure 7.7 – a. - Schematic representation of the rhombohedral $R\bar{3}c$ unit cell within the cubic $Pm\bar{3}m$ unit cell. **b. -** Visualisation of the relation linking the real and the reciprocal space representation of the rhombohedral $R\bar{3}c$ unit cell. **c. -** First Brillouin zone of the rhombohedral space group with the positions extracted from Setyawan *et al.* [99] **d. -** Calculated phonon branches. The Raman active phonon modes are displayed on this diagram.

  - $\boldsymbol{k}_\Gamma = (0,0,0)_{\text{cubic}}$ or $(0.5,0.5,0.5)_{\text{cubic}}$

- **L point:** Equivalent to the eight vector wave vector star Λ points in the cubic unit cell.
  - $\boldsymbol{k}_L = (0,0.5,0)_{\text{rhom}}$
  - $\boldsymbol{k}_L = (0.25,-0.25,0.25)_{\text{cubic}}$ or $(0.75,0.25,0.75)_{\text{cubic}}$

- **Z point:** Equivalent to the eight vector wave vector star Λ points in the cubic unit cell.
  - $\boldsymbol{k}_Z = (0.5,0.5,0.5)_{\text{rhom}}$
  - $\boldsymbol{k}_Z = (0.25,0.25,0.25)_{\text{cubic}}$ or $(0.75,0.75,0.75)_{\text{cubic}}$

- **F point:** Equivalent to the M and X points.
  - $\boldsymbol{k}_F = (0.5,0.5,0)_{\text{rhom}}$
  - $\boldsymbol{k}_F = (0,0,0.5)_{\text{cubic}}$ or $(0.5,0.5,1)_{\text{cubic}}$

The points are displayed in the first Brillouin zone shown in Figure 7.7.**c.**. The phonon branches along the lines interconnecting these points in the reciprocal space are shown in Figure 7.7.**d.**. On the same figure are displayed the Raman active modes.

The integration has been performed along three directions in the reciprocal space always starting from Γ. The directions are: Γ to L, Γ to Z and finally Γ to F. The expected Raman lineshapes for the A_{1g} and E_g are shown in Figure 7.8.**a.** and **b.**.

The phonon confinement calculations were performed to obtain a qualitative impression as to when this effect could have an impact on the Raman signature of LNO film. The position and width fo the A_{1g} was approximated through the fit of a lorentzian lineshape. The variations follow a similar trend as in the previously displayed experimental measurements but they suggest a much earlier onset. Using a rough estimation Γ to L has the latest onset with roughly 12 nm, while Γ to Z and Γ to F report 25 nm and 20 nm, respectively. This estimation corresponds to the change of regime extrapolated through the intersection of the tangents of the trend. In reality, because of the inability of the fitted lorentzian lineshape to properly capture the shape, the onset is under-evaluated and starts at larger thicknesses as reported. the most extreme value of 12 nm would correspond to a film thickness of 30_{pc} unit cells. This is three times earlier than then change in trend reported through our Raman spectroscopy investigation of ultrathin $LaNiO_3$. We therefore deduce that it is unlikely that the phonon confinement is the driving force behind the observed spectral variations.

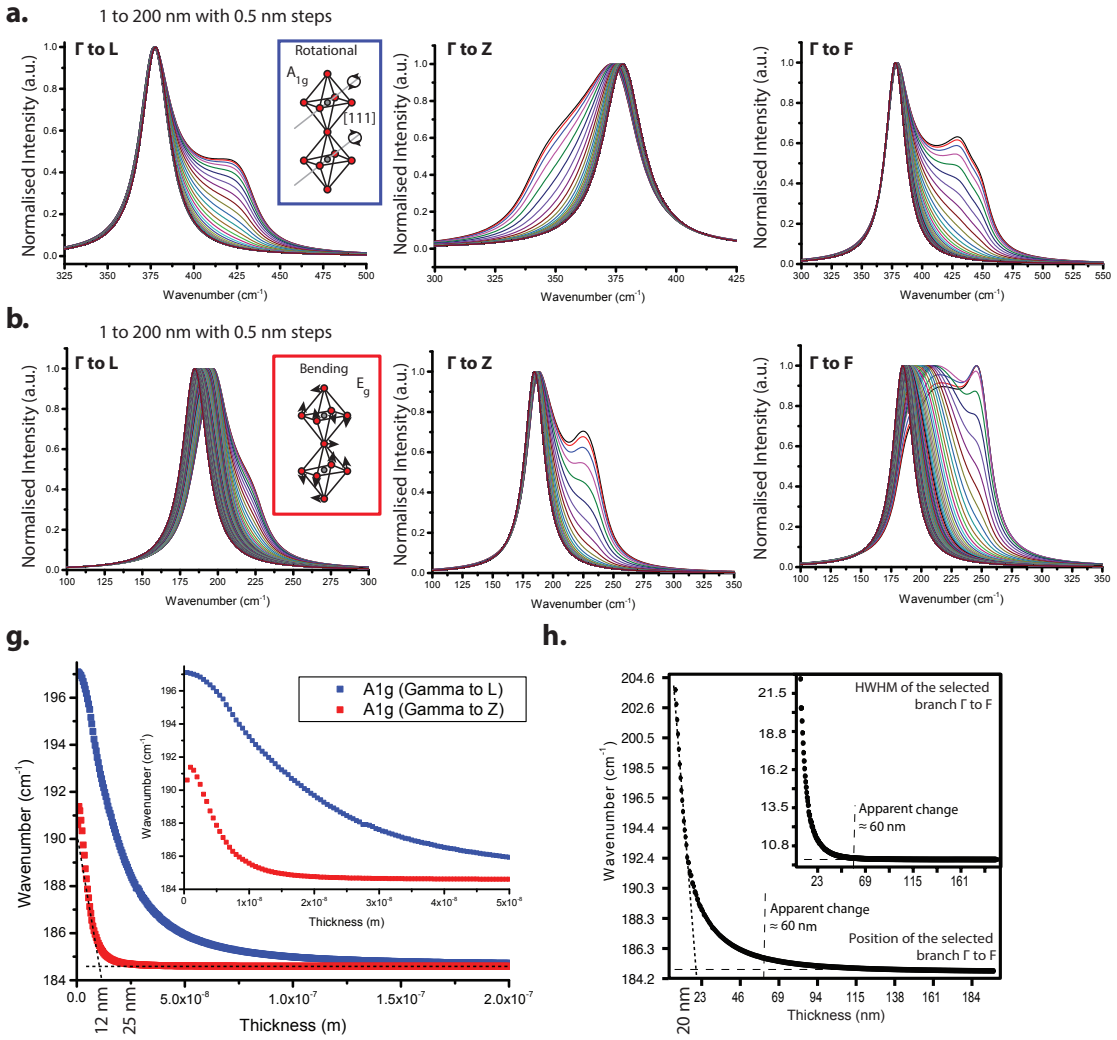

Figure 7.8 – a. Computed spectra resulting from the phonon confinement of the A_{1g} rotational mode along the Γ to L, Γ to Z and finally Γ to F directions. **b.** Same as **a.** but for the E_g bending mode. **c.** Evolution of the position and HWHM of the peaks presented in **a.** along the Γ to L and Γ to Z directions. **d.** Evolution of the position and HWHM of the peaks presented in **a.** along the Γ to F direction.

7.6 Comparison with *ab-initio* calculations of the film

Having established the experimental signature of the ultrathin film, and the unlikeliness to explain them by the phonon confinement model, we now consider a structural explanation through simulations. A part of the calculations associated to the inter-lanthanum distance was shown in Chapter 2.5.2 extracted from Fowlie *et al.* [53] and calculated by Dr. J. Íñiguez at the Luxembourg Institute of Science and Technology.

Figure 7.9.**a.** visualises a direct measurement of the inter-Lanthanum distance along the c axis normalised over the bulk LAO value extracted form the TEM measurements previously shown in Figure 2.7.**b.**. The equivalent quantity extracted from the calculations are shown in Figure 7.9.**b.**, which were obtained by running first-principles simulations in which finite $LaNiO_3$ films of different widths, and the $LaAlO_3$ substrate, were treated explicitly. Both show strong similarities, in particular a three region arrangement composed as follow: surface region, semi-relaxed film region and interface region. The calculated tilt angles of octahedra are shown in Figure 7.9.**c.**. The reliability of the calculations is expressed through the similarities in the structural arrangements between the measurement and the calculations.

These structural calculations lay the groundwork for the phonon A_{1g} soft mode estimations. The equilibrium solution is distorted by moving the oxygen atoms within the $LaNiO_3$ film so as to mimic anti-phase rotations of the O_6 octahedra about the $[111]_{pc}$ axis, and compute the harmonic energy variation. We thus obtain the energy curvature κ_{soft}, and approximate the mode frequency as $\omega_{\text{soft}} = \sqrt{\kappa_{\text{soft}}/m_{\text{O}}}$, where m_{O} is the mass of the oxygen atom. Note that here we are assuming that the eigenvector of the soft tilting mode of the films, which feature a large $a^-a^-c^-$-type monoclinic distortion – can be approximated by the well-known symmetry-determined tilting eigenmode of the cubic crystal; this seems a sensible approximation that would be exact if we were dealing with the $R\bar{3}c$ phase of bulk $LaNiO_3$. This approach allows us to avoid explicit and very costly calculations of the dynamical matrix of the thin films.

The results, shown in Figure 7.9.**d.**, are qualitatively close to our experimental Raman measurements, displaying a similar hardening in the limit of very thin films. Indeed, the difference in frequency between the thin and thick limits is about 15 cm^{-1} according to the first-principles estimation, while 14 cm^{-1} where obtained experimentally.

Furthermore, the interpretation of the computed effect is as follows: For the thinnest films, the energy variation is controlled by the $LaNiO_3$ surface, which is relatively stiff against the O_6 tilting mode. Interestingly, this result is consistent with the known equilibrium structure of the film surface, which features strongly suppressed tilts, as shown in Fowlie *et al.* [53]. Thus, our results for ω_{soft} are physically sound and consistent with experimental observations, thus letting us believe that the calculations provide the correct explanation for the mode hardening observed in the thinner films.

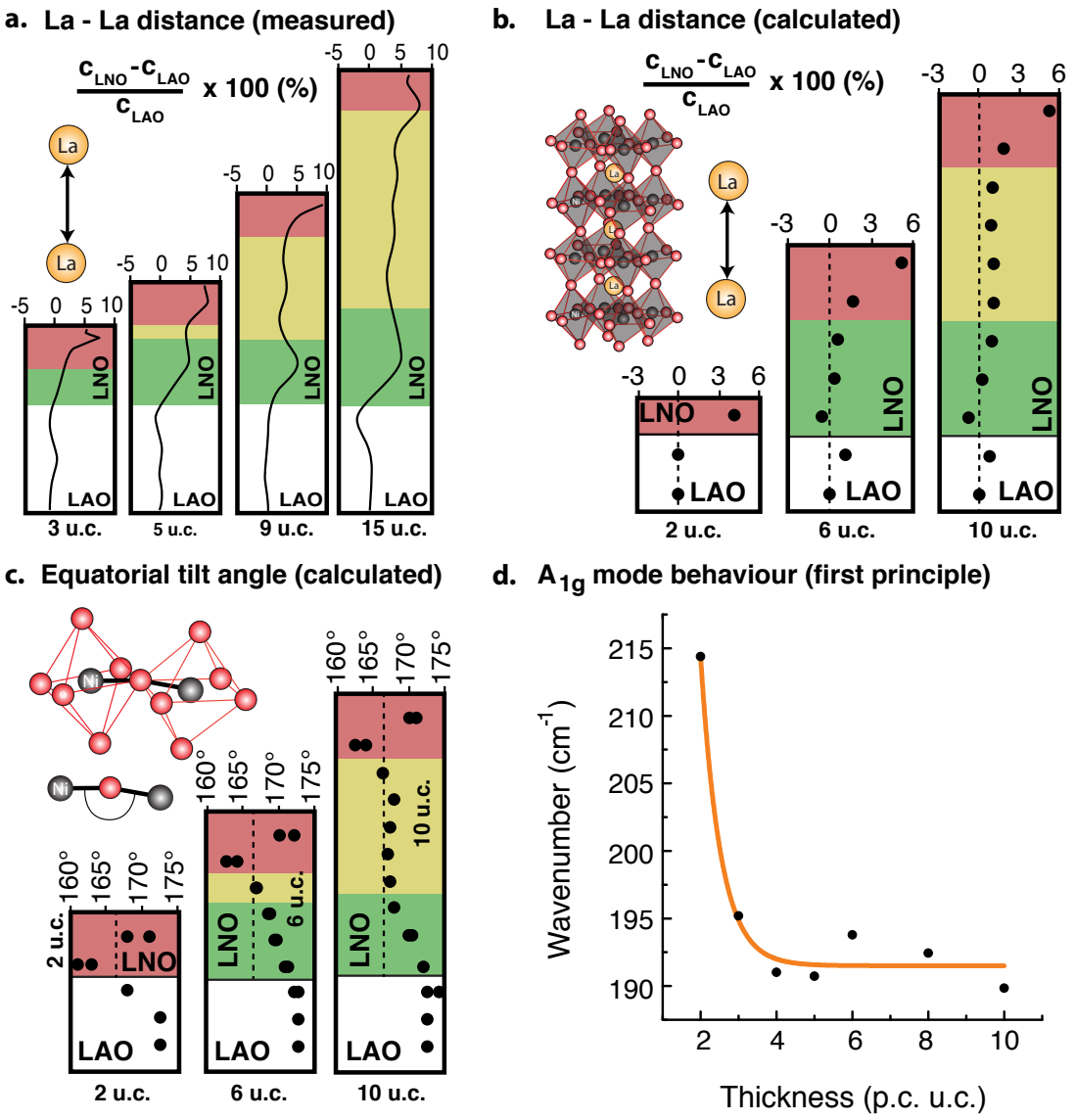

Figure 7.9 – a. Inter Lanthanum distances normalised over the Bulk LAO distances for the TEM images shown in Figure 2.7. **b.** Same quantity as a. for the calculated structure. **c.** Octahedra tilt angles extracted from the calculated structure. **d.** Calculated A_{1g} frequencies from the calculated structures at different thicknesses.

7.7 Depth Measurement: Second treatment

The initial investigation of the dataset through the PCA (Section 7.7.2) was performed on a limited spectral range, to capture the least amount of signature generated by LAO. The argument, at the time, was that *parasitic* substrate contributions within the film component hinder its accurate interpretation. The calculation results (supported by TEM measurements) of the last section ought to change this by suggesting the distortion of the interface layers of LAO as the film thickness decreases. Similar to the film signal, the PCA performed on the whole spectral range was treated to search for evidence supporting this claim.

Figure 7.10.**a.** shows the covariance of the first 20 components obtained from the PCA on a range from 100 to 550 cm^{-1} (the depth profile measurement datasets were already introduced in Section 7.7.2). This data in combination with the associated scores justified the consideration of only the first three components. Figure 7.10.**b.** shows the scores with their respective rescaling factors. As already suggested, their shapes are more complex in comparison with the one presented in Section 7.4. Nevertheless, it is possible to qualitatively attribute one score belonging to a component that describes the substrate (black) and two others describing the film region (red and blue). The components associated to these scores are displayed in Figure 7.10.**c.**, **d.** and **e.**. The inset reveals that Figure 7.10.**c.** corresponds accurately to the substrate signature (comparable with the substrate component of Figure 7.5.**a.**). The magnified insets in Figure 7.10.**d.** and **e.** reveal the film signatures (comparable with the film component of Figure 7.5.**a.**). This justifies their appellation as first and second film component respectively. Figure 7.10.**a.** emphasised that the two film components (except at 3_{pc} u.c. film thickness) possess the same covariance and therefore the same interpretation weight. Yet, we already established in the previous PCA study (on the restricted range) that one component suffices to express the signal generated by the film in the range from 180 to 550 cm^{-1} (Section 7.4). It is therefore very likely that the shapes of the LNO A_{1g} and E_g modes, located respectively at 215 and 415 cm^{-1}, are identical in both components.

These two film components also show feature attributed to the substrate. This indicates that an alteration of the substrate signature is expressed at the interface through the two film components. In the next subsection an investigation of the LNO part of the components will be performed and compared to the results obtained in Section 7.4. Once it is established that the present PCA study does not alter the initial results for LNO a more profound investigation of the substrate contributions will be performed.

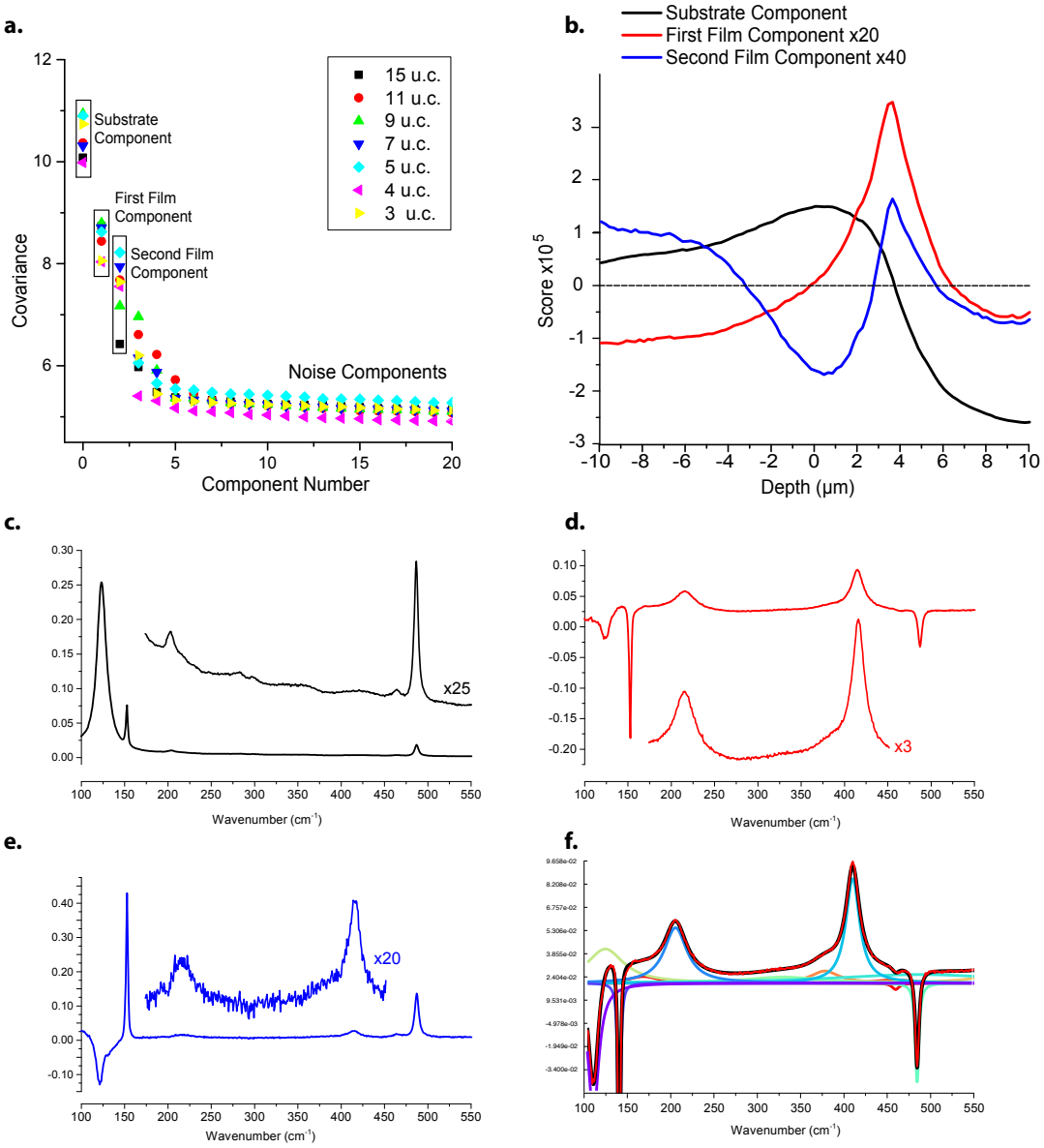

Figure 7.10 – a. Covariance of the first 20 components of each provided sample of LNO on LAO epitaxially grown along the $[001]_{pc}$ orientation. **b.** Score of the first three components of LNO on LAO for a sample thickness of 7_{pc} u.c. **c.** Substrate component for LNO on LAO for a sample thickness of 7_{pc} u.c. **d.** First sample component **e.** Second sample component **f.** Fit of the first sample component with positive and negative lorentzian peaks.

7.7.1 Investigation of the LNO contribution

In order to trace the LNO contribution in the present film components, it has to be fitted in its entirety. This includes the visible modes of both LNO and LAO. While they represent a limited amount of peaks, the arbitrary sign of the amplitudes challenges the fit and therefore the interpretation. The fitting methods, described in Chapter 6.2, were utilised to fit the two film components. An example of such a fit can be seen in Figure 7.10.**f.**. The most rational approach at this point corresponds to fit only peak that were already known in the previous LNO and LAO investigations. This is particularly important as a less broad negative lorentzian line shape on top of a broader positive lineshape gives the appearance of two distinct positive lorentzians. This can lead to misinterpretations of the signature. Such an example can be seen on the A_{1g} mode at 205 cm^{-1} in the third component seen in Figure 7.10.**e.**.

The correct fit allows to subtract the lineshapes of the substrates modes (positive or negative) and retrieve the signal of the ultrathin LNO film. The processed signals can be seen in Figure 7.11.**a.** and **b.** for the first and second film component respectively. For latter, we have to acknowledge that its LNO contribution is much weaker and its interpretation could be prone to errors. The position and HWHM evolution with the thickness of the LNO A_{1g} and E_g modes are displayed in Figure 7.11.**c.** through **f.**. Similar to the previous PCA investigation the trends were fitted with exponential decay functions. The first observation is that the retrieved values from the first and second film components match within the fit error. This is important as it qualitatively states that no major variation of the LNO signature is observed in-between the film components.

Furthermore the trends with thickness show an steep increase in their width and position an onset at approximately 10_{pc} u.c. This is in agreement with the previous PCA investigation performed in Section 7.7.2, including the anomaly in the width of the 9_{pc} u.c. thick sample. The same anomaly can be observed in the previous study. The position of the E_g mode, which could still partly be followed without the PCA, shows an increase of approximately 10 cm^{-1} from 15_{pc} to 3_{pc} u.c.

Having established that the results on LNO stay unchanged regarding the previous interpretations, we now investigate the contributions of the LAO substrate in these components. This will be done in the next subsection.

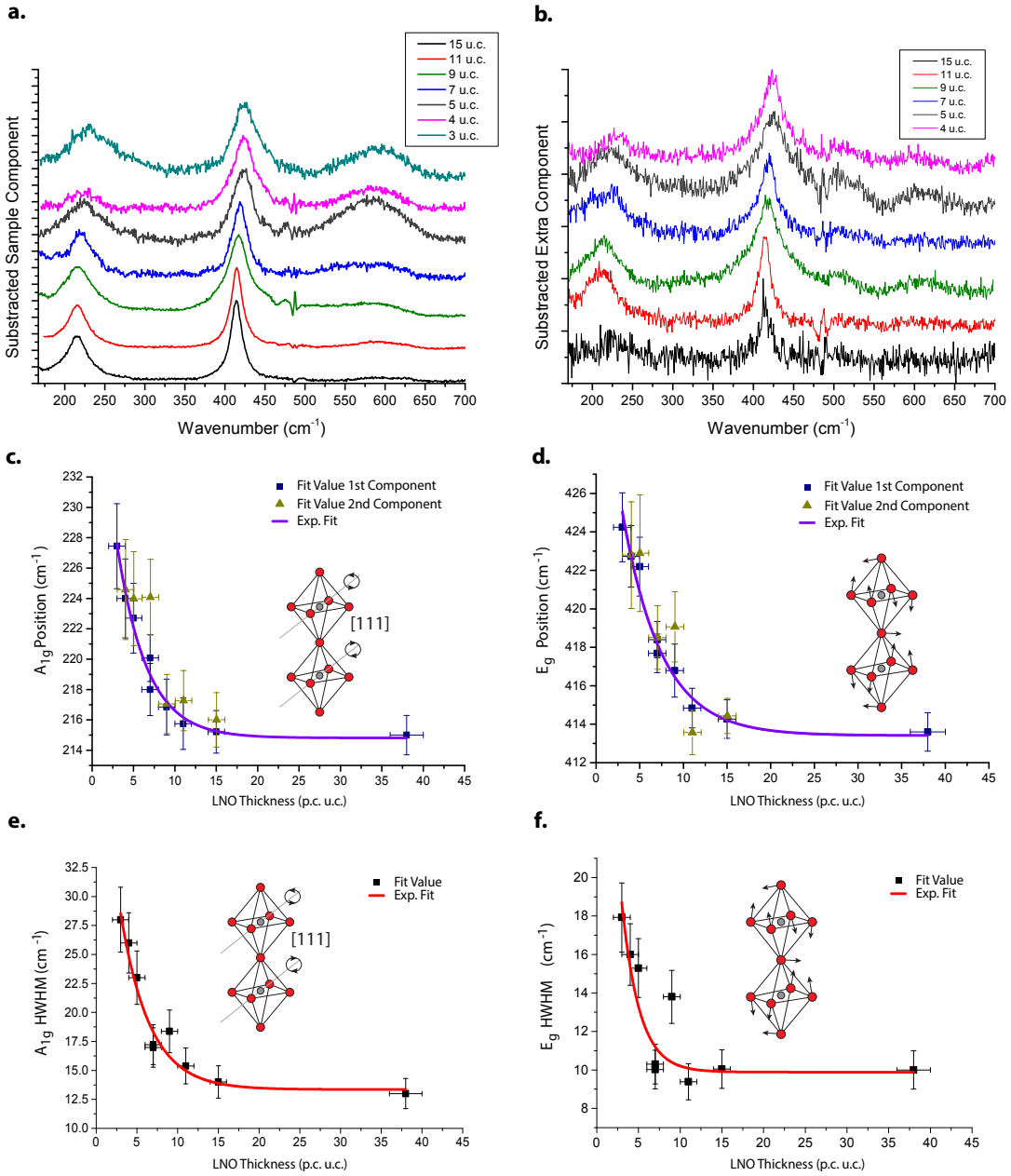

Figure 7.11 – a. Corrected film component of LNO on LAO epitaxially grown along the $[001]_{pc}$ orientation with all substrate modes subtracted and normalised. **b.** Corrected second film component of LNO on LAO epitaxially grown along the $[001]_{pc}$ orientation with all substrate modes subtracted and normalised. **c. & e.** Position and HWHM of the A_{1g} mode extracted through the fit prior to the correction. **d. & f.** Position and HWHM of the E_g mode extracted through the fit prior to the correction.

7.7.2 Investigation of the LAO contribution

The results from both the *ab initio* calculations and the TEM measurements indicate that the last unit cells of the LAO substrate are affected by the epitaxial strain induced from the thin film. Such an effect should induce a change in the lattice parameters of the affected unit cells and therefore alter its Raman signature. LAO crystallises in the same space group as LNO, namely $R\bar{3}c$ with the same occupied Wyckoff positions. As a result it presents the same vibration patterns. The identified modes can be assigned as shown in Figure 7.12.**a.** according to an investigation by Abrashev *et al.* [95].

To have a better *a priori* knowledge on what information the PCA could provide, an initial study of the virgin LAO substrate was performed (no film deposited). The same approach, namely a depth profile measurement followed by a PCA investigation, was utilised. This led to two distinct PCA components, which can be see with their associated scores in Figure 7.12. Fitting these reveals that both LAO E_g modes, located at 152 and 487 cm^{-1}, are found at the same position in both components. On the other hand the LAO A_{1g} mode, located at 124.9 cm^{-1} in the first components is shifted to 126.7 cm^{-1} in the second component. As this mode is related to the tilt vibration of the oxygen octahedra along the $[111]_{pc}$ orientation it is directly linked to the rhombohedral order parameter (similar to LNO as explained in Section 7.1). A shift of this peak towards higher wavenumbers would therefore indicate an increase of the inter-octahedral tilt angle of LAO within the surface layer. Using the formulation of Illiev *et al.* [97] of 23.5 cm^{-1}/deg would correspond to a change in the tilt angle of ≈0.07°. In summary, the Raman depth profile spectroscopy aided by PCA is able to measure tilt variations at the surface of LAO. This comforts us that the PCA, on the depth profiles of ultrathin LNO films epitaxially deposited on LAO, should be able to capture and identify the minor variations of the substrate at the interface.

The first component resulting from PCAs performed on the entire spectral range of the depth profile measurements (100 to 600 cm^{-1}) of all ultrathin LNO films deposited on LAO are pre-

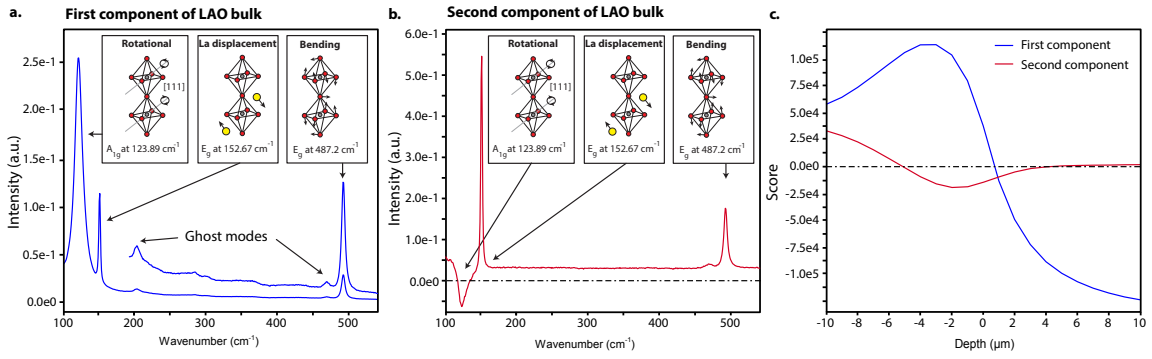

Figure 7.12 – a. First component of the PCA performed of a depth profile measurement of a virgin LAO substrate. **b.** Second component. **c.** Score associated to the first and second component.

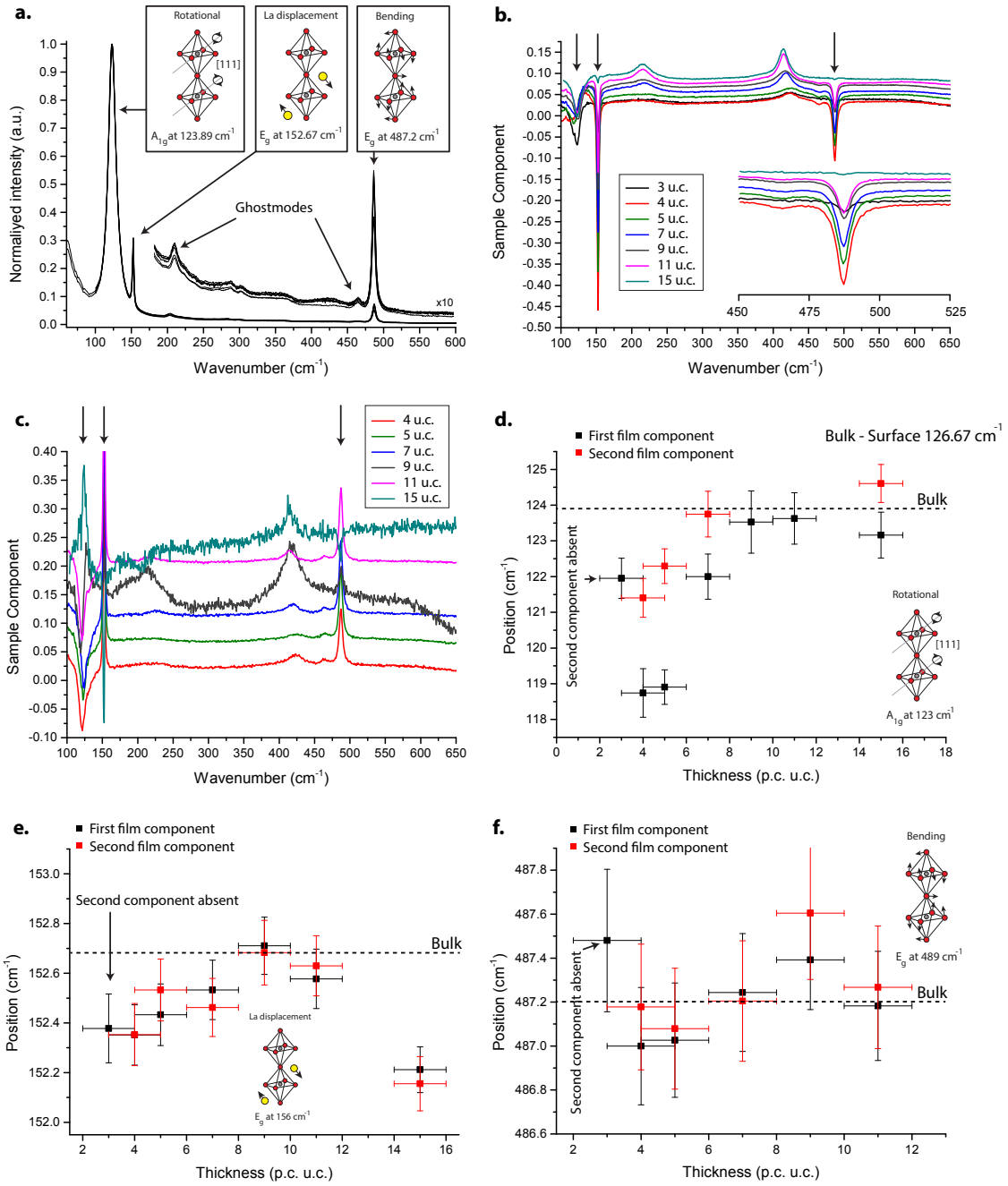

Figure 7.13 – a. Mode assignment of the substrate components extracted through a PCA from the depth measurements performed on ultrathin films of LNO epitaxially deposited on LAO along the $[001]_{pc}$ orientation. **b.** First film component of the same samples. **c.** Second film component of the same samples. **d.** Position of the A_{1g} mode of LAO extracted from **b.** and **c.** **e.** Same for the E_g La displacement mode. **f.** Same for the E_g distortion mode.

sented in Figure 7.13.**a.**. An important point is the observation of a very strong similarity with the first component signature obtained from virgin substrate (Figure 7.12.**a.**), thus suggesting the absence of a parasitic LNO signature. Furthermore, all these signatures are equivalent, meaning that no variation of the substrate is contained within the first component. The second and third component (except for 3_{pc} u.c. thick LNO, which has no second film component) are shown in Figure 7.13.**b.** and Figure 7.13.**c.**, respectively. In both cases the substrate modes are marked by arrows. Interestingly, the second film component for 15_{pc} u.c. shows no signature for the E_g mode usually found at 487 cm^{-1}.

The fits of these components are the same as the ones presented in Section 7.7.1 for the determination of the LNO film modes behaviours. Here, the focus of the investigations was simply shifted towards the substrate modes. Their respective positions are shown in Figure 7.12.**d.** through **f.**. Similarly to what was obtained in the bulk measurements, the two identified E_g seem to barely shift. On the other hand, the peak located at the position of the A_{1g} tilt mode shifts from 124.8 in the bulk to 118.7 cm^{-1} at 4_{pc} u.c. Using the formulation of Illiev *et al.* [97] of 23.5 cm^{-1}/deg would correspond to a change in the tilt angle of $\approx$-0.25°.

The interpretation of these variations have to be done in a cautious manner. The first point being that the fit of the A_{1g} mode in the first and second film component has proven to be difficult and could therefore contain errors. The second part is that, in contrary to LNO, the contribution of the LAO A_{1g} mode is not located at the same position in these components. Therefore it is rather complicated to guess how these behave when considered together. It is also not clear if the formulation introduced by Illiev is accurate in the limit of epitaxial systems. The only certainty that can be gained of this investigation is that the tilt angle of the LAO substrate is altered at the interface with LNO, which is consistent with the TEM measurements and the *ab initio* calculations.

7.8 Conclusion and perspectives for LNO on LAO

In the present investigation the structure of ultrathin $LaNiO_3$ (LNO) films epitaxially deposited on $LaAlO_3$ (LAO) was investigated using Raman depth profile measurements analysed through the Principal Component Analysis (PCA). No symmetry break was observed in the Raman signature down to film thicknesses of 3_{pc} u.c., thus, suggesting that the insulating behaviour is triggered by another mechanism. TEM measurements in tandem with *ab-initio* calculations concluded that in the ultrathin regime the effects induced by the LNO surface cannot be neglected anymore. By tracing the inter lattice distance and octahedral tilt arrangement it was possible to distinguish three distinct regions of the LNO sample structure:

- A clearly distinct but thickness invariant crystallographic arrangement at the surface of about 2_{pc} unit cells.
- Another region that scales linearly with the thickness showing the anticipated arrangement from epitaxially strained LNO on LAO. This region is inexistent when the sample is too thin as it requires a critical stabilisation thickness.
- The last layer consisting of an epitaxially distorted structure of 2-4_{pc} u.c.. Similar to the surface layer, the size of this distortion seems to be thickness independent, unless the sample becomes too thin to accommodate both the epitaxial and the surface layer in which case the latter seems to take the upper hand.

The structural simulations were then used to calculate the behaviour of phonons. Their evolution with the thickness showcased a similar trend to the experiment, namely an upwards shift of the mode frequencies. The critical value that was obtained at 10_{pc} u.c. corresponds to the measured critical value at which the films start to present a decrease in its conductivity.

Furthermore, this investigation allowed to measure the dynamical fingerprint of an ultrathin film deposited onto a substrate, which, to the best of our knowledge, has never been achieved before. Even for the thinest film, at 3_{pc} u.c. (1.2 nm), no breakdown of the Raman signature was observed, thus, suggesting that the oxygen octahedra vibration of epitaxially deposited film do not vanish. It also seems from the results obtained in this chapter, that the phonon confinement is not observed within the investigated epitaxial systems. The findings of this chapter thus open the venue to investigate even ultrathin films of oxides.

Within the last section, the signal of the substrate at the interface was investigated. Signature shifts were present but rather complicated to interpret at the time. We consider that this investigation could be pushed further. It also suggests that Raman spectroscopy has the potential to investigate the interface behaviour of distinct compounds and could therefore be used more extensively in the study of perovskite heterostructures.

Chapter 8

Neodymium Nickel Oxide $NdNiO_3$ (NNO)

8.1 Motivation

$NdNiO_3$ (NNO) was introduced in Chapter 2.6. Within the present section we recall some notions that motivate this investigation. In the bulk, NNO possesses a metal to insulator transition (MIT) at 200 K, which is simultaneously accompanied by a Néel transition. It is known that the MIT is accompanied by a structural transition from orthorhombic $Pbnm$ in the conducting phase to monoclinic $P2_1/n$ in the insulating phase. The detailed mechanism is described for the whole nickelate family in chapter 2. One of the motivations to investigate $NdNiO_3$ is its close proximity to a region of interest of the phase diagram where the MIT and Néel transition (NT) temperature dissociate. In this context the compound has been epitaxially deposited on a wide ranges of substrates to alter the transition temperatures and potentially discover novel behaviours. All but one configuration have been found to decrease the transition temperature. One exception reported: the MIT temperature of $NdNiO_3$ epitaxially deposited on $[111]_{pc}$ oriented $NdGaO_3$ (further referenced to as NGO) increases from 200 K to 330 K [55] and dissociates from the Néel transition temperature. Both critical temperatures were determined through resistivity and resonant X-Ray reflectivity measurements. The question that persists is how the structure of NNO is modified in this configuration: is the transition behaviour comparable to either of its nickelate counterparts or is a novel mechanism at work.

In this chapter we aim at addressing this question. A first part will introduce the NNO structure with the associated Raman signature. This will be followed by a depth profile measurement investigation at ambient temperature accompanied by the Non-Negative Matrix Factorisation (NMF) to dissociate the NNO film from the NGO substrate signature. This will then allow us to perform a detailed temperature dependant investigation. An empiric comparison with published

data on $SmNiO_3$ will be performed with the aim to determine if the present sample uses a similar mechanism and can therefore be compare to other nickelate, and thus can be placed in the same single-parameter phase diagram as the other nickelates.

8.2 Raman signature of NNO

This section will provide a description of the Raman activity of the two crystalline phases of NNO, namely $Pbnm$ and monoclinic $P2_1/n$ [100]. A schematic representation of the crystal structures can be seen in Figure 8.1.**a.**. It has been shown in former studies that Raman spectroscopy clearly distinguishes between these structural phases [56, 101], thus making it an ideal tool to study the structural transition in nickelates. The characteristics are the following:

Metallic NNO in the *Pbnm* space group: The octahedral tilt pattern expressed in the Glazer notation is $a^-a^-b^+$. The resulting unit cell parameters are shown in Table 8.1 [102]. Such an arrangement gives rise to 60 normal modes, 24 of which are Raman active:

$$\Gamma_{\text{Raman}}^{Pbnm} = 7A_{1g} + 7B_{1g} + 5B_{2g} + 5B_{3g}. \tag{8.2.1}$$

Note that switching from the $Pnma$ to the $Pbnm$ phase, which are equivalent through a circular permutation of the axes leads to a rearrangement of the B_{1g}, B_{2g} and B_{3g} modes. The Raman tensors associated to Raman active modes in the $Pbnm$ phase are [103]:

$$A_g = \begin{pmatrix} a & 0 & 0 \\ 0 & b & 0 \\ 0 & 0 & c \end{pmatrix} \tag{8.2.2}$$

$$B_{1g} = \begin{pmatrix} 0 & d & 0 \\ d & 0 & 0 \\ 0 & 0 & 0 \end{pmatrix}, B_{2g} = \begin{pmatrix} 0 & 0 & e \\ 0 & 0 & 0 \\ e & 0 & 0 \end{pmatrix}, B_{3g} = \begin{pmatrix} 0 & 0 & 0 \\ 0 & 0 & f \\ 0 & f & 0 \end{pmatrix} \tag{8.2.3}$$

Insulating NNO in the $P2_1/n$ space group: This phase is the result of a differentiation of the initially symmetry equivalent oxygen octahedra into two different variants. This change induces a loss of two out of the three mirror plane symmetries present in $Pbnm$. The resulting unit cell parameters are shown in Table 8.1 [102]. Such an arrangement gives rise to 60 normal modes of whom 24 modes are Raman active:

$$\Gamma_{\text{Raman}}^{P2_1/n} = 12A_g + 12B_g. \tag{8.2.4}$$

The Raman tensors associated to Raman active modes in the $P2_1/n$ phase are [104]:

$$A_g = \begin{pmatrix} a & 0 & d \\ 0 & b & 0 \\ d & 0 & c \end{pmatrix}, B_g = \begin{pmatrix} 0 & e & 0 \\ e & 0 & f \\ 0 & f & 0 \end{pmatrix} \tag{8.2.5}$$

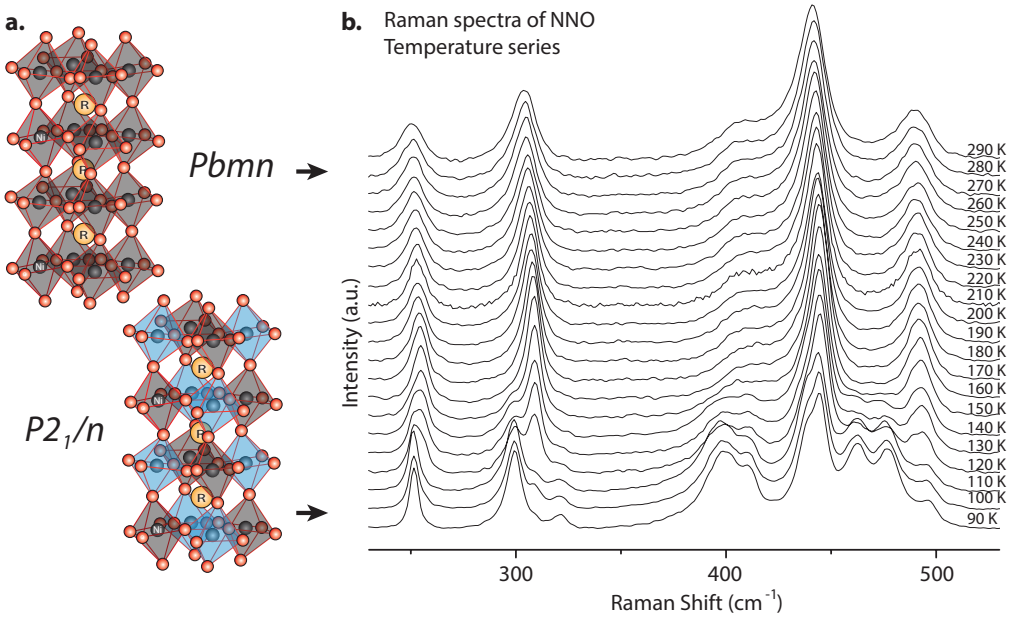

Figure 8.1 – a. Representation of the changes between $Pbnm$ and $P2_1/n$ as the charge dispropornation induces two sets of non equivalent octahedra. **b.** Temperature series of NNO deposited on LAO marking the phase transition at 160 K. Reproduced from Girardot *et al.* [56]

NNO in the $Pbmn$ phase (at 290 K)

a = 5.38712(2), b = 5.38267(2), c = 7.60940(3) Å			
Atom	Wyckoff Position	Representative	Experimental Values (Å)
Nd	4c	(x,y,1/4)	(0.9958(2),0.0350(1), 1/4)
Ni	4b	(1/2,0,0)	(1/2, 0, 0)
O1	4c	(x,y,1/4)	(0.0692(9), 0.4896(9), 1/4)
O2	8d	(x,y,z)	(0.7165(9), 0.2870(9), 0.0394(9))

NNO in the $P2_1/c$ phase (at 50 K)

a = 5.37783(5), b = 5.38846(4), c = 7.60511(6) Å, β = 90.061(1)°			
Atom	Wyckoff Position	Representative	Experimental Values (Å)
Nd	4c	(x,y,z)	(0.99321(1), 0.03910(7), 0.2495(3))
Ni1	2d	(1/2,0,0)	(1/2, 0, 0)
Ni2	2c	(1/2,0,1/2)	(1/2, 0, 1/2)
O1	4e	(x,y,z)	(0.0752(17), 0.4866(9),0.2521(29))
O2a	4e	(x,y,z)	(0.7143(29), 0.2762(29), 0.0267(16))
O2b	4e	(x,y,z)	(0.2187(26), 0.2036(29), 0.9470(17))

Table 8.1 – Tables listing the unit cell parameters and Wyckoff positions of the atoms for the $Pbnm$ and $P2_1/n$ phase of NNO (Extracted from Garcia-Muñoz *et al.*[102]).

Most of the 24 modes show variations of their frequency and vibration patterns across the MIT transition. In 2001 Zaghrioui *et al.* [104] published an extensive investigation of the Raman mode peak around the MIT of NNO. All reference of the mode will be given by their initial frequency observed at the lowest measured temperature:

- The modes at 150, 200, 250, 400, 490 cm^{-1} show little variations across the transition. The variation of the peak positions follow approcimately the temperature driven unit cell expansion.
- The behaviour of the modes at 300 and 315 cm^{-1} is discussed in the litterature. Zaghrioui *et al.* [104] argued with a splitting of a degenerate Raman mode, yet the data published by Girardot *et al.* [56] in Figure 8.1.**b.** does not suggest a split *per se*. Besides, the Raman modes in $Pbnm$ are not degenerate and cannot split strictly speaking. Further investigations are necessary to understand the variations in this region.
- The modes at 490 and 625 showcase an abrupt shift in the position across the transition.
- The modes at 60 and 460 cm^{-1} vanish as NNO enters the metallic phase.

The detailed investigation of thin NNO films deposited epitaxially on $LaAlO_3$ along $[001]_{pc}$ by Girardot *et al.* [56] reveals similar signature changes at the transition. The extracted spectra between 90 and 290 K are displayed in Figure 8.1.**b.**. The signature for orthorhombic *Pbnm* and monoclinic $P2_1/n$ configurations are the ones above and below 160 K respectively.

In summary, three distinct regions can be perceived as interesting for Raman spectra of NNO. The first one is situated in the vicinity of 250 cm^{-1} closely followed by the second one around 300 cm^{-1}. Both present the least amount of Raman modes, thus, rendering them more accessible for the following interpretation. The third region, located between 400 and 500 cm^{-1} contains the majority of the spectral signatures. Unfortunately, the amount of closely packed Raman mode does not guarantee a stable fitting nor identification, let alone understanding of their behaviour.

8.3 Identifying the modes of NNO

The strong variations in the signature through the MIT of NNO led us to believe that a clearer assignment of the phonon and their vibration patterns is required. To this effect Dr. H. Zhao and Dr. J. Íñiguez performed first principal calculation of the structure and phonons by using the VASP code [105, 106], based on the projected augmented wave (PAW) method [107]. This included the employment of generalised gradient approximation (PBEsol functional) [108] with a effective Hubbard U correction [109] of 2.0 eV for Ni. The following electrons were included to solve the structure: the Nd $5s^2\ 5p^6\ 5d^1\ 6s^2$, the Ni $3p^6\ 3d^9\ 4s^1$ and the O $2s^2\ 2p^4$ electrons. The

$4f$ electrons of the Nd atom were frozen as core electrons during the simulations. The electronic wave functions is presented in a plane wave basis, with an energy cut off at 500 eV. During the simulations, a 20-atom cell is considered represented as a $\sqrt{2} \cdot \sqrt{2} \cdot 2$ multiple of the 5-atom perovskite unit cell, with a $6 \cdot 6 \cdot 4$ k-point mesh grid for the reciprocal space integrals. The full structural relaxations is carried out with a force convergence criteria of 0.005 eV/Å. It is after the structural calculations that the zone-centre (Γ) phonons are computed through finite differences.

It was found that the calculated Raman active modes above 170 cm^{-1} expresses vibrations involving only the oxygen octahedra. This is why the representation of the vibration patterns in Figure 8.2 does not include vibrations linked to the Nd atoms. The modes involving solely the oxygen octahedra for $NdNiO_3$ in the $Pbnm$ metallic paramagnetic (top) and $P2_1/n$ antiferromagnetic insulating phase (bottom) are shown in Figure 8.2. Similar modes in both phases were referenced with the same letter to allow for an easier identification. These are also identified in Table 8.2.

ID	Octahedral Mode Description	Rotation axis (if rotation)	Frequency $Pbnm$	Frequency $P2_1/n$
a	Anti-phase rotation	$[001]_{pc}$ ($[001]_{orth}$)	180 cm^{-1}	200 cm^{-1}
b	In phase rotation	$[110]_{pc}$ ($[100]_{orth}$)	196 cm^{-1}	223 cm^{-1}
c	In phase rotation	$[001]_{pc}$ ($[001]_{orth}$)	215 cm^{-1}	228 cm^{-1}
d	In phase rotation	$[110]_{pc}$ ($[100]_{orth}$)	252 cm^{-1}	-
e	In anti-phase rotation	$[111]_{pc}$ ($[101]_{orth}$)	307 cm^{-1}	-
f	Octahedral breathing mode	-	600 cm^{-1}	281 cm^{-1}

Table 8.2 – Table summarising the calculated octahedral modes of interest in the $Pbnm$ and $P2_1/n$ phases of NNO.

A *very* surprising observation within this phase transition is the shift of the octahedral breathing mode by over 300 cm^{-1}. It is observed in Figure 8.2, that despite the symmetry lowering from $Pbnm$ to $P2_1/n$, the vibration mode characters are essentially preserved. This investigation also justifies why no reference to the terminology of mode splitting between the metallic and the insulating regime is used. We simply observe the disappearance of some phonon vibrations and the appearance of others. A particular effort was done to identify modes involving rotation of the oxygen octahedra (tilt modes).

The phonons of most interest in the current investigation, located at 252 and 307 cm^{-1} in the metallic phase have been, with the help of the presented calculations, identified as two rotational modes of the oxygen octahedra.

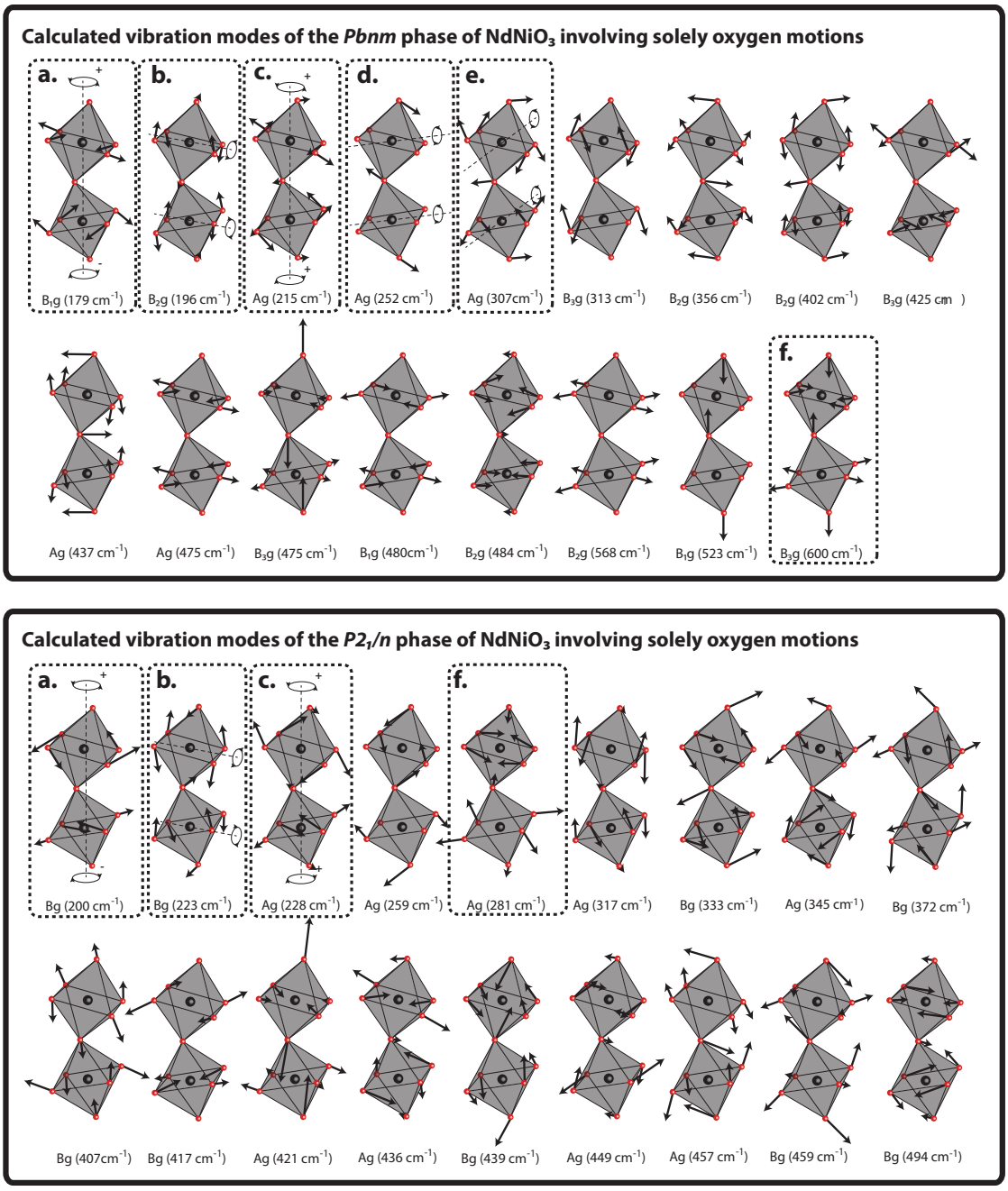

Figure 8.2 – Calculated vibrations modes of the oxygen octahedra for $NdNiO_3$ in the $Pbnm$ metallic paramagnetic (top) and $P2_1/n$ antiferromagnetic insulating phase (bottom). Modes with strong similarities related to the rotation or breathing of the oxygen octahedra have been marked with similar letters.

8.4 Raman signature of NGO $[111]_{pc}$

Neodymium gallate ($NdGaO_3$ or NGO) is the perovskite used as a substrate in the present investigation. Like NNO, it crystallises into the $Pbnm$ space group at room temperature. As the same Wyckoff positions are occupied, the same number of 24 Raman active vibration modes are obtained. These are located at different vibrational energies than for NNO. The modes of NGO measured through Raman spectroscopy along the $[111]_{pc}$ orientation, in the spectral range explored within the current investigation are displayed in Figure 8.3. The mode assignment has been done based on the work of Suda *et al.* [110]. The A_g tilt mode located at 336 cm^{-1} has a vibrational pattern equivalent to the NNO mode at 307 cm^{-1} in the $Pbnm$ phase. It would, therefore be interesting to follow the behaviour of these equivalent modes.

The complexity of this spectrum in addition to the signature of NNO displayed in Figure 8.1 renders this investigation challenging. Fortunately, no phase transition has been reported in NGO within the temperature range explored within the present investigation [111]. This means that only the thermal expansion of the unit cell volume should be observed within the variations of the Raman signature with the temperature.

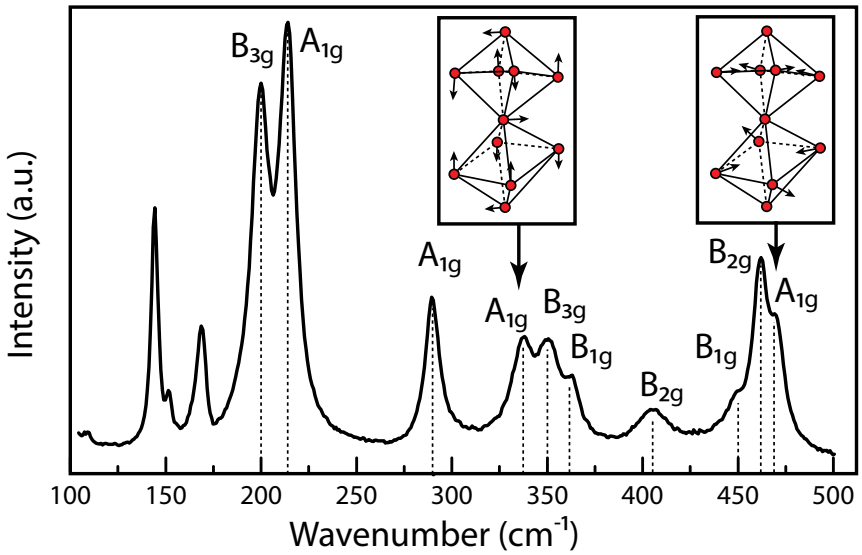

Figure 8.3 – Spectra of NGO measured through Raman spectroscopy along the $[111]_{pc}$ orientation. Mode assignment according to Suda *et al.* [110]. Identification of a tilt mode at 336 cm^{-1} and an in phase stretching mode at 471 cm^{-1}.

8.5 Investigating Raman depth profiles by NMF

The Raman signature of thin NNO films epitaxially deposited on $[111]_{pc}$ oriented NGO is expected to be very complex. This can be *guessed* through the superposition of the individual signatures of NNO and NGO, resulting in a strong overlap of their features. In fact, only one mode of NNO, located at 250 cm^{-1}, is found to not overlap. Therefore, the clear separation of the modes belonging to the NNO film from the modes belonging to the NGO substrate is a real challenge.

We therefore propose to use a depth profile measurement analysed through the Non Negative Matrix Factorisation (NMF) method introduced in Chapter 6.3.4. The contour map representation of the depth profile acquisition used within this investigation is shown in Figure 8.4. Using the NMF with an initial set of three randomly generated components led to the fitted result presented in Figure 8.4.**b.** with the associated scores in **c.**. In this case, the NMF performed an accurate separation of the film and substrate components, as can be seen by the absence of any features of the substrate within the sample component (the inverse statement being also true). The necessity of allowing two components to fully describe the NGO contribution with the depth constitutes an interesting artefact. The sole difference between the two signatures concerns two A_g modes located respectively at 336 and 471 cm^{-1} previously identified in Figure 8.3. The associated scores suggest a suppression of these modes at the interface with NNO, which could also be linked to the extraordinary increase of the MIT temperature of NNO, which motivated this work (Section 8.1).

The Raman depth profile acquisition was performed at ambient temperature ($\approx$295 K), meaning that, according to the work performed by Catalano *et al.* [55], the film should be in its insulating phase. The fit of the sample component can be visualised in Figure 8.5. It captures some features that were not observed by Zaghrioui *et al.* [104]. According to their work a strong signature change should be observed in the vicinity of 300 cm^{-1} as we transit from the metallic to the insulating state. This is observed in the computed film component but seems to be more complex than reported in the literature. The single mode of the metallic phase is replaced by three distinct Raman modes. The presence of the third contribution is justified by the inability to fit the component accurately with only two lorentzians. Another essential peak is clearly visible at 250 cm^{-1}. It is accompanied by neighbouring mode located at 240 cm^{-1}, which can barely be seen in the investigation by Zaghrioui *et al.* [104] and is not mentioned at all by Girardot *et al.* [56].

Unfortunately, it is impossible for us to perform depth profiles measurements while the sample is located inside the cryostat, as the associated optics do not provide a sufficiently high numerical aperture. This is why the present investigation relies on the identification of the Raman modes of NNO deposited on NGO along the $[111]_{pc}$ orientation at the room temperature. This lays the ground work for the following temperature investigation by allowing to fit the temperature dependant spectra in the most accurate manner.

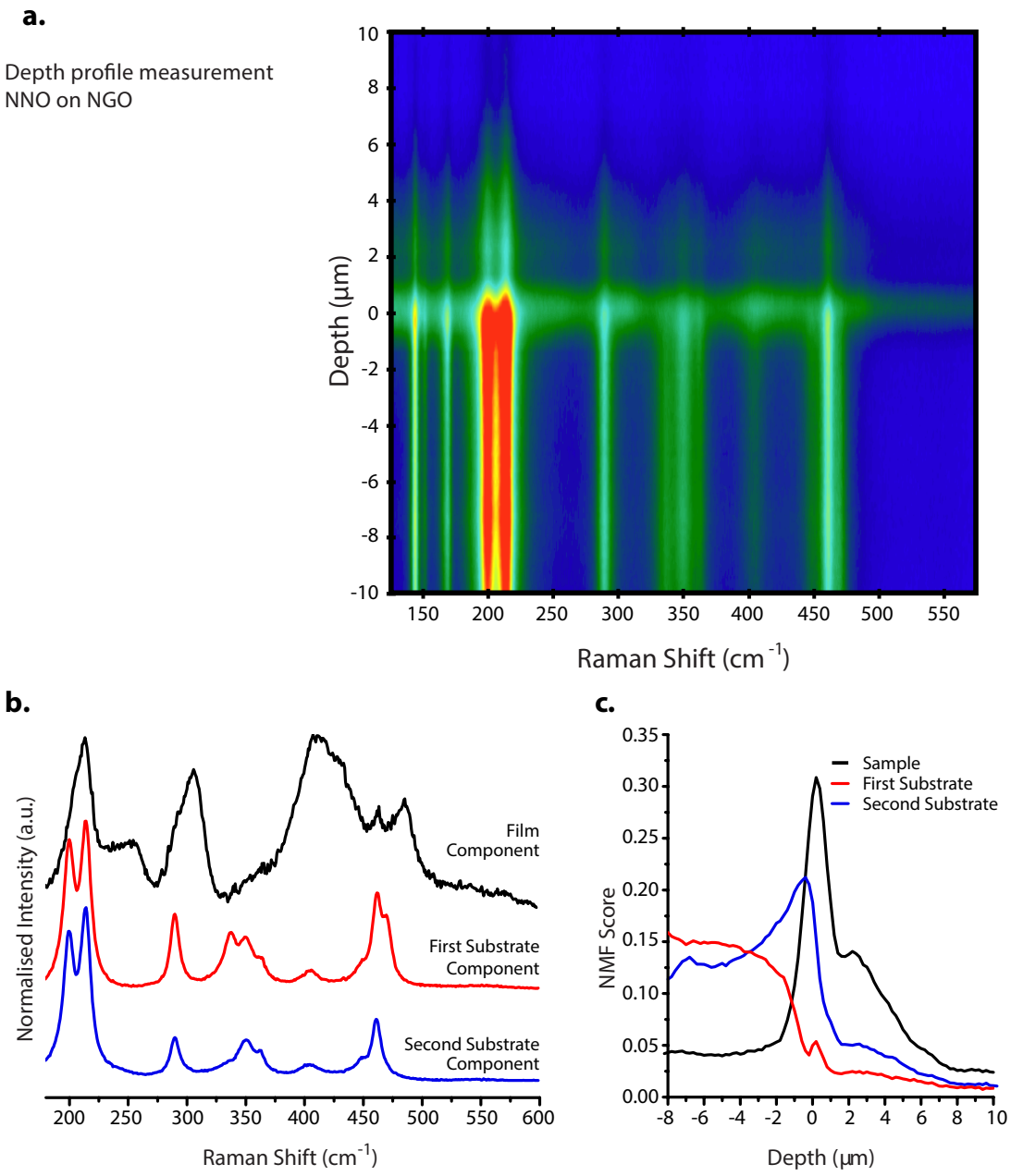

Figure 8.4 – a. Depth profile intensity map of NNO deposited epitaxially on NGO along the $[111]_{pc}$ orientation. Many modes are visible in this configuration already. **b.** NMF components for three allowed computation vectors on the depth measurement shown in **a.**. **c.** Associated component scores.

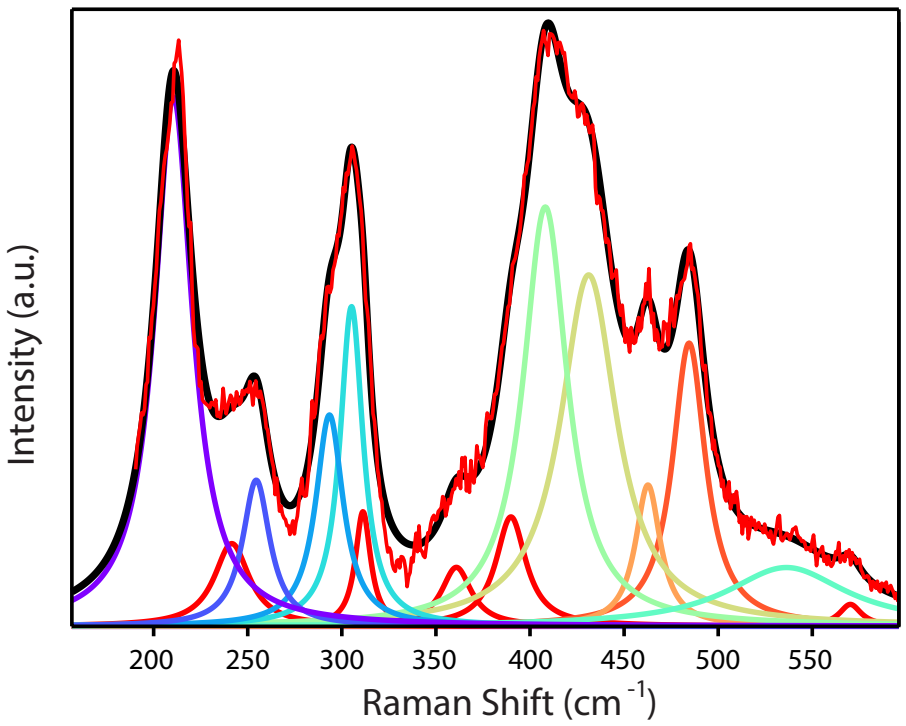

Figure 8.5 – Fit of the previously introduced NNO film components obtained through the NMF analysis of the Raman depth profile measurement shown in Figure 8.4.

8.6 NNO: Raman Temperature investigation

8.6.1 Acquisition

All temperature measurements were performed with the Renishaw InVia Raman spectrometer described in Chapter 3.4 with a monochromatic laser radiation of 633 nm, a grating of 2400 cm^{-1} and a 50x magnifying long working distance objective at a power of 0.9 mW (10% filter). A Linkam cryostat stage cooled through liquid Nitrogen was used for temperatures down to 90 K, while a liquid helium cooled cryostat from oxford instruments allowed temperatures as low as 5 K. The measurement was performed in a classical backscattering geometry along the $[111]_{pc}$ pseudo-cubic, corresponding to the $[101]_{ortho}$ orthogonal, crystallographic axis. The measurements were taken with a 10 K interval without changing the orientation of the sample. The acquisition was of 30 x 60 s per temperature. A cascade representation of the obtained raw Raman dataset is shown in Figure 8.1.**a.**

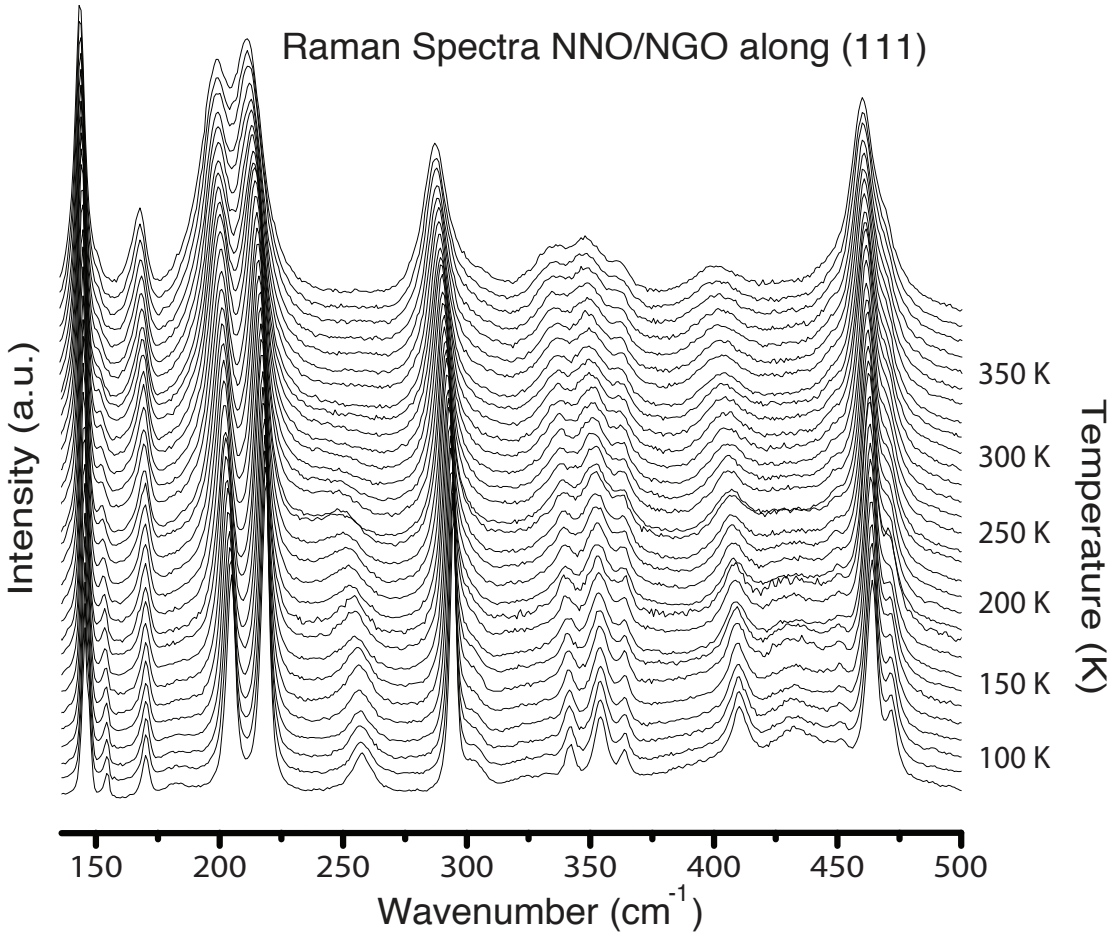

Figure 8.6 – Data obtained from a Raman temperature series from 90 to 390 K of NNO epitaxially deposited on NGO along the $[111]_{pc}$ orientation.

8.6.2 Fit of the temperature series

All temperature dependent acquisitions were fitted using the software presented in Chapter 6.5, developed during the PhD, allowing the direct visualisation of all parameters. The baseline was limited to a constant offset. The rest of the signature required 30 distinct lorentzian lineshapes, resulting in a total of $30 \cdot 3 + 1 = 91$ distinct parameters. In order to increase the reliability of the fit, some parameters were constrained to physically reasonable behaviours. In particular, given that the substrate does not undergo any anomaly or phase transition, its peaks were constrained to follow a linear temperature evolution, both in their position and width. The initial positions of NNO were taken from the initial depth investigation at room temperature in section 8.5. The fits can be seen in Figure 8.7.

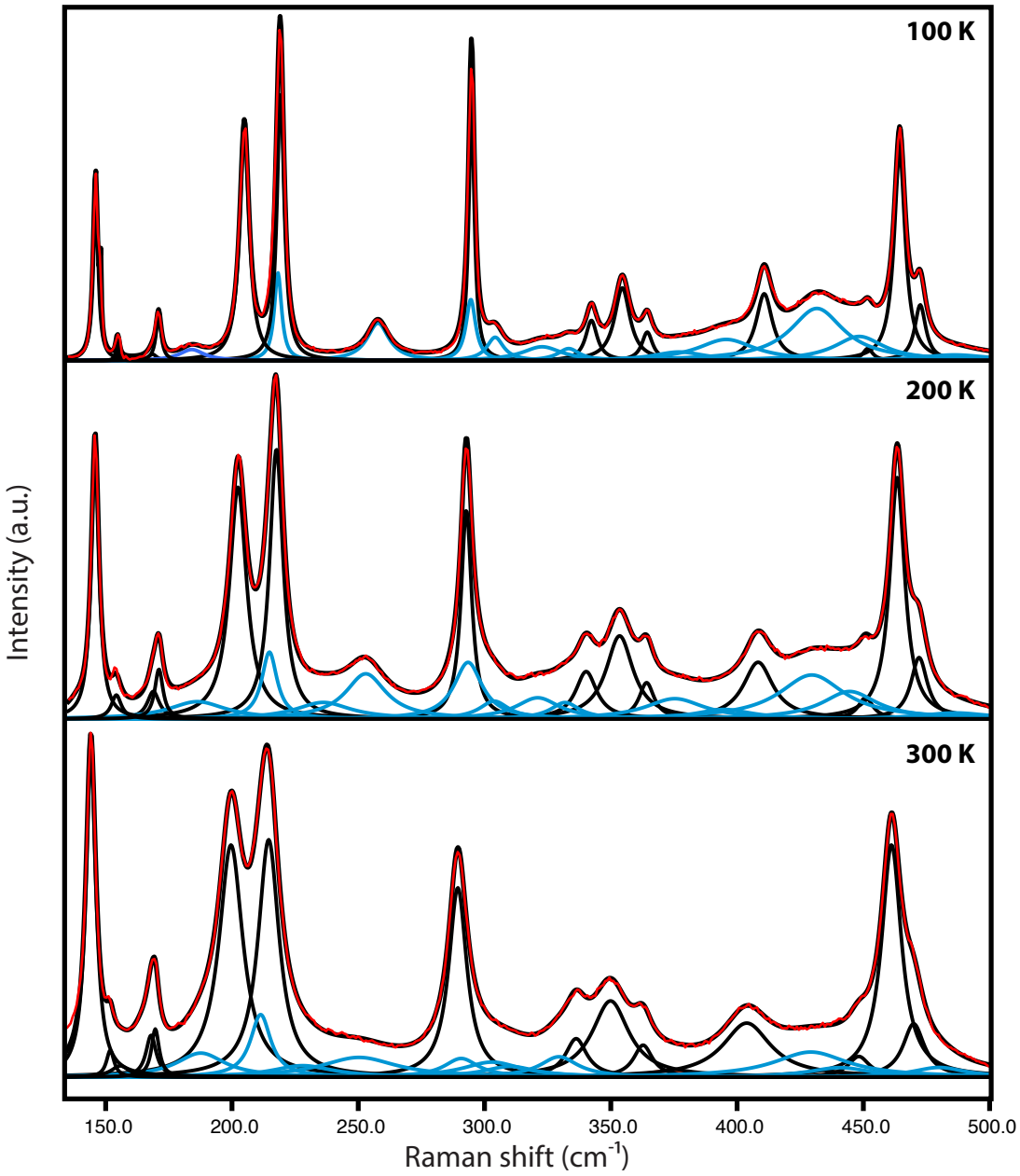

Figure 8.7 – Fit example of a spectra from NNO deposited epitaxially along the $[111]_{pc}$ orientation of NGO at 100, 200, 300 K. The blue lineshapes represent identified sample modes, while the black one correspond to substrate contributions.

8.6.3 Description of the Temperature evolution

Figure 8.8.**b.** showcases the modes that were followed in the present investigation of NNO on NGO along the $[111]_{pc}$ direction. A brief identification of the modes relates them to the already published modes by Zaghrioui *et al.* [104] in Figure 8.8.**a.**. A case by case comparison is drawn in the following part:

- **Mode (a) at 218 cm^{-1} (at 5 K)**: This corresponds to an in-phase rotational vibration of the oxygen octahedra along the $[001]_{pc}$ ($[001]_{orth}$) direction. This mode has been particularly complicated to identify due to its proximity to the the strong substrate peaks. The NMF allowed to assure its presence and comprehensive fitting determined its evolution. It follows the same type of variation change around the transition as reported by Zaghrioui *et al.* [104].
- **Mode (b) at 258 cm^{-1} (at 5 K)**: This corresponds to an in phase rotational vibration of the oxygen octahedra along the $[110]_{pc}$ ($[100]_{orth}$) direction. This mode has been shown to undergo a drastic change in position as the metal to insulator transition occurs both by Zaghrioui *et al.* [104] and Girardot *et al.* in 2008 [56]. The present case shows the same characteristic but for the width of the variation.
- **Mode (d) at 305 cm^{-1} (at 5 K)**: This corresponds to an in anti-phase rotational vibration of the oxygen octahedra along the $[111]_{pc}$ ($[101]_{orth}$) direction. The study performed by Zaghrioui *et al.* [104], with a rather low statistic, already reported the splitting of this mode as the structure goes from $Pbnm$ to $P2_1/n$. This was interpreted as the differentiation of the oxygen octahedra inducing two distinct modes in the monoclinic $P2_1/n$ phase. The data acquired by Girardot *et al.* in 2008 [56] related to NNO deposited on $LaAlO_3$ also reported the apparition of two new bands at 300 and 330 cm^{-1} when reaching the monoclinic $P2_1/n$ phase.

  Similarly to these measurements, the present investigation shows variations in the rotational mode accompanied by the appearance of another signature around 290 cm^{-1}. With the help of the calculations (Section 8.3) we could establish, that the mode appearing next to the rotational mode is an octahedral breathing mode. It was calculated the same vibration mode should be found around 600 cm^{-1} in the $Pbnm$ phase.

In summary, the identified modes of NNO emphasising, that the transition is indeed between the two phases of NNO, namely $Pbnm$ and $P2_1/n$. A correction of the interpretation of the behaviour around 300 cm^{-1} is necessary in respect to the literature.

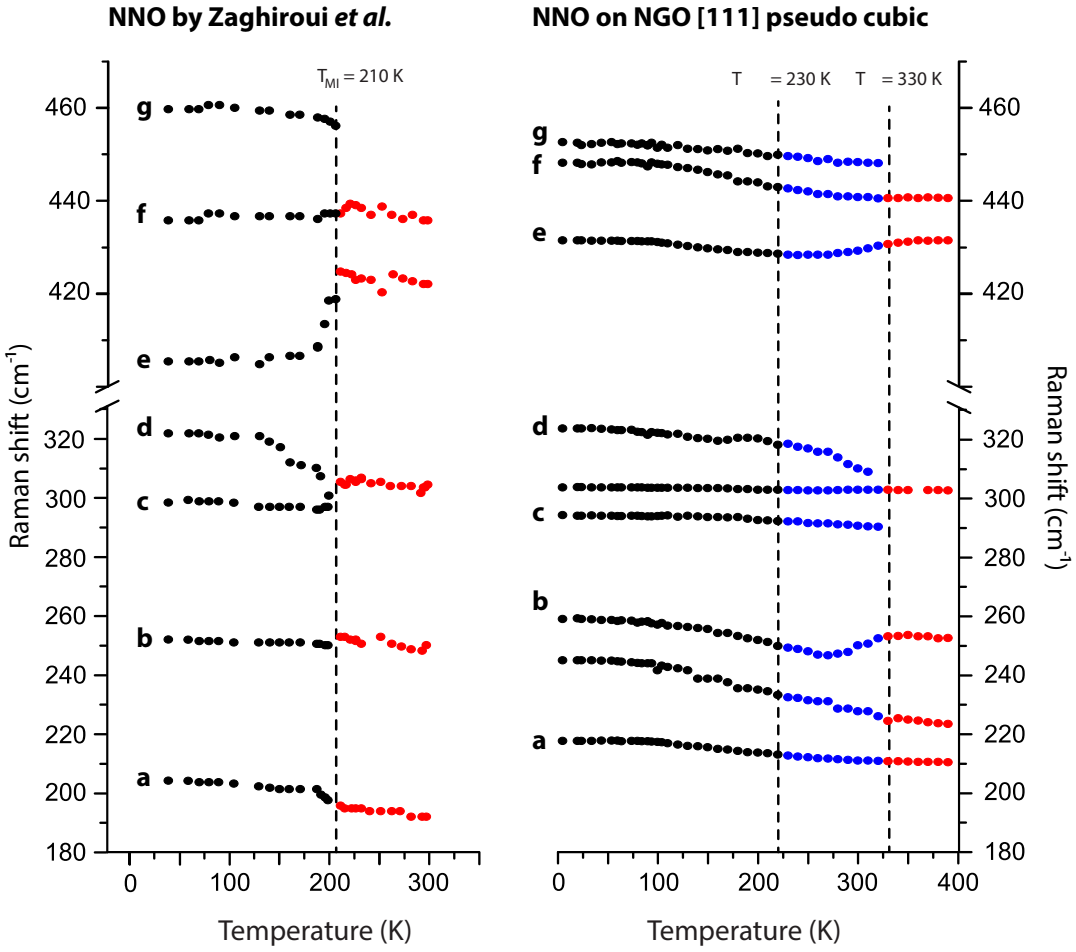

Figure 8.8 – a. Data reproduced from Zaghrioui *et al.* [104] showing the variation of NNO Raman peaks through the meta to insulator transition. **b.** Position from the fit of NNO deposited along the $[111]_{pc}$ direction of NGO (Figure 8.1.**b.**)

8.7 $SmNiO_3$ across the MIT

In the NNO films deposited on NGO along the $[111]_{pc}$ orientation are placed into the phase diagram, as proposed by Catalano *et al.* [55], they end up in close proximity with $SmNiO_3$ (SNO). In the following, we want to evaluate whether this proximity holds also up from a structural point of view. This consists in comparing their Raman signature changes across the MIT transition. Prior to this, a brief introduction of SNO and its Raman signature is necessary.

$SmNiO_3$ (SNO) is the first nickelate compound of the series where the MIT and Néel transitions occur at distinct temperatures. It undergoes the same structural transition from $Pbnm$ in the metallic to $P2_1/n$ in the insulating phase as the other nickelates. This results in 24 Raman active modes, as introduced for NNO. The Raman spectra of SNO on LAO extracted from an investigation by Girardot *et al.* [56] is presented in Figure 8.9.**a.**. To ensure a certain consistency between the data treatments, the raw data was refitted (like in section 8.6.2). The obtained peak positions are shown in Figure 8.9.**b.**.

The improved fitting allows to explore a region above 400 cm^{-1} which is much richer in Raman modes than previously reported. The region below 350 cm^{-1} shows similarities with the trends reported by the literature. The three modes, involving the tilting or breathing of the oxygen octahedra are well defined, allowing us to compare them with the one of NNO (previously investigated in Section 8.2):

- The mode located in the vicinity of 270 cm^{-1} (97 K) corresponds to the rotational mode equivalent to the mode 250 cm^{-1} of NNO.
- The mode located in the vicinity of 320 cm^{-1} (97 K) corresponds to the breathing mode equivalent to the mode 295 cm^{-1} of NNO.
- The mode located in the vicinity of 340 cm^{-1} (97 K) corresponds to the stretching mode equivalent to the mode 307 cm^{-1} of NNO.

All of the modes of SNO seem shifted towards higher wavenumber compared to their counterparts in NNO. Having identified these modes and the counterparts in NNO it is now possible to do a comparison study of their evolution through the MIT. The next section will treat the octahedra rotation modes of NNO on LAO, NNO on NGO followed by SNO on LAO. This will then be followed by an investigation of the breathing and stretching modes.

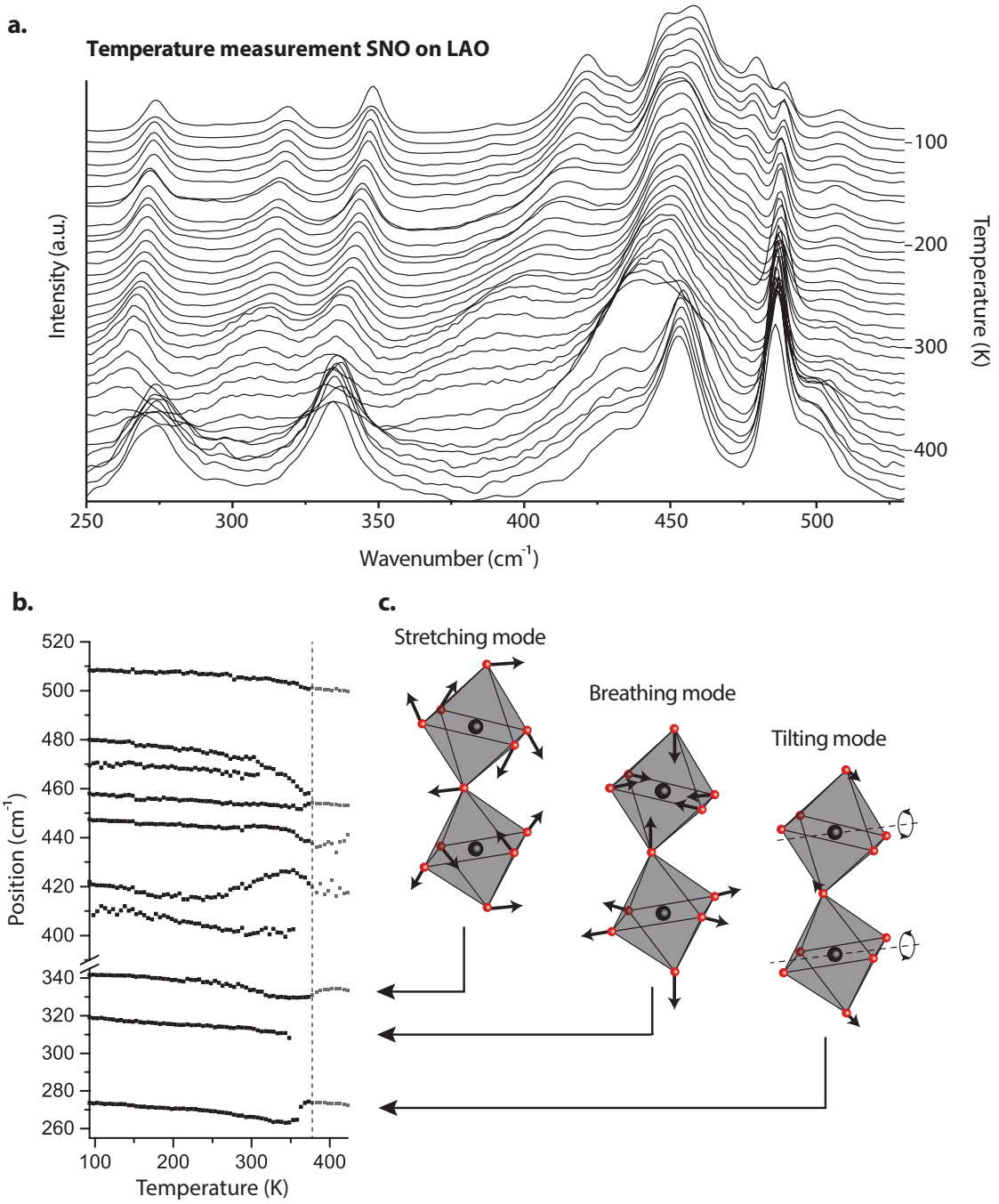

Figure 8.9 – a. Raman spectra of SNO on LAO extracted from the work of Girardot *et. al.* for a temperature range from 93 to 423 K [56]. **b.** Fit result for the data displayed in **a.**. **c.** Modes assigned to the region below 350 cm^{-1}.

8.8 Comparing NNO and SNO

In order to confirm the position of NNO on $NGO_{[111]}$ in the phase diagram we will compare its signature to the nearest neighbours, namely SNO and NNO on LAO. The three modes of NNO that will be compared have been identified for SNO in the previous section (Figure 8.9.**c.**).

The evolution of the tilt modes is displayed in Figure 8.10.**a.** through **c.** for NNO on LAO [56], NNO on NGO and SNO on LAO [56], respectively. All three cases show a characteristic behaviour in the region of the MIT, namely an upwards shift of the frequency. The magnitude of the shift seems to be different depending on the compound. It is 4 cm^{-1} for NNO on LAO, 7 cm^{-1} for NNO on $NGO_{[111]}$ and 10 cm^{-1} for SNO on LAO. The abruptness of the change seems to also vary from sample to sample. While NNO and SNO on LAO seem to have a very abrupt transition with a ΔT of about 28 and 35 K, NNO on $NGO_{[111]}$ shows a larger intermediate regime of about 50 K.

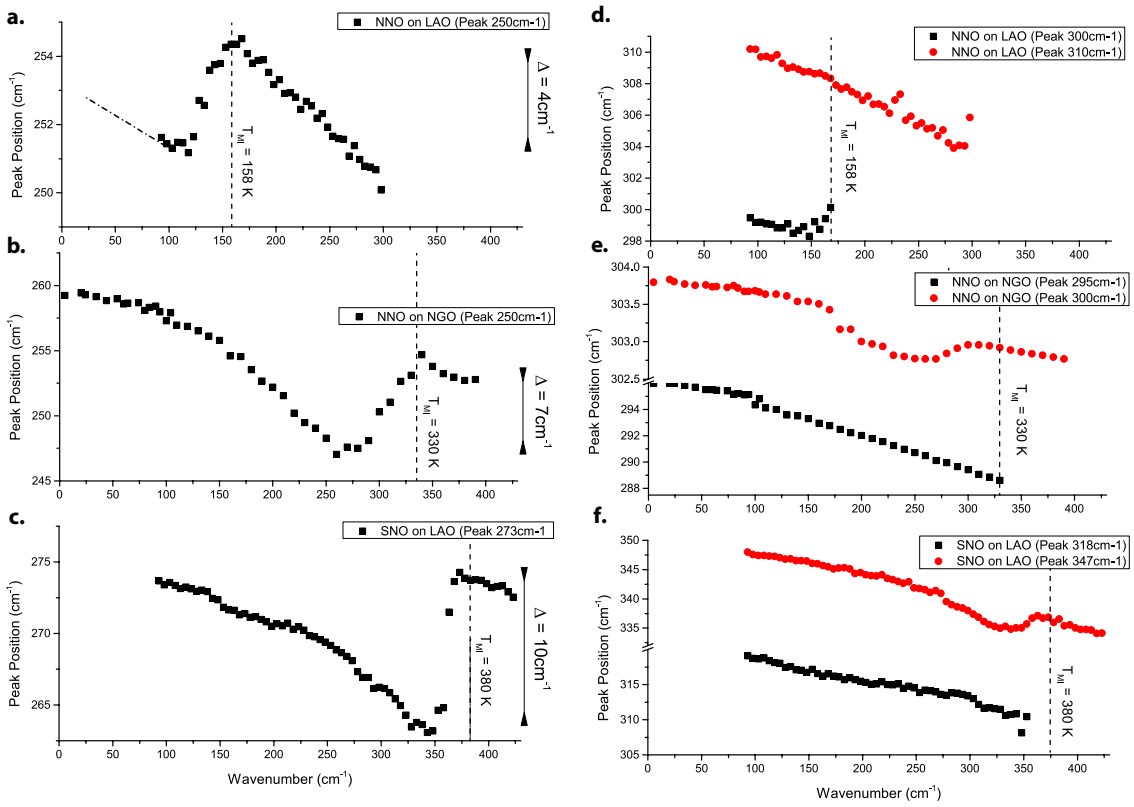

Figure 8.10 – a. - c. Evolution of the tilt mode is displayed for NNO on LAO [56], NNO on NGO and SNO on LAO [56] respectively. **d. - f.** Evolution of the oxygen breathing and distortion modes for NNO on LAO [56], NNO on NGO and SNO on LAO [56] respectively.

Furthermore, Figure 8.10.**a.** through **c.** report the disappearance of the octahedral breathing mode of the $P2_1/n$ phase as the compounds enter the metallic $Pbnm$ phase. This could be the most striking observation allowing to identify the transition from $P2_1/n$ to $Pbnm$. Within the same figures, the evolution of the mode associated to a tilting of the oxygen octahedra along the $[111]_{pc}$ is presented. Little resemblance between the NNO deposited on NGO and NNO deposited on LAO can be drawn. On the other hand, a very strong resemblance of the signature can seen between NNO on NGO and SNO on LAO.

8.9 Conclusion on NNO on NGO

The previous report of NNO thin films epitaxially deposited along the $[111]_{pc}$ of NGO performed by Catalano *et al.* [55], investigated the resistive and magnetic behaviour to pinpoint the respective MIT and Néel transition temperatures. The increased MIT temperature now located at 330 K was argued to be close to the transition of $SmNiO_3$ at 380 K, thus justifying their close proximity in the updated phase diagram. It was, within the same work, suggested that in the present arrangement, NNO should adopt structural characteristics similar to SNO. Unfortunately, at the time, no structural investigation was proposed to strengthen this claim.

In the present chapter have added the necessary structural analysis of the sample using Raman spectroscopy under temperature. This included a depth profile measurement at ambient temperature combined with a Non-Negative Matrix Analysis (NMF) to distinguish the contributions from the NNO film from the ones of the NGO substrate. A calculation of the modes in both the metallic $Pbnm$ and insulating $P2_1/n$ phases allowed a clear identification of the Raman features of NNO across the MIT. Another, already published, dataset of SNO on LAO was refitted and compared with the investigated sample across the MIT transition. Very strong similarities were observed, thus suggesting that the structures are comparable.

This structural investigation further justifies the position in the phase diagram attributed to NNO thin films epitaxially deposited along the $[111]_{pc}$ of NGO. Using the solid solution investigation introduced in Chapter 2.6.1 it is possible to draw a tendency lines for the MIT transition temperature depending on these two parameters. It is then possible to place NNO on LAO [56], NNO on NGO along the $[111]_{pc}$ and SNO on LAO [56] with the obtained and verified MIT temperatures. The result is shown in Figure 8.11.

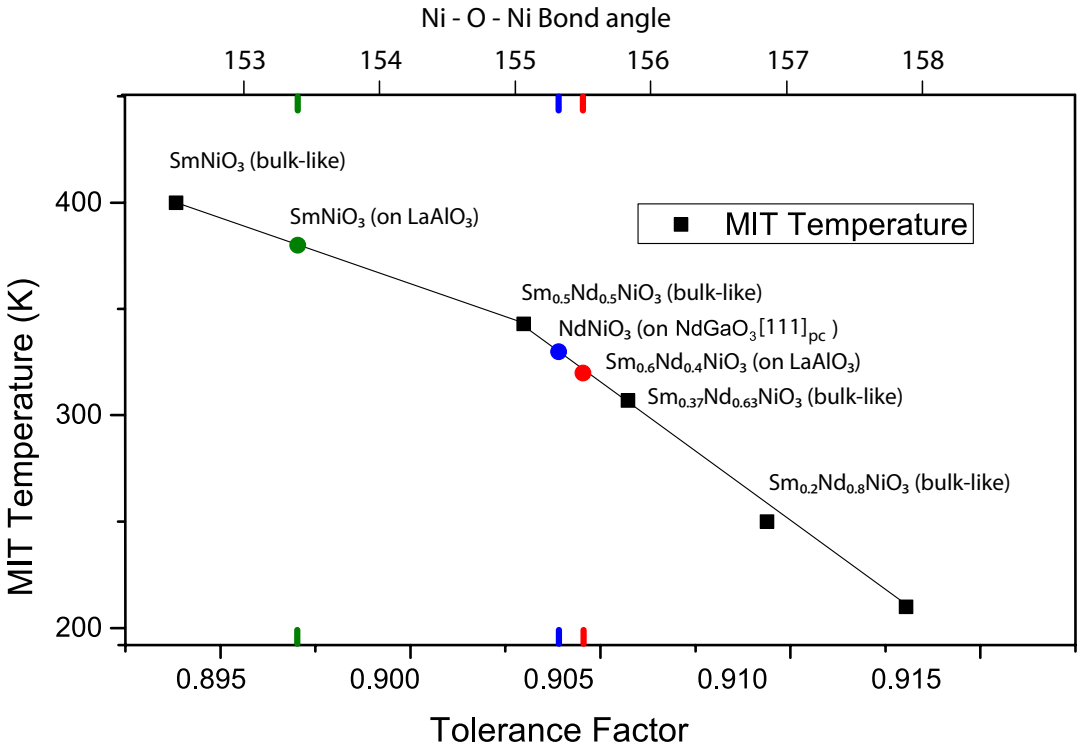

Figure 8.11 – Phase diagram of the nickelates between $SmNiO_3$ and $NdNiO_3$ with the added transition temperatures of the solid solutions and the epitaxial samples investigated in this chapter.

Part V

Conclusion

Summary

In this work, we have presented results on the structural properties of ultrathin rare-earth nickelate films by Raman Spectroscopy. Our results contribute to the general development of the advanced experimental methods needed to investigate size and interface effects in functional oxides, which are increasingly relevant, both for their fundamental understanding and their application potential.

The extremely small size of the films were an experimental challenge, and has required the development of specific measurement and analysis strategies. This included the creation of a multidimensional dataset through depth profile acquisitions, in combination with multivariate analysis tools that were employed to extract the signature of the film (Chapter 6). Different analysis strategies had to be used in both selected cases, in order to adapt to the specificities of the samples. This ultimately gave access to the signature of ultrathin films down to 3_{pc} u.c. in LNO (Chapter 7) as well as the temperature dependence of the Raman modes in NNO(Chapter 8).

For the LNO films deposited along the $[001]_{pc}$ orientation of LAO, Raman depth profile measurements in combination with a Principal Component Analysis (PCA) was able to dissociate the signals from the film and the substrate (Chapter 7). The evolution of the LNO peaks does not suggest any phase transition, thus, suggesting that a mechanisms unrelated to the MIT of other nickelates is triggering the insulating state. This was further validated by *ab initio* calculations and TEM imaging. All acquired data point towards the following: as LNO becomes very thin, the surface layer ($\approx 2_{pc}$ u.c.), which is the most rigid part of the structure, imposes its structural and insulating characteristic. In the ultrathin regime this continues to a point where the surface of the film alters the interfacial unit cells of the substrate.

For the NNO films deposited along the $[111]_{pc}$ orientation of NGO, depth profile measurements in combination with a Non-negative Matrix Factorisation (NMF) enabled to dissociate the signals from the film and the substrate (Chapter 8). This was particularly challenging as most signature elements of NNO were superposed with the ones of NGO. The dissociation was therefore performed at room temperature. The acquired knowledge was then utilised to fit the entire temperature series from 5 to 390 K. This allowed to compare the behaviour of the Raman signature at the MIT with $SmNiO_3$ (SNO). This allowed to back the proposed position of the film in the phase diagram of nickelates by a structural measurement.

Continuation of this work can be envisioned at several levels.

An avenue opened by this work is the investigation of the *substrate*'s distortion at the interface by Raman spectroscopy. Indeed, in both LNO and NNO films, it was shown that some alteration of the substrate's spectrum could be measured. In LNO, DFT calculations also give indication for strong structural variations for the thinnest films. In NNO, it was suggested that the deposition along the $[111]_{pc}$ orientation affects the tilting modes of the NGO substrate, which might point to a suppression of these modes at the interface. These observations were unexpected and

could not be investigated further within the frame of this work, but they are promising results that should be validated and extended to other systems.

More generally, we expect this methodology to be useful for a much wider range of functional oxide thin films, perovskites or others, and we hope that this work will stimulate Raman studies on samples that are classically considered too challenging. An interesting continuation could also be the study of perovskite heterostructures such as layered superlattices using Raman depth profile measurements. This could allow the investigation of the dynamical behaviour such as motion of the oxygen octahedra and could add to the investigation of these materials.

Appendix A

Understanding and modelling the Raman acquisition process

A.1 Understanding the Raman apparatus

The Raman apparatus described in this section is schematised in Figure A.1. Note that this representation of the Raman optical system is inspired from Yutaka Maruyama and Wataru Kanematsu and described in *Confocal volume in laser Raman microscopy depth profiling* [78]. While the numerical values differ in terms of focal lengths, distances and lens radiuses, the same type setup can be used. Please note that the dimensions shown in Figure A.1 are only schematic.

The first step of setting up a model system is to define its referential. The commonly accepted representation is to have the a fixed optical system and a moving sample environment. The Raman collector lens (located in **II**) named L_1 is the first optical element located over the sample and is considered as the origin in z along the optical axis, such that $z_1 = 0$. The second lens (located in **IV**) named L_2 is placed at z_2, separated by a distance $D = z_2 - z_1$ from L_1. The Pinhole (located in **V**) called P is located at the focal position f_2 of L_2. The intrinsic parameters of each optical element are as follow:

- **Collector Lens L_1:** The collector lens is important as it processes the illumination and the collection. the optical system positions are all expressed in respect to this lens. Hence it's position $z_{L1} = 0$. The lens possesses a radius and a focal length denoted by r_{L1} and f_{L1} respectively. The proximation is a 0 extent confocal lens with no aberrations.
- **Pinhole Lens L_2:** The pinhole lens is located at a distance D from the first length with $z_{L2} = D$. In analogy to the collector lens it has a radius r_{L2} and a focal length f_{L2}.
- **Pinhole P:** The pinhole is located at the focal point after the pinhole lens at the position $z_P = D + f_{L2}$. Note that this optical element also has a radius r_P representing a cut-off parameter.
- **Sample(s) and Substrate(s) :** The sample(s) and substrate(s) will have three main attributes. Their thickness, their refractive index and their absorption coefficients. These are supposed fixed across the sample. Note that the refractive index determines the speed of light within the sample and therefore is relevant to do the geometric calculations. The index of each element will be denoted by n_i where i expresses the order. 0 representing the top most layer and increases for each element encountered until the substrate. In the same way the absorption coefficients and depth will be expressed by σ_i and d_i respectively. The sample position depends only on the stage position. When the focal point of L_1 is located exactly on at the interface to the top most sample. To process the illumination is a more convenient reference system we introduce $Z_0^{stage} = -f_{L1}$ which is the entered around the focal position of L_1.
- **Common parameters:** Some of the parameters belong to the entire system. This includes the illumination and acquisition wavelength denoted λ_{in} and λ_{out} respectively.

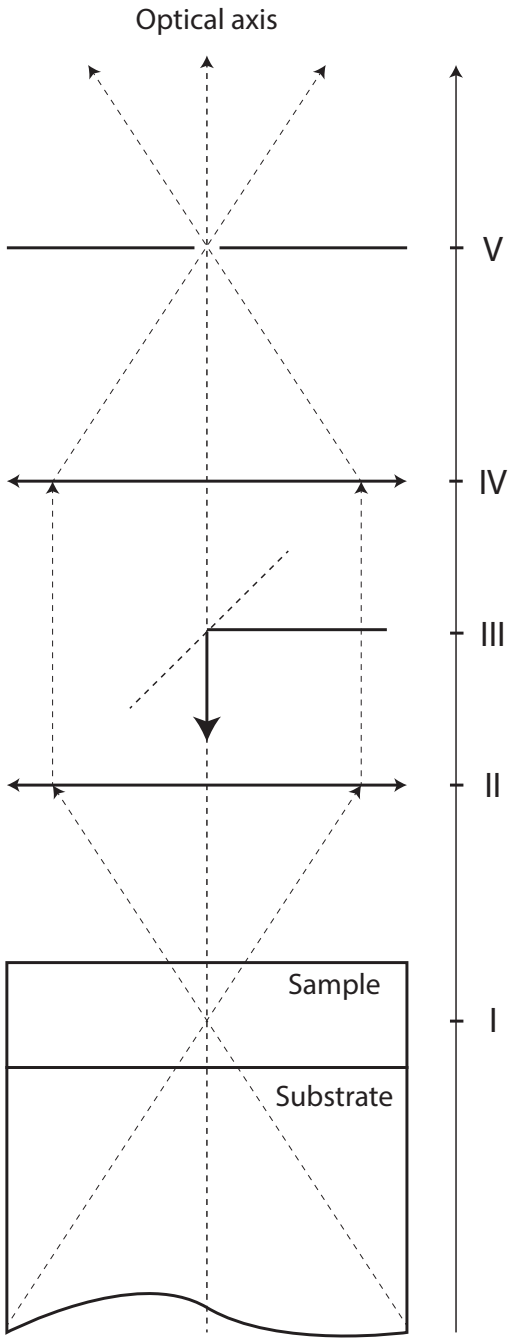

Figure A.1 – Schematic representation of the lens system of the Raman apparatus. The dimensions are not up to scale. Position **I** represents the focal point of the lens situated in **II**, while **V** represents the pinhole located at the focal point of the second lens in **IV**. In **III** is located the mirror directing the laser beam onto the first lens, effectively illuminating the sample.

Two parameters are particularly essential to the understanding of the materials and their respective interfaces. The refraction index will effectively influence the light behaviour such as the evolution of the shape from the monochromatic gaussian laser radiation. The absorption on the other hand will manage the signal attenuation for the inbound radiation and the emitted Raman response. It is noteworthy that both the refractive index $n_i(\lambda)$ and absorption coefficients $\sigma_i(\lambda)$ of a compound i are wavelength λ dependant. and need to be computed accordingly. To avoid overloading the expressions (λ) was dropped in all following equation.

The radius of each element acts as a acceptance filter, not letting light pass when the position on the element is outside the definition radius. Using these definitions of the optical elements we can process the illumination and acquisition.

A.2 Depth of field

As previously explained it was found that depth of field is the true limiting factor of the currently investigated method of Raman depth profiling. The depth of field is commonly related to a negative factor in microscopy that makes it difficult to image object that are not within the same plane. This becomes even more apparent when the magnification of the imaging objective is high. Scanning electron microscope for example have a very high depth of field, allowing for stunning imagining of objects with high magnifications (and not limited by the diffraction limit). Having a low depth of field is therefore often considered a limitation, unless the aim is to achieve the highest possible vertical resolution. This is the case of Raman depth profiling. The depth of field in the vicinity of the focal length is proportional to:

$$DOF \quad \propto \quad \frac{1+m}{m^2} \tag{A.2.1}$$

where m is the magnification. The exact equation takes also into account the circle of confusion and the focal-number. With this approximate formula alone it is possible to see that when m increases the depth of field decreases. The highest magnification objectives available are in the range of 100x. This is why high magnification objectives where used in all following depth measurements.

The need of high magnifying objectives means a low working distance, often in the range of a few hundred micrometers. This has been found to limit the applications other than the classical setup. In fact special objectives are used for temperature measurements with a much higher working distance allowing to accommodate for the temperature stage. The long focal distance objectives have been found to have a very large dept of field thus rendering the numerical interpretation of depth measurements challenging if not to say impossible.

A.3 Illumination processing

As shown in Figure A.1 computing the intensity at each point in the sample consists of processing a gaussian beam through a Lens (L_1 in our case) and then compute the refractions at the different interfaces between successive samples and substrates. the intensity at a given point (z,r) of a gaussian wave goes as follows:

$$I(z,r) = I_0 \cdot \left(\frac{w_0}{w(z)}\right)^2 \cdot \exp\left(\frac{-2r^2}{w(z)^2}\right), \tag{A.3.1}$$

$$w(z) = w_0 \cdot \sqrt{1+\left(\frac{(z-z_0)\lambda_{in}}{\pi w_0^2}\right)^2}, \tag{A.3.2}$$

where I_0 represents the initial gaussian intensity w_0 is the waist at $z = z_0$ and $w(z)$ is the waist at a given distance z. The coordinates are expressed in a cylindrical referential as we have a clear rotation symmetry around the optical axis. Inspired by the work of Yutaka Maruyama and Wataru Kanematsu [78], we place ourselves in the same optical arrangement leading to the following conditions:

- **Source distance to L_1** As the lens is far away in comparison with the focal length f_{L1} we can assume that the source is infinitely far away and that the intensity maximum is located at the focal point after the lens. But the beam keeps his gaussian properties regardless of the L_1, including its formulation and parametrisation.
- **The initial waist:** The gaussian beam's initial waist w_0 is an intrinsic property associated to the laser cavity and stays unchanged as long as the beam type is not altered.
- **Asymptotic divergence:** The asymptotic divergence on the other hand is affected by the refractive indices at the interfaces. The z_0 at which $w(z_0) = w_0$ is shifted by $(1 - n_i/n_{i+1}) \cdot \Delta$, where $\Delta = Z^{stage} - Z_0^{stage}$. This can be expressed as either a compression or decompression of the gaussian beam z extent.

Following this formalism each sample in the series sees a beam with the same initial waist w_0 but a different asymptotic divergence $w_i^{\Delta}(z)$ related to the shift in z_0, where i is the index of the sample and Δ the relative position of Z^{stage}. Rewriting $w_i^{\Delta}(z)$ to accommodate for the i interface results in:

$$w_i^{\Delta}(z) = w_0 \cdot \sqrt{1+\left(\frac{(z-\Gamma_i(\Delta)) \cdot \lambda_{in}}{\pi w_0^2 \cdot n_i}\right)^2}, \tag{A.3.3}$$

$$\Gamma_i(\Delta) = \Delta \cdot \prod_{l=0}^{i}\left(1-\frac{n_l}{n_{l-1}}\right) \tag{A.3.4}$$

It is important to note that the sum of equation A.3.4 goes only until i which is the index of the sample containing the position z. Using equation A.3.3 and A.3.4 as a substitute to A.3.2 in the gaussian formulation of equation A.3.1, gives us the accurate non absorbed refracted beam.

To investigate the absorptive properties of the beam through geometrical construction, the curvature radius in (z,r) of the gaussian beam is required. In each point z of the optical axis ($r=0$) the beam has a curvature radius defined by the Gaussian formulation:

$$R_i(r,z) = (z-\Gamma_i(\Delta)) \cdot \left[1+\left(\frac{\pi w_0^2}{(z-\Gamma_i(\Delta)) \cdot \lambda_{in}}\right)^2\right]. \tag{A.3.5}$$

The radius tends to infinity when z approaches $(z-\Gamma_i(\Delta))$ indicating a planar perimeter surface. With increasing z the second term on the right becomes negligible and the radius can be linearly approximated.

Unfortunately, this expression is valid for $r=0$. As soon as this condition is not met, a, effective position z_{eff} has to be computed and reinfected into equation A.3.5 that will effectively provide the exact radius at (z,r). Using the radius it is possible to compute the angle of incidence of the intensity in a point (r,z). If we write down the equations linking $z_i = (z-\Gamma_i(\Delta))$, r and z_{eff} we obtain:

$$\begin{aligned} R_i(z_{eff}) \cdot \sin(\theta_0) &= r & \text{(A.3.6)} \\ R_i(z_{eff}) \cdot \cos(\theta_0) &= (z_i + R_i(z_{eff}) - z_{eff}). & \text{(A.3.7)} \end{aligned}$$

Rewriting the first line of these equation to express θ_0 leads to :

$$\theta_0 = \text{asin}\left(\frac{r}{R_i(z_{eff})}\right). \tag{A.3.8}$$

If we now rewrite everything in terms of z_{eff}, we obtain the following equations:

$$\begin{aligned} R_i(z_{eff}) \cdot \cos\left[\text{asin}\left(\frac{r}{R_i(z_{eff})}\right)\right] &= (z_i + R_i(z_{eff}) - z_{eff}), \\ \left(z_{eff}+\frac{\gamma^2}{z_{eff}}\right) \cdot \cos\left[\text{asin}\left(\frac{r}{z_{eff}+\frac{\gamma^2}{z_{eff}}}\right)\right] &= z_i + \frac{\gamma^2}{z_{eff}}. \end{aligned} \tag{A.3.9}$$

At this point there is no need to solve this equation in an analytical way. Therefore fast approximations can be used to find z_{eff} iteratively. The parameters z_{eff} is of outmost importance as he allows us to find the radius of curvature of the point (z,r) and then find the angle θ_0 of defining the normal vector to the propagations surface of the intensity. This ange will be used to process the ray path and determine the absorption coefficient applied to the light in (z,r).

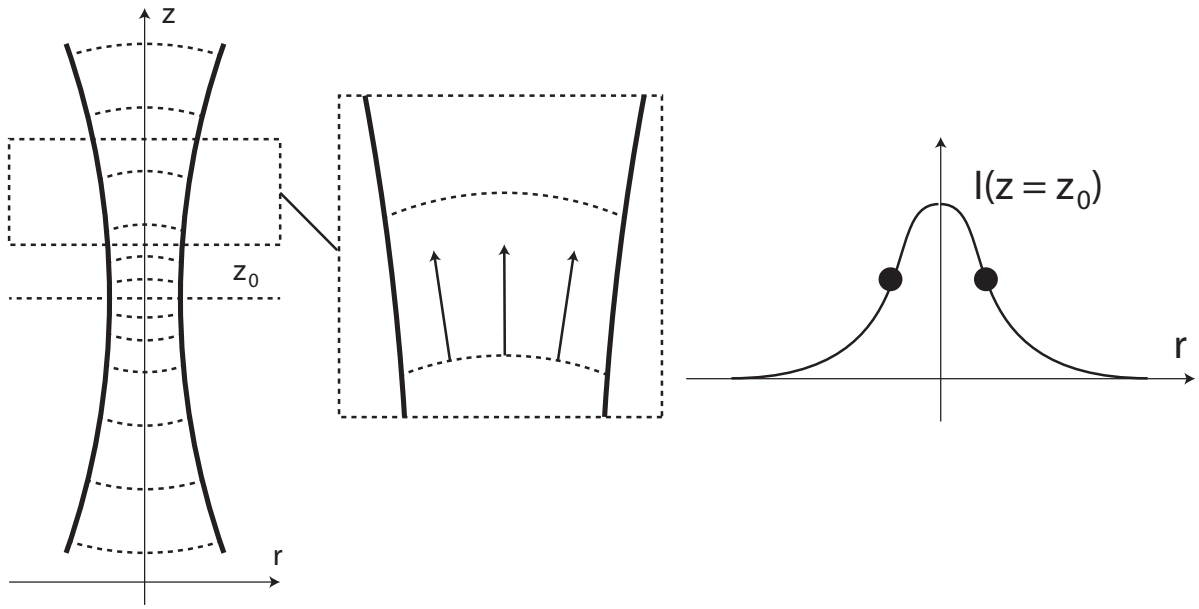

Figure A.2 – Schematic representation of the lens system of the Raman apparatus. The dimensions are not up to scale. Position **I** represents the focal point of the lens situated in **II**, while **V** represents the pinhole located at the focal point of the second lens in **IV**. In **III** is located the mirror directing the laser beam onto the first lens, effectively illuminating the sample.

The path traveled l_i in each layer i of the sample substrate arrangement is necessary to process the linear absorption σ_i. The total absorption coefficient at a point (z,r) is therefore:

$$\Sigma(z_i,r) = \sum_{k=0}^{i} \sigma_k \cdot l_k, \tag{A.3.10}$$

with the final Intensity $I(z,r)$ expressed through the non absorbed intensity $I_0(z,r)$ as follows:

$$I(z_i,r) = I_0(z_i,r) \cdot 10^{-\Sigma(z_i,r)}. \tag{A.3.11}$$

The angle θ_i respective to the normal vector to the interface plane, follows the simple refraction laws:

$$n_k \sin(\theta_k) = n_{k-1} \sin(\theta_{k-1}). \tag{A.3.12}$$

As this relation does in no circumstance involve the distance traveled and simply expresses the angles, and this relation is true between all interfaces, it is possible to express any term in function of the first one, leading to:

$$\theta_k = \text{asin}\left(\frac{n_0}{n_k}\sin(\theta_0)\right). \tag{A.3.13}$$

When the sample is completely passed through, the projected cosine of the distance is l_k is the sample thickness d_k. In the sample i where z_i is located, the projected distance is l_i is expressed according to the sum of all previous samples and the position itself:

$$l_k = \begin{cases} \frac{d_k}{\cos\left[\text{asin}\left(\frac{n_0}{n_k}\sin(\theta_0)\right)\right]}, \text{ if } k \neq i \\ \frac{z_i - \sum_{g=0}^{i-1} d_g}{\cos\left[\text{asin}\left(\frac{n_0}{n_k}\sin(\theta_0)\right)\right]}, \text{ if } k = i. \end{cases} \tag{A.3.14}$$

Finishing with this allows us to process the effective absorption of a gaussian beam across an arbitrary number N of interfaces.

A.4 Final formulation of the Illumination prepared for the Acquisition

In a effort to summarise the last section, all important equations used to process the intensity $I(z_i, r)$ in any point (z, r) from the total gaussian intensity I_0^{Tot} are shown as follows:

$$I_0(z,r) = I_0^{Tot} \cdot \left(\frac{w_0}{w(z)}\right)^2 \cdot \exp\left(\frac{-2r^2}{w(z)^2}\right), \tag{A.4.1}$$

$$\text{with } w_i^{\Delta}(z) = w_0 \cdot \sqrt{1 + \left(\frac{(z-\Gamma_i(\Delta))\cdot\lambda_{in}}{\pi w_0^2 \cdot n_i}\right)^2}, \text{ and } \Gamma_i(\Delta) = \Delta \cdot \prod_{l=0}^{i}\left(1 - \frac{n_l}{n_{l-1}}\right) \tag{A.4.2}$$

$$R_i(r, z_i) = z_i \cdot \left[1 + \left(\frac{\gamma}{z_i}\right)^2\right], \text{ with } z_i = (z - \Gamma_i(\Delta)) \text{ and } \gamma = \frac{\pi w_0^2}{\lambda_{in}}, \tag{A.4.3}$$

$$I(z_i, r) = I_0(z_i, r) \cdot 10^{-\Sigma(z_i, r)}, \text{ with } \Sigma(z_i, r) = \sum_{k=0}^{i} \sigma_k \cdot l_k, \tag{A.4.4}$$

$$\text{with } l_k = \begin{cases} \frac{d_k}{\cos\left[\text{asin}\left(\frac{n_0}{n_k}\sin(\theta_0)\right)\right]}, & \text{if } k \neq i \\ \frac{z_i - \sum_{g=0}^{i-1} d_g}{\cos\left[\text{asin}\left(\frac{n_0}{n_k}\sin(\theta_0)\right)\right]}, & \text{if } k = i. \end{cases} \quad \text{and } \theta_0 = \text{asin}\left(\frac{r}{R_i(z_{eff})}\right). \tag{A.4.5}$$

The mathematical understanding is far from easy as this formulation includes a case based representation.

A.5 Acquisition processing

The acquisition involves all sample parts that the light has to cross and all optical elements of the lens/pinhole system described in Figure A.1. The illumination section focused on the gaussian shape of the beam. This part will assume a spherical shape wavefront being created in each point (z^a, r), where z^a is the z coordinate in respect to the first lens L_1.

A.5.1 Effective Distance from L_1

Similar the change of the gaussian beam central position expressed in equation A.3.4, each point (z^a, r) has an apparent position called (z^a_{eff}, r), due to the refractive indexes. This means that their is an intensity distribution depending in the both the object position and the position on which the ray arrives at the lens. For notation purposes we call this position $(0, r' = 0)$, assuming that $\vec{r'}$ is a normalised vector defined along the origin of the lens in $(0,0)$ and $(0, r)$ of the object onto the lens.

The above mentioned change of coordinates is described in Figure 5.4. Geometrically it simplifies the equations. In fact each point on the lens described by the circle of radius r' is equivalent

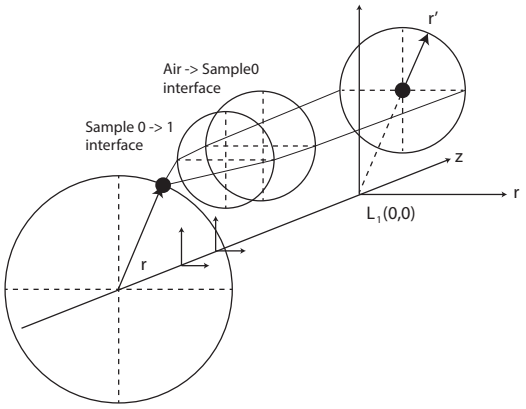

Figure A.3 – Change of coordinate representation. The position coordinates on the lens are expressed in terms of the object position projected onto the lens. The two circles along the way indicate the interfaces showcasing their refractive properties.

in terms of provided intensity, thus preserving the rotational symmetry of the system.

All equations will treat the radial coordinate representation. An effective distance z^a_{eff} is necessary to calculate the object to lens distance seen through the reactive system, that are the samples and substrate. The formulation is as follows:

$$z^a_{eff} = L_{eff} \cdot \cos(\theta^a_0(r')), \tag{A.5.1}$$

with:

$$L_{eff} = \sqrt{(z^a_{eff})^2 + (r')^2},$$

where $\theta^a_0(r')$ is the angle at which the ray impacts the lens. A point source in a medium of refraction index n_0 radiating spherically appears at a distance n_0/n_1 to an observer located in a medium of index n_1. This is why it is possible to express z^a_{eff}, depending solely on distances traveled through each medium z_i and the associated refractive index:

$$z^a_{eff} \quad = \quad \sum_{l=0}^{i} z_i \cdot n_i. \tag{A.5.2}$$

Reintroducing this into equation A.5.1, leads to:

$$\theta^a_0(r') \quad = \quad \text{acos}\left(\frac{z^a_{eff}}{\sqrt{\left[z^a_{eff}\right]^2 + [r']^2}}\right) \tag{A.5.3}$$

This concludes the expressions necessary to the definition of the rays impacting on the coordinate r'. The use of the angle $\theta_0^a(r')$ will be further explained in the next section related to the absorption. Using the standard expression of a spherical wave leads to the following:

$$I_0^a(z_i^a, r, r') = \frac{I(z_i^a, r)}{\sqrt{\left[z_{eff}^a\right]^2 + [r']^2}} \tag{A.5.4}$$

A.5.2 Processing absorption to L_1

The last section analytically expressed $\theta_0^a(r')$ that will be used as the reference point to calculate the physical length l_k that any ray spends in the sample k. Following the refraction laws using the following equation:

$$n_{k+1}\sin(\theta_{k+1}^a(r')) = n_k \sin(\theta_k^a(r')), \tag{A.5.5}$$

$$\theta_k^a(r') = \text{asin}\left[\frac{n_0}{n_k}\sin(\theta_0^a(r'))\right], \tag{A.5.6}$$

$$l_k = \frac{d_k}{\cos\left(\text{asin}\left[\frac{n_0}{n_k}\sin(\theta_0^a(r'))\right]\right)}, \tag{A.5.7}$$

where d_k is replaced with $z_i^a - \sum_{g=0}^{i-1} d_g$ when $i = k$. Coming back the definition of the absorption explained in equation A.3.10:

$$\Sigma^a = \sum_{k=0}^{i} l_k \sigma_k, \tag{A.5.8}$$

This means that finally the intensity reaching the lens in the point r' has the following intensity $I^a(z_i^a, r, r')$:

$$I^a(z_i^a, r, r') = \frac{I(z_i^a, r)}{\sqrt{\left[z_{eff}^a\right]^2 + [r']^2}} \cdot 10^{-\Sigma^a} \tag{A.5.9}$$

A.5.3 Image from a Lens

For any given lens L_j of focal length f_j multiple cases arise. Theses cases depend on the object position. While L_1 deals with physical objects, L_2 can have real as well as imaginary objects. As an example, the image of the first lens can be located after the second lens position. In this case the treatment is different, as of the image was located before L_2. On top of that, the first focal point of a lens represents a singularity. The position $(z_{object}^j, r_{object}^j)$ and $(z_{image}^j, r_{image}^j)$ respectively represent the positions of the object and image in respect to z_{lens}^j the position of the lens. In the following part a summary of each case will be described.

- **The object is located at $z^j_{object} = -\infty$:**
  When $z^j_{object} = -\infty$, the image is located at the distance:

$$z^j_{image} = f_j \tag{A.5.10}$$

  While L_1 does not encounter this situation it can produce an image located at infinity, which corresponds to this scenario for L_2. A beam coming from infinity has parallel rays and therefore no parameter r^j_{image}. The position is expressed through the angle of incidence ψ^j_{image}, leading to:

$$r^j_{image} = \tan(\psi^j_{image}) \cdot f_j \tag{A.5.11}$$

- **The object is located before $z^j_{object} < -f_j$:** This situation is the most classical regime for a normal concave lens. The distance from the focal point will determine the distance after the lens through the following equation:

$$z^j_{image} = \frac{f_j \cdot z^j_{object}}{z^j_{object} - f_j}, \tag{A.5.12}$$

  and the magnification given by:

$$M = \frac{z^j_{image}}{z^j_{object}}, \tag{A.5.13}$$

  ultimately resulting in :

$$r^j_{image} = M \cdot r^j_{object}. \tag{A.5.14}$$

- **The object is located at $z^j_{object} = -f_j$:**
  When the position of the object satisfies $z^j_{object} = -f_j$:

$$z^j_{image} = +\infty \tag{A.5.15}$$

  Rather than r^j_{image} the second position parameter is expressed through ψ^j_{image}, which is the angle of the beam, as all rays travel in parallel.

- **The object is located at $z^j_{lens} > z^j_{object} > f_j$:** This case calls upon the creation of a virtual image situated before the lens and most probably before the initial object. The formalism is similar to the one expressed when the object is located before the lens' focal position:

$$z^j_{image} = -\left(\frac{f_j \cdot |z^j_{object}|}{f_j - |z^j_{object}|}\right), \tag{A.5.16}$$

and the magnification given by:

$$M = \frac{z^j_{image}}{z^j_{object}}, \tag{A.5.17}$$

ultimately resulting in :

$$r^j_{image} = M \cdot r^j_{object}. \tag{A.5.18}$$

- **The object is located at $z^j_{object} > z^j_{lens}$:** not defined .....
- **The object is located at $z^j_{lens} = +\infty$:** There is no difference between the object being at $-\infty$ or $+\infty$, which means that the same formalism can be used, leading to:

$$z^j_{image} = f_j \tag{A.5.19}$$

$$r^j_{image} = \tan(\psi^j_{image}) \cdot f_j. \tag{A.5.20}$$

A.5.4 Image from L_1 and L_2

it is necessary to process the images from L_1 and L_2 in order to process the ray tracing arithmetics of effective projections described in the next paragraph. To each point object in the samples and substrate will be associated an image coordinate called $P^{L_1}_{image} = (z^1_{image}, r^1_{image})$ and $P^{L_2}_{image} = (z^2_{image}, r^2_{image})$ for L_1 and L_2 respectively. Note that this way of proceeding does not take into account aberrations by the lens system. This would result in a smearing off of the ray traceability.

A.5.5 Projecting L_2 and P back onto L_1

The easiest way to compute the photon ratio passing through consecutive element of the system, is to project these elements onto a common plane and then evaluate the throughput on this plane. In this case, having a point source radiating spherically, it is more convenient to project the effective image of L_2 and P back onto L_1. As each ray from a point (z^a_{eff}, r) creates two images (virtual or real) $(z^a_{L_1}, r)$ and $(z^a_{L_2}, r)$, through which each ray has to pass through, it is possible to trace the limits of L_2 back onto L_1 and from P onto L_2 and finally L_1. Projecting a surface through a point is equivalent to a centre-symmetric operation, which conserves the shape and merely inverts and scales the coordinate system. The symmetry conservation of the system is solely dependant in the Pinhole shape. Using a circular pinhole allows to ignore the angular component of the object. On top of that, as stated in the previous section, the object, the images, and the centre of the lenses and pinhole are aligned along the same axis $\vec{r}$. meaning that their respective images will conserve the alignment of their centres.

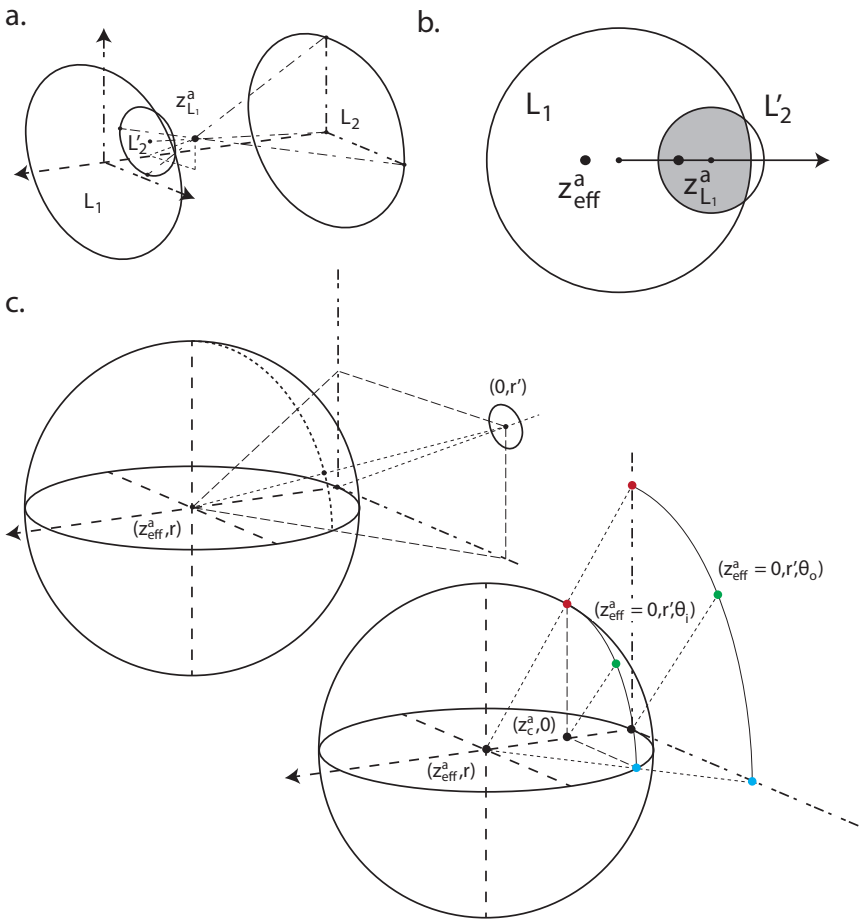

Figure A.4 – a. Visualisation of the projection mechanism of L_2 onto L_1 through the image of the object located at $z^a_{L_1}$. **b.** Explanation of the region overlap. **c. Top** An circular shape located at $(z^a_{eff} = 0, r')$ is seen distorted by the point source located at (z^a_{eff}, r). **c. Bottom** In cylindrical coordinates, where $\vec{z}$ is defined perpendicular to the tangent surface of the circle of radius z^a_{eff} and the lens surface and θ represents the angular position about $\vec{z}$, each arc whom's centre is in $(z^a = 0, r = 0)$ leads to an arc centred at z^a_c.

A.5.6 Effective Projection

All rays allowed through the projections of L_2 and P on L_1 are emitted by a point source that has a radial spread. This means the surface seen by the source is not the same depending on the distance to it. This is similar to seeing a two dimensional object at a grazing angle, its extent becomes negligible. In order to calculate the solid angles representing the optical radiation effectively going through the two dimensional surface, it is projected onto a sphere of that can be of arbitrary radius. For mathematical and geometrical purposes it is easier to consider a sphere of radius z^a_{Jeff}, that was introduced in equation A.5.1. Figure A.4 depicts the referential system.

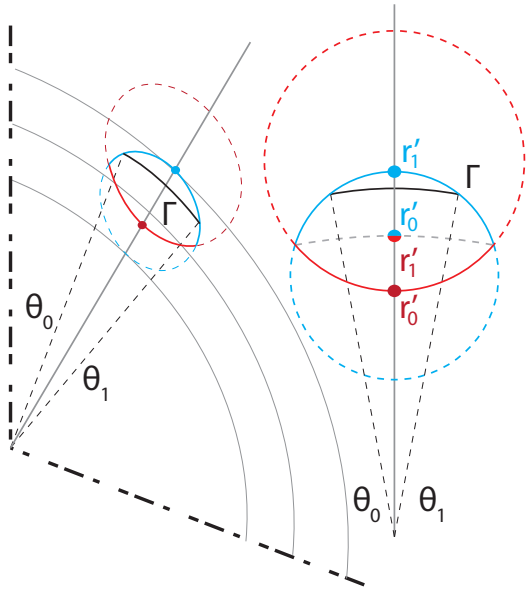

Figure A.5 – Visualisation of the arc and the angle limits θ_0 and θ_1 in the cylindrical referential system. The object is described through the projection of the diverse optical elements in the previous section.

Projecting any shape onto a spherical surface (also called goniometric projection) where each point is expressed according to the coordinate and the sphere centre can be complicated as the distortions only conserves rotational symmetries around the $\vec{z}$ axis. This means that a circle centred around $(z^a_{eff} = 0,0)$ should result in a effective surface that can be integrated along the cylindrical coordinates of the sphere. This is visualised in Figure A.4 (bottom). In cylindrical coordinates, where $\vec{z}$ is defined perpendicular to the tangent surface of the circle of radius z^a_{eff} and the lens surface and θ represents the angular position about $\vec{z}$, each arc whom's centre is located in $(z^a = 0, r = 0)$ leads to an arc centred at z^a_c.

This means that for a given distance r', in any given object on the lens, there is an arc of length Γ_{arc} which describes the ratio $\gamma_{arc}(\Gamma_{arc}, r')$ as follows:

$$\gamma_{arc}(\Gamma_{arc}, r') = \frac{\Gamma_{arc}}{2\pi r'}, \tag{A.5.21}$$

with:

$$\Gamma_{arc} = \int_{\theta_0}^{\theta_1} \text{Object}(r', \theta) d\theta = 2 \cdot \int_{0}^{\theta_1} \text{Object}(r', \theta) d\theta, \tag{A.5.22}$$

θ_0 and θ_1, being the boundaries by the object defined in the cylindrical coordinate system as shown in Figure A.5. $\gamma_{arc}(\Gamma_{arc}, r')$ is then conserved through the goniometric projection, meaning that the only integrable quantity is the circle of centre z^a_c and radius 0.

The surface through which the rays pass at the lens is determined by the overlapping surface elements of consecutive circular objects. This means that the border of this element is not continuous and made up of different circular segments. Figure A.5 showcases the scenario where only two circular objects are present. These form two intersection points between their perimeters, which are symmetrical in respect to the radial axis $\vec{r'}$. Supposed that we have two circular objects of respective centres r'_i and r'_{i+1} on $\vec{r'}$ with respective radiuses R_i and R_{i+1}. We set the referential to have it's origin at r'_i and call $l_{intersec}$ the distance of the orthogonally projected intersection point of r'_i. Then it is possible to write:

$$l_{intersec} = \frac{\left(r'_{i+1} - r'_i\right)^2 - R_i^2 + R_{i+1}^2}{2 \cdot \left(r'_{i+1} - r'_i\right)}. \tag{A.5.23}$$

The orthogonally projected distance of the intersection point from the radial axis $\vec{r'}$, m is described by:

$$m_{intersec} = R_i^2 - l_{intersec}^2. \tag{A.5.24}$$

Now by using simple trigonometric relations it is possible to calculate the real distance of the intersection point from $(z^a = 0, r = 0)$ $r'_{intersec}$, which determines the coordinate of its radial projection $\vec{r'}$:

$$r'^i_{intersec} = \sqrt{R_i^2 - l_{intersec}^2 + (r'_i + l_{intersec})^2}, \tag{A.5.25}$$

with the associated angle $\Psi^i_{intersec}$ for the element i:

$$\Psi^i_{intersec} = \arcsin\left(\frac{r'^i_{intersec} - r'_i}{R_i}\right). \tag{A.5.26}$$

The integration limits of each circular element is therefore given by either the maximal extent of it given by $r'^i_{intersec} = r'_i \pm R_i$ or by the $r'_{intersec}$ described in the previous equation (when applicable) for the lower and upper integration bounds. An example can be seen in Figure **??**

The integration itself will be performed on the sphere after the goniometric projection. The relation translates a coordinate r' into an angular value. The angle $\theta_{r'}$ is expressed between the optical axis $\vec{z}$ and a vector describing the spacial orientation from $(z^a = z^a_{eff}, r)$ to $(z^a = 0, r')$. $\theta_{r'}$ can be expressed as:

$$\theta_{r'} = \arcsin\left(\frac{r'}{\sqrt{(r')^2 + (z^a_{eff})^2}}\right), \tag{A.5.27}$$

leading to the inverse equation:

$$r'(\theta_{r'}) = \frac{\sin^2(\theta_{r'}) \cdot (z^a_{eff})^2}{1 - \sin^2(\theta_{r'})}, \tag{A.5.28}$$

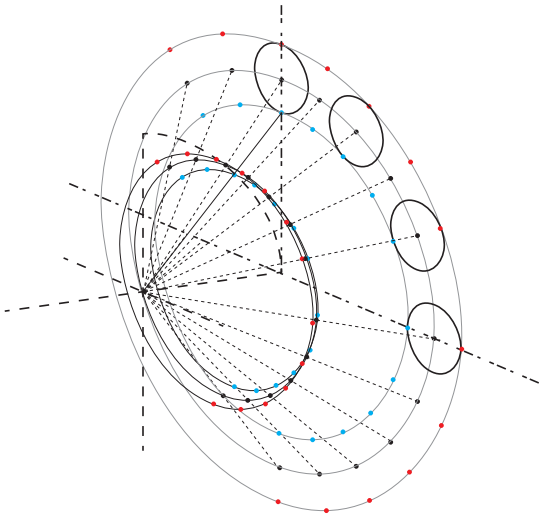

Figure A.6 – Intensity evolution of the two modes selected from Figure 5.7. Note that the sample and substrate modes behave as expected in Figure 5.5

meaning that also the integration boundaries of the integral can be expressed as $\theta^i_{intersect}$ using the previous relation with $r' = r'^i_{intersec}$. It also means that the previously defined arc ratio $\gamma_{arc}(\Gamma_{arc}, r')$ (Equation A.5.22) can be expressed as $\gamma_{arc}(\Gamma_{arc}, \theta_{r'})$. The absorption needs also to be taken into account through it's radial coordinate. In fact equation **??** already stipulates that γ_{abs} the absorption only varies along r' and thus $\theta_{r'}$. The arc coefficient explained in equation A.5.22 is integrated from $\theta_0 = 0$ to θ_1, which is the intersection angle at which the circle of radius r' located at ($z_{eff} = 0$, $r' = 0$) with the object i and can be expressed using equation A.5.23 as follows:

$$\theta_1(r'(\theta_{r'})) = \arccos\left(\frac{r_i'^2 - r'(\theta_{r'})^2 + R_i^2}{2r_i' \cdot r'(\theta_{r'})}\right), \tag{A.5.29}$$

meaning that the final arc $\Gamma_{arc}(r')$ length is expressed as:

$$\Gamma_{arc}(r'(\theta_{r'})) = \theta_1(r'(\theta_{r'})) \cdot r'(\theta_{r'}). \tag{A.5.30}$$

The effective surface will therefore immediately account for the absorption. Using all the previously expressed elements we obtain:

$$S_{effective} = \sum_{i}^{elements} \int_{\theta^i_{intersect}}^{\theta^{i+1}_{intersect}} \gamma_{abs}(r'(\theta_{r'})) \cdot \gamma_{arc}(r'(\theta_{r'})) \cdot 2\pi (z^a_{eff})^2 d\theta_{r'}. \tag{A.5.31}$$

Using this formulation it is possible to obtain the end surface on a sphere through goniometric projection with their weight of absorption. The flux of a point source radiating through a spherical surface with radius z^a_{eff} is expressed through the initial intensity divided by the spherical surface

$4\pi \cdot (z^a_{eff})^2$. This is why the intensity $I_{collect}(z,r)$ going through the effective surface is written:

$$I_{collect}(z,r) = I_0(z,r) \cdot \frac{S_{effective}}{4\pi \cdot (z^a_{eff})^2}, \tag{A.5.32}$$

where z^a_{eff} is defined in relation with z^a through the index system between sample and substrates.

Bibliography

[1] R. H. Mitchell, *Perovskites*. Modern and Ancient, Jan. 2002.

[2] Y. Tokura, "Metal-insulator phenomena in perovskites of transition metal oxide," *Physica B: Physics of Condensed Matter*, vol. 237, pp. 1–5, July 1997.

[3] S. Catalano, M. Gibert, J. Fowlie, J. Iñiguez, J.-M. Triscone, and J. Kreisel, "Rare-earth nickelates RNiO3: thin films and heterostructures," *Reports on Progress in Physics*, pp. i–27, Dec. 2017.

[4] A. R. Chakhmouradian and P. M. Woodward, "Celebrating 175 years of perovskite research: a tribute to Roger H. Mitchell," *Physics and Chemistry of Minerals*, vol. 41, pp. 387–391, May 2014.

[5] *Mineral Database*, vol. 1. Mineral Data Publishing, 1 ed., Oct. 2005.

[6] V. M. Goldschmidt, "Die Gesetze der Krystallochemie," *Naturwissenschaften*, vol. 14, no. 21, pp. 477–485, 1926.

[7] R. S. Roth, "Classification of perovskite and other ABO3-type compounds," vol. 58, pp. 1–14, Feb. 1957.

[8] M. L. Medarde, "Structural, magnetic and electronic properties of perovskites (R = rare earth)," *Journal of Physics: Condensed Matter*, vol. 9, pp. 1679–1707, Feb. 1997.

[9] A. M. Glazer and IUCr, "Simple ways of determining perovskite structures," *Acta Crystallographica Section A: Crystal Physics, Diffraction, Theoretical and General Crystallography*, vol. 31, pp. 756–762, Nov. 1975.

[10] C. J. Howard, H. T. Stokes, and IUCr, "Group-Theoretical Analysis of Octahedral Tilting in Perovskites," *Acta Crystallographica Section B*, vol. 54, pp. 782–789, Dec. 1998.

[11] A. M. Glazer, "The classification of tilted octahedra in perovskites," *Acta Crystallographica Section B Structural Crystallography and Crystal Chemistry*, vol. 28, pp. 3384–3392, Nov. 1972.

[12] H. A. Jahn and E. Teller, “Stability of Polyatomic Molecules in Degenerate Electronic States. I. Orbital Degeneracy,” in *Proceedings of the Royal Society of London. Series A*, pp. 220–235, The Royal Society, July 1937.

[13] S. Roberts, “Dielectric and Piezoelectric Properties of Barium Titanate,” *Physical Review*, vol. 71, pp. 890–895, June 1947.

[14] F. Bloch, “Über die Quantenmechanik der Elektronen in Kristallgittern,” *Zeitschrift für Physik*, vol. 52, no. 7-8, pp. 555–600, 1929.

[15] J. H. d. Boer and E. J. W. Verwey, “Semi-conductors with partially and with completely filled3d-lattice bands,” in *Proceedings of the Physical Society*, pp. 59–71, IOP Publishing, Aug. 1937.

[16] IUPAC, “Compendium of Chemical Terminology,” pp. 1–1670, Mar. 2012.

[17] N. F. Mott, “Metal-Insulator Transition,” *Reviews of Modern Physics*, vol. 40, pp. 677–683, Oct. 1968.

[18] N. F. Mott, “The Basis of the Electron Theory of Metals, with Special Reference to the Transition Metals,” in *Proceedings of the Physical Society*, pp. 416–422, H. H. Wills Physical Laboratory, University of Bristol, IOP Publishing, July 1949.

[19] J. Zaanen, G. A. Sawatzky, and J. W. Allen, “Band gaps and electronic structure of transition-metal compounds,” *Physical Review Letters*, vol. 55, pp. 418–421, July 1985.

[20] T. Mizokawa, H. Namatame, A. Fujimori, K. Akeyama, H. Kondoh, H. Kuroda, and N. Kosugi, “Origin of the Band Gap in the Negative Charge-Transfer-Energy Compound NaCu2,” *Physical Review Letters*, vol. 70, pp. 1565–1565, Mar. 1993.

[21] S. Middey, J. Chakhalian, P. Mahadevan, J. W. Freeland, A. J. Millis, and D. D. Sarma, “Physics of Ultrathin Films and Heterostructures of Rare-Earth Nickelates,” *Annual Review of Materials Research*, vol. 46, pp. 305–334, July 2016.

[22] M. C. Weber, M. Guennou, N. Dix, D. Pesquera, F. Sánchez, G. Herranz, J. Fontcuberta, L. López-Conesa, S. Estradé, F. Peiró, J. Iñiguez, and J. Kreisel, “Multiple strain-induced phase transitions in LaNiO3thin films,” *Physical Review B*, vol. 94, pp. 014118–11, July 2016.

[23] F. C. Frank and J. H. van der Merwe, “One-Dimensional Dislocations. I. Static Theory,” *Proceedings of the Royal Society A: Mathematical, Physical and Engineering Sciences*, vol. 198, pp. 205–216, Aug. 1949.

[24] D.-M. D. Hwang, “Strain relaxation in lattice-mismatched epitaxy,” *Materials Chemistry and Physics*, vol. 40, no. 4, pp. 291–297, 1995.

[25] T. Wang, K. Ganguly, P. Marshall, P. Xu, and B. Jalan, "Critical thickness and strain relaxation in molecular beam epitaxy-grown SrTiO 3films," *Applied Physics Letters*, vol. 103, pp. 212904–5, Nov. 2013.

[26] G. Sclauzero, K. Dymkowski, and C. Ederer, "Tuning the metal-insulator transition in d1and d2perovskites by epitaxial strain: A first-principles-based study," *Physical Review B*, vol. 94, pp. 245109–11, Dec. 2016.

[27] C. Ederer and N. A. Spaldin, "Effect of Epitaxial Strain on the Spontaneous Polarization of Thin Film Ferroelectrics," *Physical Review Letters*, vol. 95, pp. 257601–4, Dec. 2005.

[28] K. J. Choi, "Enhancement of Ferroelectricity in Strained BaTiO3 Thin Films," *Science*, vol. 306, pp. 1005–1009, Nov. 2004.

[29] N. A. Pertsev, A. G. Zembilgotov, and A. K. Tagantsev, "Effect of Mechanical Boundary Conditions on Phase Diagrams of Epitaxial Ferroelectric Thin Films," *Physical Review Letters*, vol. 80, pp. 1988–1991, Mar. 1998.

[30] C. He, T. D. Sanders, M. T. Gray, F. J. Wong, V. V. Mehta, and Y. Suzuki, "Metal-insulator transitions in epitaxial LaVO 3and LaTiO 3films," *Physical Review B*, vol. 86, pp. 081401–4, Aug. 2012.

[31] D. Simpson, "Multiferroics: progress and prospects in thin films," pp. 1–9, Dec. 2006.

[32] G. Catalan, "Progress in perovskite nickelate research," *Phase Transitions*, vol. 81, pp. 729–749, July 2008.

[33] J. A. Alonso, J. L. García-Muñoz, M. T. Fernández-Díaz, M. A. G. Aranda, M. J. Martínez-Lope, and M. T. Casais, "Charge Disproportionation in RNiO3 Perovskites: Simultaneous Metal-Insulator and Structural Transition in YNiO3," *Physical Review Letters*, vol. 82, pp. 3871–3874, May 1999.

[34] J. Torrance, P. Lacorre, A. Nazzal, E. Ansaldo, and C. Niedermayer, "Systematic study of insulator-metal transitions in perovskites RNiO3 (R=Pr,Nd,Sm,Eu) due to closing of charge-transfer gap," *Physical Review B*, vol. 45, no. 14, pp. 8209–8212, 1992.

[35] T. C. Huang, W. Parrish, H. Toraya, P. Lacorre, and J. B. Torrance, "High-temperature crystal structures of orthorhombic and rhombohedral PrNiO3," *Materials Research Bulletin*, vol. 25, no. 9, pp. 1091–1098, 1990.

[36] I. I. Mazin, D. I. Khomskii, R. Lengsdorf, J. A. Alonso, W. G. Marshall, R. M. Ibberson, A. Podlesnyak, M. J. Martínez-Lope, and M. M. Abd-Elmeguid, "Charge Ordering as Alternative to Jahn-Teller Distortion," *Physical Review Letters*, vol. 98, pp. 241–4, Apr. 2007.

[37] U. Staub, G. I. Meijer, F. Fauth, R. Allenspach, J. G. Bednorz, J. Karpinski, S. M. Kazakov, L. Paolasini, and F. d'Acapito, "Direct Observation of Charge Order in an Epitaxial NdNiO3Film," *Physical Review Letters*, vol. 88, pp. 1039–4, Mar. 2002.

[38] K. Haule and G. L. Pascut, "Mott Transition and Magnetism in Rare Earth Nickelates and its Fingerprint on the X-ray Scattering," *Scientific Reports*, vol. 7, pp. 1–7, Aug. 2017.

[39] J. L. García-Muñoz, J. Rodríguez-Carvajal, and P. Lacorre, "Neutron-diffraction study of the magnetic ordering in the insulating regime of the perovskites RNiO3 (R=Pr and Nd)," *Physical Review B (Condensed Matter)*, vol. 50, pp. 978–992, July 1994.

[40] A. E. Bocquet, T. Mizokawa, T. Saitoh, H. Namatame, and A. Fujimori, "Electronic structure of 3d-transition-metal compounds by analysis of the 2p core-level photoemission spectra," *Physical Review B (Condensed Matter)*, vol. 46, pp. 3771–3784, Aug. 1992.

[41] T. Mizokawa, A. Fujimori, H. Namatame, K. Akeyama, and N. Kosugi, "Electronic structure of the local-singlet insulator NaCuO2," *Physical Review B (Condensed Matter)*, vol. 49, pp. 7193–7204, Mar. 1994.

[42] T. Mizokawa, D. I. Khomskii, and G. A. Sawatzky, "Spin and charge ordering in self-doped Mott insulators," *arXiv.org*, pp. 11263–11266, Aug. 1999.

[43] T. Mizokawa, A. Fujimori, T. Arima, Y. Tokura, N. Mōri, and J. Akimitsu, "Electronic structure of PrNiO3 studied by photoemission and x-ray-absorption spectroscopy: Band gap and orbital ordering," *Physical Review B (Condensed Matter)*, vol. 52, pp. 13865–13873, Nov. 1995.

[44] S. Johnston, A. Mukherjee, I. Elfimov, M. Berciu, and G. A. Sawatzky, "Charge disproportionation without charge transfer in the rare-earth-element nickelates as a possible mechanism for the metal-insulator transition.," *Physical Review Letters*, vol. 112, pp. 106404–106404, Mar. 2014.

[45] H. Park, A. J. Millis, and C. A. Marianetti, "Site-Selective Mott Transition in Rare-Earth-Element Nickelates," *Physical Review Letters*, vol. 109, p. 156402, Oct. 2012.

[46] S. Johnston, A. Mukherjee, I. Elfimov, M. Berciu, and G. A. Sawatzky, "Charge Disproportionation without Charge Transfer in the Rare-Earth-Element Nickelates as a Possible Mechanism for the Metal-Insulator Transition," *Physical Review Letters*, vol. 112, pp. 106404–5, Mar. 2014.

[47] S. Catalano, M. Gibert, V. Bisogni, O. E. Peil, F. He, R. Sutarto, M. Viret, P. Zubko, R. Scherwitzl, A. Georges, G. A. Sawatzky, T. Schmitt, and J.-M. Triscone, "Electronic transitions in strained SmNiO 3thin films," *APL Materials*, vol. 2, pp. 116110–8, Nov. 2014.

[48] V. Scagnoli, U. Staub, A. M. Mulders, M. Janousch, G. I. Meijer, G. Hammerl, J. M. Tonnerre, and N. Stojic, "Role of magnetic and orbital ordering at the metal-insulator transition in NdNiO3," *Physical Review B*, vol. 73, pp. 420–4, Mar. 2006.

[49] J. L. García-Muñoz, J. Rodríguez-Carvajal, P. Lacorre, and J. B. Torrance, "Neutron-diffraction study of RNiO3 (R=La,Pr,Nd,Sm): Electronically induced structural changes

across the metal-insulator transition," *Physical Review B (Condensed Matter)*, vol. 46, pp. 4414–4425, Aug. 1992.

[50] G. Gou, I. Grinberg, A. M. Rappe, and J. M. Rondinelli, "Lattice normal modes and electronic properties of the correlated metal LaNiO 3," *Physical Review B*, vol. 84, pp. 144101–13, Oct. 2011.

[51] R. J. Angel, J. Zhao, and N. L. Ross, "General Rules for Predicting Phase Transitions in Perovskites due to Octahedral Tilting," *Physical Review Letters*, vol. 95, pp. 536–4, July 2005.

[52] S. J. May, J. W. Kim, J. M. Rondinelli, E. Karapetrova, N. A. Spaldin, A. Bhattacharya, and P. J. Ryan, "Quantifying octahedral rotations in strained perovskite oxide films," *arXiv.org*, p. 014110, Feb. 2010.

[53] J. Fowlie, M. Gibert, G. Tieri, A. Gloter, J. iguez, A. Filippetti, S. Catalano, S. Gariglio, A. Schober, M. Guennou, J. Kreisel, O. St phan, and J.-M. Triscone, "Conductivity and Local Structure of LaNiO 3Thin Films," *Advanced Materials*, vol. 29, pp. 1605197–5, Mar. 2017.

[54] F. Capon, P. Ruello, J.-F. Bardeau, P. Simon, P. Laffez, B. Dkhil, L. Reversat, K. Galicka, and A. Ratuszna, "Metal–insulator transition in thin films of R xR 1– x´NiO 3compounds: DC electrical conductivity and IR spectroscopy measurements," *Journal of Physics: Condensed Matter*, vol. 17, pp. 1137–1150, Feb. 2005.

[55] S. Catalano, M. Gibert, V. Bisogni, F. He, R. Sutarto, M. Viret, P. Zubko, R. Scherwitzl, G. A. Sawatzky, T. Schmitt, and J.-M. Triscone, "Tailoring the electronic transitions of NdNiO3 films through (111)pc oriented interfaces," *APL Materials*, vol. 3, p. 062506, June 2015.

[56] C. Girardot, J. Kreisel, S. Pignard, N. Caillault, and F. Weiss, "Raman scattering investigation across the magnetic and MI transition in rare earth nickelate RNiO3 (R = Sm, Nd) thin films," *arXiv.org*, p. 104101, July 2008.

[57] A. Smekal, "Zur Quantentheorie der Dispersion," *Die Naturwissenschaften*, vol. 11, pp. 873–875, Oct. 1923.

[58] J. W. Strutt, "On the Scattering of Light by small Particles." Cambridge University Press, Cambridge, 2009.

[59] C. V. Raman and K. S. Krishnan, "A new type of secondary radiation," *Nature*, vol. 121, p. 501, 1928.

[60] D. A. Long, *The Raman effect: A unified Treatment of theory of Raman Scattering by Molecules*. A Unified Treatment of the Theory of Raman Scattering by Molecules, Chichester, UK: Wiley, May 2002.

[61] R. P. Feynman, R. B. Leighton, and M. L. Sands, *The Feynman Lectures on Physics: Mainly electromagnetism and matter*. Addison Wesley Publishing Company, 1965.

[62] F. Schwabl, *Advanced Quantum Mechanics*. Springer Science & Business Media, Aug. 2008.

[63] A. K. Arora, M. Rajalakshmi, T. R. Ravindran, and V. Sivasubramanian, "Raman spectroscopy of optical phonon confinement in nanostructured materials," *Journal of Raman Spectroscopy*, vol. 38, no. 6, pp. 604–617, 2007.

[64] M. A. Islam, J. M. Rondinelli, and J. E. Spanier, "Normal mode determination of perovskite crystal structures with octahedral rotations: theory and applications," *Journal of Physics: Condensed Matter*, vol. 25, pp. 175902–15, Apr. 2013.

[65] G. F. Koster, *Properties of the thirty-two point groups*. The MIT Press, Dec. 1963.

[66] D. S. Knight and W. B. White, "Characterization of diamond films by Raman spectroscopy," *Journal of Materials Research*, vol. 4, pp. 385–393, Mar. 1989.

[67] S. A. Solin and A. K. Ramdas, "Raman Spectrum of Diamond," *Physical Review B*, vol. 1, pp. 1687–1698, Feb. 1970.

[68] A. K. Arora and M. Rajalakshmi, "Phonon confinement in nanostructured materials," *... of Nanoscience and ...*, 2004.

[69] H. Richter, Z. P. Wang, and L. Ley, "The one phonon Raman spectrum in microcrystalline silicon," *Solid State Communications*, vol. 39, no. 5, pp. 625–629, 1981.

[70] I. H. Campbell and P. M. Fauchet, "The effects of microcrystal size and shape on the one phonon Raman spectra of crystalline semiconductors," *Solid State Communications*, vol. 58, no. 10, pp. 739–741, 1986.

[71] D. Bersani, P. P. Lottici, and X.-Z. Ding, "Phonon confinement effects in the Raman scattering by TiO2 nanocrystals," *Applied Physics Letters*, vol. 72, pp. 73–75, Jan. 1998.

[72] Z. M. Nassar and M. H. Yükselici, "The Effect of Strain and Grain Size on Phonon and Electron Confinements in TiO 2Thin Films," *physica status solidi (b)*, vol. 71, pp. 1700636–14, Feb. 2018.

[73] N. Begum, A. S. Bhatti, F. Jabeen, S. Rubini, and F. Martelli, "Lineshape analysis of Raman scattering from LO and SO phonons in III-V nanowires," *Journal of Applied Physics*, vol. 106, pp. 114317–6, Dec. 2009.

[74] D. V. Murphy and S. R. J. Brueck, "Optical Microanalysis of Small Semiconductor Structures," *MRS Proceedings*, vol. 17, p. 253, Feb. 2011.

[75] M. Born and E. Wolf. Cambridge: Cambridge Univ. Press, 1999.

[76] L. Gasparov, T. Jegorel, L. Loetgering, S. Middey, and J. Chakhalian, “Thin Film Substrates from the Raman spectroscopy point of view,” *arXiv.org*, pp. 465–469, Oct. 2013.

[77] V. G. Sathe and A. Dubey, “Broken symmetry in LaAlO 3single crystal probed by resonant Raman spectroscopy,” *Journal of Physics: Condensed Matter*, vol. 19, pp. 382201–8, Aug. 2007.

[78] Y. Maruyama and W. Kanematsu, “Confocal volume in laser Raman microscopy depth profiling,” in *Journal of Applied Physics*, pp. 103107–103107, National Institute of Advanced Industrial Science and Technology, Tokyo, Japan, Nov. 2011.

[79] N. J. Everall, “Confocal Raman microscopy: common errors and artefacts,” *The Analyst*, vol. 135, no. 10, pp. 2512–11, 2010.

[80] A. L. Stancik and E. B. Brauns, “A simple asymmetric lineshape for fitting infrared absorption spectra,” *Vibrational Spectroscopy*, vol. 47, pp. 66–69, May 2008.

[81] X. Li, T. Yang, S. Li, D. Wang, Y. Song, and S. Zhang, “Raman spectroscopy combined with principal component analysis and k nearest neighbour analysis for non-invasive detection of colon cancer,” *Laser Physics*, pp. 1–9, Feb. 2016.

[82] Y. H. Ong, M. Lim, and Q. Liu, “Comparison of principal component analysis and biochemical component analysis in Raman spectroscopy for the discrimination of apoptosis and necrosis in K562 leukemia cells,” *Optics Express*, vol. 20, pp. 22158–, Sept. 2012.

[83] X. Li, R. Zhou, Y. Xu, X. Wei, Y. He, X. Li, R. Zhou, Y. Xu, X. Wei, and Y. He, “Spectral unmixing combined with Raman imaging, a preferable analytic technique for molecule visualization,” *Applied Spectroscopy Reviews*, vol. 0, pp. 1–22, Sept. 2016.

[84] K. Pearson, “LIII.On lines and planes of closest fit to systems of points in space,” *Philosophical Magazine Series 6*, vol. 2, no. 11, pp. 559–572, 1901.

[85] H. Hotelling, “Analysis of a complex of statistical variables into principal components.,” *Journal of Educational Psychology*, vol. 24, no. 6, pp. 417–441, 1933.

[86] R. Chávez-Arroyo, S. Lozano-Galiana, J. Sanz-Rodrigo, and O. Probst, “On the Application of Principal Component Analysis for Accurate Statistical-dynamical Downscaling of Wind Fields,” *Energy Procedia*, vol. 40, pp. 67–76, 2013.

[87] J. F. SCOTT, “Prospects for Ferroelectrics: 2012–2022,” *ISRN Materials Science*, vol. 2013, no. 7, pp. 1–24, 2013.

[88] G. F. Nataf, N. Barrett, J. Kreisel, and M. Guennou, “Raman signatures of ferroic domain walls captured by principal component analysis,” *Journal of Physics: Condensed Matter*, vol. 30, no. 3, p. 035902, 2017.

[89] S. Sra and I. S. Dhillon, “Generalized Nonnegative Matrix Approximations with Bregman Divergences,” in *Advances in Neural Information Processing Systems 18* (Y. Weiss, B. S. o. lkopf, and J. C. Platt, eds.), pp. 283–290, MIT Press, 2006.

[90] “Algorithms for Non-negative Matrix Factorization,” pp. 1–7, Jan. 2016.

[91] J. Kim and H. Park, “Fast Nonnegative Matrix Factorization: An Active-Set-Like Method and Comparisons,” *SIAM Journal on Scientific Computing*, vol. 33, pp. 3261–3281, Jan. 2011.

[92] J. Kunc, Y. Hu, J. Palmer, C. Berger, and W. A. de Heer, “A method to extract pure Raman spectrum of epitaxial graphene on SiC,” *arXiv.org*, p. 201911, July 2013.

[93] H. Kim and H. Park, “Nonnegative Matrix Factorization Based on Alternating Nonnegativity Constrained Least Squares and Active Set Method,” *SIAM Journal on Matrix Analysis and Applications*, vol. 30, pp. 713–730, Jan. 2008.

[94] N. Chaban, M. Weber, S. Pignard, and J. Kreisel, “Phonon Raman scattering of perovskite LaNiO3 thin films,” *arXiv.org*, p. 031915, June 2010.

[95] M. V. Abrashev, A. P. Litvinchuk, M. N. Iliev, R. L. Meng, V. N. Popov, V. G. Ivanov, R. A. Chakalov, and C. Thomsen, “ Comparative study of optical phonons in the rhombohedrally distorted perovskites LaAlO 3 and LaMnO 3 ,” *Physical Review B*, vol. 59, no. 6, pp. 4146–4153, 1999.

[96] J. F. Scott, “Raman Study of Trigonal-Cubic Phase Transitions in Rare-Earth Aluminates,” *Physical Review B*, vol. 1, no. 2, pp. 942–942, 1970.

[97] M. N. Iliev, M. V. Abrashev, J. Laverdière, S. Jandl, M. M. Gospodinov, Y. Q. Wang, and Y. Y. Sun, “Distortion-dependent Raman spectra and mode mixing in RMnO3perovskites (R=La,Pr,Nd,Sm,Eu,Gd,Tb,Dy,Ho,Y),” *Physical Review B*, vol. 73, pp. 413–6, Feb. 2006.

[98] R. Scherwitzl, S. Gariglio, M. Gabay, P. Zubko, M. Gibert, and J.-M. Triscone, “Metal-insulator transition in ultrathin LaNiO3 films.,” *Physical Review Letters*, vol. 106, p. 246403, June 2011.

[99] W. Setyawan and S. Curtarolo, “High-throughput electronic band structure calculations: Challenges and tools,” *Computational Materials Science*, vol. 49, pp. 299–312, Aug. 2010.

[100] A. Mercy, J. Bieder, J. Iñiguez, and P. Ghosez, “Structurally triggered metal-insulator transition in rare-earth nickelates,” *Nature Communications*, vol. 8, pp. 1–6, Nov. 2017.

[101] M. Zaghrioui, A. Bulou, P. Laffez, and P. Lacorre, “Raman study of metal-insulator transition in NdNiO 3 thin films,” *Journal of Magnetism and Magnetic Materials*, vol. 211, pp. 238–242, Mar. 2000.

[102] J. L. García-Muñoz, M. A. G. Aranda, J. A. Alonso, and M. J. Martínez-Lope, "Structure and charge order in the antiferromagnetic band-insulating phase of NdNiO3," *Physical Review B*, vol. 79, pp. 134432–5, Apr. 2009.

[103] I. S. Smirnova, "Normal modes of the LaMnO 3 Pnma phase: comparison with La 2CuO 4 Cmca phase," *Physica B: Physics of Condensed Matter*, vol. 262, pp. 247–261, Apr. 1999.

[104] M. Zaghrioui, A. Bulou, P. Lacorre, and P. Laffez, "Electron diffraction and Raman scattering evidence of a symmetry breaking at the metal-insulator transition of NdNiO3," *Physical Review B*, vol. 64, pp. 225–4, Aug. 2001.

[105] G. Kresse and J. Furthmüller, "Efficient iterative schemes for ab initio total-energy calculations using a plane-wave basis set," *Physical Review B (Condensed Matter)*, vol. 54, pp. 11169–11186, Oct. 1996.

[106] G. Kresse and D. Joubert, "From ultrasoft pseudopotentials to the projector augmented-wave method," *Physical Review B*, vol. 59, pp. 1758–1775, Jan. 1999.

[107] P. E. Blöchl, "Projector augmented-wave method," *Physical Review B*, vol. 50, no. 24, pp. 17953–17979, 1994.

[108] J. P. Perdew, A. Ruzsinszky, G. I. Csonka, O. A. Vydrov, G. E. Scuseria, L. A. Constantin, X. Zhou, and K. Burke, "Restoring the Density-Gradient Expansion for Exchange in Solids and Surfaces," *Physical Review Letters*, vol. 100, pp. 136406–4, Apr. 2008.

[109] S. L. Dudarev, G. A. Botton, S. Y. Savrasov, C. J. Humphreys, and A. P. Sutton, "Electron-energy-loss spectra and the structural stability of nickel oxide: An LSDA+U study," *Physical Review B (Condensed Matter and Materials Physics)*, vol. 57, pp. 1505–1509, Jan. 1998.

[110] J. Suda, T. Mori, H. Saito, O. Kamishima, T. Hattori, and T. Sato, "First-order Raman spectra and lattice dynamics of a NdGaO3crystal," *Physical Review B*, vol. 66, pp. 174302–9, Nov. 2002.

[111] O. Kamishima, H. Koyama, R. Takahashi, Y. Abe, T. Sato, and T. Hattori, "Raman study on symmetry analysis in NdGaO3," *Journal of Physics: Condensed Matter*, vol. 14, pp. 3905–3919, Apr. 2002.